UNIVERSITA' DEGLI STUDI DI PARMA

Dottorato di ricerca in
INGEGNERIA INDUSTRIALE

Ciclo XXVII

Experimental and numerical study of linear vibrations of a thin plate in contact with bounded liquid

Coordinatore:
Chiar.mo Prof. INGEGNER AGOSTINO GAMBAROTTA

Tutor:
Chiar.mi Proff.: INGEGNER LUCA COLLINI,
INGEGNER ELISABETTA MANCONI,
INGEGNER MARCELLO VANALI

Dottoranda: INGEGNER
MICHELA BONELLI



UNIVERSITÀ DEGLI STUDI DI PARMA

FACOLTÀ DI INGEGNERIA
Dipartimento di Ingegneria Industriale

DOTTORATO DI RICERCA
XXVII CICLO

Experimental and numerical study of linear vibrations of a thin plate in contact with bounded liquid

Michela Bonelli

Tutor:

Prof. Ing. Luca Collini

Prof.ssa Ing. Elisabetta Manconi

Prof. Ing. Marcello Vanali

Table of contents

INTRODUCTION 4

ABSCTRAT 7

LITERATURE REVIEW 8

CHAPTER 1: The System 14

CHAPTER 2: Experimental Scanning Laser of the Plate Surface 30

CHAPTER 3: Modal Analysis: Theory and Practice 79

CHAPTER 4: Mobility Measurement Technique 131

CHAPTER 5: Experimental Modal Analysis of the Thin Plate 149

CHAPTER 6: Modal Shapes and Parameters Extraction 172

CHAPTER 7: Hydroelastic Vibrations based on Finite Element Method 228

ACKNOWLEDGMENTS 259

REFERENCES 260

Introduction

The experimental study of structural vibration has always provided a major contribution to understand and to control the many vibration phenomena encountered in practice.
Since the very early days awareness of vibrations, experimental observations have been made in order to better understand the nature of vibration response levels, and to validate theoretical models and predictions. In fact, by analysing the dynamic response to suitable excitation sources, it is possible to define the mechanical properties of the structures, as well as to identify typical features within their global behaviour. The analysis of structural vibration is necessary to calculate the natural frequencies of a structure, and the response to the expected excitation. From the analysis it can be seen which structural parameters most affect the dynamic response so that, if an improvement or change in the response is required, the system can be modified in the most appropriate way. Very often, the dynamic response can only be effectively controlled by changing the damping in the structures: there are many sources of damping to consider and the ways of changing the damping using both active and passive methods require an understanding of their dynamic performance. The two vibration measurement objectives indicated above represent two corresponding types of tests. The firs is one where vibration forces or, more usually, responses are measured during "operation" of the system under study, while the second is a test where the structure or components are vibrated with a known excitation. This type of test, including both the data acquisition and its subsequent analysis, is nowadays called ***Modal Testing***. There are many applications to which the results from a modal test may be put and several of these are, in fact, quite powerful. Perhaps the most commonly used application is *the measurement of vibration modes* in order to compare these with corresponding data produced by finite element or other theoretical model.
This application is often born out of a need or desire to validate theoretical model with the intention of predicting response levels to complex excitations. For this specific application, all that is required from the test are: accurate estimates of natural frequencies, descriptions of the mode shapes using appropriate elements and accuracy to permit their identification, correlation with those to theoretical model.

The development of the procedure outlined above is the ***correlation***. This method allows to combine quantitatively the two sets of data (experimental and theoretical results) in order to identify the causes of discrepancies between predicted and measured properties. Modal Test is also applied with the intention of producing a mathematical model of a component which may then be used to incorporate that component into a structural assembly. Here again, it is a fully quantitative model that is sought, with accurate data required for natural frequencies, modal damping and mode shapes, with the added constraint that all modes must be included simultaneously. It is not sufficient to confine the model to certain individual modes, as may be done for the previous comparisons or correlations, since out-of-range modes will influence the structure's dynamic behaviour in a given frequency range of interest for the complete assembly. Also, it is not possible to ignore certain modes which exist in the range of interest even if it may present some difficulties for measurement or analysis. A different application for the model produced by a modal test is that of *force determination*. There are a number of situations where knowledge of the dynamic forces causing vibration is very important even where direct measurement of these forces is not practical. For these cases, one solution is offered by a process able to combine measurements of the response caused by the forces with mathematical description of the transfer functions of the structure in order to deduce the forces. This process can be very sensitive to the accuracy of the model used for the structure and so it is essential that the model itself must be derived from measurements: in other words, via a modal test. There are different test methods to investigate the behaviour of a structure subjected to excitations, for example, *harmonic*, *random* and *transient vibrations*. Many approaches toward this task have been taken, including direct measurement of the required information, mathematical modeling and exact solution of the resulting partial differential equation(s) of motion, discrete finite element modeling and solution of the resulting large array of second-order differential equations, energy method, and the joining together of solutions corresponding to subsets of the total system. Real structures and machines are made up of components possessing finite levels of rigidity and mass, and non-perfect energy transfer characteristics. As a result the imposition of external or internal loads, during operation of the structure or machine, will lead to nonzero deformations at all times and will under certain conditions lead to high amplitude vibrations at specific frequencies, or to instabilities of the static and dynamic deformations.

It is very important in modern engineering practice to be able accurately to predict these deflections, instabilities and high amplitude vibrations, so that control can be exercised over the static and/or dynamic stress levels, response amplitude levels, and transmitted noise levels in accordance with the needs of the particular application. In the last years, the use of *Modal Test* techniques have received a great attention due to their importance in various engineering applications: for example, a series of experimental tests have been addressed to very light structures in order to obtain natural frequencies and mode shapes, because one needs to understand the real behaviour of the structure subjected to various stresses from both inside and from the outside environment, so as to ensure an adequate stability and structural strength, while maintaining a reduced weight. Thin-walled structures in the form of plates and shells are encountered in many branches of technology, such as civil, mechanical, aeronautical, marine, and chemical engineering. Such a widespread use of plate and shell structures arises from their intrinsic properties. When suitably designed, even very thin plates, and especially shells, can support large loads. Thus, they are utilized in structures such as aerospace vehicles in which light weight is essential. The vibration of plates and shells, and the fundamental concepts of dynamic analysis for free and forced vibrations of unstiffened and stiffened plate and shell structures are considered principally for aeronautical and space structures. Furthermore, the presence of thin walls in contact with a liquid is studied through the use of vibration with the aim of understanding the interaction between fluid and structure. It is also necessary to point out that, in certain operating contexts, vibration is an undesired phenomenon that should be deleted, or at least reduced in order to ensure a match between the vibration response and some specified shapes or performance criteria. For example, vibration of an automobile or truck can lead to driver discomfort and eventually, fatigue. Structural or mechanical failure can often result from sustained vibration (e.g., cracks in airplane wings); electronic components used in airplanes, automobiles, machines and so, may also fail because of vibration, shock, and/or sustained vibration input.

Abstract

In this paper the dynamical response of a thin plate in contact with a liquid (water) on one side has been experimentally studied, considering different filling levels. The free liquid surface is free to slosh and the water is delimited by practically rigid walls, except for the thin plate. In particular, the specific case of rectangular tank with a vibrating thin plate wall is analyzed in the present study. In particular, the execution of the *linear tests* is the primary objective of this thesis: the five experimental tests have been realized with the aim to describe the dynamic response (natural frequency) of the thin plate, both when the tank is empty that when the tank is filled with different levels of liquid. For this purpose, the liquid-coupled natural frequencies of the plate are obtained carrying out ***Modal Analysis*** which allows to extract ***Modal Shapes*** of the thin plate. The Modal Shapes have been derived from the ***Frequency Response Functions*** (**FRFs**) measured by the use of a Mesh Grid Points which consent to calculate, for each point, the dynamical response of the plate as a result of an excitation transmitted to the system. In particular, the plate deflection due to hydrostatic pressure plays a significant role in changing the plate nonlinearity, and experimental tests carried out by the use of a scanning laser confirm a non-linear dependency between the hydrostatic pressure exerted by the liquid on the plate surface and its consequent deformation. In order to check and verify the experimental results, three-dimensional finite element analyses is also carried out for the plate-tank system using a commercial computer code, ***Comsol Multiphysics***. In this specific study, numerical simulations have been particularly useful to verify and quantify the deviation between numerical natural frequencies obtained during the experimental tests and those achieved by the **FEM analysis**. In this regard, it is necessary to emphasize that the plate presents microscopic geometric imperfections, can not be eliminated and attributable, mainly, to the processes of machining and to thermal stress.

Literature Review

Many researchers have investigated the change in natural frequencies when a structure is in contact with a liquid. There have been many theoretical and experimental researchers on the dynamic characteristics of single plate in contact with water. The hydroelastic vibration on a floating plate has been studied by **Robinson** and **Palmer** [1]. **Ginsberg** and **Chu** [2] developed an alternative method to derive the mode shapes of a plate in contact with a heavy fluid. A formulation to study dynamics of a flexible bottom plate resting on elastic foundation of an otherwise rigid container has been considered by **Chiba** [3]. **Chiba** [4] also developed experiments on non-linear hydroelastic vibration of clamped free shells that were empty and partially filled with water. **Grant A.Vogl** and **Michael W.Hyer** [5] considers the linear vibration characteristics of square laminates relative to their room-temperature static equilibrium configurations. A *Rayleigh–Ritz* approach combined with *Hamilton's principle* is used to provide approximate solutions to this vibration problem. A finite element model is also used to study the vibration characteristics and to compare with the findings for the developed analysis. **Ivan D. Breslavsky**, **Marco Amabili**, **Mathias Legrand** [6] examined Static deflection as well as free and forced large-amplitude vibrations of thin rectangular rubber plates under uniformly distributed pressure. The non-linear elastic deformation of the material, and geometrical non-linearity were described by a *neo-Hookean* constitutive law. Some investigators have analysed the problem of the occurrence of simultaneous resonances in a parametrically-excited and simply-supported rectangular plate. **Hai Nguyen** [7], in regard to the dynamic instability of a thin and flat rectangular plate, worked out an analysis based on the dynamic analogue of *Von Karman's large-deflection theory*, and the governing equations are satisfied using the orthogonally properties of the assumed functions. The fundamental study in the analysis of large-amplitude vibrations of rectangular plates is due to **Marco Amabili** [8] who elaborated a study relating to the non-linear vibrations of rectangular plates having different boundary conditions. Three different boundary conditions are considered and results are compared: (i) simply supported plates with immovable edges; (ii) simply supported plates with movable edges; and (iii) fully clamped plates; the effect of geometric imperfection was also investigated. A theoretical method is developed to investigate free vibrations of circular plates immersed in fluids and a series of experimental tests are presented to validate the model.

Recent studies have been developed thanks to research carried out by **Ehsan Askari**, **Kyeong-Hoon Jeong** and **Marco Amabili** [9]; these researchers presented a theoretical method to investigate free vibrations of circular plates immersed in a liquid-filled container with free surface. Natural frequencies and mode shapes are obtained using *the Rayleigh–Ritz method*, taking fluid–structure interaction into account. In many engineering disciplines the interaction of a liquid having a free surface with an elastic member of the structure is of some interest. **Bauer** [10] executed a research based on coupled hydroelastic frequencies of an incompressible and frictionless liquid in a circular cylindrical container, of which the free liquid surface is covered by a flexible membrane or an elastic plate. The purpose of the study was to know the coupled frequencies as they appear through the interaction of liquid *and* structure. Plate structures are widely used in almost every aspect of engineering applications, including aerospace, civil, and electronics. A study has been proposed by **Civalek Ö** [11], where different approaches for geometrically non-linear static analysis of rectangular plates have been investigated. Plates with thickness variations can be advantageous in modern structures due to their unique features, such as weight savings, stiffness enhancement, optimized load carrying, and tailored dynamic design (e.g., shifting natural frequency). For this reason, **Gang Wang** and **Ahmet Unal** [12] carried out an evaluation about free vibration of stepped thickness rectangular plates using the spectral finite element method (*SFEM*). The experimental studies concerning nonlinear vibrations of plates and shells are experimentally studied by **M. Amabili** and **S. Carra** [13]. In this type of research the aim of the project was to understand the behaviour of a stainless-steel thin rectangular plate carrying different concentrated masses. The plate is vertically and horizontally tested in order to investigate the gravity effect. Harmonic excitation is applied by using *electrodynamic exciter* and the plate vibration is measured by using a *laser Doppler vibrometer* with displacement decoder. Results showed that concentrated masses have no effect on the trend of nonlinearity of the vertical plate, while they played a role in case of the plate is horizontal because the static flexural deflection caused by gravity reduces the hardening-type nonlinearity. Initial geometric imperfection (deviation from flat surface in vertical position) of the plate is measured and taken into account; it played a significant role.

The literature presents a large number of studies dealing with different boundary conditions, different solution methods and complicating effects. In this regard, **M. Amabili**, **R. Garziera** and **S. Carra** [14] carried out a study referring to the understanding of the liquid effects on the natural frequencies and initial deflection of the plate due to hydrostatic pressure. The free liquid surface is free to slosh and the water is delimited by practically rigid walls, except for the thin plate. Numerous studies have been performed to investigate free and forced vibrations of thin isotropic plates in partial contact with a fluid. Some of the most complete reviews on the subject have been presented by **Korosh Khorshid** and **Sirwan Farhadi** [15]; one of these studies analyzed the hydrostatic vibration of a laminated composite rectangular plate partially in contact with a bounded fluid. Wet dynamic transverse displacements of the plate were approximated by a set of admissible trial functions which required to satisfy the clamped and simply supported geometric boundary conditions. Natural frequencies of the plate coupled with sloshing fluid modes were calculated using *Rayleigh-Ritz method* based on minimizing the Rayleigh quotient. Another important study was performed by **Shahrokh Hosseini-Hashemi**, **Khorshidi Karimi** and **Payandeh** [16] concerning with free vibration analysis of a moderately thick with internal line support. Then, natural frequencies of the plate were presented for different fluid levels, fluid densities, aspect ratios, thickness to length ratios and boundary conditions. The vibration characteristics of rectangular plates have attracted the interest of many researchers; plates resting on elastic foundation shave found considerable applications in structural engineering problems. Reinforced-concrete pavements of highways, airport runways, foundation of storage tanks and swimming pools. In this respect, free vibration analysis of vertical rectangular Mindlin plates resting on Pasternak elastic foundation and fully or partially in contact with fluid on their one side was investigated for different combinations of boundary conditions thanks to **Sh. Hosseini Hashemi**, **Mahmoud Karimi**, and **H. Rokni Damavandi Taher** [17]. The plate was assumed to be one of vertical rectangular walls of a container in contact with fluid. In order to analyze the interaction of the plate with the elastic foundation and fluid system, three displacement components of the plate were expressed in the *Ritz method*.

In the paper written by **M. Amabili** and **G. Dalpiaz** [18], the bulging modes (i.e., modes where the walls oscillate moving the liquid)of the flexible bottom annular plate of an otherwise rigid annular cylindrical container are taken into consideration. The use of simplifying hypothesis about the mode shapes of the plate in contact with the liquid (wet modes) were the same in *vacuo*; the approach based on the non-dimensionalized added virtual mass incremental factor is applied, so that all numerical computations can be made non-dimensional. The accuracy of this method is checked by using the *Rayleigh–Ritz method*, which removes the restrictive hypothesis on the wet mode shapes. In addition to this, several experimental modal analyses were performed on two different test tanks filled with different water levels in order to verify the accuracy of the theoretical results. One of the important issues related to fluid–solid interaction in various containers is the sloshing of liquid in partially filled tanks. The *sloshing phenomenon* can be described as the highly non-linear movement of the free surface of liquids inside tanks. It is usually set off by some external excitation of the tank (motion of the vehicle, sea waves, earthquakes, etc.). The amplitude of the slosh, in general, depends on the nature, amplitude and frequency of the tank motion, liquid-fill depth, liquid properties and tank geometry. For example, when the frequency of the tank motion is close to the natural frequency of **the interaction between sloshing fluid and structure**, the enhanced fluid motion creates localized high impact loads on the tank walls and ceiling which can cause structural damage. The problem of modeling the solid–fluid interaction in partially filled liquid containers finds applications in numerous engineering fields, including the airspace industry (rockets, satellites), road and naval transportation, and has become in recent years an object of keen interest from researchers. The paper, written by **S. Rebouillat** and **D. Liksonov** [19], focused in particular on the sloshing phenomenon and on the numerical approaches used to predict the sloshing wave amplitude, frequency, pressure exerted on the walls and the effect of sloshing on the stability in the container environment: the methods used in then were exposed and classified according to the problem formulations employed. They concerned, primarily, **finite-elements and finite-differences methods applied to Euler or Lagrangian fluid and solid domains,** as well as the smoothed particle method. Issues related to modeling the free-surface of the fluid, fluid–solid interface and to numerical coupling were exposed. The results obtained by various numerical methods were discussed in comparison with experimental results.

S. Nicolici and **R.M. Bilegan** [20] presented a paper related to the problem of modeling the *fluid–structure interaction* (***FSI***) in partially filled liquid containers. The study was based on the sloshing phenomena and on the coupling computational fluid dynamics (***CFD***) analysis with the finite element stress analysis (***FEA***) used to predict the sloshing wave amplitude, convective mode frequency, pressure exerted on the walls and the effect of sloshing on the anchoring points forces. The interaction between fluids (water and air) and tank wall was modeled considering full and one-way coupling. Using the time history of an earthquake excitation, the results of the FSI model were compared with those obtained employing simplified mechanical models given in design codes. The coupling phenomenon was found to influence the sloshing effect, the impulsive pressure being amplified by the wall elasticity. The applied FSI methodology demonstrated to be feasible in testing a 3D full coupled ***CFD/FEA*** storage tank subjected to a long time history excitation. Many investigators have developed some approximate solutions to predict the changes in the natural frequencies when a rectangular plate is in contact with a liquid. Also, an analytical method to calculate the wet natural frequencies of rectangular tank with several classical boundary conditions, partially filled with an ideal liquid was suggested thanks to **Kyeong-Hoon Jeong** [21]. Wet dynamic displacements of the tank were approximated by combining the orthogonal polynomials, satisfying the boundary conditions, since the rectangular tank was composed of four rectangular plates. The vibration modes of the facing plates of the tank were divided into two categories: symmetric and anti-symmetric modes with respect to the planes passing through the center of the tank and perpendicular to the free liquid surface. An eigenvalue problem was derived using the *Rayleigh–Ritz method*; consequently, the wet natural frequencies of the rectangular tank were extracted. Another important article, written by **Kyeong-Hoon Jeong** [22], took into account free vibration of a rectangular flexible open U-Type container partially filled with a liquid. The liquid potential displacement was appropriated to the Laplace equation and liquid boundary conditions were derived, and the wet dynamic modal functions of a half of the container was expanded by the *Finite Fourier Transform*. **Heung-Seok Kang** and **Kyeong-Hoon Jeong** [23] suggested to elaborate a theoretical dynamic model of the fuel assembly submerged in a coolant in order to study free vibration of a bundle of identical rectangular plates fully in contact with an ideal liquid. The proposed theoretical method was verified by observing an excellent agreement with three-dimensional finite element analysis results

for a clamped-clamped-free-free boundary condition. The effect of the liquid gap between the plates on the normalized natural frequencies was discussed. The natural frequencies of an elastic thin plate placed into a rectangular hole and connected to the rigid bottom slab of a rectangular container filled with fluid having a free surface were studied by **Y. K. Cheung** and **D. Zhou** [24]. The fluid was assumed to be incompressible, "inviscid" and "irrotational", and the effect of surface waves was neglected. An analytical-Ritz method was developed to study the vibratory characteristics of the plate in contact with the fluid. First of all, the exact expression of the motion of the fluid was obtained, in which the unknown coefficients were determined by using the method of separation of variables and the method of *Fourier Series Expansion*. Then, the Ritz approach was used to obtain the frequency equation of the system; the added virtual mass incremental (***AVMI***) matrices were obtained for plates with arbitrary boundary conditions. Finally, a convergence study was carried out and some numerical results were given. **A. Ergin** and **B. Ugurlu** [25] presented a boundary integral equation method in conjunction with the method of images, in order to investigate the dynamic behaviour (wet frequencies and associated mode shapes) of fluid storage tanks. In the analysis of the linear fluid–structure system, it was assumed that the fluid was ideal, and fluid forces were associated with inertial effects of the contained fluid. This implied that the fluid pressure on the wetted surface of the structure was in phase with the structural acceleration. The in *vacuo* dynamic properties of the dry structure were obtained by using standard finite element software. In the wet part of the analysis, the fluid–structure interaction effects were calculated in terms of the generalized **added mass coefficients** by use of the boundary integral equation method together with the method of images in order to impose the $\Phi=0$ boundary condition on the free surface. The fluid storage tanks in this investigation were assumed partially or completely filled with water.

1. The System

The basic elements of the structure used for experimental investigations are fundamentally two:

- The stainless-steel thin rectangular plate which represents a flexible wall of the steel container;
- The steel tank which is considered as a support for the plate;
- The frame which, thanks to the presence of twenty-four bolts, allows to fix the plate to the front of the tank.

In particular, the order of assembly of the entire setup provides first of all the mounting of the plate on the tank, which is subsequently anchored to the plate with the function of the underlying base via a total of four brackets that grasp laterally two at the "tank" on the relative support. Only after this operation, the thin plate is mounted and turned it into a constitutive part of the tank. The intention of this section is to report a brief description of the apparatus which constitutes the experimental system for testing in the laboratory, which is constituted only by the plate, as previously described, also by the frame and the tank. The tank is made by a box-steel to which the cover and a side are removed. The underside of the cover is made wider and it is hooked onto the basic structure, which ensures greater stability during the tests. The frame, instead, is formed by a square steel, which can be thought of as a box, formed by four lengths of steel glued and bound between them by means of screws and on which is screwed the plate. It was decided to use this solution because, in the first place, allows to position the plate in both vertical and horizontal, supporting different faces on the reference plane, without the need provide for the construction of special frames and, in the second place this frame can be easily stopped and bound to the floor. Below, some 3D drawings are presented to clarify the structure of the frame and the dimensions used.

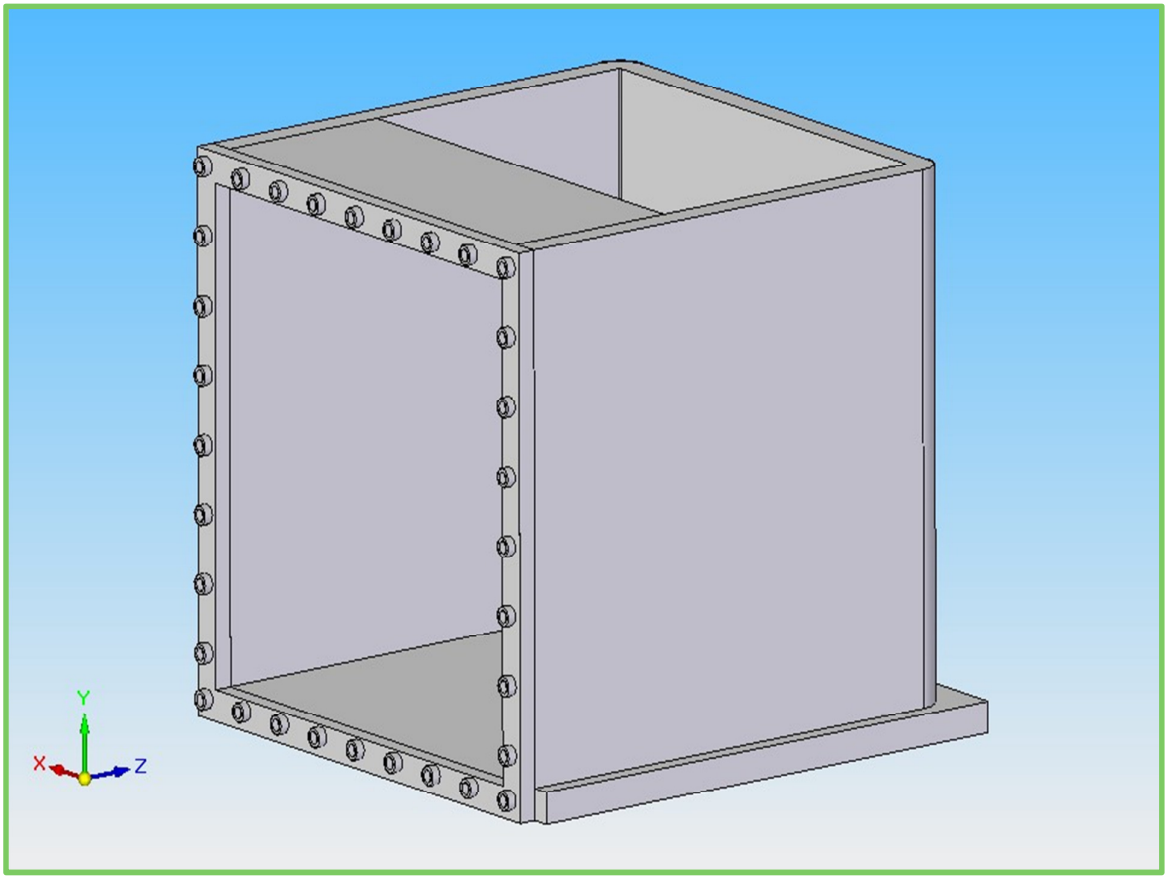


Figure 1: the system plate and tank.

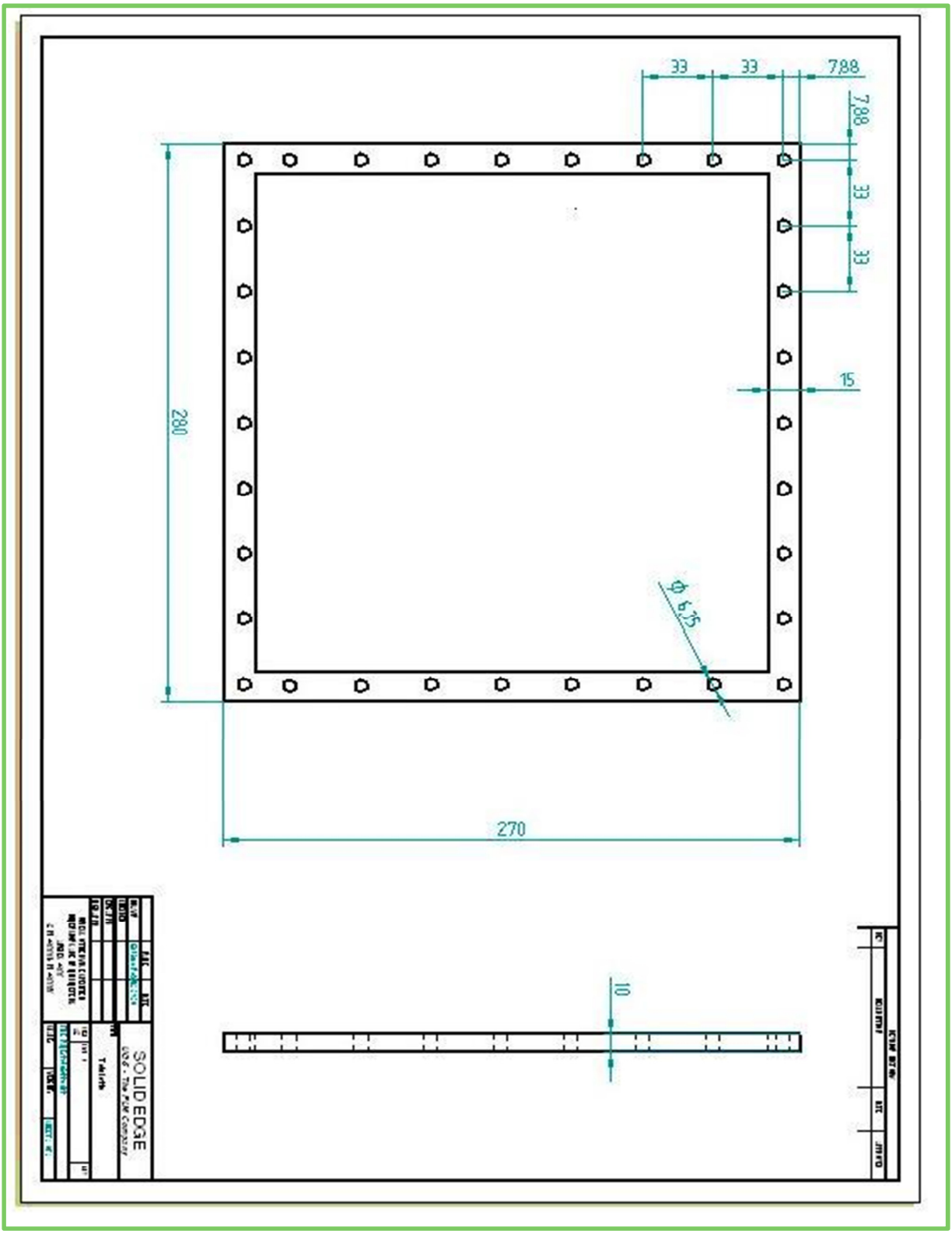


Figure 2: the dimensions of the frame.

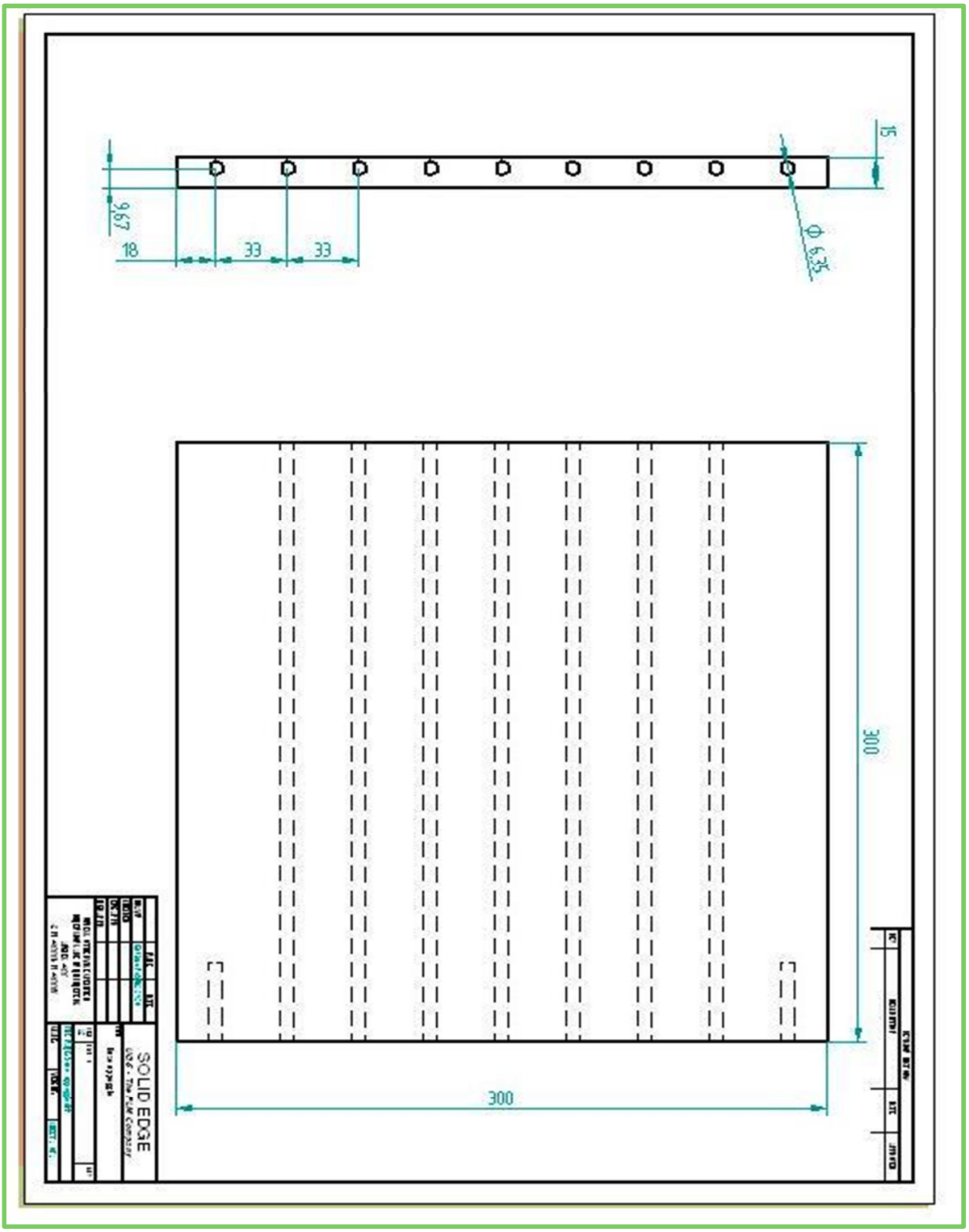


Figure 3: the base of the tank.

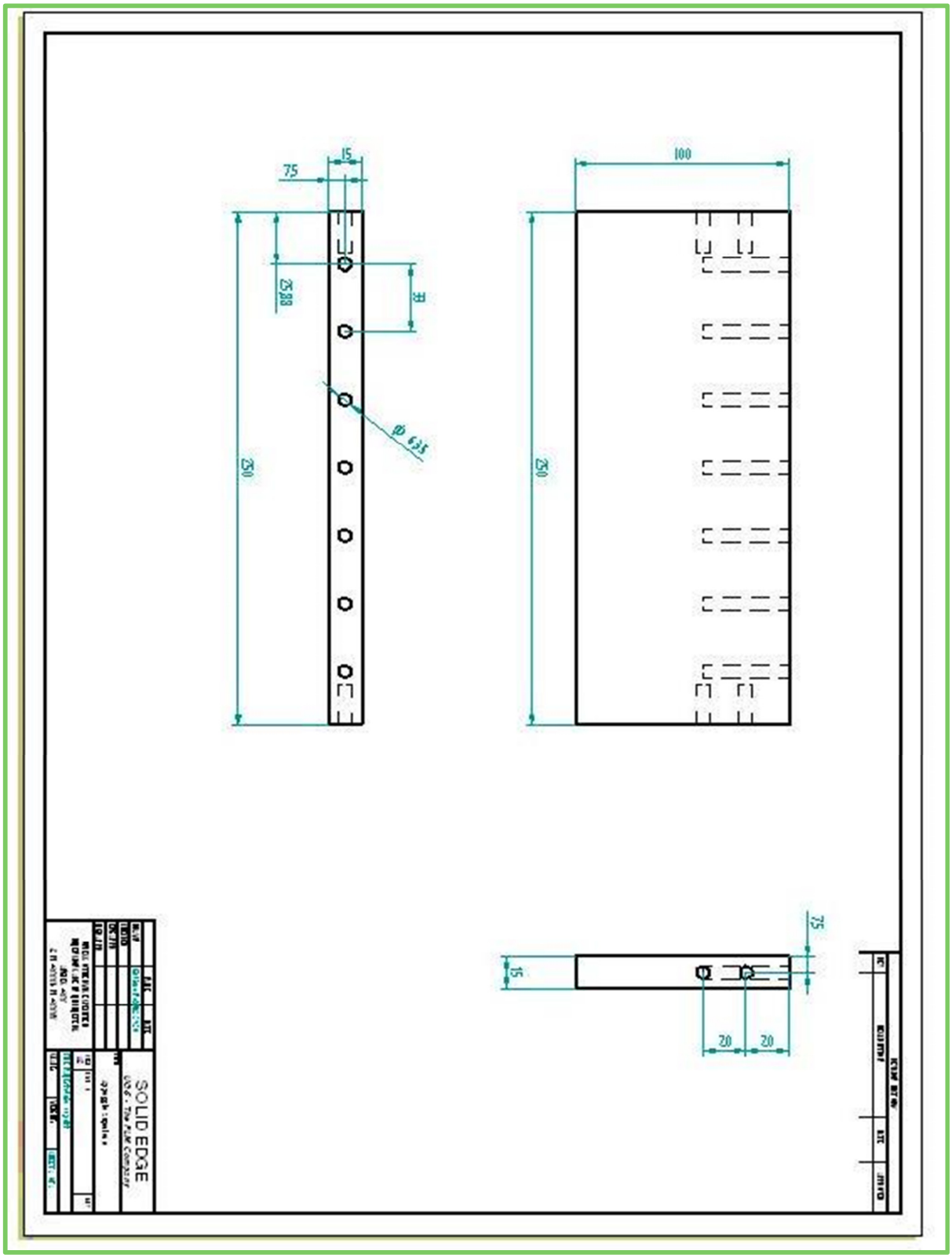


Figure 3: the back support.

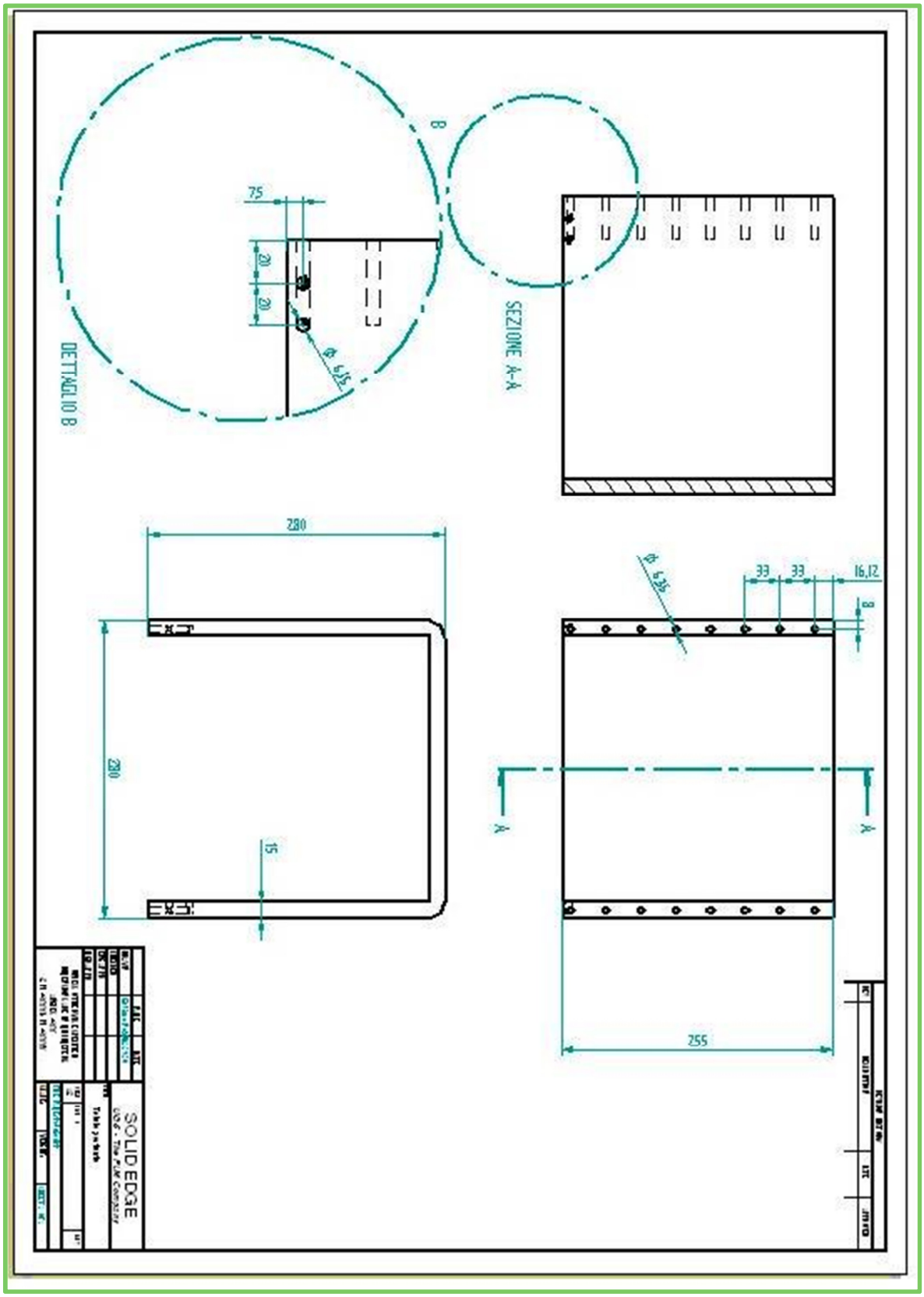


Figure 4: U-shape frame.

1.1 Description and characteristics of the tank

The steel tank was designed and built in the laboratories of the Department of Industrial Engineering at the University of Parma. To make the frame resistant to corrosion, it was decided to use as constructive material of stainless steel with designation UNI ISO AISI 430, which is perfectly able to resist corrosion caused by water and is, at the same time, one of the less expensive stainless steels. To keep the output signal from the instrument that measures the vibrations (*Laser Doppler Vibrometer*) as "clean" as possible, the tank is constituted by elements obtained from a foil of a thickness varying between 10 and 15 [mm]. This solution has made the components of the container very thick compared to the thin plate and, consequently, they vibrate in a very different way than the plate. Furthermore, because the density of steel is equal to 7860 [kg /m^3] and the volume of material used reaches the value of $3{,}6x10^{-3}$ [m^3], the total weight of the structure extend, when it is empty, 28 kg, making the tank very heavy and therefore able to absorb easily vibrations that are transmitted to it. Entering now more specifically in the description of the frame, it made up of four main elements:

- *Base;*
- *U-shaped frame;*
- *Back support of the plate;*
- *Cover sheet.*

1.2 Description of the base

The base is a foil (see figure 3 and 5) subjected only to some simple machining operations. Its main function consists to form a basis for the entire assembly, and, in addition to this, it sets all the elements of the framework such as the "*U-Frame*", the "back support of the plate"and the"cover sheet" which, besides being connected to each other, found in the base an element of fixing and stabilizing. Due to its rather large size and its considerable weight, the base is able to absorb the vibrations that are generated during the tests; moreover, being also much wider than the rest of the structure, it is possible to connect the tank to the base with one or several grips (in this case, two brackets for each side of fixed support plate and butress base). From the constructive point of view, it has a thickness even to 15 [mm] with a quarry "U" on the surface "A" which allow to get a reference for the placement of all other components of the framework as well as to correct the return elastic that the frame "U" inevitably shows, being the latter obtained by cold bending of a sheet of stainless steel of a thickness of 10 [mm]. Because there is a certain springback subsequently to the deformation, after the execution of the bending, the framework "U" does not present its sides perpendicular to each other but they are characterized by certain error from the point of view of perpendicularity: for this reason, the contact surface between the plate and the steel tank was again subjected to milling for making this contact perfectly flat. On the surface "B" are present seven M5x10 threaded holes; their purpose is to fixe the base to the plate that will be subject to testing and its lid, which will be fixed to the frame "U". Then there are five through-holes of a diameter of 7 [mm] and six hollow circular (concentric respect to the through-holes) with a diameter even to 12 [mm] and a depth even to 6 [mm], see Figure 3. In this way, these elements are nothing more than housings for socket head cap screws with the name "Screw Uni 5931 M6x15-12.9", used to constrain the framework “U” in the vertical direction with the base.

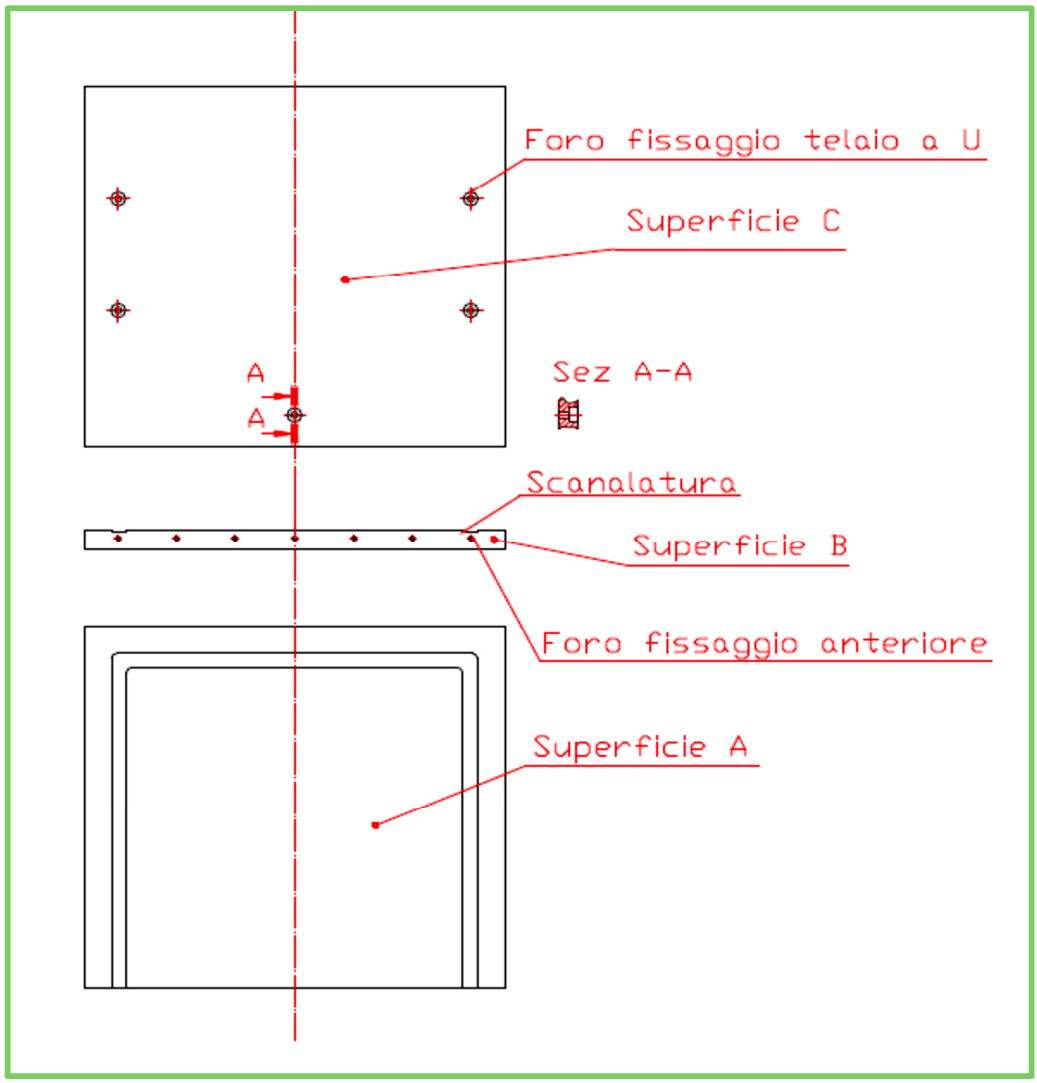


Figure 5: the back support and and the cover sheet.

1.3 Description of the vertical section “U”

This element has the function of supporting for the thin plate, for its lid and the back support (see figure 6). The frame "U" is positioned on the structure, so as to allow the interlocking of the latter inside the slot that has been realized on the base. The frame, then, was fixed to the base through the use of screws 5 having the name "Uni-Screw 5931 M6x15-12.9" arranged in the slots positioned on the lower surface of the base (surface "C"). The object has been realized starting from a flat plate of a thickness even to 10 [mm], trimmed thanks to a machine for laser cutting. Subsequently, the piece obtained was folded by calculating the size that the foil would have to present initially, in order to, once folded, have the dimensions requests. The buttonholes have been made with the aim of making possible the attachment of the back support of the plate with the frame "U": the elliptical shape was specially designed to ensure a precise and correct position of this support. The position of this component with respect to the other constituent elements of the structure is very important because it is necessary that during the tests the plate is placed on a perfectly flat surface, uniform and squarely: for this motive, the buttonholes allow to obtain this result. There are twelve holes M5x10 on the surface "D" in order to ensure that the clamping forces on these components, and then the forces of constraint of the plate, were not concentrated only in certain areas, creating abnormal stresses in it that could have affected adversely the outcome of the tests: the use of twelve points of constraint allows a fairer and more uniform distribution of forces. Finally, there are five holes M6x10 on the surface "E" which have the purpose to firmly secure the frame to the "U" to the base. Even on the surface "E" and "K" were then carried out milling operations: in the case of the surface "E", this operation has been performed to make it more flat; the milling on the surface "K", instead, was performed only for aesthetic purposes because the bending operation had left surfaces irregularities on it.

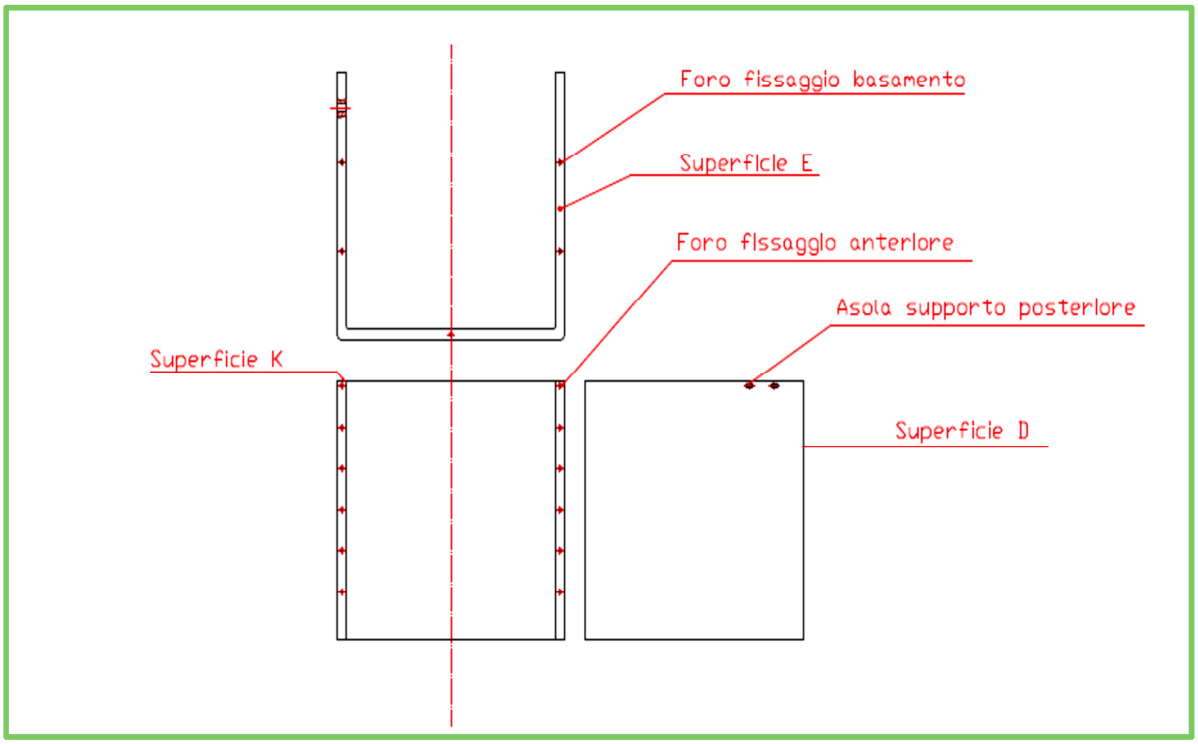


Figure 6: vertical section U and its components.

1.4 Description of the back support

The back support for the thin plate is obtained from a foil of thickness even to 10 [mm]; the main function is to create a reinforce for the upper part of plate. This support is positioned on the framework by means of coupling with the support "U" thanks to four screws called "screw UNI 5931 M4x15-12.9";these screws are made to pass through the buttonholes in order to be coupled to four threaded holes M4x10 made on surfaces, "G" and "H" (see figure 7). Then, there are threaded holes on the surface "F", "G" and "H": these holes, located on the surface "F", are realized in a particular way so that the intersection with the holes of the surfaces "G" and "H" is prevented. There are also threaded holes on the surface "F", "G" and "H": the external holes arranged on the surface "F" were made so as not to go to intersect with the holes of the surfaces "G" and "H". As far as the surface "F", since it will have a direct contact with the plate, it is necessary that its finish surface had no imperfections in order to create a very good coupling along the common boundary between the surface "F" and the plate: for this reason, the surface has been submitted a further milling. A similar processing has been performed on the surfaces "B" and "D", the interface between plate and tank. Finally, the function of the back support is to create a reinforcement able to absorb a possible unbalance of the upper part of the plate, especially during the experimental tests in which the steel slab is subjected to stresses that may create a structural damage such as to endanger the success of the tests performed.

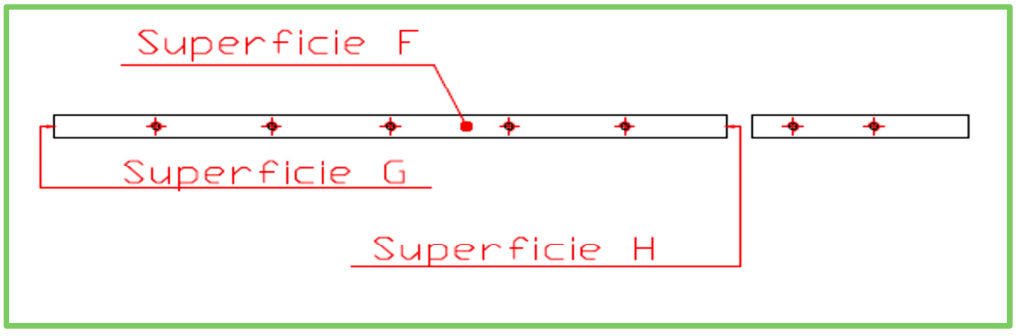


Figure 7: section of the back support.

1.5 General Description of the thin plate

Experiments have been conducted on a bolted (almost clamped) AISI 304 stainless steel rectangular plate with the following dimensions and material properties:

- *Young's modulus: $E = 198$ [GPa];*
- *Poisson coefficient: $\nu = 0.3$;*
- *Mass density: $\rho = 7850$ [kg / m^3];*
- *Length (horizontal direction): $a = 0.270$ [m];*
- *Width (vertical direction): $b = 0.263$ [m];*
- *Thickness: $h = 0.0005$ [m].*

The dimensions of the plate have been chosen in order to allow a good coupling with the supporting structure. In this regard the plate, during the tests, must be perfectly bound and must not undergo other displacements than those related to the vibrations provided: for this reason, it is necessary to create a structure as rigid as possible having only the function of support, in order to avoid that the structure could have an effect on the vibration modes of the plate. It is then connected to the structure by a bond of "interlocking" obtained through the realization of equidistant holes, arranged along the entire perimeter of the slab. The connection between the thin plate and the front wall of the tank has been realized through a stainless-steel rectangular frame placed in front of the plate in order to keep it locked and to increase the stiffness of the structure on the boundaries of the plate. Silicon has been also inserted to guarantee watertight. The stainless-steel frame, the rectangular thin plate and the tank are united by twenty-four stainless-steel screws (M6) located on through holes and fixed by nuts on the outside of the tank wall. The number of screws has been chosen with the purpose to make the boundary conditions of the plate as uniform as possible and to avoid the escape of liquid (water). After these operations, the free surface of the plate (namely internal to the edges defined by the contact plate-frame) that will be subject to the experimental tests, has the following dimensions:

- *Length (horizontal direction): $a = 0.250$ [m]*;
- *Width (vertical direction): $b = 0.240$ [m]*.

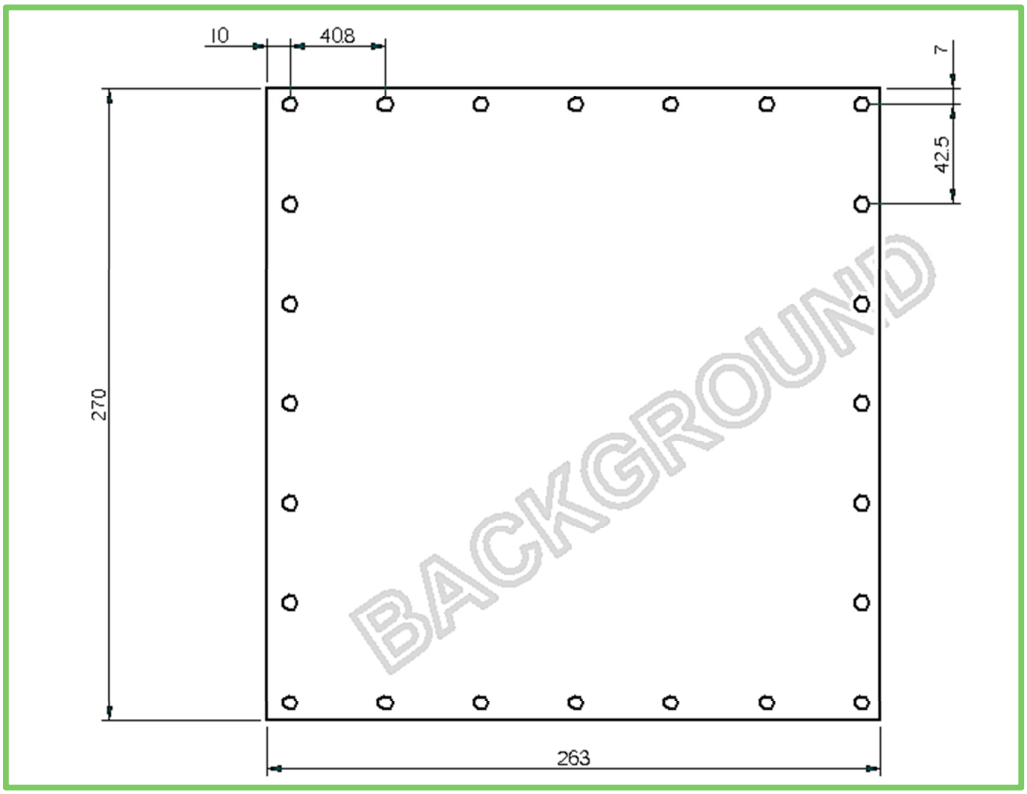


Figure 8: Drawing and dimensioning of the plate.

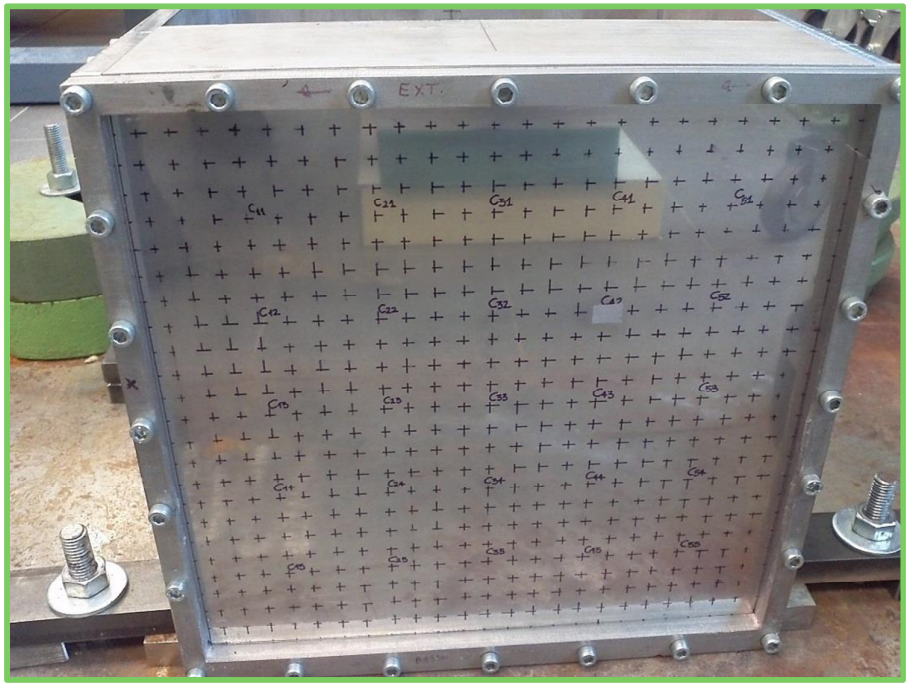


Figure 9: the plate, the frame and the bottonholes.

1.6 Setting of the plate on the framework

The mounting operation plans to perform a centring of the holes, as precise as possible, trying to match the hole axis of on the plate with the hole axis on the frame. At this point, the frame is placed on the plate and screws are inserted into the holes. Subsequently, the screws are tightened using a torque wrench set to a value of tightening torque even to 5 $N \cdot m$. The value chosen for the tightening torque is the result of a compromise between the lower surface deformation of the plate and the requirement to ensure a perfectly tight of the tank. In fact, This torque is able to ensure a satisfactory flatness of the points on the edge of the free surface of the plate without applying a compression of the frame overly aggressive, thus avoiding to generate, during the scanning phase of the plate, positive values are too high (i.e. characterized by a relative displacement towards the interior of the tank) on the points that are close to of the frame: in fact, in this area are found high values of surface deformation due to the pressure that bolts exert on the plate. The tightening method adopted is reported into the diagram below, with the order followed for tightening the bolts (see figure 10). The screws were not immediately tightened with the tightening torque indicated above, but it has gone through a series of intermediate tightening so as not to stress further the plate avoiding, in this way, tensions and possible deformations of the plate: it has time to adapt and unwind itself, with a final result of a lower preload. The tightening of the screws is crossed: first, it is carried out the tightening of screws positioned at the top of the frame, then, in succession, the screws arranged along the sides of the frame. The first bolt to be tightened is the central one, placed on the bottom horizontal row: this choice is due to the identification of a slight buckling outward in the central area of the lower plate surface, visible to the naked eye, when the plate is not mounted on the tank. For this reason, it was decided to start the tightening blocking the bolt on *"centre cross"* closer to the deformed area. The tension is, in this way, downloaded on the whole surface, allowing to distribute the load progressively from the inside to the outside in the radial direction. This procedure allows to download the surface tension following the directions shown in figure 11 (i.e. along the diagonal from the centre to the four corners tightened to the last).

Thanks to the technique adopted, it is possible to achieve greater planarity eliminating and/or reducing potential buckling due to the complex and delicate realization of the plate during the execution phase of the blanking. The tightening process of the screws is shown in figure ().

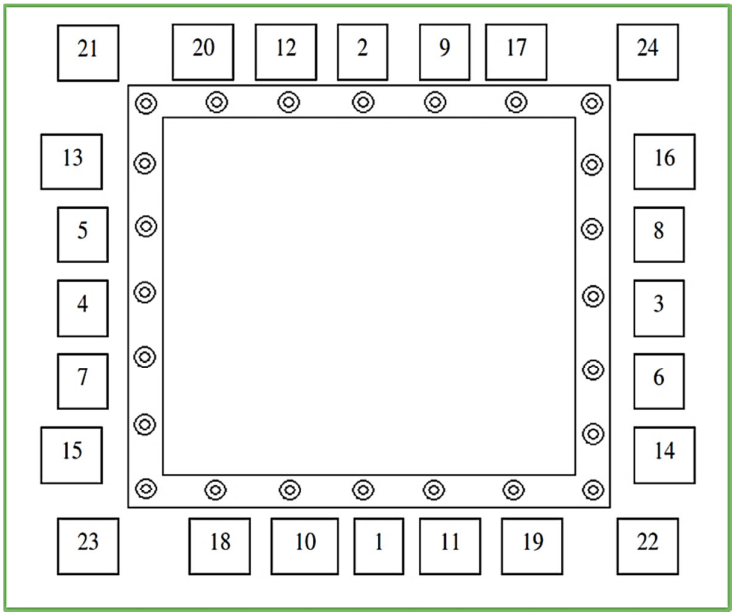


Figure 10: the diagram of tightening method used.

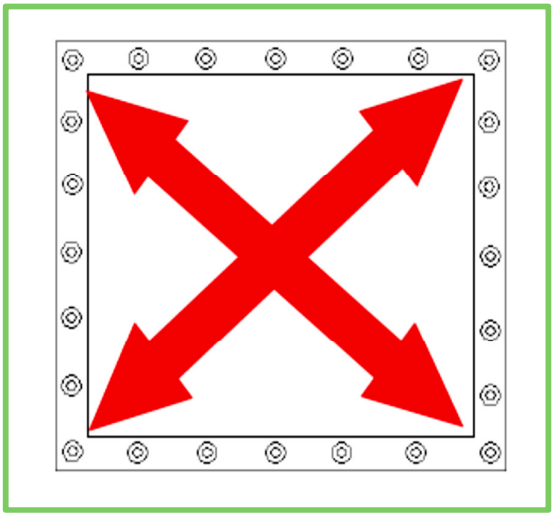


Figure 11: distribution and direction of surface tension during the fixing of the plate.

2. Experimental scanning laser of the plate surface

An experimental scanning of the surface has been realized for both empty tank and for different filling levels of water in order to:

- Found-out eventual unexpected non-planarity of the plate surface;

- Validate the non-linear calculation of the pre-deformed geometry of the plate: imperfections on the surface of the bolted plate must be taken into account, since they significantly affect the structural behaviour of the plate causing a deviation from the ideal flat surface of a thin plate.

Metals are valuable assets for different types of industries, for instance in the form of containers, pipelines, railway lines and thin plates and panels. Surface breaking defects in such components are of great concern due to safety implications; if left untreated the consequences could be disastrous. Examples of typical surface defects include: rolling contact fatigue in railway lines, stress corrosion cracking in pipelines and Non-destructive testing (*NDT*) techniques have proved to be key tools for detecting and characterising such defects, in particularly those techniques that utilise **MICRO TRIANGULATION LASER SENSOR**. Laser triangulation sensors operate with a laser diode, which projects a visible light spot onto the surface of the measurement target. The light reflected from the spot is imaged by an optical receiving system onto a position-sensitive element. If the light spot changes its position, this change is imaged on the receiving element and evaluated. The common triangulation sensor focuses the laser beam via a special arrangement of precision lenses in order to detect a measuring object of just a few microns in size. For profiling and scanning application the small spot size is a prerequisite for the needed spatial resolution. In some applications the surface structure of a shiny object causes unwanted speckle noise. In this case special models with a collimated beam or a small laser line can be used. Depending on the model and the specifications of the laser used, the measurement range, in terms of displacement, goes from a minimum of 0.5 [mm] to a maximum of 2000 [mm].

Laser sensors are suited for almost every application where the measuring object can be detected optically. Every industry which requires a non-contact measurement takes advantage of this wear free technology which measures without any impact on the target. The common triangulation sensor focuses the laser beam via a special arrangement of precision lenses in order to detect a measuring object of just a few microns in size. For profiling and scanning application the small spot size is a prerequisite for the needed spatial resolution. In some applications, the surface structure of a shiny object causes unwanted speckle noise: in this case, special models with a collimated beam or a small laser line must be used. In addition to this, the *Triangulation Laser Scanner* is able to measure in real time with a consistent update rate of the data thanks to a dynamic surface compensation. The distance information for the triangulation principle is obtained via the reflection of the laser beam. Surface roughness in the sub-micrometre range causes interference in the laser spot, which leads to measurement errors being obtained. This physical effect is particularly predominant in shiny, highly polished objects: the laser provides reliable measurements due to a square light spot; The point-shaped laser beam has now been widened using a special square lens and projected onto the target. The light spot is absorbed by a receiving array and evaluated. As the light spot is averaged using a special software algorithm, interference is completely filtered out. Through the unique **RTSC** function, the amount of reflected light from the target surface is compensated for during continuous exposure and in real-time. The exposure time or the amount of light produced by the laser is optimally matched to the reflection characteristics of the target surface. In the case of direct reflection the laser beam is reflected in one direction and so a special alignment of the sensor is required. The reflected laser beam is guided into the receiving array by tilting the sensor and is then directly converted into an electrical signal by the integrated controller. The alignment of the sensor on the measuring object is effected by means of special mounting templates. Another important application is the localization of micro defects on the surface of plates and panels: in fact, the *Triangulation Laser Scanner* is particularly used to identify and locate not only geometric imperfections but also those deriving, inevitably, from industrial processes, storage and transport operations. This type of laser is able to single out very small depressions and protrusions that could adversely modify the structure dynamic answerback, especially when the thickness is very thin.

2.1 Laser Scanner

The laser is a device capable of emitting a beam of **coherent light**, **monochromatic** and, with some exceptions, **concentrated in a highly collimated beam** straight through the process of stimulated emission. Furthermore, the brightness (luminance) of the laser sources is very high compared with that of traditional light sources. The laser, from the physical point of view, is nothing more than an electromagnetic radiation, or light wave, having the following characteristics:

- ***Monochromatic***: it must be composed of a single frequency of light;

- ***Spatial Coherence*** : it must be composed of a wave that is not radiated in all directions as that of the springs of the traditional type, but propagates at a great distance and with extreme directionality;

- ***Temporal Coherence***: it must be made up of waves of the same frequency and the same phase which are added to one another giving rise to a train of light that can be pushed with high intensity and high power.

Of course a light radiation can have a different wavelength. In the case of the laser radiation may be ultraviolet (i.e. having a wavelength between 200 nm and 400 nm), visible (between 400 and 700 [nm]) or infrared (between 700 and 3000 [nm]).



Figure 12: Laser scanner triangulation and the setting device used for the regulation of initial parameters.

2.2 Sensor Laser Scanner

The mechanics of the instrument allows to materialize a direction of acquisition and the laser rangefinder acquires a distance along the same direction. The result of the acquisition is a set of points in space scattered in a more or less regular basis which is commonly called the **point cloud**. The laser scanner on the market today are many and each of them has different characteristics in the principle of acquisition, in the achievable accuracy, in the extent and speed of acquisition. Despite the many differences between them laser sensors ca be classified into two categories, according to the principle of acquisition used:

- ***Distance-measuring Laser***;
- ***Triangulation Laser Sensor***:

The laser scanner can also be classified according to other features that are related to the ***Laser Sensor Position***. Two different type of laser can be distinguished:

- ***Laser Static***;

- ***Mobile Laser***:

Static instruments are generally employed in the lines of mechanical control, for the monitoring of deformations or movements and for the detection of geometric imperfections. They generally have a fixed position in time and always acquires the same image. Laser scanner mobile or portable are, instead, the most used in topography. Using the laser triangulation, the measurement is performed by detecting the angle through which the receiver sees the *"laser beam"* refracted from the surface of the object with respect to the original direction of emission of the same radius (figure)

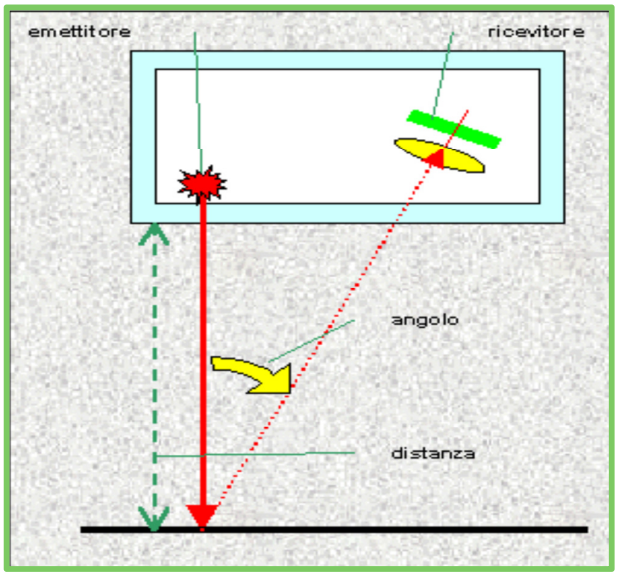


Figure 13: diagram of the measuring system of laser triangulation.

Triangulation laser gauges are the most used for measurements ranging from a few millimetres up to 10 metres. Depending on the application, it is possible to adopt instruments that use a type of receiver **PSD** (***Position Sensor Detector***) or **CCD** (***Charge Coupled Device***). The PSD sensors allow to realize very precise measurements with very low frequencies (10 to 100 [Hz]); while the CCD sensors provide excellent accuracy with high frequency ($>$ 1000 [Hz]).The gauges equipped with PSD sensors are not suitable for dynamic applications, but rather for static measurements; in this case, in addition to the vertical resolution (dz), it is required to attend to the longitudinal resolution (dx). It is important to take into account the cadence of measurement in the direction of material advancement. The longitudinal resolution (dx) is adjusted by the following formula:

$$dx = v/f \tag{1}$$

Where:

dx: *longitudinal resolution* $[mm]$;
v: *feed rate* $\left[\frac{mm}{s}\right]$;
f: *frequency measurement* $[Hz]$.

It must also be carefully evaluated the material surface that is measured. On irregular or just wavy surfaces, it may be necessary to filter the signal by calculating sample means for a defined set measures. When there are the presence of moving materials, it is more appropriate using gauges equipped with a CCD sensor. This type of sensor is practically independent from surface characteristics of the material and, for this reason, it allows a much higher frequency of reading. A particularly reflective surface (*mirror effect*) could request to change the position of the instrument so that the laser beam is inclined with respect to the perpendicular which connects the beam-emitting lens to the centre of point selected on the surface; in this way, there is an increase of the signal reception. (see Figure 1.29). The gauges equipped with CCD sensors are provided with a self-regulation of the power emitted according to the level of the return signal, in order to prevent the possible saturation (*blooming*) of the CCD sensor. In all cases where there are measurements of moving objects is, however, necessary to respect the geometric configuration of the instrument (see Figure 1.30).

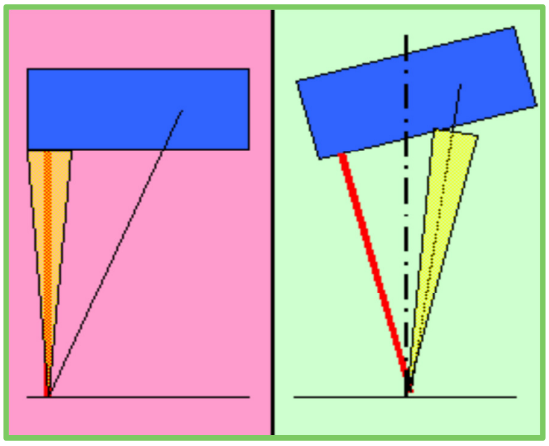


Figure 14: Angle of the signal emitted from the triangulation laser.

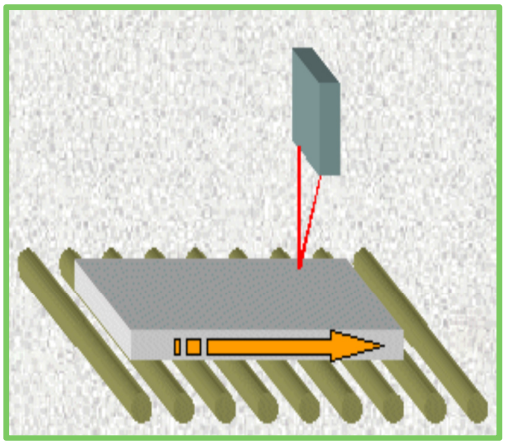


Figure 15: CCD sensors installed on the measurement equipment.

2.3 The sensor laser characteristics

It is possible to distinguish instruments at small-scale (<1[m], typically triangulation laser with sub-millimetre accuracy); lasers at medium-range (1[m] to 50 [m], or distance-measuring triangulation sensor with accuracies from 0.2[mm] to [6]mm) and long-range instruments (50[m] to 6000[m], distance-measuring with accuracies from 5[mm] to 2[cm]). Of course one must not forget that the flow rate of a laser is a function of the type of material struck by the beam and, in particular, the reflectivity of the material at the wavelength of the laser. If the reflectivity is greater than the delivery rate will be higher; if, instead, the reflectivity is lower (and therefore the greater part of the energy absorbed), the flow will be lower. This is simply because the reflected beam from the surface propagates in the atmosphere that is no more than a transparent body. For this reason, it has the ability to absorb, transmit and reflect any electromagnetic radiations. Although, within the limits of operability of lasers the effect of attenuation of the signal laser is small enough: it is easily demonstrated by empirical evidences that the effect of attenuation increases as much as the distance identified. If the portion of the beam reflected from a surface is particularly weak, this disperses quickly in the environment; therefore, the maximum distance detectable in this case decreases. the “head” of the laser sensor is shown in figure 16.



Figure 16: the “head” of the laser sensor ***NRA NAiS® 1282.***

The lights, which are positioned on the “head” of the laser sensor, have the purpose to evaluate the output signal during the execution of the measures. If the measure is into the range, namely, when the measured data is between the HIGH and LOW limit values, the light is “green”; instead, when the measured data becomes less than the LOW limit values, the light is “purple”; finally, when the measured data exceeds the HIGH limit values, the light is “black”.

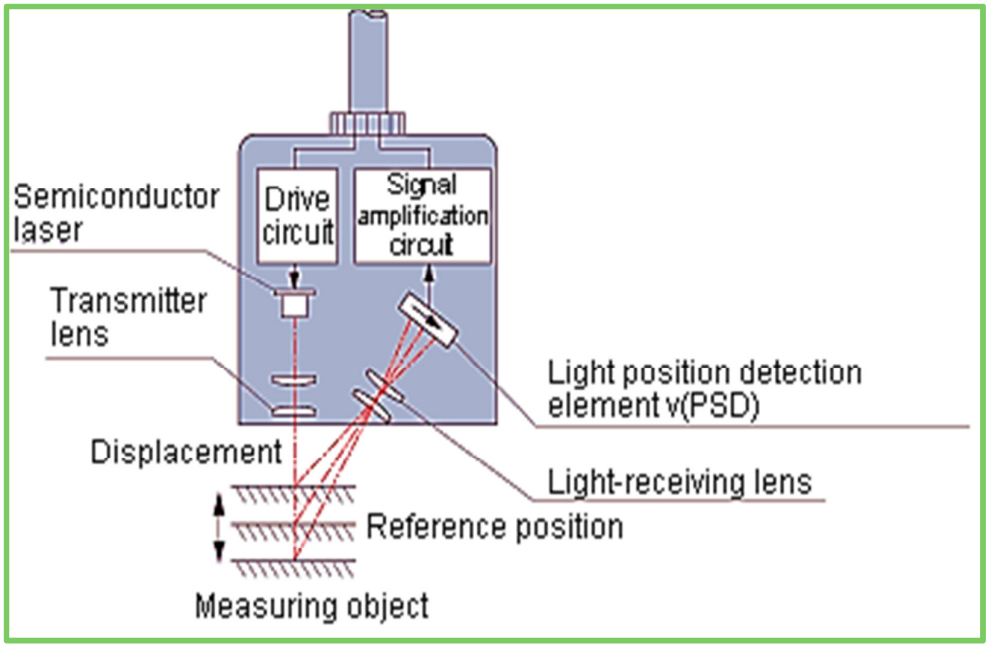


Figure 17: sensor configuration and emission of the laser beam.

2.4 Experimental set-up for the scanning surface

The experimental scanning of the plate has been carried out in the Laboratory of Mechanical Vibrations at the University of Parma, by organizing a specific measurement set-up using a milling machine, as shown in figure (18). The decision to use a torque equal to 5 [N·m] to constrain the plate to the frame has been influenced by the need to satisfy the requirement of flatness, without however subjecting the edges of the free surface of the plate to excessive traction due to a tightening too aggressive. In fact, a value of tightening torque too high could deform excessively the edge of the plate not respecting, in this way, the condition of planarity. The low mechanical elasticity prevents the plate to return to its natural configuration after having applied a load: the plate, subjected to an increasing load (hydrostatic pressure), is not able to reacquire the previous flatness when the load is removed. For the scansion a drill-cutter machine has been employed, since it allows to implement with great precision translational offsets of both the horizontal work surface, that of the spindle: the work plan of the milling machine enable to obtain very precise movements along the three directions of space with the help of three cranks. The steel tank has been placed on the horizontal plane of the milling machine. In this configuration, you must choose a System of Cartesian axes (*xyz*) as a reference to define the movement of the working plane with respect to the laser sensor positioned on the spindle of the milling machine, which can be moved with a very high precision. The axis parallel to the length of the thin plate is called *x*; the axis parallel to the width of the plate is called *y*; the axis orthogonal to the plate is called *z*. The triangulation laser sensor has been connected to the spindle through the use of a cylindrical rod, as shown in figure (19), with the emission of the laser beam in the perpendicular direction to the plate. This rod was made with the intention of entering perfectly into the spindle and, due to its length, the vertically movement of the laser is prevented during the measurement. The measuring system is based on a laser triangulation principle, where the laser projector generates waves on the plate surface (685 [nm] wavelength and 15 [μs] pulse duration of the light source) with a beam dimensions at the focus point distance equal to 0.7×1.2 [mm]. Part of the light rays which come from the target object by means of diffuse reflection produce a light spot on the position sensing device (***PSD***). This light spot varies depending on the displacement of the target object.

By measuring the fluctuations in the light spot, the laser sensor is able to measure the distance of the target object. The parameters related to the optical geometry of the apparatus are then numerically optimized until the minimum deviation (the sum of the squared errors) between the measured points and the reference surface is found. The major advantage of this procedure is that all the transformation parameters can be determined in a single measuring step, i.e., the camera's internal parameters (focal length, central point and distortion), the projector's distortion and the projector's position relative to the camera (rotation and translation). The measurable range of the sensor in *z* direction varies from +20 [mm] to -20 [mm], which is calculated as a standard deviation between the real distance of a point and the nominal (or ideal) distance of the same, considering the surface totally flat. The gauge must be mounted so that the face of the laser, on which the projector and receiver are placed, remain perpendicular to the feed direction. The laser triangulation **NRA NAiS® 1282** used is an instrument that has an accuracy of 4 micron and belongs to safety class 2. The laser to run correctly must be disposed at a distance of 8 [cm] from the object that shall be measured. At this distance, the laser beam is located within the *"range of fire"*, therefore, both the sensor and the *"unit control system"* will have the yellow light always fixed and turned on. Furthermore, in order to perform a scansion reliable and correct, in each grid point, both the orange light, that the yellow light will remain fixed and turned on. The orange light indicates that the laser beam is correctly emitted from the gauge, whereas the yellow light indicates that the distance between the sensor and the surface is correct. When installing the sensor, it is necessary that the target is placed in the measurable range using the *"range indicator"* (**LED**): it flashes when a target is in the range of admissibility, and comes on when a target is around the centre point distance. Under alarm conditions, the **LED** happens to turn on or flash even if the target is not in the measurable range.

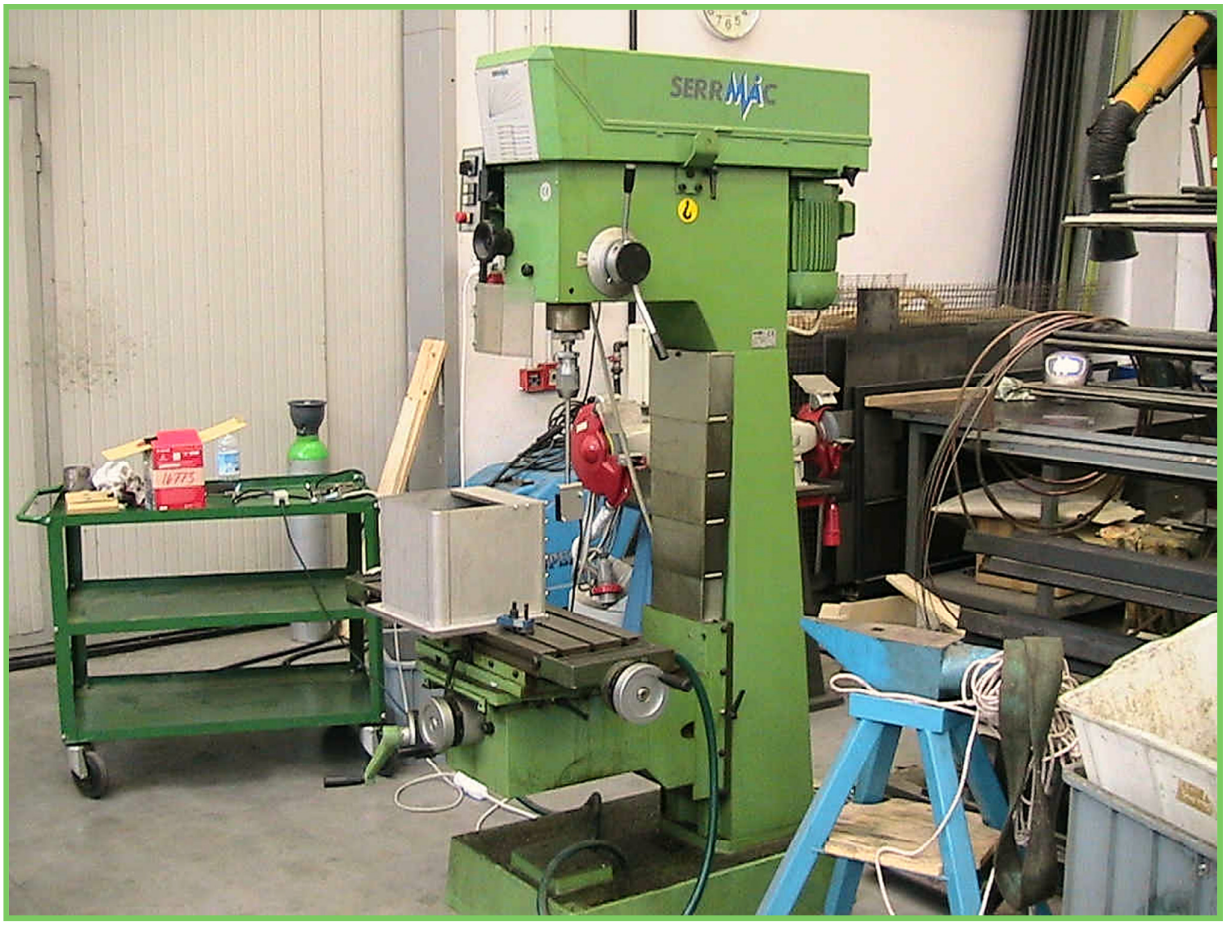


Figure 18: the milling machine used for moving the laser beam on the surface of the plate.

2.5 The grid points

The points have been identified starting from a grid obtained by dividing the total area of the plate in twenty-four horizontal and vertical sectors (twenty-five rows and twenty-five columns), shown in figure (22). The intersection of the separation lines of the various sectors has led to a series of points which have been termed with the letter *"C"* to which has been assigned a subscript for the row number and the column number to identify the position of each point inside the grid (see figure 22). The total number of points is equal to 625. The laser triangulation performs, for each point, a measurement representative of the relative displacement between the considered point and a grid point taken as a *"reference"*: the value attributed to this point is obtained by setting the display of the controller to zero (0.00). The grid points, which has been drawn directly on the surface of the plate, is a tool of great importance for this kind of measurements because it allows to evaluate the displacement from the ideal condition of planarity in detail and limited to a very small area. Moreover, a grid of points so thick has contributed to realize a graphic reconstruction of the plate surface extremely faithful to the real surface: in fact it is neither perfectly flat nor perfectly symmetrical. It should be specified that the grid points has been used to define a ***Model Geometry.*** In effect, these points represent the locations where displacements are calculated and each point is labelled with a ***node***. A node is identified by a name, a location and an orientation; collections of nodes can also be formed into a groups.

- *Node name:* a node will usually be assigned a number to identify it;

- *Node location:* the geometry of the structure is defined relative to a global coordinates system and the location of a node, for example in the 2D space, is defined by a set of two coordinates;

- *Node orientation:* each node has a nodal coordinate system in which the relative displacement of a point is detected. The orientation of this system is related to the global coordinate system.

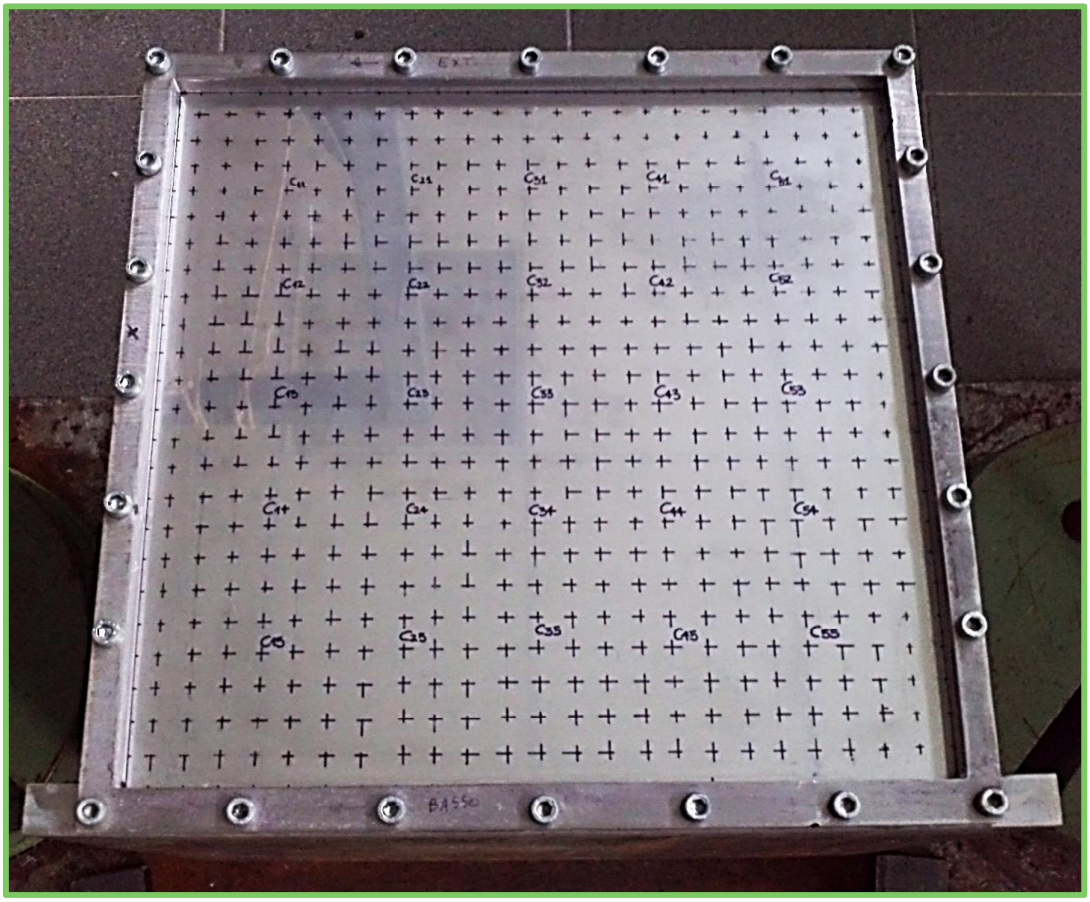


Figure 22: the 625 points used for scansions and the 25 points used for modal analysis, marked with the letter $\mathbf{C_{ij}}$ *(the subscript* $\mathbf{i}$ *denotes the row, while the subscript* $\mathbf{j}$ *denotes the column).*

2.6 Surface reconstruction

The problem of recovering the 3D shape of a surface, also known as surface reconstruction, has been a hot topic of research for the last 20 years or so, with several methods reported in the literature. Given partial information about an unknown *surface U*, the goal of such methods is to construct, to the extent possible, a compact representation of a *surface model S* that approximates U. Depending on the available information about the surface (2D sections, clouds of points, grid of curves, interactive surface sketching, etc.), qualitatively different approaches can be formulated in order to tackle this issue. Other classical input data include ***iso-parametric curves*** on the surface and even mixed information, such as scattered points, contours plots and data points. For instance, algorithms based on ***2D cross-sections*** make use of the fact that data are organized into contours which lie, at their turn, in parallel planes. Other methods use a grid of iso-parametric curves to infer the geometry and topology of the underlying surface. In most cases, however, available information about the surface is typically a dense set of (either organized or scattered) 3D data points obtained by using some sorts of scanner devices, the most common data point acquisition technique in reverse engineering applications. In such a case, the reconstructed surface can be described using three different representations providing different levels of accuracy, ranging from the coarsest (polygonal meshes) to the finest ***NURBS surfaces*** (where NURBS stands for non-uniform rational B-spline, by far the most common surface representation in real world applications). NURBS surfaces are the most powerful and most common free-form parametric surfaces because of their flexibility, versatility, and the fact that they represent well a wide variety of shapes in a very compact and intuitive mathematical form. This is the preferred form for detailed surfaces, since they faithfully represent real objects: the initial input is a (possibly massive) set of 3D data points which is a typical output obtained from the utilization of scanner methods, for example, *Triangulation Laser Scanner*. Depending on the nature of these data points, two different approaches are employed: ***interpolation*** and ***approximation***. Approximation techniques are specially recommended when data are not exact, but subjected to measurement errors. Another important reason to choose approximation could be the great computational effort required to obtain surfaces by interpolating an infinite number of data, such as curve forms.

Interpolation functions toolbox can be implemented to *MATLAB* environment, a programmable computation environment for many kinds of prototype, testing and research purposes. It is also possible to modify algorithms to make the NURBS toolbox work more efficiently. *MATLAB* is used via the command line or via m-files. There are two kinds of m-files. First format of the m-file is a function (M-function): a function in *MATLAB* can take in several input parameters and it can return several output parameters. Second format of the m-file is like the input from the command line; in this case all commands in m-file are executed just like the commands from the command line. The results, obtained graphically through the elaboration of data with the use of *MATLAB,* are presented, here, in the form of curves level with 10 degrees of intensity with relative areas of fitting: these curves connect the points of the plate with the same strain value (*red*: positive deviation, deformation towards the inside of the tank; *blue*: negative variance, deformed towards the outside of the tank). Another method of displaying the results allows to visualize on the 3D screen, the position of points detected by providing the relevant plan interpolating path used by the program, which agree to apply a tolerance that takes into account the possible *non-perfect orthogonality* of the laser beam with respect to the sheet.

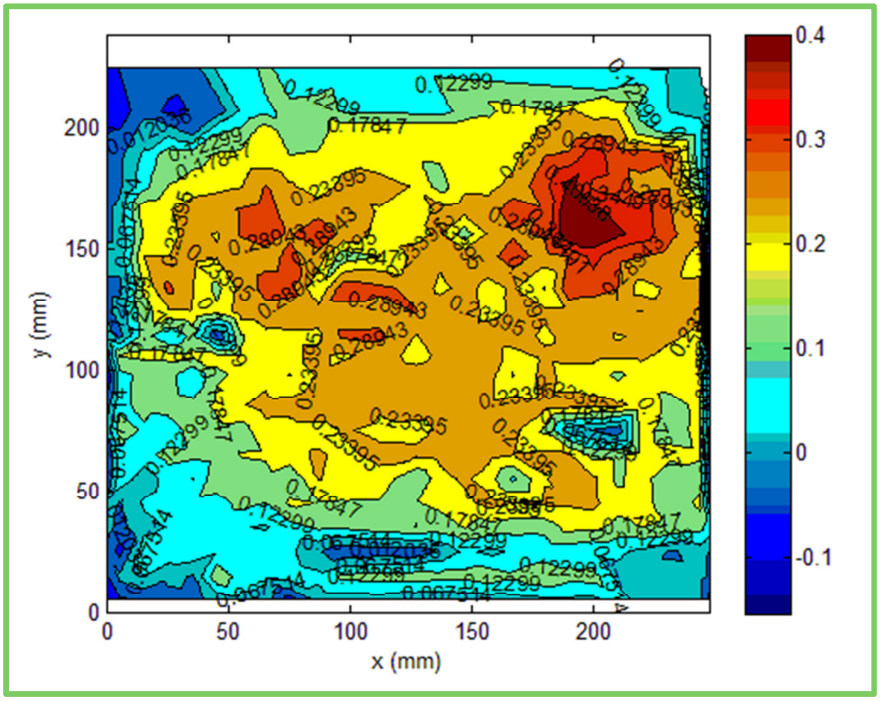


Figure 25:contour plot of the plate surface and level curves when the tank is empty.

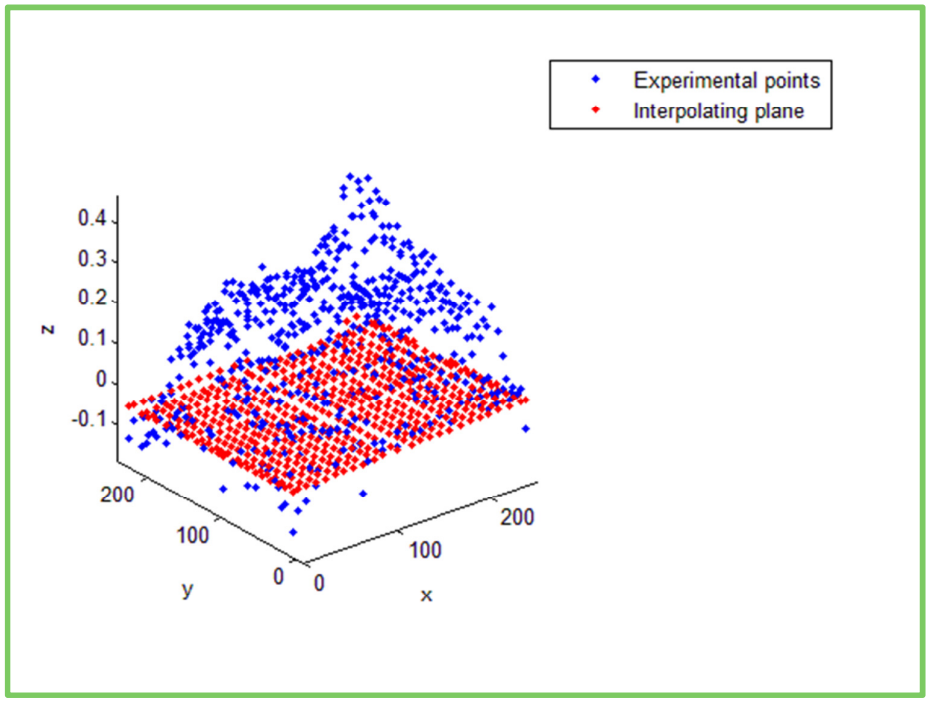


Figure 26: interpolating plane for scatter points of the plate not in contact with liquid.

The points painted in blue are those measured experimentally both on the edge that the free surface of the sheet, while those painted in red are the interpolating points of the plane, which is of different flatness. The main purpose of the interpolating plane is to obtain the best representation of the surface of the plate trying to minimize the distance between the points belonging to the plane and interpolating points obtained experimentally. as is shown in figure (26): the experimental values are, often, so polarized that is very difficult to derive realistic representations of the surface and qualitatively correct. For this reason, it is necessary to phase out those points that are located on the edges of the plate. These points are, in fact, characterized by values which differ significantly from the remaining points cloud and consequently also by interpolating the points of the plane. It is important to highlight that the points located on the edges are essentially characterized by an increased deformation caused by clamping by means of bolts. In fact, if the tightening torque was increased, the points would be deviating more toward the inside of the tank, while if the torque were to be decreased, it would reduce the tensions and superficial stress, but the points would be moved away towards the outside of the tank.

2.7 Implementation in MATLAB: Polynomials and Curve Fitting

This section describes how the computation of the approximating and interpolating surfaces is implemented. The implementation is done in *MATLAB* because of its great computational ability and built-in functions to work with matrices: *MATLAB* is a very suitable tool for this task; it is fast and provides reliable, well-tested routines for efficient matrix manipulations. It also contains a bulk of resources regarding the solving of systems of equations; besides, *MATLAB* provides excellent graphical options and optimized code for input/output interaction and high performance computations. Almost all basic data structures in *MATLAB* are matrices (two or one dimensional). Polynomials are no exception. As *MATLAB* is primarily a numerical software system, the coefficients are by default floating point numbers. With curve fitting we will see how to reduce errors on approximate data. *MATLAB* represents a polynomial

$$p(x) = p_1 x^n + p_2 x^{n-1} + \cdots + p_n x + p_{n+1} \qquad (1)$$

by a row vector $p = [p(1)\, p(2) \ldots p(n+1)]$ of the MATLAB's coefficients. (Note that compared with the representation $\sum_{i=0}^{n} p_i x^i$ used in many textbooks, 's vector is reversed and its subscripts are increased by 1). Here are three problems related to polynomials:

1. **Evaluation**: given the coefficients evaluate the polynomial at one or more points;

2. **Root finding**: Given the coefficients find the roots (the points at which the polynomial evaluates to zero);

3. **Data fitting**: Given a set of data $\{x_i; y_i\}_{i=1}^{m}$ find a polynomial that "fits" the data.

The standard technique for evaluating $p(x)$ is ***Horner's method***, which corresponds to the nested representation:

$$p(x) = \big(\ldots\big((p_1x + p_2x)x + p_3\big)x + \cdots + p_n\big)x + p_{n+1} \qquad (2)$$

Function $polyval$ carries out ***Horner's method***: $y = polyval(p, x)$. In this command x can be a matrix, in which case the polynomial is evaluated at each element of the matrix (that is, in the array sense). Evaluation of the polynomial p in the matrix (as opposed to array) sense is defined for a square matrix argument $\boldsymbol{X}$ by

$$p(x) = p_1X^n + p_2X^{n-1} + \cdots p_nX + p_{n+1}I \qquad (3)$$

The command $Y = polyvalm(p, X)$ carries out this evaluation.

The roots (*or zeros*) of p are obtained with $z = roots(p)$. Of course, some of the roots may be complex even if p is a real polynomial. The function $poly$ carries out the converse operation: given a set of roots, it constructs a polynomial. Thus if z is an *n-vector*, then $p = poly(z)$ gives the coefficients of the polynomial:

$$p(x) = p_1x^n + p_2x^{n-1} + \cdots + p_nx + p_{n+1} = (x - z_1)(x - z_2)\ldots(x - z_n) \qquad (4)$$

(The normalization $p_1 = 1$ is always used.) The function $poly$ also accepts a matrix argument: for a square matrix $\boldsymbol{A}$, $p = poly(A)$ returns the coefficients of the characteristic polynomial $det(x\boldsymbol{I} - A)$.

Regarding the numerical procedures for realizing experimental measurements, the calculation of the best *interpolation plane* has been carried out taking into consideration all points of the grid, also the points close to the edges of the frame: in fact, the deflection surface and the stress distribution near the border of the frame influence in a considerable way the behaviour of the plate. In addition, all stress components due to external loads exerted by bolts are not distributed uniformly and, consequently, the *compressive strength* produced by concentrated loads in the vicinity of these points must also be considered if the intention is to obtain an exact description of the deflection of the plate. The ***Data Fitting problem*** can be addressed with $polyfit$. Suppose the data $\{x_i; y_i\}_{i=1}^{m}$has distinct x_i values, and the purpose is to find a polynomial p of degree at most n such that $p(x_i) \approx y_i$, $i = 1{:}\,m$. The $polyfitfunction$ computes the least squares polynomial fit, that is, it determines p so that the mathematical expression (5) is minimized.

$$\sum_{i=1}^{m}(p(x_i) - y_i)^2 \qquad (5)$$

The syntax is $p = polyfit(x, y, n)$. Specifying the degree n so that $n \geq m$ produces an interpolating polynomial, that is, $p(x_i) = y_i, i = 1{:}\,m$, so the polynomial fits the data exactly. In this case, the MATLAB function $polyfit$ has been used on both direction of the "ideal plane" containing the surface of the plate, in order to find out the coefficients representing the slopes of the interpolating plane in the space. Then z-quote of the best interpolating plane has been determined by evaluation and minimization of the sum of square distances between each possible interpolating plane and all experimental points. MATLAB has functions for interpolation in one, two and more dimensions. Function $interp1$ accepts $x(i)$, $y(i)$ data pairs and a further vector x_i. It fits an interpolant to the data and then returns the values of the interpolant at the points in x_i: $yi = interp1(x, y, xi)$. The vector x must have monotonically increasing elements. Four types of interpolations are supported, as specified by a fourth input parameter, which is one of: $'nearest'$ or neighbour interpolation, $'linear'$: linear interpolation (default), $'spline'$or cubic spline interpolation, and $'cubic'$ interpolation.

Linear interpolation puts a line between adjacent data pairs, while nearest neighbour interpolation reproduces the y value of the nearest x point. MATLAB also has two functions for two-dimensional interpolation: $griddata$ and $interp2$. The syntax for $griddata$ is:

$$\boldsymbol{ZI} = griddata(x, y, z, \boldsymbol{XI}, \boldsymbol{YI});$$

$$[XI, YI, ZI] = griddata(x, y, z, xi, yi);$$

$$[\dots] = griddata(\dots, method);$$

$\boldsymbol{ZI} = griddata(x, y, z, \boldsymbol{XI}, \boldsymbol{YI})$ fits a surface of the form $z = f(x, y)$ to the data in the (usually) non-uniformly spaced vectors (x, y, z). The function $griddata$ is able to interpolate this surface at the points specified by $(\boldsymbol{XI}, \boldsymbol{YI})$ to produce $\boldsymbol{ZI}$. The surface always passes through the data points. $\boldsymbol{XI}$ and $\boldsymbol{YI}$ usually form a uniform grid (as produced by $meshgrid$). $\boldsymbol{XI}$ can be a row vector, in which case it specifies a matrix with constant columns. Similarly, $\boldsymbol{YI}$ can be a column vector, and it specifies a matrix with constant rows.

$[\boldsymbol{XI}, \boldsymbol{YI}, \boldsymbol{ZI}] = griddata(x, y, z, xi, yi)$ returns the interpolated matrix $\boldsymbol{ZI}$ as above, and also returns the matrices XI and YI formed from row vector x_i and column vector y_i. These latter are the same as the matrices returned by $meshgrid$.
$[\dots] = griddata(\dots, method)$ uses the specified interpolation method:

- $'linear'$: Triangle-based linear interpolation (default);
- $'cubic'$: Triangle-based cubic interpolation;
- $'nearest'$: Nearest neighbour interpolation.

Another important function, used to elaborate and visualize the experimental results of the scanning surface, is: $contour(Z)$ and $[C, h] = contourf(\dots)$.
$Contour(Z)$ draws a contour plot of matrix Z, where Z is interpreted as heights with respect to the x-y plane. Z must be at least a 2-by-2 matrix that contains at least two different values. The number of contour lines and the values of the contour lines are chosen automatically based on the minimum and maximum values of Z. The ranges of the x- and y-axis are $[1:n]$ and $[1:m]$, where $[m, n] = size(Z)$. It is possible label the contour lines using the function: $clabel(C, h)$. The function inserts only those labels that fit within the contour, depending on the size of the contour. The level curves shown in the figure () refer to the outer surface of the plate. in this experimental phase, it was decided to use a Spatial Reference System (xyz) in order to define the relative displacement along the z axis with respect to the ideal configuration of the plate perfectly flat. Note, also, that for the relative displacement is meant the deviation in the orthogonal direction to the plate with respect to the point ($x = 0, y = 0,\ z = 0$), taken as reference in order to associate to each point of the grid a tern of values that describes the exact location. In order to give meaning to the data so elaborate, it is assumed that a negative sign of the z-coordinate represent a deformation towards the observer, while a positive sign represents a deformation towards the inside of the tank.
The $contouring$ display functions compute, plot, and label "$isolines$" (contour lines) for one or more matrices. These displays vary according to whether they plot plain contour lines, filled contour lines, raised contours, or contours in concert with mesh or surface plots. The contour function calculates the contour matrix for the other contour functions. It is a low-level function that is not called from the command line. The contouring algorithm first determines which contour levels to draw. If you specified the input vector v, the elements of v are the contour level values, and $length(v)$ determines the number of contour levels generated. The height matrix Z has associated X and Y matrices that locate each value in Z at the intersection of a row and a column, or these matrices are inferred when they are unspecified. The row and column widths can vary, but typically they are constant (i.e., Z is a regular grid).

The function $[C, h] = contourf(\dots)$, instead, returns a *contour matrix*, C, that contains the x, y coordinates and contour levels for contour lines derived by the low-level *contourc* function, and a handle, h, to a contourgroup object containing the filled contours. The matrix C is defined in the following mode:

$$C=\begin{bmatrix} value1 & xdata(1) & xdata(2) \dots \\ numv & ydata(1) & ydata(2) \dots \end{bmatrix} \quad (6)$$

The first row of the column that begins each definition of a contour line contains the contour value, as specified by v. Underneath that value is the number of (x, y) vertices in the contour line. Remaining columns contain the data for the (x, y) pairs. As can be noted, the figure (25) shows an example of a *scanning surface* in which are highlighted the local deformation and the non-perfect surface regularity through the use of level curves. The level curves allow to identify different areas on the surface which differ from each other by the value of the relative deviation in the z direction. In addition, using the function *contourplot*, it is possible to create a colour map associating to each area a colour which indicates the relative displacement expressed, in this case, in millimetres.

2.8 Geometric Imperfections of the Plate: Results

The *buckling* behaviour of shell structures is generally influenced by their initial imperfections, which occur during the manufacturing and construction stages. This variability of initial imperfections together with their pronounced influence on the load carrying capacity of shells has been proved to be responsible for the large scatter observed in the experimental results. In addition to initial geometric imperfections, other sources of imperfections such as the variability of thickness, material properties, boundary conditions and misalignment of loading are also responsible for the reduction as well as the scatter of the buckling load of shell structures
In this thesis, the effect of material and thickness imperfections are not investigated, but only the buckling due to random geometric imperfections on the plate surface. It is necessary to keep in mind that the concept of an initial imperfect structure is introduced involving not only geometric deviations of the shell structure from its perfect geometry but also a spatial variability of the modulus of elasticity as well as of the thickness of the shell. As has been said above, the plate used for the analyses presented experimental already small surface imperfections which have been appropriately evaluated before starting to perform the modal analysis in order to qualitatively measure the effect of these imperfections on the natural frequencies of vibration of the plate. In fact, the images that will be shown below, were obtained by a specific program for calculating the local deformations distributed unevenly on the surface of the plate. The scan of the sheet is made by placing the laser beam on the selected points and recording the values in Volt indicated on the display. At this stage it must pay attention to the fact that the laser could go out of range. To prevent this from happening, it was positioned on a laser LED, which has the task to report if this happens.

Implementation of data

The implementation of the data is processed using a program that performs an interpolation to derive the plane interpolating the points and, subsequently, calculates the distances of the points from this plane to obtain the deformed shape of the plate.
The program used in the analysis of the data is a program developed at the University of Parma in **MATLAB** environment. This program takes as input two matrices formed respectively by:

- A matrix containing the coordinates of the points of the plate measured. It was decided to use a system in the space formed by the values *x*, *y* and *z*. *Z* values are the values measured with the laser;

- A matrix containing the coordinates of the points belonging to the edge of the lamina. Always *x*, *y*, and *z* will be the matrix that will be used for interpolation.

The program, using the first and the second matrix, it will perform an interpolation of the data to derive the plan that best approximates the measured data. Subsequently, knowing the plane interpolating, the program will be derived buckling values of the plate and will represent these values through graphs and 2D contour levels. These curves will be analyzed to know the actual deformation of the plate. The data obtained by the deformations will be useful to make a comparison between the natural frequencies of vibration obtained experimentally and those obtained using a finite element model. Before starting to scan the plate, it is essential to understand the flatness of the surface and to establish, through various measures, the possible convergence, i.e. what is the minimum value of points to be taken on the surface of the sheet to be able to understand the degree deformation. Moreover, at this stage of measures, the object is to try to understand if the found values may influence, and in what manner, the non-perfect planarity between the surface of the sheet and the normal plane to the laser beam.

In order to achieve the best possible parallelism between the two plans, it is necessary, first, doing some measurements on points of the grid that seem to be characterized by lower surface deformation: if on the display of the laser sensor appears the value $0.00\,Volt$, then the two planes are parallel. In the case where this value does not appear on the display, it is appropriate to rotate the tank in order to ensure the necessary convergence (parallelism) of the sheet surface and the laser beam.
It must be said though, that if there were some error of parallelism between the plate and the laser, it would be offset by the program used for processing the data: it allowed to obtain *Level Curves* using a plane that interpolates experimental having the function to delete a non-perfect orthogonality between the laser beam and the plane of the plate itself. The accuracy of laser triangulation is equal to:

$$4\mu m = 4 \cdot 10^{-6}\, m \qquad (1)$$

that, according to the law of relative conversion equal to a range of:

$$-0.50 \leq V \geq +0.50 \qquad (2)$$

Where: $1\ kHz = 10^{-3} Hz$.

The operation of *"scanning surface"* consists to carry out the static measurement of the offset value of each grid point with respect to the selected point as the reference to which is assigned the value *"zero"*.
The following figure shows the system of reference axes used on the plate surface to define the displacements of the laser beam (Fig.). For this test, the experimental point taken as a reference to *"flatness zero"* on the grid is located on the edge corresponding to the centre bolt of the first row from the top, which translated into metric coordinates according to the reference system adopted, is located in position **(125 ; 232)** millimetres.

During the scanning is necessary that the value of the reference point *"zero"* remains fixed, or in any case, within the range of values considered acceptable. It is always appropriate taking care not to perform the measurement exactly on the point, because the layer of marker, used to identify and draw the point, at this level of precision can distort the measurement taken.
For each measurement on the display, the values are expressed in volts, which will be then converted into millimetres thanks to a mathematical law conversion. For the triangulation laser **NAIS® ANR 1282** the conversion law is the following:

$$5[V] = 20 \cdot 10^{-3}\, m \qquad (3)$$

After completing the scan, it must create a table that shows, for all points, the following values indicating the actual position on the grid of the point considered:

- *the value on the horizontal axis (coordinate "x")*;
- *the value on the vertical axis (coordinate "y")*;
- *the value on the "z" indicates the removal (positive value) and the approach (negative value) the point with respect to the "zero" reference.*

The data contained in the table will subsequently be converted into a file text *"txt"* in order to be able to be processed by the computer by means of a computer code that, thanks to a special function, realizes a plan interpolating respect to which it is possible to display on a chart all relative displacements with respect to the fixed point as a reference.

The table (1) shows in tabular format the scanning surface of the grid points belonging to the first row located in the lower part of the plate: in the list, for each point, there are the coordinates x, y and z. Note that the z coordinate was obtained experimentally by scanning and, therefore, it was necessary to convert the value found from Volt to millimetres.

X(cm)	X(mm)	Y(cm)	Y(mm)	Z(V)	Z(mm)
0,00	0,00	0,00	0,00	0,00	-1,080
0,50	5,00	0,00	5,00	0,00	-1,052
1,50	15,00	0,00	15,00	0,00	-1,320
2,50	25,00	0,00	25,00	0,00	-1,328
3,50	35,00	0,00	35,00	0,00	-1,400
4,50	45,00	0,00	45,00	0,00	-1,764
5,50	55,00	0,00	55,00	0,00	-1,760
6,50	65,00	0,00	65,00	0,00	-1,760
7,50	75,00	0,00	75,00	0,00	-1,720
8,70	87,00	0,00	87,00	0,00	-1,800
9,70	97,00	0,00	97,00	0,00	-1,484
11,20	112,00	0,00	112,00	0,00	-1,112
12,70	127,00	0,00	127,00	0,00	-1,368
13,70	137,00	0,00	137,00	0,00	-1,640
14,70	147,00	0,00	147,00	0,00	-1,244
15,70	157,00	0,00	157,00	0,00	-1,244
16,70	167,00	0,00	167,00	0,00	-1,288
18,00	180,00	0,00	180,00	0,00	-1,500
19,00	190,00	0,00	190,00	0,00	-1,504
20,00	200,00	0,00	200,00	0,00	-1,736
21,00	210,00	0,00	210,00	0,00	-1,720
22,00	220,00	0,00	220,00	0,00	-1,560
23,20	232,00	0,00	232,00	0,00	-1,604
24,40	244,00	0,00	244,00	0,00	-1,692
24,90	249,00	0,00	249,00	0,00	-1,056

Table 1: example of scanning surface of the grid points.

Before analysing the various graphs, it is useful to describe a command which has been used in *MATLAB*. The command $A = B$ is used to describe where the interpolating plane must interpolate the points cloud, namely the set of all 625 grid points. In fact, in the original program the interpolating plan used the edges of the plate as a reference; in particular, in the program only the points close to the edges of the plate are used in order to calculate the interpolating plane. Using the command $A = B$ there is the possibility of interpolating the set of points not only with the edges, but also with all the grid points. The concluding part of this chapter is constituted by the description of the graphs obtained with this series of analyses.

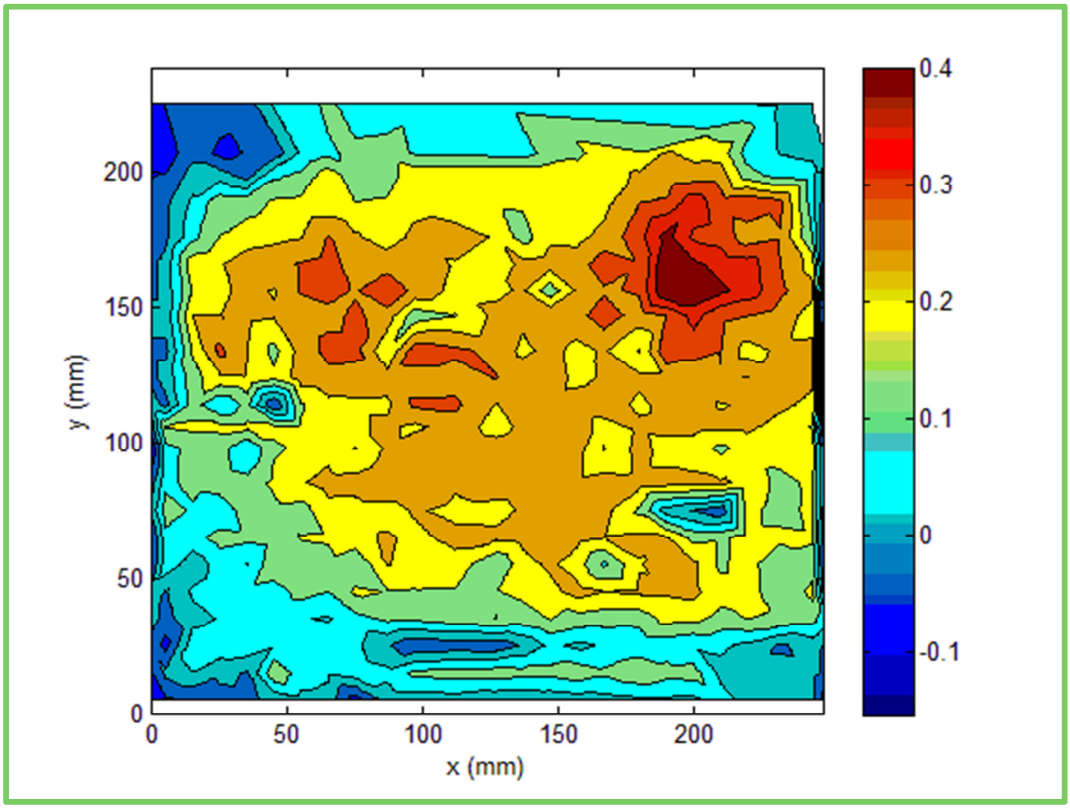


Figure 26: scanning surface of the thin plate: it is not in contact with liquid.

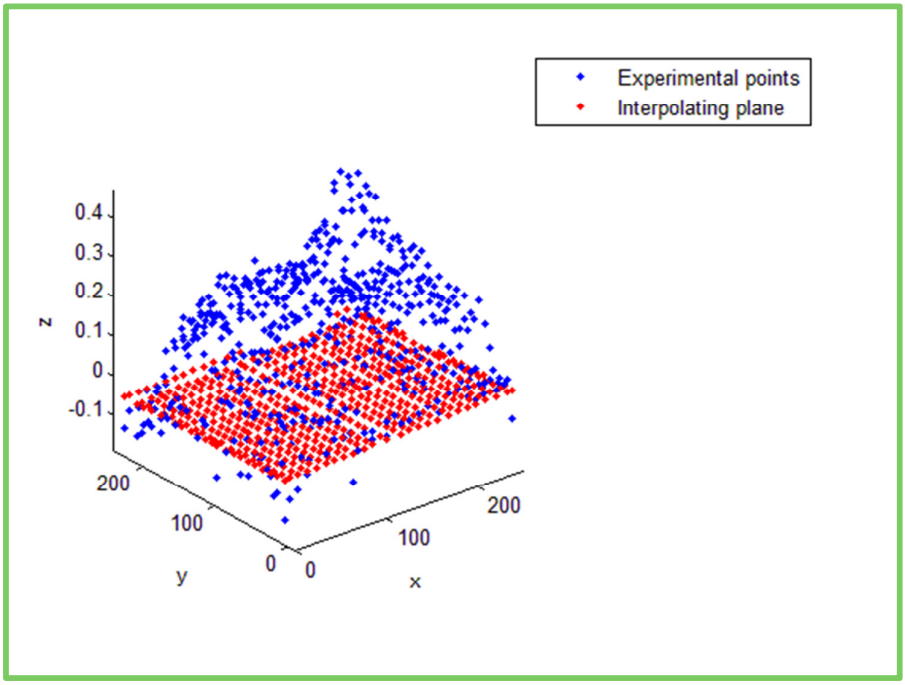


Figure 27: scatter plot of the surface, the plate is not bounded with liquid.

As can be seen, the best results in terms of flatness without excessive stress on the edge points have been obtained by a torque equal to 5 Nm: torque values are higher due to excessive deformation of the plate, especially in the points near the edges. This is verified experimentally by scanning laser, in fact, the values associated with each grid point adjacent to the edge are positive. The positive sign indicates a shift away from these points relative to the laser beam. In this condition, therefore, it would create an additional strain which is added to the micro surface deformations already present on the plate. The figure above shows through level curves areas of the plate more subject to deformation, the extent of this deformation in terms of displacement and where these are located. In this case, only the plate is mounted on the frame and the inner surface delimiting the internal volume of the tank is not in contact with the liquid: the deformations are exclusively due to surface imperfections and not to the volume load exerted by the liquid. It may be noted that the plate has a depression in the upper right having a depth of about 0.4 millimetres; there are moreover three other zones with depth equal to 0.3 millimetres that move away from the laser light beam, placed in the central area at the top. There are also, of the protrusions both in the lower part of the plate in the upper left: this last is particularly significant to the experimental analysis as, in this area, there

is a shift toward the light beam equal to 0.2 millimetres. These significant deformation probably were caused mainly by the fact that the plate has already been used for other tests, in which the frame was filled with water and the hydrostatic forces, due to the volume of liquid, caused over time a permanent deformation in the plate, as can be seen for every graphs reported below. It is necessary to specify that the number of scansions performed corresponds to the number of levels of the liquid chosen for the filling of the tank. In particular, the interaction of the plate with a wall of the liquid domain is presented and shown: the liquid pressure as well as the deformation of the plate have been analyzed and reworked graphically to highlight shear stresses and strain along the plate boundaries.

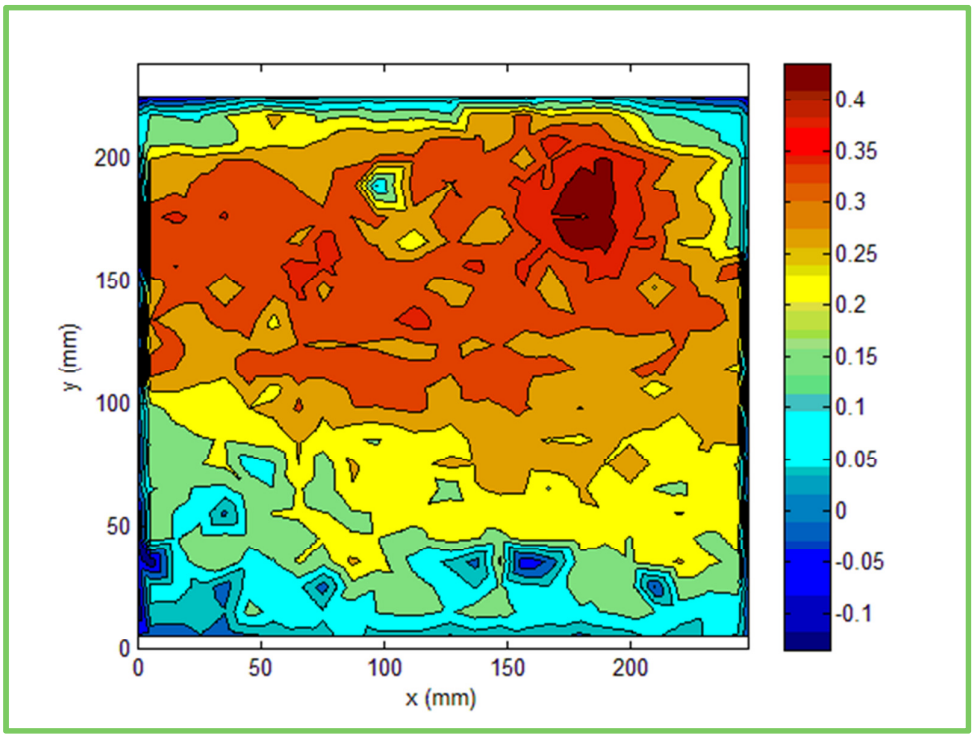


Figure 27: level curves of the plate, the filling level is equal to 6 [cm].

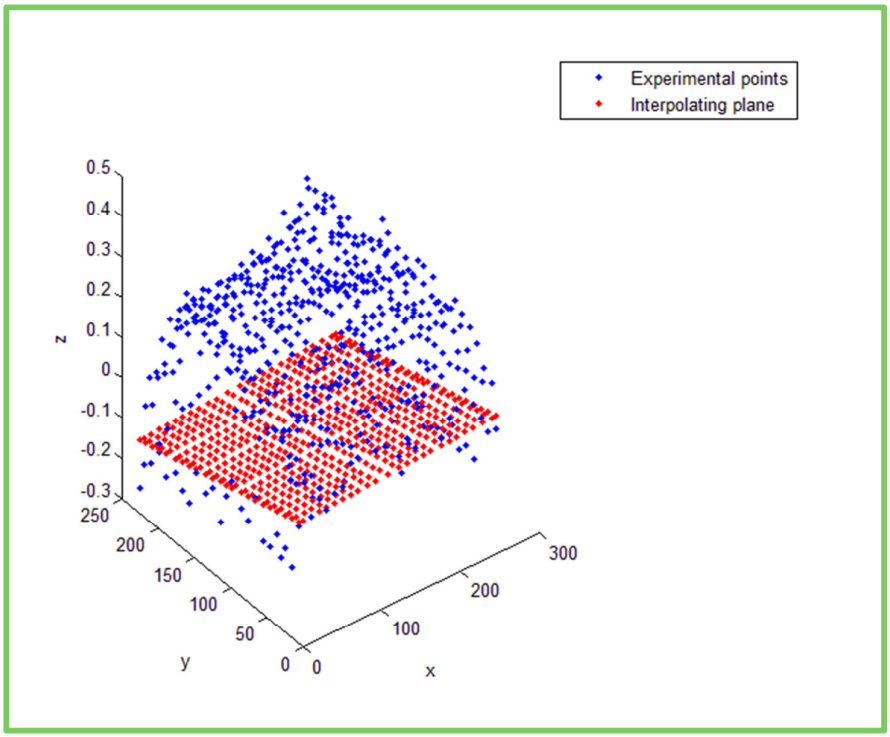


Figure 28: scatter plot of the surface, the filling level is equal to 6 [cm].

As can be seen from the figure (27), there is a substantial difference from the case where the plate is not in contact with the liquid. All this is essentially due to the fact that the mass of liquid is still too small to exert a force on the plate surface such as to generate the efforts able to significantly change the initial conformation of the plate. The depression in the upper right is still present, although its size increased slightly, as well as its depth is increased from 0.4 to 0.5 [mm]. It is also noted that the left edge of the plate appears, in this case, less deformation towards the outside, but a more accentuated and distributed protuberance in the lower part of the plate. Another important difference that can be highlighted compared to the case where the plate is not in contact with the liquid, is given by the presence of a protrusion in the lower part of the lamina, more pronounced and more uniformly distributed on the surface. This deformation, more evident in the lower part of the slab, is generated from the stress, strains and deflections which develop under the action of hydrostatic pressure.

Figure (29) shows as the hydrostatic pressure is able to generate to generate a force such as to move the points of the edge towards negative values, i.e. the distance between the scanned surface and the point of emission of the laser beam is decreased. the edges most affected by the influence of the pressure exerted by the liquid are: the bottom edge and the left vertical edge.

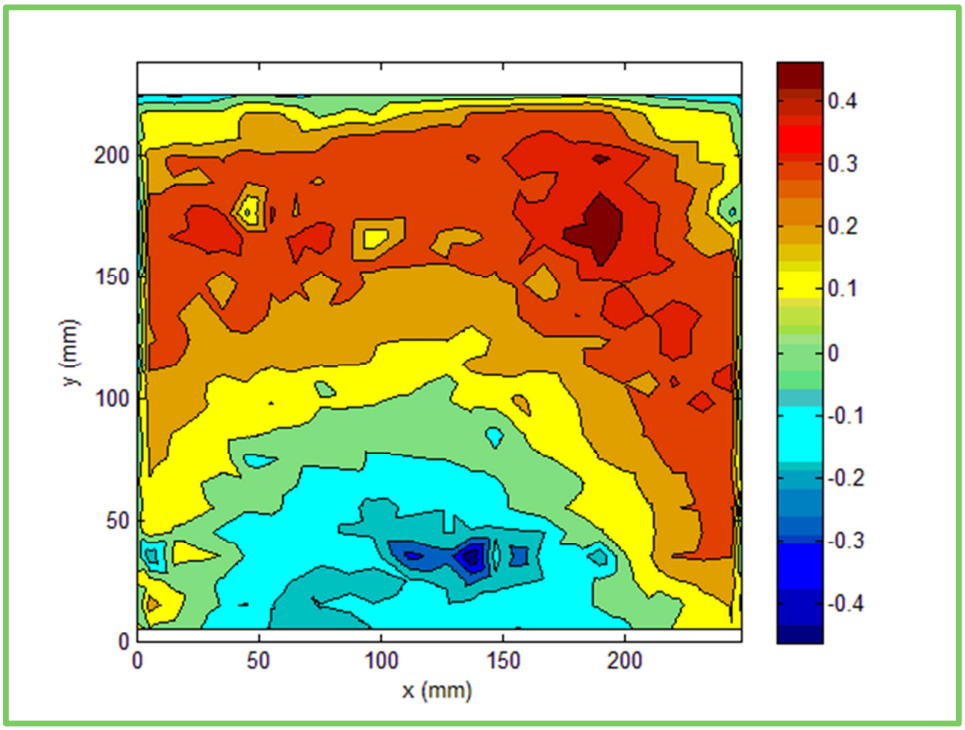


Figure 29: level curves of the plate, the filling level is equal to 12 [cm].

In the figure above, it is shown how the hydrostatic pressure has made more evident the hump at the bottom of the plate, visible also in the case where the liquid level is equal to 6 centimetres. Here, the hump is wider and distributed more uniformly on the surface. In order to obtain the level curves, it has been necessary to eliminate the points belonging to the bottom edge and those belonging to the upper edge.

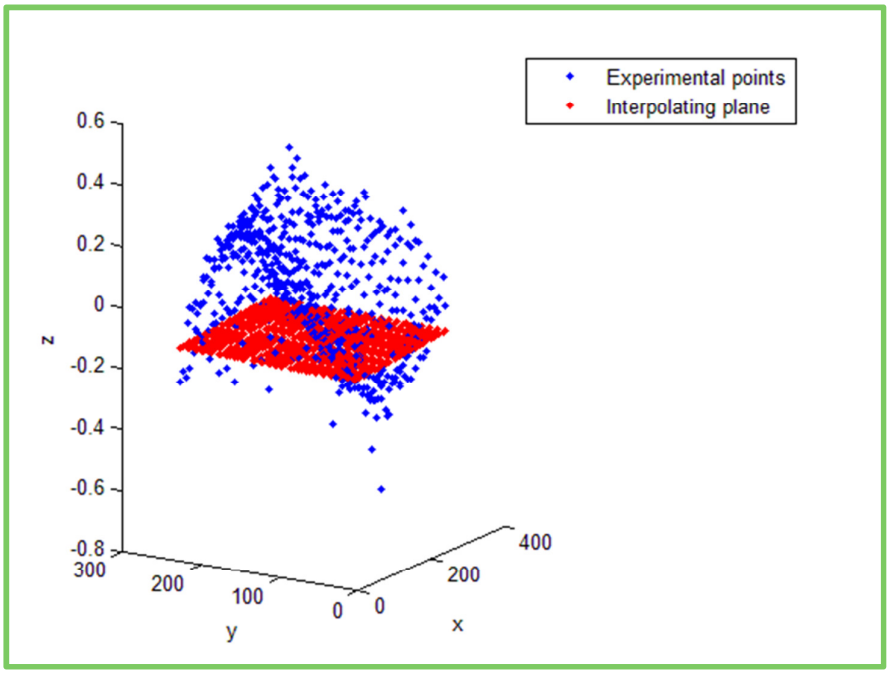


Figure 30: scatter plot of the surface, the filling level is equal to 12 [cm].

The edge points and those located on the free surface of the plate are subject to a pressure whose intensity is increased: the majority of points, especially those along the sides of the plate are characterized by negative values and the surface presents a deformation uprising towards the outside of the tank.

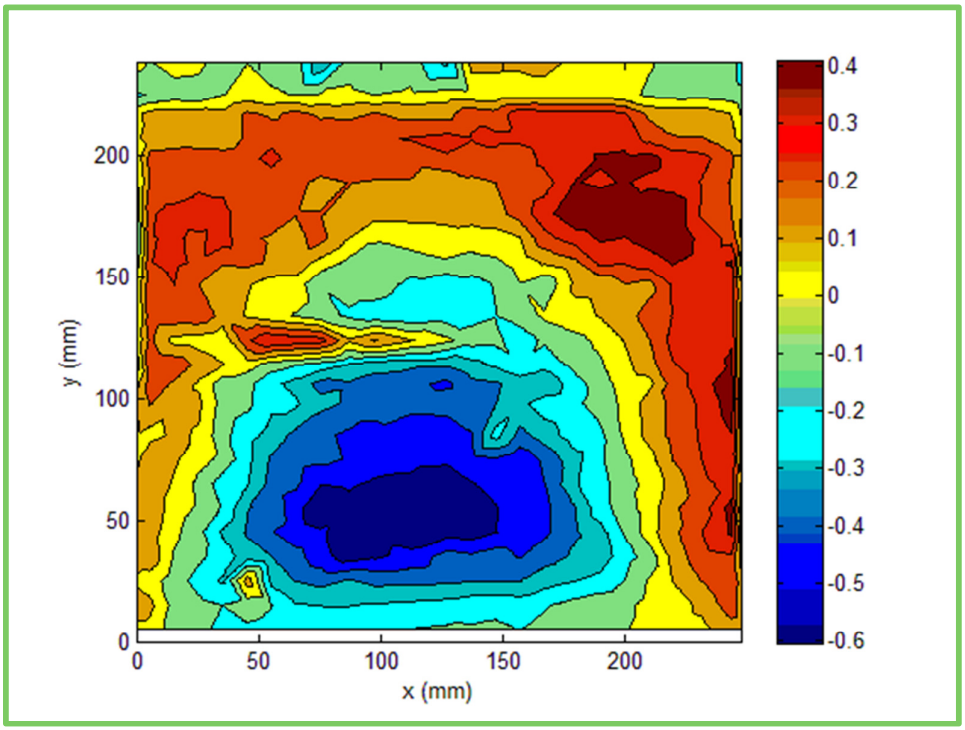


Figure 31: scansion of the surface, the filling level is equal to 18 [cm].

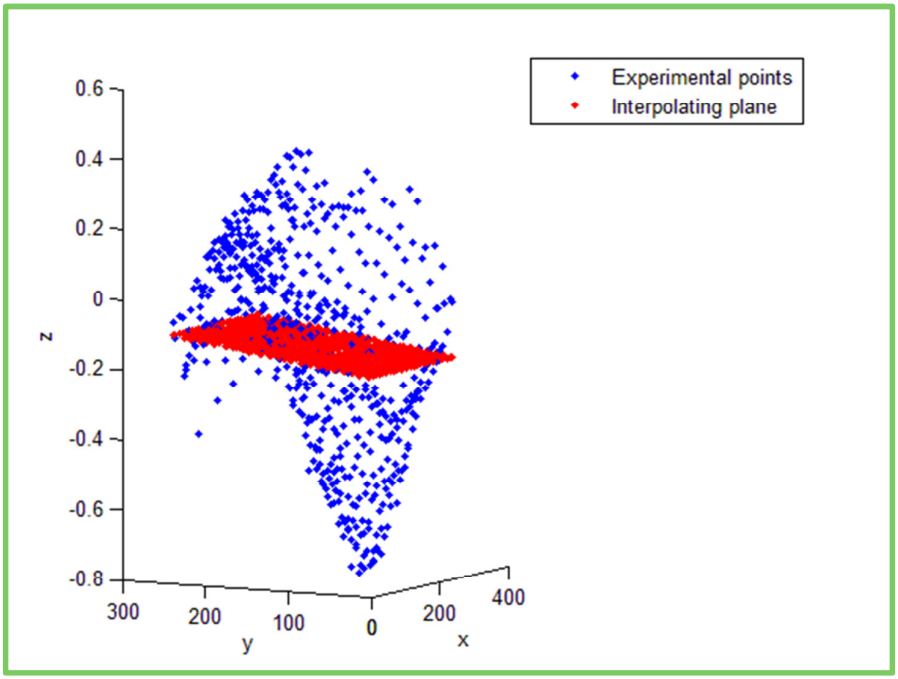


Figure 32: scatter plot for the liquid level equal to 18 [cm].

Figure (31) and (32) show that the values obtained experimentally have moved increasingly away from the interpolating plane due to the hydrostatic pressure which having *triangular form*, exerts its maximum intensity on the bottom of the container. its action, on the contrary, decreases with progressive increase of the height; its action is equal to zero on the free surface of the liquid contained within the tank.

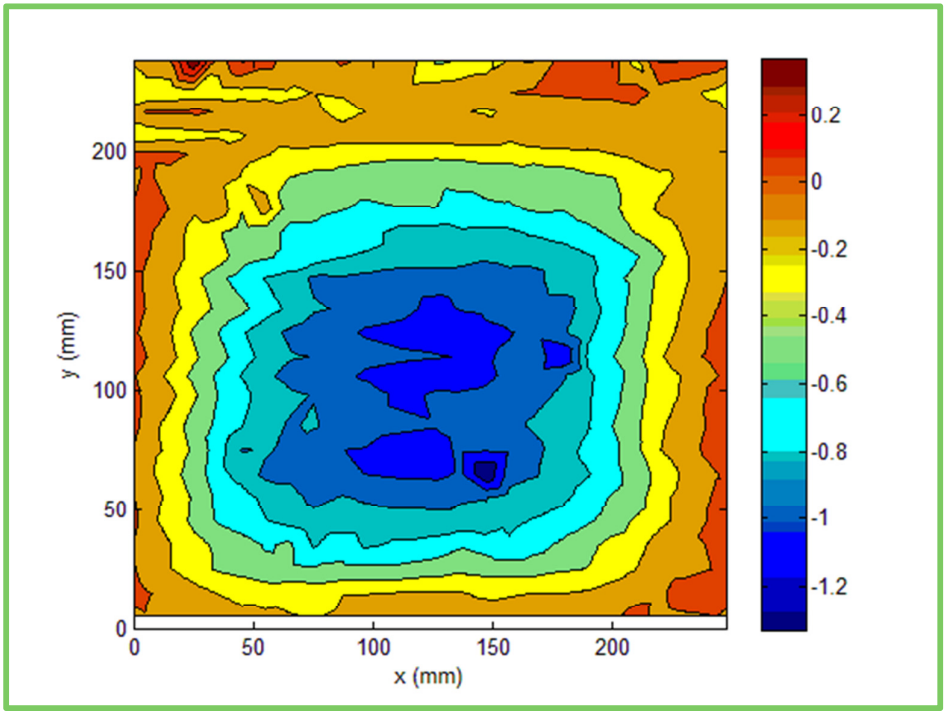


Figure 33: central hump of the plate for liquid filling level of 23 [cm], the area of the surface having a blue colour shows that the concavity is facing outwards (the minimum value the minimum deviation achieved with respect to the reference point 0.00*, is equal to* $-\mathbf{1.3}$ *[mm]).*

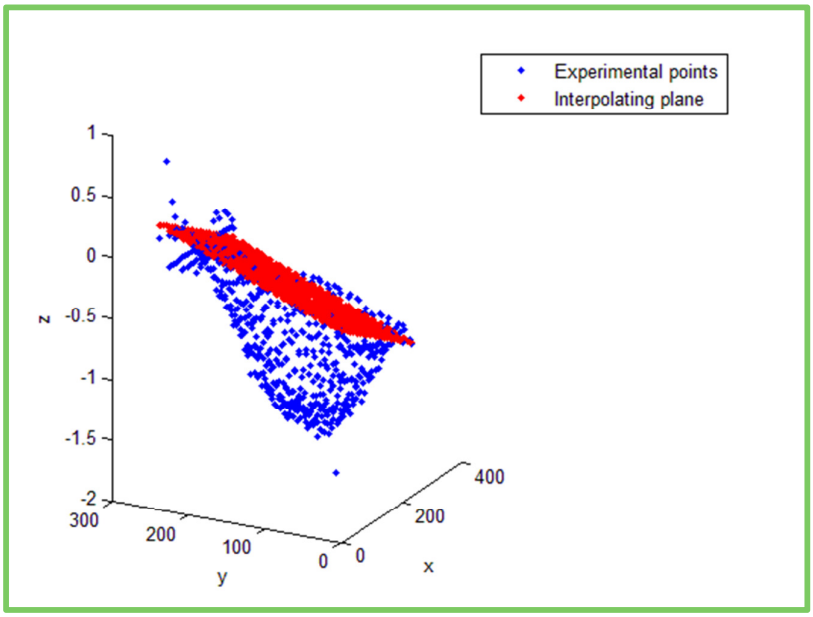


Figure 35:scatter plot for the liquid level equal to 23 [cm], the experimental pattern points reproduce the central hump shown in figure 34.

It can be argued, after performing the five scans, that the central deformation caused by the force exerted by the hydrostatic pressure has reached, through the measurement of the points, ***offset values greater than the thickness of the plate*** (plate's deformations are more larger than its thickness) *These large deformations* necessarily have to be evaluated and taken into account during the excitation of the plate by means of an instrumented hammer: the frequency response is sure to be different compared to the case where the plate is perfectly flat. It can be argued, after performing the five scans, that the central deformation caused by the force exerted by the hydrostatic pressure has reached, through the measurement of the points, offset values greater than the thickness of the plate. these large deformations necessarily have to be evaluated and taken into account during the excitation of the plate by means of an instrumented hammer: the frequency response is sure to be different compared to the case where the plate is perfectly flat. The reduced thickness of the plate makes it much more subject to the risk of deformation; probably the surface deformation caused by the volume of liquid will have accentuated the strains already present on the surface, but it will also create new ones, therefore, the plate once After completing his studies, the plate will no longer be used.

2.9 Hydrostatic Pressure exerted on the Plate: theoretical model

The force that the pressure exerts on the plate surface is expressed as a function of the thickness of the plate: the decrease in thickness causes an increase of the pressure force acting on the part of surface in contact with the liquid. In order to describe the effect of hydrostatic pressure upon the surface of the plate, it must introduce, in this section, a brief survey of the *Theory of Plates and Shells* that will be useful for the development of all equations and relations will be given to explain the behaviour of simply supported rectangular plates. The classical theories of plates and shells are an important application of the Theory of Elasticity, which deals with relationships of forces, displacements, stresses, and strains in an elastic body. When a solid body is subjected to external forces, it deforms, producing internal strains and stresses. The deformation depends on the geometrical configuration of the body, on applied loading, and on the mechanical properties of its material. In the theory of elasticity we restrict our attention to *linear elastic materials*, i.e. the relationships between stress and strain are linear, and the deformations and stresses disappear when the external forces are removed. The classical theory of elasticity assumes the material is *homogeneous* and *isotropic*, i.e. its mechanical properties are the same in all directions and at all points. The fundamental assumptions of the linear, elastic, small-deflection theory of bending for thin plates may be stated as follows:

1. The material of the plate is elastic, homogeneous, and isotropic;

2. The plate is initially flat;

3. The deflection (the normal component of the displacement vector) of the mid-plane is small compared with the thickness of the plate. The slope of the deflected surface is therefore very small and the square of the slope is a negligible quantity in comparison with unity;

4. The straight lines, initially normal to the middle plane before bending, remain straight and normal to the middle surface during the deformation, and the length of such elements is not altered. This means that the vertical shear strains γ_{xz} and γ_{yz} are negligible and the normal strain σ_z may also be omitted. This assumption is referred to as the "*hypothesis of straight normal*";

5. The stress normal to the middle plane, σ_z, is small compared with the other stress components and may be neglected in the stress–strain relations;

6. Since the displacements of a plate are small, it is assumed that the middle surface remains unstrained after bending.

Assume that a simply supported rectangular plate is loaded as shown in figure (). Proceeding as in the case of a uniformly distributed load, the deflection of the plate is given in the form:

$$w = w_1 + w_2 \tag{1}$$

In which

$$w_1 = \frac{q_0}{360D}\left(\frac{3x^5}{a} - 10ax^3 + 7a^3x\right) = \frac{2q_0a^4}{\pi^5 D}\sum_{m=1,2,3,\ldots}^{\infty}\frac{(-1)^{m+1}}{m^5} sin\frac{m\pi x}{a} \tag{2}$$

represents the deflection of a strip under the triangular load. This expression satisfies the differential equation:

$$\frac{\partial^4 w}{\partial x^4} + 2\frac{\partial^4 w}{\partial x^2 \partial y^2} + \frac{\partial^4 w}{\partial D^4} = \frac{q}{D} = \frac{q_0 x}{aD} \tag{3}$$

and the boundary conditions:

$$\begin{cases} w = 0 \\ \frac{\partial^2 w}{\partial x^2} = 0 \end{cases} \qquad \text{for } x = 0 \; and \; y = 0 \tag{4}$$

The part w_2 is taken in the form of a series

$$w_2 = \sum_{m=1}^{\infty} Y_m sin\left(\frac{m\pi x}{a}\right) \tag{5}$$

where the function Y_m is a function of y only. It is assumed that the sides $x = 0$ and $x = a$ are simply supported. Hence is terms of series (5) satisfies the boundary conditions $w = 0$ and $\frac{\partial^2 w}{\partial x^2} = 0$ on these two sides. It remains to determine Y_m in such a form as to satisfy the boundary conditions on the sides $y = \pm b/2$ and also the equation (3) of the deflection surface.
The expression of Y_m can be taken in the form:

$$Y_m = \frac{qa^4}{D}\left(A_m cosh\frac{m\pi y}{a} + B_m \frac{m\pi y}{a} sinh\frac{m\pi y}{a} + C_m sinh\frac{m\pi y}{a} + D_m \frac{m\pi y}{a} cosh\frac{m\pi y}{a}\right) \tag{6}$$

Substituting expressions (2) and (5) into equation (1), it obtains:

$$w = \frac{q_0 a^4}{D}\sum_{m=1}^{\infty}\left[\frac{2(-1)^{m+1}}{\pi^5 m^5} + A_m cosh\frac{m\pi y}{a} + B_m \frac{m\pi y}{a} sinh\frac{m\pi y}{a}\right] sin\left(\frac{m\pi x}{a}\right) \tag{7}$$

where the constants A_m and B_m are to be determined from the conditions:

$$\begin{cases} w = 0 \\ \frac{\partial^2 w}{\partial y^2} = 0 \end{cases} \qquad \text{for } y = \pm\frac{b}{2} \tag{8}$$

From these conditions it finds:

$$\frac{2(-1)^{m+1}}{\pi^5 m^5} + A_m cosh\alpha_m + B_m \alpha_m sinh\, a_m = 0 \tag{9}$$

$$(2B_m + A_m)\, cosh\alpha_m + B_m \alpha_m sinh\, a_m = 0 \tag{10}$$

where $\alpha_m = \frac{m\pi b}{2a}$.

Solving them, it finds:

$$A_m = -\frac{(2+\alpha_m tanh\alpha_m)(-1)^{m+1}}{\pi^5 m^5 cosh\alpha_m} \tag{11}$$

$$B_m = \frac{(-1)^{m+1}}{\pi^5 m^5 cosh\alpha_m} \tag{12}$$

The deflection of the plate along the x axis is:

$$(w)_{y=0} = \frac{q_0 a^4}{D}\left[\frac{2(-1)^{m+1}}{\pi^5 m^5} + A_m\right] sin\left(\frac{m\pi x}{a}\right) \tag{13}$$

The deflection at the center of the plate is:

$$(w)_{y=0} = \frac{q_0 a^4}{D}\left(0.002055 sin\frac{\pi x}{a} - 0.000177 sin\frac{2\pi x}{a} + 0.000025 sin\frac{3\pi x}{a} - \cdots\right) \tag{14}$$

$$(w)_{x=a/2\,,y=0} = 0.00203\frac{q_0 a^4}{D} \tag{15}$$

By equating the derivative of expression (14) to zero, the maximum deflection is at the point $x = 0.557a$. This maximum deflection, which is $0.00206\ q_0 a^4/D$, differs only very little from the deflection at the middle as given by formula (15). The point of maximum deflection approaches the center of the plate as the ratio b/a increases. For $b/a = \infty$, as for a strip [see expression (2)], the maximum deflection is at the point $x = 0.5193a$. When $b/a < 1$, the point of maximum deflection moves away from the center of the plate as the ratio b/a decreases.

The deflection at several points along the x axis (figure 36) are given in table (2). It is seen that, the ratio b/a increases, the deflections approach the values calculated for a strip. For $b/a = 4$ the differences in these values are about $1\frac{1}{2}$ *per cent*. It is possible calculating the deflection of a plate for which $b/a > 4$ with satisfactory accuracy by using formula (2) for the deflection of a strip under triangular load.

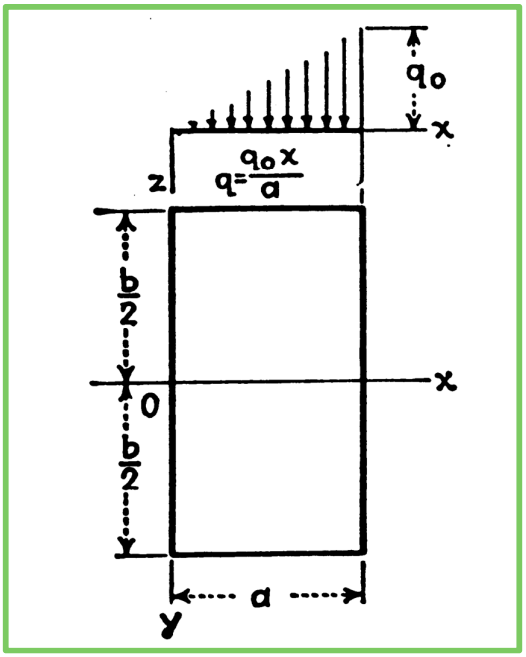


Figure 36: deflection of a thin plate under hydrostatic pressure.

b/a	$x = 0.25a$	$x = 0.50a$	$x = 0.60a$	$x = 0.75a$
1	0.00131	0.00203	0.00201	0.00162
1.1	0.00158	0.00243	0.00242	0.00192
1.2	0.00186	0.00282	0.00279	0.00221
1.3	0.00212	0.00319	0.00315	0.00248
1.4	0.00235	0.00353	0.00348	0.00273
1.5	0.00257	0.00386	0.00379	0.00296
1.6	0.00277	0.00415	0.00407	0.00317
1.7	0.00296	0.00441	0.00432	0.00335
1.8	0.00313	0.00465	0.00455	0.00353
1.9	0.00328	0.00487	0.00475	0.00368
2.0	0.00342	0.00506	0.00494	0.00382
3.0	0.00416	0.00612	0.00592	0.00456
4.0	0.00437	0.00641	0.00622	0.00477
5.0	0.00441	0.00648	0.00629	0.00483
∞	0.00443	0.00651	0.00632	0.00484

Table 2: numerical factor α for deflections of a simple supported rectangular plate under hydrostatic pressure

$$q = q_0 x/a, \quad b > a \quad (w)_{y=0} = \alpha \frac{q_0 a^4}{D}.$$

Boundary Conditions: *Simply Supported Edges*

If the edge $x = a$ of the plate is simply supported, the deflection w along this edge must be zero. At the same time this edge can rotate freely with respect to the edge line; i.e. , there are no bending moments M_x along this edge. This kind of support is represented in figure (37). The analytical expressions for the boundary conditions in this case are:

$$(w)_{x=a} = 0 \qquad \left(\frac{\partial^2 w}{\partial x^2} + \nu \frac{\partial^2 w}{\partial y^2}\right)_{x=a} \tag{16}$$

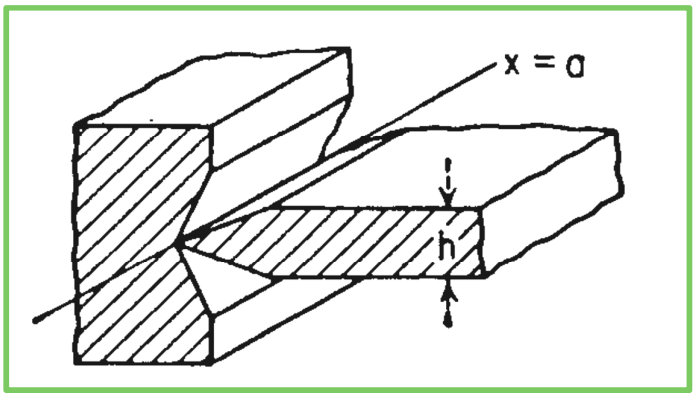


Figure 37: representation of simply supported edge.

Observing that $\frac{\partial^2 w}{\partial y^2}$ must vanish together with w along the rectilinear edge $x = a$, the second of the conditions (16) can be rewritten as: $\frac{\partial^2 w}{\partial x^2} = 0$ or also $\Delta w = 0$. Equations (16) are therefore equivalent to the equations (17), which do not involve *Poisson's ratio* ν.

$$(w)_{x=a} = 0 \qquad (\Delta w)_{x=a} = 0 \tag{17}$$

The bending moments M_x and M_y are founded by substituting expression (6) for deflections in equations (18) and (19).

$$M_x = -D\left(\frac{\partial^2 w}{\partial x^2} + \nu\frac{\partial^2 w}{\partial y^2}\right) \tag{18}$$

$$M_y = -D\left(\frac{\partial^2 w}{\partial y^2} + \nu\frac{\partial^2 w}{\partial x^2}\right) \tag{19}$$

$$M_{xy} = M_{yx} = D(1-\nu)\frac{\partial^2 w}{\partial x \partial y} \tag{20}$$

Along the x axis $(y = 0)$ the expression for M_x is given by the equation (21):

$$(M_x)_{y=0} = q_0 a^2 \sum_{m=1}^{\infty} \frac{2(-1)^{m+1}}{\pi^3 m^3} sin\frac{m\pi x}{a} + q_0 a^2 \pi^2 \sum_{m=1}^{\infty} m^2[(1-\nu)A_m - 2\nu B_m] sin\left(\frac{m\pi x}{a}\right)$$

The first sum on the right-hand side of this expression represents the bending moment for a strip under the action of a triangular load and is equal to $(q_0/6)(ax - x^3/a)$. Using expressions (11)and (12) for the constants A_m and B_m in the second sum, it obtains:

$$(M_x)_{y=0} = \frac{q_0(ax - x^3)}{6a} - \frac{q_0 a^2}{\pi^3}\sum_{m=1}^{\infty}\frac{2(-1)^{m+1}}{m^3 cosh\alpha_m}[2 + (1-\nu)\alpha_m tanh a_m]\, sin\left(\frac{m\pi x}{a}\right) \tag{22}$$

The series thus obtained converges rapidly and a sufficiently accurate value of M_x can be realized by taking only the first few terms. In this way the bending moment at any point of the x axis can be represented by the equation

$$(M_x)_{y=0} = \beta q_0 a^2 \tag{23}$$

where β is a numerical factor depending on the abscissa x of the point. In a similar manner the equation (24) is given

$$\left(M_y\right)_{y=0} = \beta_1 q_0 a^2 \qquad (24)$$

The numerical values of the factors β and β_1 are given in table (). It is seen that for $b \gtreqless 4a$ the moments are very close to the values of the moments in a strip under a triangular load.

b/a	$M_x = \beta a^2 q_0, \quad y = 0$				$M_y = \beta_1 a^2 q_0, \quad y = 0$			
	$x = 0.25a$	$x = 0.50a$	$x = 0.60a$	$x = 0.75a$	$x = 0.25a$	$x = 0.50a$	$x = 0.60a$	$x = 0.75a$
1.0	0.0132	0.0239	0.0264	0.0259	0.0149	0.0239	0.0245	0.0207
1.1	0.0156	0.0276	0.0302	0.0289	0.0155	0.0247	0.0251	0.0211
1.2	0.0179	0.0313	0.0338	0.0318	0.0158	0.0250	0.0254	0.0213
1.3	0.0200	0.0346	0.0371	0.0344	0.0160	0.0252	0.0255	0.0213
1.4	0.0221	0.0376	0.0402	0.0367	0.0160	0.0253	0.0254	0.0212
1.5	0.0239	0.0406	0.0429	0.0388	0.0159	0.0249	0.0252	0.0210
1.6	0.0256	0.0431	0.0454	0.0407	0.0158	0.0246	0.0249	0.0207
1.7	0.0272	0.0454	0.0476	0.0424	0.0155	0.0243	0.0246	0.0205
1.8	0.0286	0.0474	0.0496	0.0439	0.0153	0.0239	0.0242	0.0202
1.9	0.0298	0.0492	0.0513	0.0452	0.0150	0.0235	0.0238	0.0199
2.0	0.0309	0.0508	0.0529	0.0463	0.0148	0.0232	0.0234	0.0197
3.0	0.0369	0.0594	0.0611	0.0525	0.0128	0.0202	0.0207	0.0176
4.0	0.0385	0.0617	0.0632	0.0541	0.0120	0.0192	0.0196	0.0168
5.0	0.0389	0.0623	0.0638	0.0546	0.0118	0.0187	0.0193	0.0166
∞	0.0391	0.0625	0.0640	0.0547	0.0117	0.0187	0.0192	0.0165

Table 3: numerical factors δ and δ_1 for bending moments of simply supported rectangular plates under hydrostatic pressure $q = q_0 x/a, \quad b > a, \ \nu = 0.3$.

The general expressions for shearing forces Q_x and Q_y are

$$Q_x = \frac{q_{0(a^2-3x^2)}}{6a} - \frac{2q_0 a}{\pi^2}\sum_{m=1}^{\infty}\frac{(-1)^{m+1}cosh\frac{m\pi y}{a}}{m^2 cosh\alpha_m}cos\frac{m\pi x}{a} \tag{25}$$

$$Q_y = -\frac{2q_0 a}{\pi^2}\sum_{m=1}^{\infty}\frac{(-1)^{m+1}sinh\frac{m\pi y}{a}}{m^2 cosh\alpha_m}sin\frac{m\pi x}{a} \tag{26}$$

The magnitude of the vertical reactions V_x and V_y along the boundary is obtained by combining the shearing forces with the derivatives of the twisting moments. Along the sides $x = 0$ And $x = a$ these reactions can be represented in the form

$$V_x = \left(Q_x - \frac{\partial M_{xy}}{\partial y}\right)_{x=0,\ y=0} = \mp\delta q_0 a \tag{27}$$

and along the sides $y = \mp b/2$ in the form

$$V_y = \left(Q_y - \frac{\partial M_{xy}}{\partial x}\right)_{y=\mp b/2} = \mp\delta_1 q_0 b \tag{28}$$

in which δ and δ_1 are numerical factors depending on the ratio b/a and on the coordinates of the points taken on the boundary. Several values of these factors are given in table (3).
The magnitude of concentrated forces that must be applied to prevent the corners of the plate rising up during bending can be founded from the values of the twisting moments M_{xy} at the corners. Since the load is not symmetrical, the reactions R_1 at $x = 0$ and $y = \mp b/2$. These reactions can be represented in the following form:

$$R_1 = n_1 q_0 ab \qquad R_2 = n_2 q_0 ab \tag{29}$$

The values of the numerical factors n_1 and n_2 are given in table (5).

b/a	Reactions $\delta q_0 a$				Reactions $\delta_1 q_0 b$			
	$x = 0$		$x = a$		$y = \pm b/2$			
	$y = 0$	$y = 0.25b$	$y = 0$	$y = 0.25b$	$x = 0.25a$	$x = 0.50a$	$x = 0.60a$	$x = 0.75a$
1.0	0.126	0.098	0.294	0.256	0.115	0.210	0.234	0.239
1.1	0.136	0.107	0.304	0.267	0.110	0.199	0.221	0.224
1.2	0.144	0.114	0.312	0.276	0.105	0.189	0.208	0.209
1.3	0.150	0.121	0.318	0.284	0.100	0.178	0.196	0.196
1.4	0.155	0.126	0.323	0.292	0.095	0.169	0.185	0.184
1.5	0.159	0.132	0.327	0.297	0.090	0.160	0.175	0.174
1.6	0.162	0.136	0.330	0.302	0.086	0.151	0.166	0.164
1.7	0.164	0.140	0.332	0.306	0.082	0.144	0.157	0.155
1.8	0.166	0.143	0.333	0.310	0.078	0.136	0.149	0.147
1.9	0.167	0.146	0.334	0.313	0.074	0.130	0.142	0.140
2.0	0.168	0.149	0.335	0.316	0.071	0.124	0.135	0.134
3.0	0.169	0.163	0.336	0.331	0.048	0.083	0.091	0.089
4.0	0.168	0.167	0.334	0.334	0.036	0.063	0.068	0.067
5.0	0.167	0.167	0.334	0.335	0.029	0.050	0.055	0.054
∞	0.167	0.167	0.333	0.333				

Table 4: numerical factors β and β_1 for reactions of simply supported rectangular plates under hydrostatic pressure $q = q_0 x/a$, $b > a$, $\nu = 0.3$.

b/a	1.0	1.1	1.2	1.3	1.4	1.5	1.6	1.7	1.8	1.9	2.0	3.0	4.0	5.0
n_1	0.026	0.026	0.026	0.026	0.025	0.024	0.023	0.022	0.021	0.021	0.020	0.014	0.010	0.008
n_2	0.039	0.038	0.037	0.036	0.035	0.033	0.032	0.030	0.029	0.028	0.026	0.018	0.014	0.011

Table 5: numerical factors n and n_1 for reactive factors R_1 and R_2 of simply supported rectangular plates under hydrostatic pressure $q = q_0 x/a$, $b > a$, $\nu = 0.3$.

Since a uniform load q_0 is obtained by superposing the two triangular loads $q = q_0 x/a$ and $q_0(a-x)/a$, it can be concluded that for corresponding values of b/a the sum $n_1 + n_2$ of the factors given in table(5) multiplied by b/a must equal the corresponding value of n, the last column in table (6).

b/a	$w_{max} = \alpha \frac{qa^4}{D}$	$(M_x)_{max} = \beta q a^2$	$(M_y)_{max} = \beta_1 q a^2$	$(Q_x)_{max} = \gamma q a$	$(Q_y)_{max} = \gamma_1 q a$	$(V_x)_{max} = \delta q a$	$(V_y)_{max} = \delta_1 q a$	$R = n q a^2$
	α	β	β_1	γ	γ_1	δ	δ_1	n
1.0	0.00406	0.0479	0.0479	0.338	0.338	0.420	0.420	0.065
1.1	0.00485	0.0554	0.0493	0.360	0.347	0.440	0.440	0.070
1.2	0.00564	0.0627	0.0501	0.380	0.353	0.455	0.453	0.074
1.3	0.00638	0.0694	0.0503	0.397	0.357	0.468	0.464	0.079
1.4	0.00705	0.0755	0.0502	0.411	0.361	0.478	0.471	0.083
1.5	0.00772	0.0812	0.0498	0.424	0.363	0.486	0.480	0.085
1.6	0.00830	0.0862	0.0492	0.435	0.365	0.491	0.485	0.086
1.7	0.00883	0.0908	0.0486	0.444	0.367	0.496	0.488	0.088
1.8	0.00931	0.0948	0.0479	0.452	0.368	0.499	0.491	0.090
1.9	0.00974	0.0985	0.0471	0.459	0.369	0.502	0.494	0.091
2.0	0.01013	0.1017	0.0464	0.465	0.370	0.503	0.496	0.092
3.0	0.01223	0.1189	0.0406	0.493	0.372	0.505	0.498	0.093
4.0	0.01282	0.1235	0.0384	0.498	0.372	0.502	0.500	0.094
5.0	0.01297	0.1246	0.0375	0.500	0.372	0.501	0.500	0.095
∞	0.01302	0.1250	0.0375	0.500	0.372	0.500	0.500	0.095

Table 6: numerical factor α for deflections of a simple supported rectangular plate under hydrostatic pressure

$q = q_0 x/a, \quad b < a \quad (w)_{y=0} = \alpha \frac{q_0 a^4}{D}$.

If the relative dimensions of the plate are such that a figure (36) is greater than b, then more rapidly converging series will be obtained by representing w_1 and w_2 by the following expressions:

$$w_1 = \frac{q_0 x}{a}\frac{1}{384D}(16y^4 - 24b^2y^2 + 5b^4) \tag{30}$$

$$w_2 = \sum_{m=1}^{\infty} X_{2m-1} cos\frac{(2m-1)\pi y}{b} \tag{31}$$

The first expression is the deflection of a narrow strip parallel to the y axis, supported at $y = \mp b/2$ and carrying a uniformly distributed load of intensity $q_0 x/a$. This expression satisfies the differential equation (3) and also the boundary conditions $w = 0$ and $\partial^2 w/y^2 = 0$ at $y = \mp b/2$.
Equation (31) represents an infinite series each term of which also satisfies the conditions at the edges $y = \mp b/2$. The functions X_{2m-1} of x are chosen in such a manner that each of them satisfies the following homogeneous equation:

$$\frac{\partial^4 w_2}{\partial x^4} + 2\frac{\partial^4 w_2}{\partial x^2 \partial y^2} + \frac{\partial^4 w_2}{\partial y^4} = 0 \tag{32}$$

so that expression (1) satisfies the boundary conditions at the edges $x = 0$ and $x = a$.

3. Modal Analysis: theory and practice

Vibration is the study of the repetitive motion of objects relative to a stationary frame of reference or nominal position (usually equilibrium). Vibration is evident everywhere and in many cases greatly effects the nature of engineering designs. The vibrational properties of engineering devices are often limiting factors in their performance. Vibration can be harmful and should be avoided, or it can be extremely useful and desired.
Information about techniques used to measure the vibrations of a system are developed; in addition, information and methods are given that are useful for designing a particular system to have specific vibrational response. The physical explanation of the phenomena of vibration concerns the interplay between potential energy and kinetic energy. A vibrating system must have a component that stores potential energy and releases it as kinetic energy in the form of motion (vibration) of a mass. The motion of the mass then gives up kinetic energy to the potential energy storing device. Vibration can occur in many directions and can be the result of the interaction of many objects It has long been recognized that many basic problems of mechanics, including those of vibrations, are nonlinear. Although the linear treatments commonly adopted are quite satisfactory for most purposes, they are not adequate in all cases. In nonlinear systems, there often occur phenomena that are theoretically impossible in linear system. The mathematical theory of nonlinear vibrations is much more complex: for instance, *modal analysis* does not apply to nonlinear systems because it depends on the *superposition of solutions* (the equations of motion are such that a linear combination of inputs to the system leads to the same linear combination of outputs, namely *responses*), which is not generally possible for nonlinear problems. It is very difficult, if not impossible, to find closed-form solutions to most nonlinear vibration problems. In recent times, many investigations have been motivated by engineering applications, such as the design of machines, foundations, structures, engines, turbines and control systems: in this case, vibration studies, even those dealing with complex engineering systems, were done by using gross models, with only a few degrees of freedom.

However, the advent of high speed digital computers made it possible to treat moderately complex systems and to generate approximate solutions in semi-closed form, relying on classical solution methods but using numerical evaluation of certain terms that can not be expressed in closed form. Another powerful numerical technique is represented by the *Finite Element Method* which is extremely useful for modeling and solving a lot of problems involving vibration analysis: for example, in finite element analysis, the vibration of the structure or the mechanical system is approximated by the motion of the points of connection between the lines of a grid, called *mesh*, that reproduces the entire body of the structure. The Finite Element Method is often used in conjunction with the modal analysis test methods and the analysis methods for multiple-degree-of-freedom systems.

3.1 Introduction to Modal Analysis

While modal analysis theory has not changed over the last century, the application of the theory to experimentally measured data has changed significantly. The advances of recent years, with respect to measurement and analysis capabilities, have caused a re-evaluation of what aspects of the theory relate to the practical world of testing. With this in mind, the aspect of transform relationships has taken on renewed importance since digital forms of the integral transforms are in constant use. The theory from the vibrations point of view involves a more thorough understanding of how the structural parameters of mass, damping, and stiffness relate to the impulse response function (time domain), the frequency response function (*Fourier*, or frequency domain), and the transfer function (*Laplace domain*) for single and multiple degree of freedom systems. One of the keys to understanding experimental modal analysis involves the comprehension of the relationships between the different domains used to describe the dynamics of a structural system. Historically, this has involved the time, frequency (*Fourier*), and *Laplace* domains. These relationships, with respect to a structural system, are the integral transforms (Fourier and Laplace) that reflect the information contained by the governing differential equations transformed to each domain. It is important to note that these are integral relationships and that the governing differential equations represent continuous relationships in each domain. As the digital approach to the measurement of data is considered, similar relationships between time, frequency, and *Z* domains can be formed that reflect the information contained by the governing finite difference equations in each domain. The relationships in this discrete case are represented by discrete transforms (*Discrete Fourier Transform*, *Z Transform*). Whether the concept is approached from the continuous or discrete case, the idea of the transform relationship is of primary importance. The concept of a transform is obviously very special. In general, there are four criteria for a mathematical process to be designated as a transform. First, the transform process must involve a change of independent variable which represents the change from one domain to another. Second, the transformed variable must be the variable of interest. Third, the transform process must be computationally very simple but unique. Finally, there must be no loss of information in the transform process. This last criteria is often the true distinction between a transform and some form of parameter estimation.

Since, with respect to modal analysis, the concepts of transforms and parameter estimation are both important, this distinction is a very important one. Before speaking about transform properties and the area of modal testing itself, it is worth to know something about different approaches to vibration measurements. From both methodical and practical points of view, it is useful to distinguish the two experimental approaches dealing with vibrations:

1. Assessment of the nature and level of vibration responses: *signal analysis;*

2. Deriving theoretical models and presumptions and their *evaluation system analysis;*

Two types of measurements correspond to these two approaches:

- Vibration responses of the machine or the structure under investigation are measured during operation conditions. Vibration diagnostics deals with this area;

- Structure or a machine part is put into vibration by means of known excitation forces, often out of its working environment. This process is substantial for modal tests. It is obvious that we are able to get more accurate and detailed information about the measured system under controlled conditions rather than by simple response measurements.

This material deals with the latter approach thoroughly. By performing a modal test, we are able to determine modal parameters of the system, thus having a base for solving many problems caused by structural vibrations. Problems with structural vibrations pose significant risks and limitations for design of a wide range of machinery products. They could be a cause of a structural integrity failure (for instance breaking of a turbine blade) or they could reduce machinery performance. At least, excessive vibrations always cause excessive noise and discomfort during operation.

There are several reasons for performing modal tests. Here they are sorted by accuracy requirements and by the degree of relationship to theoretical analysis:

- Identification of modal parameters (natural frequencies, modal shapes and modal damping respectively) without relationship to theoretical model. Doing this, we can discover e.g. whether excessive vibrations during operation are caused by resonance and what the excited modal shape looks like;

- Identification of modal parameters to compare the experimentally obtained data with corresponding data obtained by FEM or other theoretical methods. The goal is to verify the theoretical model before other calculations such as responses to different loads are carried out. For this, it is necessary: precise determination of natural frequencies, identification of modal shapes with such precision that their comparison with computed modal shapes is possible, matching the corresponding modal shapes together;

- Correlation of experimental and theoretical results - two sets of data are numerically compared in order to precisely identify the causes of discrepancy between the calculated and measured properties;

- Using modal testing to obtain a mathematical model of a component that can be included in a complex one. This approach is often used for theoretical analysis of complex structures. It requires accurate values of natural frequencies, modal damping and modal shapes. All modes must be included, it is not possible to fit the model to a few individual natural frequencies. Excluded modes affect dynamic behaviour of the entire structure in the observed frequency range. This application is more demanding than all previous ones;

- Creating a model that can be used to predict the impact of structural modifications to the original test structure. It is a smaller change than in the case of the substructures, so here are a little lower accuracy requirements than in the previous case. Yet, in both of these cases complications usually occur with non-measured rotational degrees of freedom;

- Using the model obtained through modal testing to determine the excitation forces. It is possible to compare responses caused by excitation forces with the mathematical description of transfer functions of the structure and, on the base of this comparison, to estimate the excitation forces.

Successful modal testing requires a combination of the three skills and knowledge:

✓ theoretical framework;

✓ accurate measurement of vibration;

✓ realistic and detailed data processing.

In this introduction, only the basis of these three requirements are presented. They will further be explained in details.

Transform Properties

The properties of transforms must be well understood in order to process data into measurements efficiently and without error. Digital data is always truncated to a limited time period and is often multiplied by a time varying function in order to enhance certain characteristics in the data. This sort of alteration of the data in the time domain has distinctly unique but often incomprehensible effects in another domain if the properties of the transform are not considered. While the complete list of transform properties for each transform can be found in numerous applied mathematics handbooks, several properties should be noted due to their frequent application in digital signal processing. First, scalar multiplication is commutative within and between domains. Therefore, calibration of signals using constant calibration factors can be performed without detrimental effect in any domain. Second, the multiplication of two functions in one domain is equivalent to the convolution of the transformed functions in the resulting domain. This property is essential for explaining the effects of weighting functions applied in the time domain

as a possible way of minimizing the effects of the bias error that will occur due to the truncation of the data in the time domain (*leakage error*). Third, differentiation in the time domain with respect to the independent time variable is equivalent to multiplication in the transformed domain by the transformed variable. This property gives a very simple algebraic way to convert data from acceleration to velocity or displacement in the frequency or Laplace domains via multiplication.
Finally, the shift theorem, which involves multiplying the time domain data by a complex function of a shift frequency $[\,cos(\omega t) + jsin(\omega t)\,]$ is the basis for most frequency-shifted *Fourier transform* algorithms used in digital signal analysers today. The schematic of this frequency-shifted Fourier transform process is shown in figure (37) for a shift of f_c Hertz.

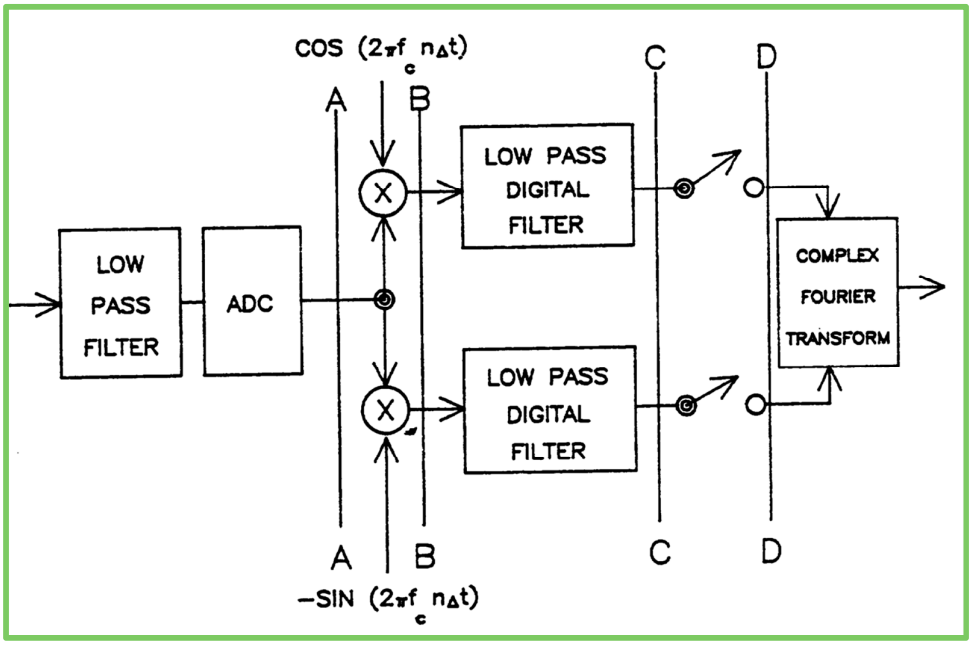


Figure 37: The schematic of frequency-shifted Fourier transform process.

3.2 Theoretical Basis of Modal Analysis

Free Vibration

In order to understand modal analysis, the comprehension of single degree of freedom systems is necessary. In particular, the complete familiarity with single degree of freedom systems as presented and evaluated in the time, frequency (Fourier), and Laplace domains serves as the basis for many of the models that are used in modal parameter estimation. This single degree of freedom approach is obviously trivial for the modal analysis case. The true importance of this approach results from the fact that the multiple degree of freedom case can be viewed as simply a linear superposition of single degree of freedom systems.

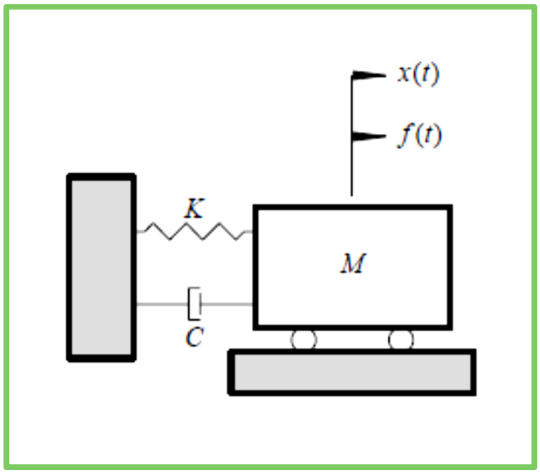


Figure 38: Spatial model of SDOF system.

The general mathematical representation of a single degree of freedom system is expressed in equation (1):

$$M\ddot{x}(t) + C\dot{x}(t) + kx(t) = f(t) \qquad (1)$$

where:

- M: Mass constant;
- C: Damping constant;
- K: Stiffness constant

By setting $f(t) = 0$, the homogeneous form of equation (1) can be solved.

$$M\ddot{x}(t) + C\dot{x}(t) + kx(t) = 0 \qquad (2)$$

From differential equation theory, the solution can be assumed to be of the form $x(t) = Xe^{st}$, where s is a complex constant to be determined. Taking appropriate derivatives and substituting into equation (2) yields:

$$(Ms^2 + Cs + K)e^{st} = 0 \qquad (3)$$

Thus, for a non-trivial solution:

$$(M\boldsymbol{s^2} + C\boldsymbol{s} + K) = 0 \qquad (4)$$

Where $\boldsymbol{s}$ is *Complex-Valued* frequency variable (*Laplace variable*).

Equation (4) is the characteristic equation of the system, whose roots λ_1 and λ_2 are:

$$\lambda_{1,2} = -\frac{C}{2M} \mp \left\{\left(\frac{C}{2M}\right)^2 - \left(\frac{k}{M}\right)\right\}^2 \tag{5}$$

Thus the general solution of Equation (2) is:

$$x(t) = Ae^{\lambda_1 t} + Be^{\lambda_2 t} \tag{6}$$

A and B are constants determined from the initial conditions imposed on the system at time $t = 0$.

For most real structures, unless active damping systems are present, the damping ratio is rarely greater than ten percent. For this reason, all further discussion is restricted to underdamped systems ($\zeta<1$). With reference to eq. (6), this means that the two roots, $\lambda_{1,2}$, are always complex conjugates. Also, the two coefficients (A and B) are complex conjugates of one another (A and A^*). For an underdamped system, the roots of the characteristic equation can be written as:

$$\lambda_1 = \sigma_1 + j\omega_1 \qquad \lambda_1^* = \sigma_1 - j\omega_1 \tag{7}$$

where

- σ_1: Damping factor;
- ω_1: Damped natural frequency.

The roots of characteristic Equation (4) can also be written as:

$$\lambda_1, \lambda_1^* = -\zeta_1 \Omega_1 \mp j\Omega_1 \sqrt{1-\zeta^2} \tag{8}$$

where

$\Omega_1 = \sqrt{\frac{k}{M}}$ undamped natural frequency.

The ***damping factor***, $\boldsymbol{\sigma_1}$, is defined as the real part of a root of the characteristic equation. The damping factor describes the exponential decay or growth of the oscillation. This parameter has the same units as the imaginary part of the root of the characteristic equation, typically radians per second.
With respect to the above result, critical damping and damping ratio can now be defined. ***Critical damping***, $\boldsymbol{C_c}$, is defined as being the damping which reduces the radical in the solution of the characteristic equation to zero. This form of representing the damping is a physical approach and therefore involves the appropriate units for equivalent viscous damping.

$$C_c = 2M\sqrt{\frac{k}{M}} = 2M\sigma_1 \tag{9}$$

The fraction of critical damping, or ***damping ratio***, $\boldsymbol{\zeta}$, is the ratio of the actual system damping to the critical system damping. This approach to the description of damping is dimensionless since the units have been normalized.

$$\zeta_1 = \frac{c}{c_c} = -\sigma_1 \Omega_1 \qquad (10)$$

Roots of characteristic equation depend on the value of damping ratio, ζ. For so called positive damping ($\zeta \geq 0$), there may be three cases, and therefore three different types of motion (see figure 38):

- $\zeta = 0$ undamped vibrations, λ_1 and λ_2 are imaginary;
- $\zeta < 1$ damped vibrations, λ_1 and λ_2 are complex conjugates;
- $\zeta \geq 1$ aperiodic movement, λ_1 and λ_2 are real.

If the real part of the pole is positive, which means that $\zeta < 0$ (negative damping), self-excited vibrations occur.

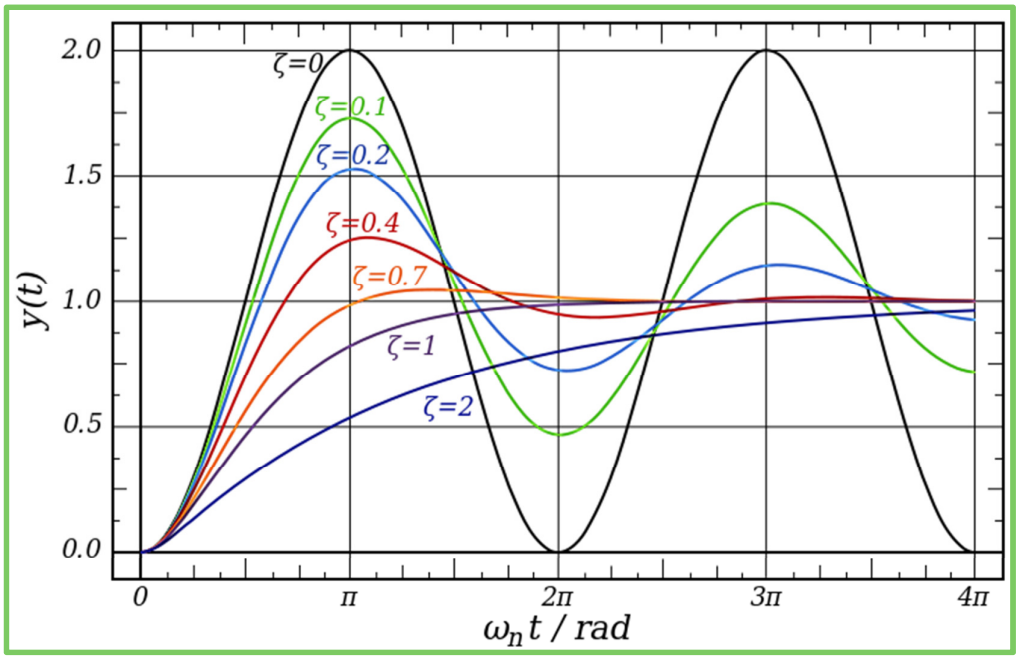


Figure 28: values of damping ratio, ζ, for three different types of motion.

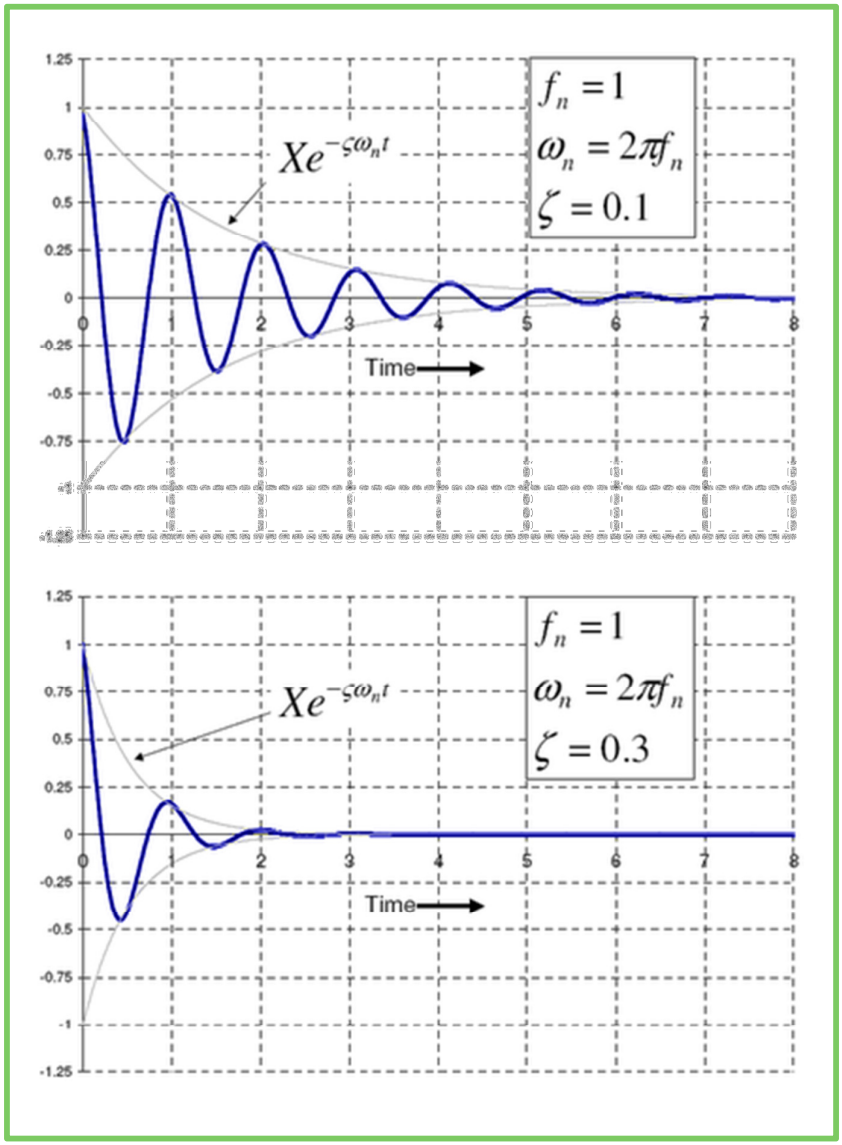


Figure 39: motion of the mass for distinctive damping ratio.

Forced Vibration

If movement is caused by acting of *harmonic force*, the equation of motion of viscously damped system has the form:

$$M\ddot{x}(t) + B\dot{x}(t) + kx(t) = f(t) \qquad (1)$$

where:

$f(t) = Fe^{i\omega t}$ harmonic excitation force;

$x(t) = Xe^{i\omega t}$ expected solution and its derivatives:

$\dot{x}(t) = i\omega Xe^{i\omega t}$

$\ddot{x}(t) = -\omega^2 Xe^{i\omega t}$

Dividing the equation (1) by mass M and putting the expected solution together with equations (5) a (8) in it gives:

$$\Omega^2 X + 2i\omega\zeta\Omega_1 X + \Omega^2 X = \Omega_1^2 \frac{F}{k} \qquad (2)$$

$$X = \frac{\Omega_1^2 . \frac{F}{k}}{\Omega_1^2 - \omega^2 + 2i\zeta\omega\Omega_1} \qquad (3)$$

where $F/k = X_{st}$ static displacement.

$F/k = X_{st}$ static displacement.

$$X = \frac{F/k}{1-\left(\frac{\omega}{\Omega_1}\right)^2+2i\zeta\frac{\omega}{\Omega_1}} \tag{4}$$

$\frac{\omega}{\Omega_1} = \eta$ is called *Tuning Factor*.

$$X = \frac{1}{1-\eta^2+i2\eta\zeta} \cdot X_{st} \tag{5}$$

$$|X| = (X_{st}) \cdot \frac{1}{\sqrt{(1-\eta^2)^2+(2\zeta\eta)^2}} \quad \text{amplitude displacement} \tag{6}$$

Now, steady state solution of equation of motion will be derived:

$$X = \frac{1}{1-\eta^2+i2\eta\zeta} \cdot \frac{F}{k} \quad \text{amplitude of displacement (complex)} \tag{7}$$

$$x(t) = Xe^{i\omega t} = \frac{1}{1-\eta^2+i2\eta\zeta} \cdot \frac{F}{k} e^{i\omega t} \quad \text{displacement time history} \tag{8}$$

Displacement is proportional to the acting force, proportionality constant is:

$$H(\eta) = \frac{1}{1-\eta^2+i2\eta\zeta} \tag{9}$$

what is so-called ***frequency response function receptance*** (dimensionless).

As the displacement is a complex number, it can be divided to the real part and imaginary part (by multiplying both numerator and denominator by denominator's complex conjugate):

$$x(t) = \left(\frac{1}{\left(1-\eta^2\right)^2+(2\zeta\eta)^2} - \frac{2\zeta\eta}{\left(1-\eta^2\right)^2+(2\zeta\eta)^2} \right) \cdot \frac{F}{k} e^{i\omega t} \tag{10}$$

It can be seen, that the displacement has one part

$$Re(x) = \left(\frac{1-\eta^2}{\left(1-\eta^2\right)^2+(2\zeta\eta)^2} \right) \cdot \frac{F}{k} e^{i\omega t} \tag{11}$$

that is in-phase with the excitation force and the second part

$$Im(x) = \left(\frac{-2\zeta\eta}{\left(1-\eta^2\right)^2+(2\zeta\eta)^2} \right) \cdot \frac{F}{k} e^{i\omega t} \tag{12}$$

that lags the excitation force at 90°. In figure (), vectors OA and OB represent real and imaginary part of displacement. Vector OC represents the amplitude of displacement given by: $\sqrt{Re^2(x) + Im^2(x)}$, thus:

$$|x(t)| = \frac{1}{\sqrt{(1-\eta^2)^2+(2\zeta\eta)^2}} \cdot \frac{F}{k} e^{i\omega t} \tag{13}$$

Displacement lags the excitation force at an angle ϑ, defined as:

$$\vartheta = arctg \frac{-2\zeta\eta}{1-\eta^2} \tag{14}$$

Steady-state solution of the equation of motion can thus be expressed in the form:

$$x(t) = \left[\frac{1}{\sqrt{(1-\eta^2)^2+(2\zeta\eta)^2}}\right] \cdot \frac{F}{k} e^{i(\omega t-\vartheta)} \tag{15}$$

The expression in square brackets is the absolute value of complex frequency response. It is often called as an ***amplification factor*** and it expresses a dimensionless ratio between the amplitude of displacement $\boldsymbol{X}$ and static displacement $\boldsymbol{F/k}$.

$$|H(\eta)| = \frac{1}{\sqrt{(1-\eta^2)^2+(i2\eta\zeta)^2}} \tag{16}$$

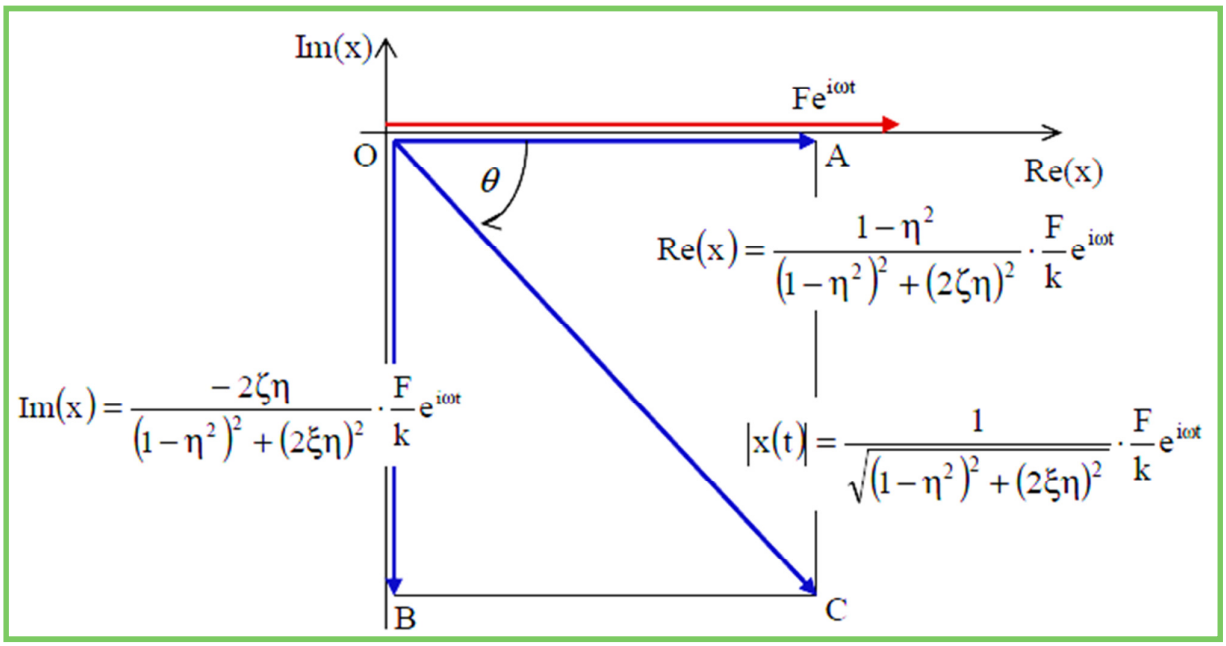


Figure 40: Relationship Between the Complex Displacement and the Excitation Force.

Frequency response function (9) is complex and it is a function of frequency (or of tuning factor, respectively) at the same time. It means that it can not be displayed in a single two-dimensional plot. Its 3D plot is in figure (). The red curve represents a damped system, the green curve represents an undamped system (in that case, the plot lies in the plane $\boldsymbol{\eta - Re(H(\eta))}$ and is two-dimensional).

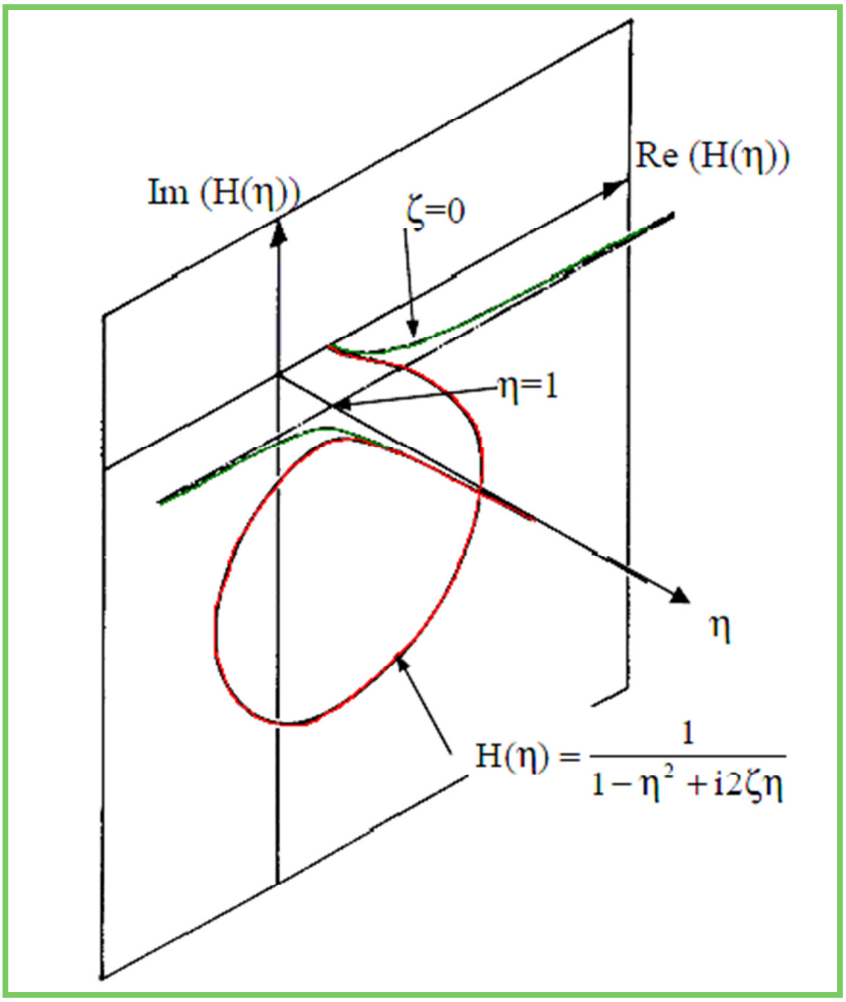


Figure 41: 3D plot of the Frequency Response Function - Undamped and Damped.

Projection of this 3D plot to the individual planes is in figure (). and in figure () left. In figure.() two of the possible ways of displaying FRF are shown simultaneous displaying of real and imaginary part of FRF as functions of frequency or of tuning factor, top left, or so called ***Nyquist Diagram*** which is plot in the plane $[\boldsymbol{Re}(\boldsymbol{H}(\boldsymbol{\eta}));\boldsymbol{Im}(\boldsymbol{H}(\boldsymbol{\eta}))]$, bottom left.
In Nyquist plot, information about the frequency is hidden: the plot is drawn from the initial frequency to the final frequency clockwise; the major part of the circle represents resonance and its vicinity. Different colours of plots are for various levels of damping, from green for an undamped system to magenta for a critically damped system ($\zeta = 1$).

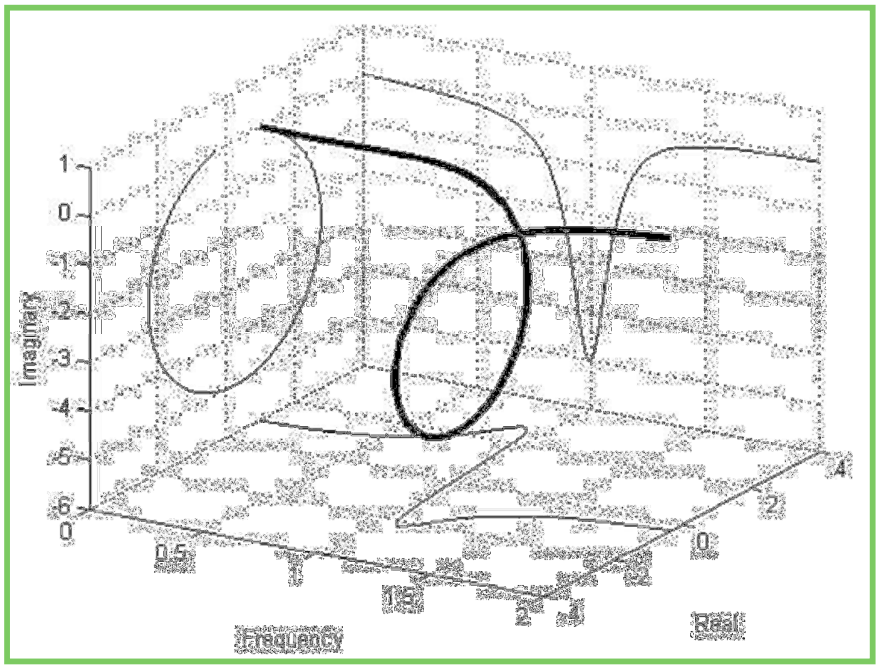


*Figure 42: 3D Plot of the Frequency Response Function (**Receptance**).*

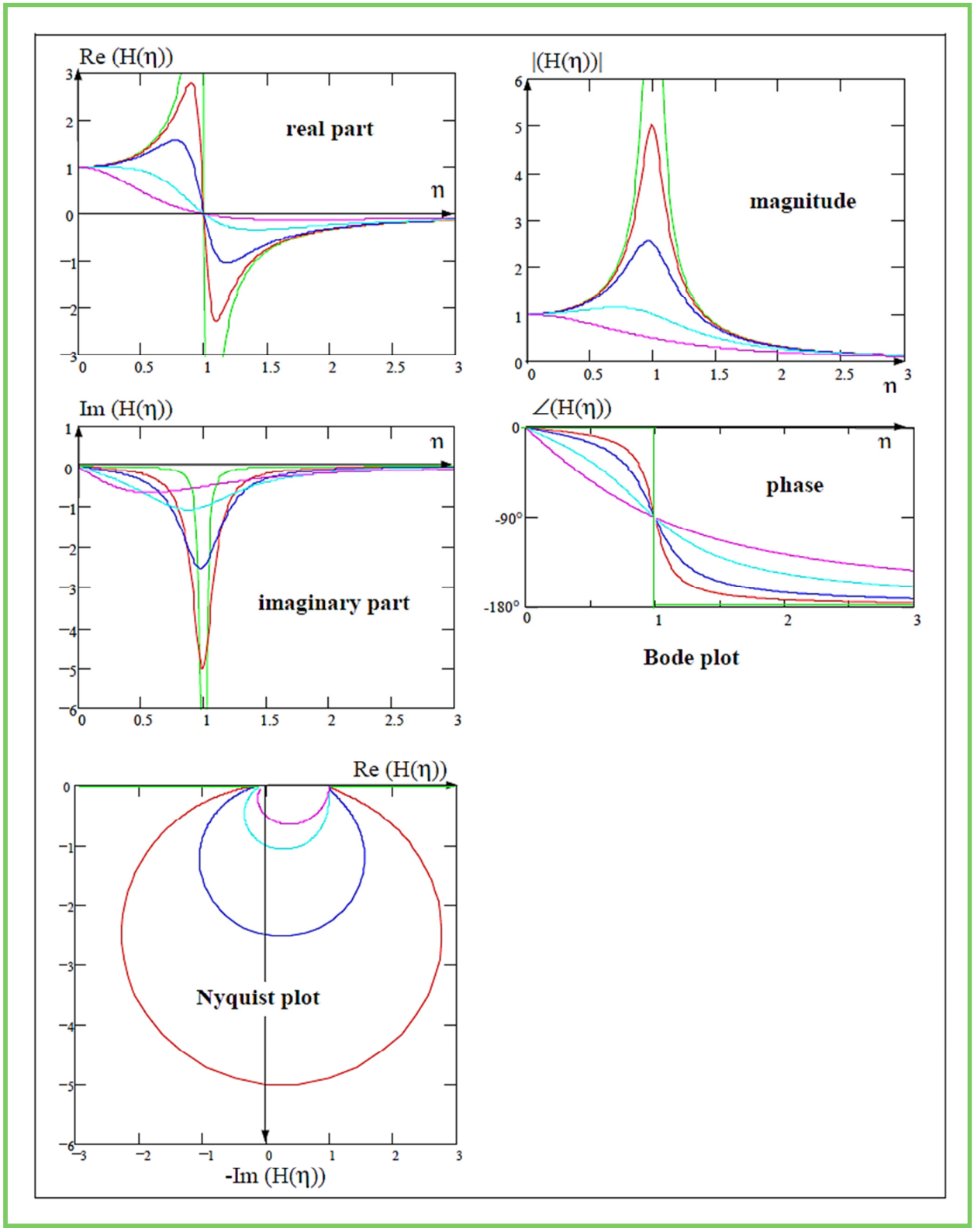


Figure 43: Various Forms of Displaying FRF - Viscously Damped System.

Single Degree-of-freedom System with Hysteretic (Structural) Damping

Close inspection of the behaviour of real structures suggests that the viscous damping model used above is not very representative when applied to **MDOF** systems. Real structures exhibit a frequency dependence that is not described by the standard viscous dashpot. A large variety of materials, when subjected to cyclic stress (for strains below the elastic limit), exhibits a stress-strain relationship which is characterised by a hysteresis loop. The energy dissipated per cycle due to internal friction in the material is proportional to the area within the hysteresis loop, and hence the name *hysteretic damping* Internal friction is independent of the rate of strain (independent of frequency) and over a significant frequency range is proportional to the displacement. Thus the damping force is proportional to the elastic force, since energy is dissipated, it must be in phase with the velocity. Thus for simple harmonic motion, the damping force is given by:

$$i\gamma kx = \frac{k\gamma}{\omega} \cdot \dot{x} \qquad (1)$$

where $\boldsymbol{\gamma}$ is called ***structural damping loss factor***:

Hysteretic model provides a much simpler analysis for **MDOF** systems but it presents difficulties to a rigorous free vibration analysis. Therefore only forced vibration analysis will be performed. Equation of motion for a **SDOF** system with structural damping can be written:

$$M\ddot{x}(t) + \frac{k\gamma}{\omega} \cdot \dot{x}(t) + kx(t) = f(t) \qquad (2)$$

Where

$f(t) = Fe^{i\omega t}$ harmonic excitation force;

$x(t) = Xe^{i\omega t}$ expected solution and its derivatives:

$\dot{x}(t) = i\omega Xe^{i\omega t}$

$\ddot{x}(t) = -\omega^2 Xe^{i\omega t}$

Equation of motion can be also rewrite as:

$$M\ddot{x}(t) + k(1 + i\gamma)x(t) = f(t) \quad (3)$$

Where $k(1 + i\gamma)$ is called the ***complex stiffness***. By setting the expected solution into the equation of motion is obtained:

$$(-M\omega^2 + k(1 + i\gamma)) \cdot X = F \quad (4)$$

After dividing equation (4) by stiffness k:

$$\left(1 - \frac{\omega^2}{\Omega_1^2} + i\gamma\right) \cdot X = \frac{F}{k} \quad (5)$$

Then, *amplitude of complex displacement* is:

$$X = \frac{1}{1-\eta^2+i\gamma} \cdot \frac{F}{k} \tag{6}$$

$$X = \frac{1}{1-\eta^2+i\gamma} \cdot X_{st} \tag{7}$$

$$|X| = \frac{1}{\sqrt{(1-\eta^2)^2+\gamma^2}} \cdot X_{st} \tag{8}$$

Expression (8) represents the *amplitude of displacement*.

Following procedure is analogous to the procedure from for a system with viscous damping.

$$x(t) = Xe^{i\omega t} = \frac{1}{1-\eta^2+\gamma^2} \cdot \frac{F}{k} e^{i\omega t} \tag{9}$$

$$x(t) = \left(\frac{1-\eta^2}{(1-\eta^2)^2+\gamma^2} - \frac{\gamma}{(1-\eta^2)^2+\gamma^2} \right) \cdot \frac{F}{k} e^{i\omega t} \tag{10}$$

$$|x(t)| = \frac{1}{\sqrt{(1-\eta^2)^2+\gamma^2}} \cdot \frac{F}{k} e^{i\omega t} \tag{11}$$

$$\vartheta = arctg\left(\frac{-\gamma}{1-\eta^2}\right) \tag{12}$$

$\boldsymbol{\vartheta}$ is the phase lag between displacement and excitation force.

$$x(t) = \frac{1}{\sqrt{(1-\eta^2)^2+\gamma^2}} \cdot \frac{F}{k} e^{i(\omega t-\vartheta)} \tag{13}$$

The expression in the square brackets is again the absolute value of frequency response, or magnification factor, and again it has the meaning of a dimensionless ratio between displacement amplitude $\boldsymbol{X}$ and static displacement $\boldsymbol{F/k}$.

$$|H(\eta)| = \frac{1}{\sqrt{(1-\eta^2)^2+\gamma^2}} \tag{14}$$

In figure (44), various types of plots of FRF with the same amount of damping as it was in figure (43). When a system is structurally damped, resonant peak in the plot of FRF amplitude does not shift to the left with increasing amount of damping, but it still remains on tuning value $\boldsymbol{\eta = 1}$; but, as damping increases, the plot does not start with amplitude equal to 1 corresponding to static displacement, but with a value less than 1. Similar differences are evident in all types of plots.

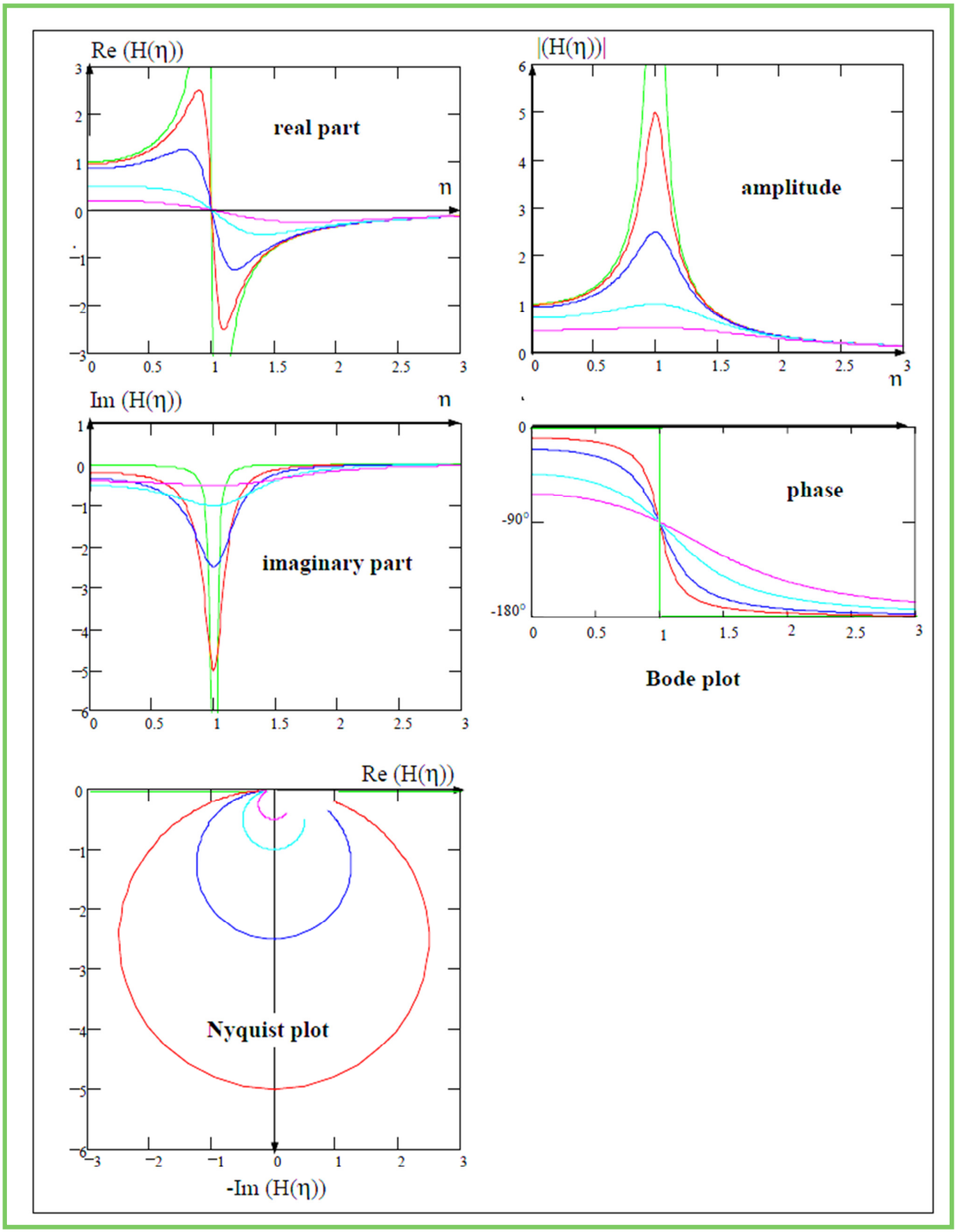


*Figure 44: Various Forms of Displaying FRF - Structurally (**Hysteretically**) Damped System.*

Multi Degree-of-freedom System (MDOF)

The real application of modal analysis concepts begin when a continuous, non-homogeneous structure is described as a lumped mass, multiple degree-of-freedom system. At this point, then modal frequencies, the modal damping, and the modal vectors, or relative patterns of motion, can be found via an estimate of the mass, damping, and stiffness matrices or via the measurement of the associated frequency response functions.
The two degree of freedom system, shown in figure (), is the most basic example of a multiple degree of freedom system. This example is a useful means for discussing modal analysis concepts since a theoretical solution can be formulated in terms of the mass, stiffness, and damping matrices or in terms of the frequency response functions.

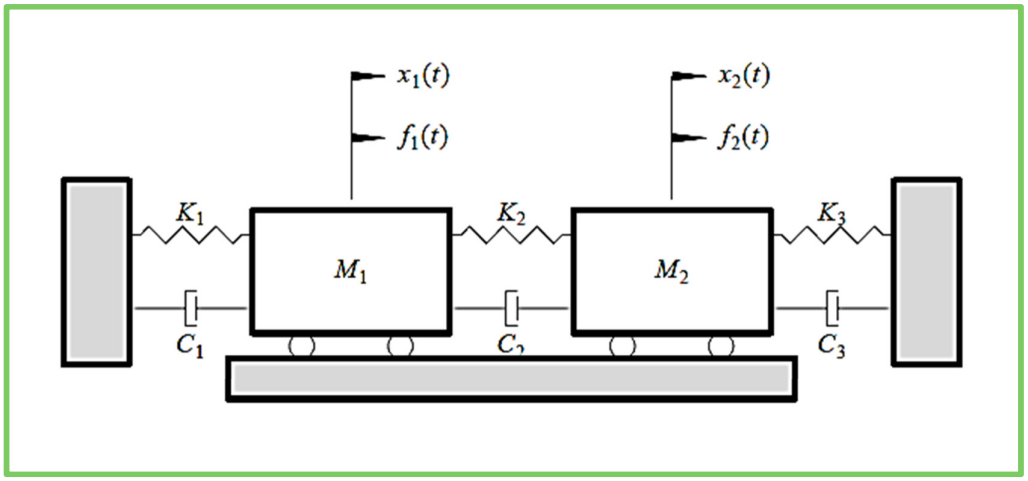


Figure45: Two Degree-of-freedom System.

The development of the frequency response function solution for the multiple degree of freedom case parallels the single degree-of-freedom case. This development relates the mass, damping, and stiffness matrices to a transfer function model involving multiple degrees of freedom. Just as in the analytical case where the ultimate solution can be described in terms of one degree of freedom systems, the frequency response functions between any input and response degree of freedom can be represented as a linear superposition of the single degree of freedom models derived previously. A damped *n*-degree-of-freedom system with a force $\boldsymbol{F}(t)$ applied on each mass, is modeled by equations of the form:

$$M\ddot{\boldsymbol{X}} + C\dot{\boldsymbol{X}} + K\boldsymbol{X} = \boldsymbol{F}(t) \qquad (1)$$

The damping matrix $\boldsymbol{C}$ is a symmetric and in a general *n*-degree-of-freedom, will be an $n \times n$ matrix. Modal analysis can be used directly to solve equation (1) if the damping matrix $\boldsymbol{C}$ can be written as a linear combination of the mass and stiffness mass. The equations of motion for the system in figure (), using matrix notation, are as follows:

$$\begin{bmatrix} M_1 & 0 \\ 0 & M_2 \end{bmatrix}\begin{bmatrix} \ddot{x}_1 \\ \ddot{x}_2 \end{bmatrix} + \begin{bmatrix} (C_1 + C_2) & -C_2 \\ -C_2 & (C_2 + C_3) \end{bmatrix}\begin{bmatrix} \dot{x}_1 \\ \dot{x}_2 \end{bmatrix} + \begin{bmatrix} (k_1 + k_2) & -k_2 \\ -k_2 & (k_2 + k_3) \end{bmatrix}\begin{bmatrix} x_1 \\ x_2 \end{bmatrix} = \begin{bmatrix} f_1 \\ f_2 \end{bmatrix} \qquad (2)$$

All concepts introduced for **SDOF** can be directly extended to the case of multi-degree of freedom systems. For example, there is one equation of motion for each degree of freedom; if generalized coordinates are used, there is one generalized coordinate for each degree of freedom. The equations of motion can be obtained from *Newton's second law* of motion or by using *the influence coefficients*. However, it is often more convenient to derive the equations of motion of a multi-degree of freedom system by using *Lagrange's equations.* There are *n* natural frequencies, each associated with its own mode shape, for a system having *n* degrees of freedom.

The method of determining the natural frequencies from the characteristic equation obtained by equating the determinant to zero also applies to these systems. However, as the number of degrees of freedom increases, the solution of the characteristic equation becomes more complex. The mode shapes exhibit a property known as *orthogonality*, which often enables to simplify the analysis of multi-degree of freedom systems.

Influence of coefficients

The equation of motion of a multi-degree of freedom system can also be written in terms of influence of coefficients, which are extensively used in structural engineering. In more complex system, it is possible express the relation between the displacement at a point and the forces acting at various other points of the system by means of influence of coefficients.
Take into consideration external forces, F_j, act on a multi-degree of freedom system, and the displacement at point i (i.e.,mass m_i) is x_{ij}. The flexibility influence coefficient, denote by a_{ij}, is defined as the deflection at point i due to a unit load at point j. Since the deflection increases proportionately with the load for a linear system, it obtains:

$$x_{ij} = a_{ij}F_j \tag{1}$$

If several forces $F_j (j = 1,2,\cdots,n)$ act at different points of the system, the total deflection at any point i can be found by summing up the contributions of all forces F_j:

$$x_i = \sum_{j=1}^{n} x_{ij} = \sum_{j=1}^{n} a_{ij}F_j\,, \quad i = 1,2,\cdots,n \tag{2}$$

Equation (2) can be expressed in matrix form as

$$\vec{x} = [a]\vec{F} \tag{3}$$

where $\vec{x}$ and $\vec{F}$ are the displacement and force vectors, and $[a]$ is the *flexibility matrix* given by:

$$[a] = \begin{bmatrix} a_{11} & a_{12} & \cdots & a_{1n} \\ a_{21} & a_{22} & \cdots & a_{2n} \\ \vdots & \vdots & \ddots & \vdots \\ a_{n1} & a_{n2} & \cdots & a_{nn} \end{bmatrix} \tag{4}$$

The stiffness influence coefficient, denoted by k_{ij}, is defined as the force at point i due to a unit displacement at point j when all the points other than the point j are fixed. The total force at point i, F_i, can be obtained by summing up the forces due to all displacements x_j ($j = 1,2,\cdots,n$):

$$F_i = \sum_{j=1}^{n} k_{ij}x_j\,, \quad i = 1,2,\cdots,n \tag{5}$$

Equation (5) can be stated in matrix form as:

$$\vec{F} = [k]\vec{x} \tag{6}$$

where $[k]$ is the *stiffness matrix given by:*

$$\begin{bmatrix} k_{11} & k_{12} & \cdots & k_{1n} \\ k_{21} & k_{22} & \cdots & k_{2n} \\ \vdots & \vdots & \ddots & \vdots \\ k_{n1} & k_{n2} & \cdots & k_{nn} \end{bmatrix} \tag{7}$$

Substituting equation (6) into equation (3), it obtains:

$$\vec{x} = [a]\vec{F} = [a][k]\vec{x} \tag{8}$$

$$[a][k] = [I] \tag{9}$$

where $[I]$ denotes the *unit matrix.* Equation (9) is equivalent to:

$$[k] = [a]^{-1} \qquad [a] = [k]^{-1} \tag{10}$$

That is, the stiffness and flexibility matrices are the inverse of one another. Note the following aspects of influence coefficients:

1. Since the deflection at point i due to unit load at point j is the same as the deflection at point j due to unit load at point i for a linear system: $a_{ij} = a_{ji}$ and $k_{ij} = k_{ji}$;

2. The flexibility and stiffness influence coefficients can be calculated from the principles of solid mechanics;

3. The influences coefficients for torsional systems can be defined in terms of unit and angular deflection it causes.

Lagrange's Equations

The equations of motion of a vibrating system can often be derived I a simple manner in terms of generalized coordinates by the use of *Lagrange's Equations.* The Lagrange formulation states that the equations of motion of a vibrating system can be derived from:

$$\frac{d}{dt}\left(\frac{\partial T}{\partial \dot{q}_j}\right) - \frac{\partial T}{\partial q_j} + \frac{\partial V}{\partial q_j} = Q_j^{(n)}, \qquad j = 1,2,\cdots,n \tag{1}$$

where $\dot{q}_j = \partial T/\partial q_j$ is the generalized velocity and $Q_j^{(n)}$ is the *nonconservative* generalized force corresponding to the generalized coordinate q_j. The forces represented by $Q_j^{(n)}$ may be dissipative (damping) forces or other external forces which are not derivable from a potential function. For example, if F_{xk}, F_{yk}, F_{zk} represent the external forces acting on the kth mass of the system in the x, y, z directions, respectively, then the generalized force $Q_j^{(n)}$ can be computed as follows:

$$\sum_k \left(F_{xk}\frac{\partial x_k}{\partial q_j} + F_{yk}\frac{\partial y_k}{\partial q_j} + F_{zk}\frac{\partial z_k}{\partial q_j}\right) = Q_j^{(n)} \tag{2}$$

where x_k, y_k, z_k are the displacements of the kth mass in the x, y, z directions, respectively. For a conservative system $Q_j^{(n)} = 0$, equation (1) takes the form:

$$\frac{d}{dt}\left(\frac{\partial T}{\partial \dot{q}_j}\right) - \frac{\partial T}{\partial q_j} + \frac{\partial V}{\partial q_j} = 0, \qquad j = 1,2,\cdots,n \tag{3}$$

3.3 Modal Parameters

The system under investigation can be described by three different types of models. Each of them is defined by system matrices:

1. **spatial model**

- $[M]$ mass matrix;
- $[k]$ stiffness matrix;
- $[C]$ viscous damping or structural (*hysteretic*) damping matrix.

Matrices are of dimensions $n \times n$, (n indicates the number of degrees of freedom, the last one is equal to the number of equations of motion).

2. **Modal Model**

- $[\lambda^2]$ spectral matrix, diagonal. Eigenvalues are on the diagonal;
- $[\Phi]$ modal matrix: columns are modal shapes;

3. **Modal Model**

- $[H(\omega)]$ FRF matrix (matrix of FRFs: frequency response functions, e.g. mobilities Y(ω) or **IRFs**: impulse response functions, symmetrical).

Performing *theoretical* vibration analysis requires to advance from a spatial model to a response model in the following steps:

1. establish equations of motion: **spatial model**;
2. free vibration analysis: **modal model**;
3. analysis of forced vibration using harmonic excitation: **response model**.

Performing *experimental* vibration analysis, it is essential to proceed in opposite direction in the following steps:

1. measurements of the appropriate set of FRFs: **response model**;
2. curve-fitting of the measured data: **modal model**;
3. further calculations: **spatial model**.

The initial step in experimental modal analysis is to obtain the response of a structure to a certain kind of excitation. This might be accomplished under operational conditions or from modal testing within a controlled test environment. Once the response measurement has been completed, the next step to be performed is the identification of the modal parameters of the structure from the measured data. For this task a broad range of modal analysis techniques have been developed over the past decades.

The decision which technique to apply in a given situation is to be based on diverse considerations, the most important of which are: Is the excitation known (which is generally the case in experimental modal analysis) or unknown (which is generally the case in operational modal analysis where the response of the structure to an ambient excitation under operational conditions is measured)? Is the data available just in the frequency domain or also in the time domain? Does a reasonable estimation of the parameters exist as a starting point for an iterative procedure to improve the initial guess? Are the structural modes well separated or closely spaced? Is it reasonable to assume a lightly damped structure?
There are several criteria for the classification of modal analysis techniques: *Phase Resonance* methods are based on an adaption of the excitation in such a way that only one single mode is excited which simplifies the post-processing of the thus obtained data quite a lot but is experimentally very extensive; *Phase Separation* methods on the other hand shift most of the effort to the post-processing of the data as quite elaborate and computationally expensive numerical methods are required to extract reliable modal information from data comprising the coexistent contribution of several modes. The most widely-used classification however distinguishes between *Frequency Domain* methods and *Time Domain* methods. In this section the mathematical basics for the understanding of the examined modal analysis techniques shall be derived and the fundamental terms and definitions shall be introduced. First, the basic concept of the *Fourier Transform* (**FT**) is explained followed by the transition from the *Continuous FT* (**CFT**) to the *Discrete FT* (*DFT*) which is essential for the practical implementation of the method as computers are only able to deal with discrete data. Subsequently, a few remarks on the effect of *leakage* and the concept of *windowing* to reduce this effect are to complete this presentation. At the end of the section the very important concept of the *Frequency Response Function* (**FRF**) which is the basis for all the frequency domain methods of modal analysis is introduced and the most important characteristics of an FRF are discussed.

Fourier Transform

The *Fourier Transformation* or *Fourier Transform* is a very fundamental mathematical instrument of signal analysis. Originally developed by Fourier for the solution of differential equations in the area of heat conduction, it soon was applied to totally different problems throughout the various disciplines of science and engineering. Initially developed as an analytical instrument and therefore constrained to the application to analytically defined and integrable functions, the real power of the Fourier Transform could only be exploited with the advent of modern computers.

$$\boldsymbol{F}(\omega) = \int_{-\infty}^{\infty} f(t) e^{i\omega t} dt \qquad (1)$$

The *Fourier Anti-Transform* can be written as follows:

$$f(t) = \frac{1}{2\pi} \int_{-\infty}^{\infty} \boldsymbol{F}(\omega) e^{i\omega t} d\omega \qquad (2)$$

In the following section the process of adapting the original version of the FT, the **CFT**, via the *Fourier Series* (already discretized in frequency but not yet in time) to a fully discretized version processable by computers, the **DFT**, is outlined, and the most important characterictics of the FT with respect to its application in signal analysis are discussed. The formulation of the FT as presented here is taken from (1).

Continuous Fourier Transform

The **CFT** of a continuous function of time, $p(t)$, is defined by:

$$\boldsymbol{P}(f) = \int_{-\infty}^{\infty} p(t) e^{-j2\pi f t} dt\,, \quad \omega = 2\pi f \tag{1}$$

Normally, $p(t)$ is considered a function of time and $P(f)$ is considered a function of frequency, with lower case letters denoting the time function and upper case letters denoting its corresponding *Fourier Transform*. The **CFT** can be interpreted as developing a function (which not necessarily needs to be periodic) into an infinite series of sinusoids and cosinusoids where the trigonometric functions form an orthogonal basis of the function space which $p(t)$ is part of. The inverse FT is defined by:

$$p(t) = \int_{-\infty}^{\infty} \boldsymbol{P}(f) e^{j2\pi f t} df \tag{2}$$

*Frequency Response Function (**FRF**)*

A very basic concept for all modal analysis techniques based on frequency domain data is the *Frequency Response Function* (**FRF**) of a system. Considering the general equation of motion, caused by an external force $f(t) = F(j\omega)e^{j\omega t}$, of a viscously damped **SDOF** system; the forced response of a **SDOF** system can be deduced. A trial solution of the form $x(t) = X(j\omega)e^{j\omega t}$ (ω the forcing frequency) inserted into the general equation of motion, yields the following solution for the amplitude $X(j\omega)$ (in frequency domain, i.e. as a function of frequency):

$$X(j\omega) = \frac{F(j\omega)}{(k-\omega^2 M)+j(\omega C)} \tag{1}$$

Physically interpreted, this means that the system responds to the external force $f(t)$ with an harmonic vibration with the forcing frequency ω and an amplitude and phase shift as determined by the complex quantity $X(j\omega)$. With the general definition of the FRF:

$$FRF := \frac{Response}{Excitation} = \frac{X(j\omega)}{F(j\omega)} \tag{2}$$

The *ratio* of a system's response to the corresponding excitation computed in frequency domain is given by the following expression for the FRF of the considered **SDOF** system:

$$\alpha(j\omega) = \frac{1}{(k-\omega^2 M)+j(\omega C)} \tag{3}$$

This special case of an FRF where the regarded response parameter is the displacement $x(t)$ is called *Receptance FRF*. It is possible to define alternative Frequency Response Functions by selecting either velocity or acceleration instead of displacement as the response parameter. With the relationships $v(t) = \dot{x}(t) = j\omega e^{j\omega t}$ and $a(t) = \ddot{x}(t) = -\omega^2 x e^{j\omega t}$, the following expressions are:

$$Mobility\ FRF = Y(j\omega) = \frac{\dot{X}(j\omega)}{F(j\omega)} = j\omega\alpha(j\omega) \tag{4}$$

$$Accelerance\ FRF = A(j\omega) = \frac{\ddot{X}(j\omega)}{F(j\omega)} = -\omega^2\alpha(j\omega) \tag{5}$$

Response Parameter R	Standard R/F	Inverse F/R
Displacement	Receptance Admittance Dynamic Compliance Dynamic Flexibility	Dynamic Stiffness
Velocity	Mobility	Mechanical Impedance
Acceleration	Inertance Accelerance	Apparent Mass

Table 7: Various Types of FRFs According to Response Parameter.

MDOF Systems

As in practical applications one never gets to deal with SDOF systems it is essential for the practical applicability of the concept to generalize the considerations about the FRF as discussed before to **MDOF** systems. Beginning with the general equation of motion a damped **MDOF** system with viscous damping:

$$M\ddot{\boldsymbol{X}} + C\dot{\boldsymbol{X}} + K\boldsymbol{X} = \boldsymbol{F}(t) \tag{1}$$

When assuming a harmonic excitation of the form $f(t) = F(j\omega)e^{j\omega t}$ the general form of the *Receptance FRF* of a viscously damped **MDOF** system shows to be the following:

$$[\alpha(j\omega)] = [K + j\omega C - \omega^2 M]^{-1} \tag{2}$$

$$\alpha_{ij}(j\omega) = \sum_{r=1}^{N} \frac{(\Phi_j)(\Phi_k)}{(k_r - \omega^2 m_r) + j(\omega c_r)} \tag{3}$$

$$c_r = 2\zeta_r \sqrt{k_r m_r} \tag{4}$$

where Φ_j denotes the j^{th} component of the r^{th} eigenvector of the system.

When dealing with the FE model of a structure, there are two possibilities to determine the FRF of the system: one can directly compute the FRF in frequency domain using the formulas given by equation (2) or equation (3). Alternatively, a transient simulation can be conducted and the FRF at a given point can be computed as the ratio of the structural response at that point to the excitation in frequency domain. Obviously, when dealing with a real structure in experimental modal testing, the latter is the only possibility to determine the FRF. Theoretically, when the excitation is applied as a force and the structural oscillation is given enough time to stabilize, both approaches should yield the same result and it should be possible to compute the correct FRF from transient measurement data.
As for an SDOF system, for **MDOF** system there are also three alternatives of FRF with using either displacement or velocity or acceleration as a response parameter, thus obtaining *Receptance*, *Mobility* or *Inertance* respectively. These three forms are exactly in the same relation as described earlier, thus:

$$[Y(\omega] = i\omega[\alpha(\omega)] \tag{5}$$

$$[A(\omega] = i\omega[Y(\omega)] = -\omega^2[\alpha(\omega)] \tag{6}$$

Using the type of *log-log plot*, individual terms in the FRF series can be plotted as separate curves. The total FRF curve is a summation of all the individual curves. However, the exact shape of the curve is not so simple to deduce as first appears because a part of the information (phase) is not shown. In fact, in some sections of each curve, the *Receptance* is actually positive in sign and in others is negative but there is no indication of this on the logarithmic plot which only shows the modulus. However, when addition of the individual components is made to determine the complete *Receptance* expression, the signs of various terms are of considerable importance.

The main difference between the point and *Transfer Receptances* is in the sign of the modal constant (the numerator) of the second mode. As the plots only show the modulus, they are apparently insensitive to this difference. However, when the two terms are added to produce the actual FRF for the MDOF system, the following characteristics will arise, which is illustrated in figure (46). In this figure, *Receptance* is plotted, but the following remarks apply for all types of FRF (Receptance, Mobility and Inertance). When considering a *Point Receptance*, the numerator in the equation (3) for all modes will always be positive, as it is a square of modal vector element. In Transfer Receptance, the numerator can be either positive or negative according to the signs of elements of eigenvectors.

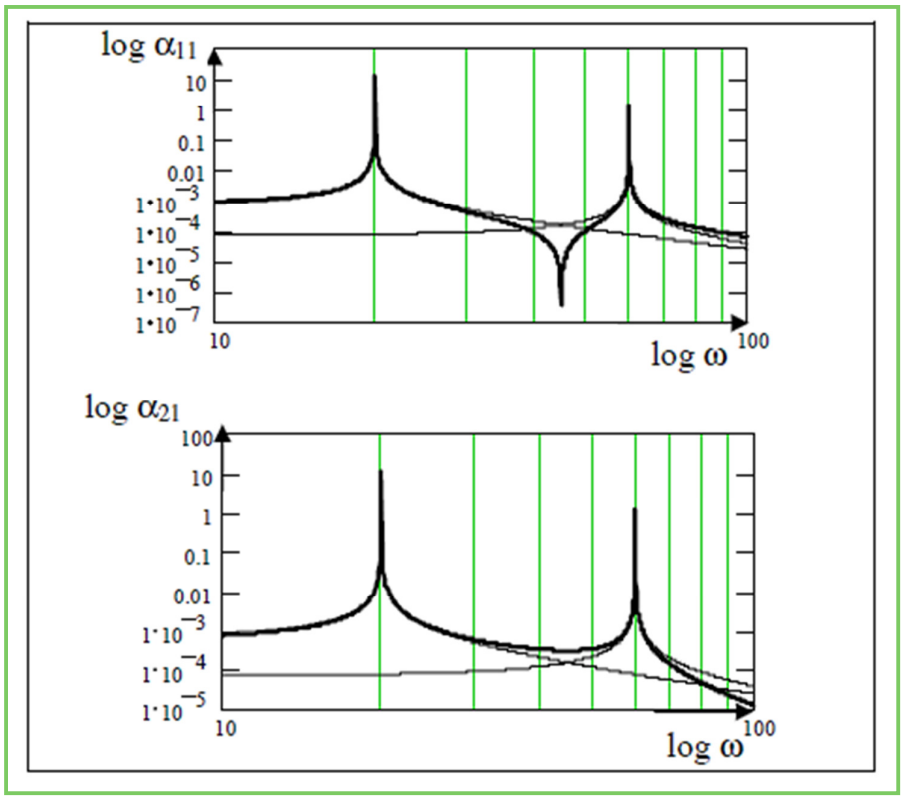


Figure 46: Point (upper) and Transfer Receptance (below) FRF Plot for Undamped 2DOF System.

At frequencies below the first natural frequency, both terms in the sum have the same sign and thus are additive, making the total FRF curve higher than each component, but as the plot uses a logarithmic scale, the contribution of the second mode at these low frequencies is relatively insignificant. Hence, the total FRF curve is only slightly above that for the first term. A similar argument and result apply at the high frequency end, above the second natural frequency, where the total plot is just above that for the second term alone. However, in the region between the two resonances, the two components have opposite signs to each other so that they are subtractive, and at the point where they cross, their sum is zero since they are of equal magnitude but of opposite sign there. On a logarithmic plot of this type, this produces the *Antiresonance characteristic* which reflects that of resonance. In the immediate vicinity of any resonance, the contribution of the term whose natural frequency is nearby is so much greater than the other one that the total is, in effect, the same as that one term. Physically, the response of the MDOF system just at one of its natural frequencies is dominated by that mode and other modes have very little influence (it applies for undamped or very slightly damped systems).

3.4 Introduction to Time, and Frequency Domains

The Time Domain

The traditional way of observing signals is to view them in the *time domain*. The time domain is a record of what happens to a parameter of the system versus time. For instance, figure (47) shows a simple spring-mass system where a pen is attached to the mass and pulled a piece of paper past the pen at a constant rate. The resulting graph is a record of the displacement of the mass versus time, *a time-domain view of displacement*. Such direct recording schemes are sometimes used, but usually it is much more practical to convert the parameter of interest to an electrical signal using a *transducer*. Transducers are commonly available to change a wide variety of parameters to electrical signals. This electrical signal, which represents a parameter of the system, can be recorded on a strip chart recorder as in figure (48). This indirect approach allows to convert the desired parameter to the displacement of the recorder pen. With the indirect system, it is possible to select a transducer that will not significantly affect the measurement. (This can go to the extreme of commercially available displacement transducers that do not even contact the mass.). The pen deflection can be easily fixed to any desired value by controlling the gain of the electronic amplifiers. This indirect system works well until the measured parameter begins to change rapidly. Because of the mass of the pen and recorder mechanism and the power limitations of its drive, the pen can move only at finite velocity. If the measured parameter changes faster than the pen velocity, the output of the recorder will be in error. A common way to reduce this problem is to eliminate the pen and use a deflected light beam to record on *photosensitive paper*. Such a device is called an *oscillograph*: since it is only necessary to move a small, lightweight mirror through a very small angle, the oscillograph can respond much faster than a strip chart recorder.

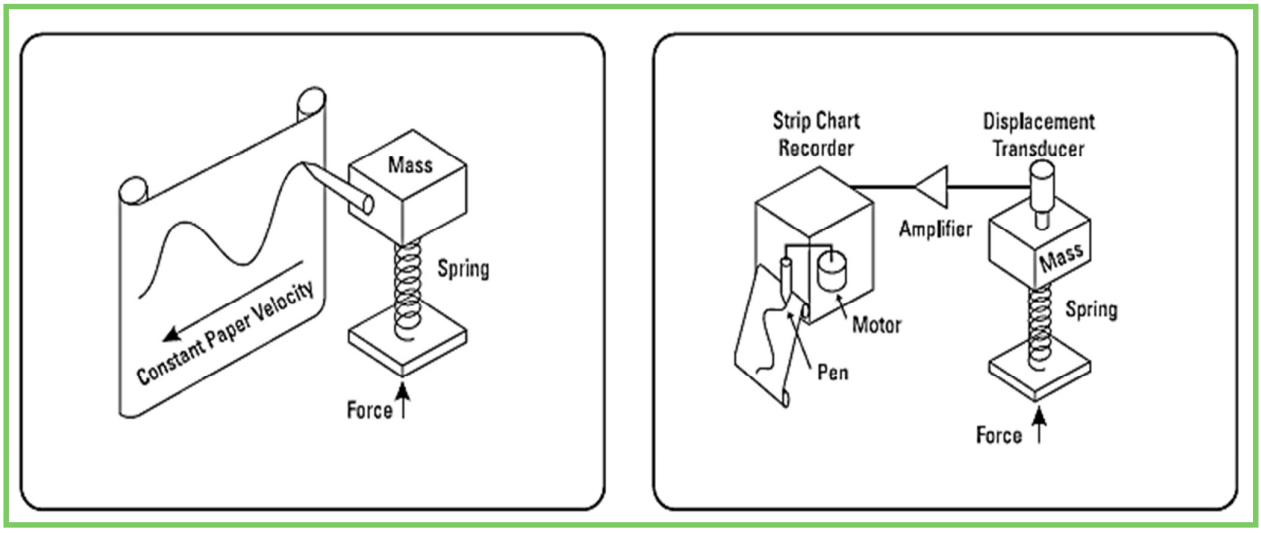


Figure 47: time-domain view of displacement for simple spring-mass system.

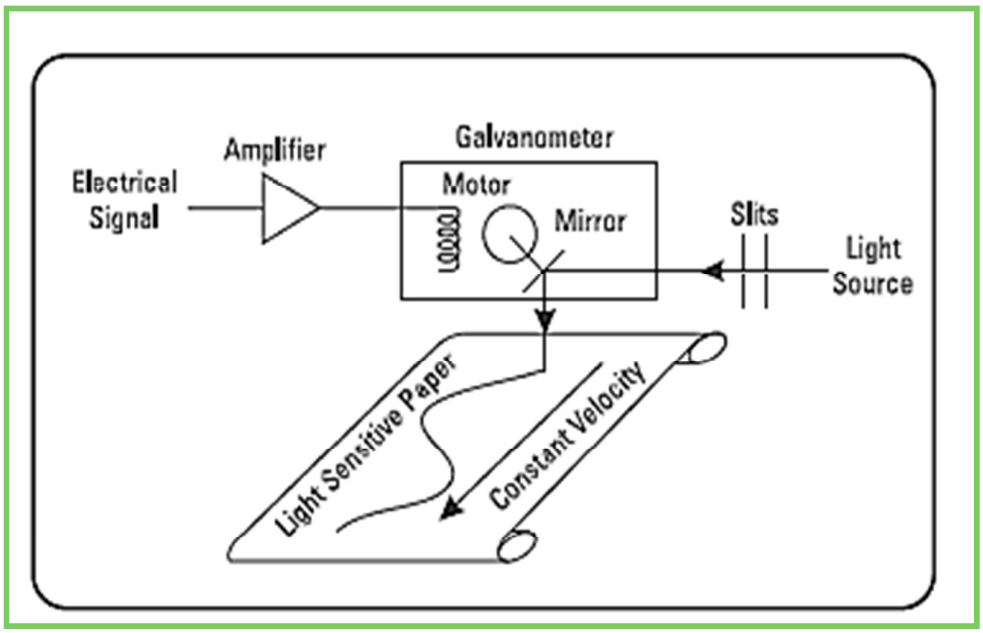


Figure 48: electrical signal which represents a parameter of the system.

The Frequency Domain

Figure (49) illustrates a simple waveform composed of two sine waves; by picking the amplitudes, frequencies and phases of these sine waves correctly, we can generate a waveform identical to our desired signal. Conversely, it can break down real world signals into these same sine waves; it is possible showing that this combination of sine waves is unique, any real world signal can be represented by only one combination of sine waves. Figure (a) is a three-dimensional graph of this addition of sine waves. Two of the axes are time and amplitude, familiar from the time domain; the third axis, frequency, allows to visually separate the sine waves that add to give complex waveform. The view of three-dimensional graph along the frequency axis is shown in figure (b): this is the time domain view of the sine waves. Adding them together at each instant of time gives the original waveform.
However, the view of the graph along the time axis in figure (c), shows a totally different picture: Here, there are axes of amplitude versus frequency, what is commonly called the *frequency domain*. Every sine wave we separated from the input appears as a vertical line. Its height represents its amplitude and its position represents its frequency. Since it knows that each line represents a sine wave, uniquely characterized our input signal in the frequency domain. This frequency domain representation of the signal is called the *spectrum* of the signal. Each sine wave line of the spectrum is called a *component of the total signal*. It is very important to understand that the information has not been neither gained nor lost, but have been only represented differently.

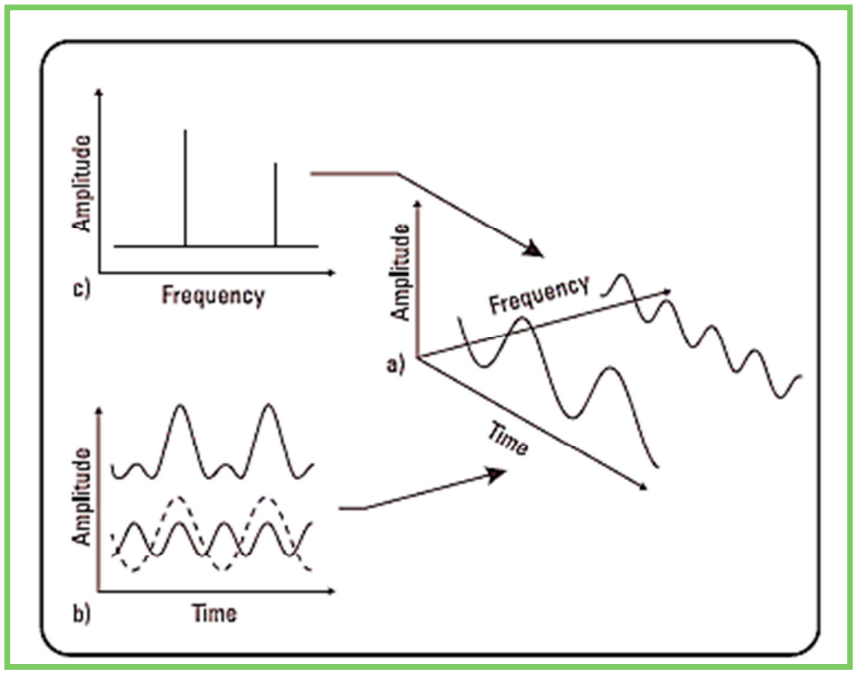


Figure 49: comparison between frequency and time domain representation.

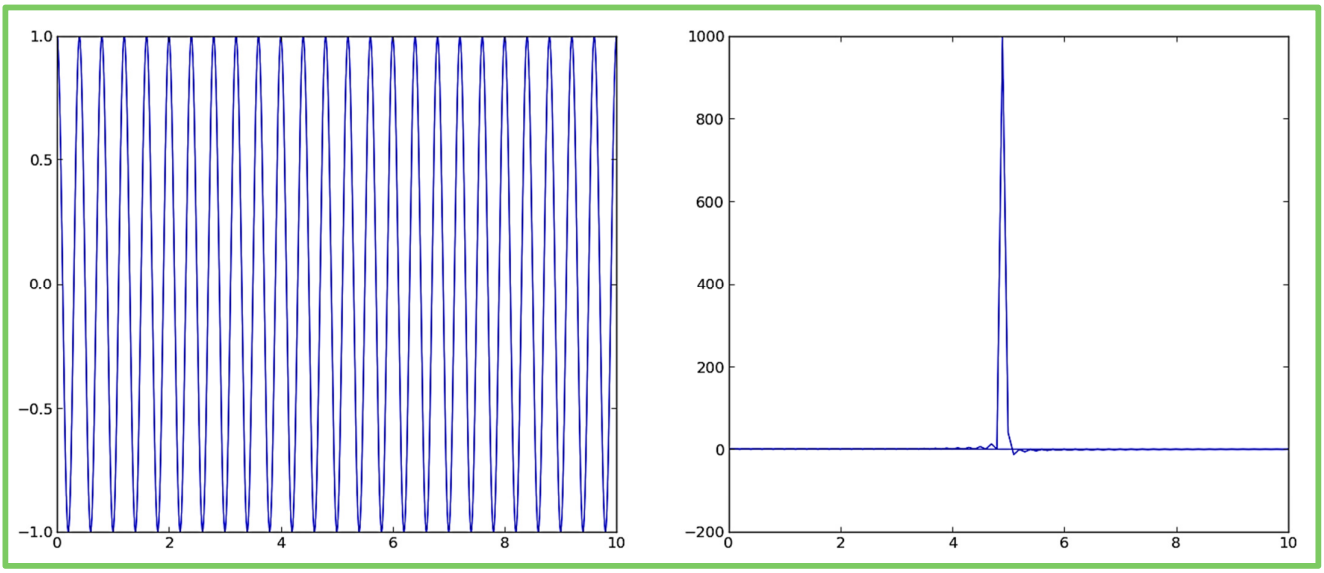


Figure 49: the frequency content in time and frequency domain of the energy applied to structure with an impact hammer.

3.5 Dual-Channel Analysis

This section introduces some terms that concern modal tests and that fall within signal processing area. The basic scheme of *dual-channel FFT* (Fast Fourier Transform) analyser is in figure (50).During a simultaneous analysis of signals in at least two channels, the signals themselves are not in the forefront any more, but rather properties of the physical system responsible for the differences between those signals. The methods can be theoretically expanded to any number of channels, but basically two of them are processed simultaneously each time. In the following text, individual functions that occur in system analysis will be described.

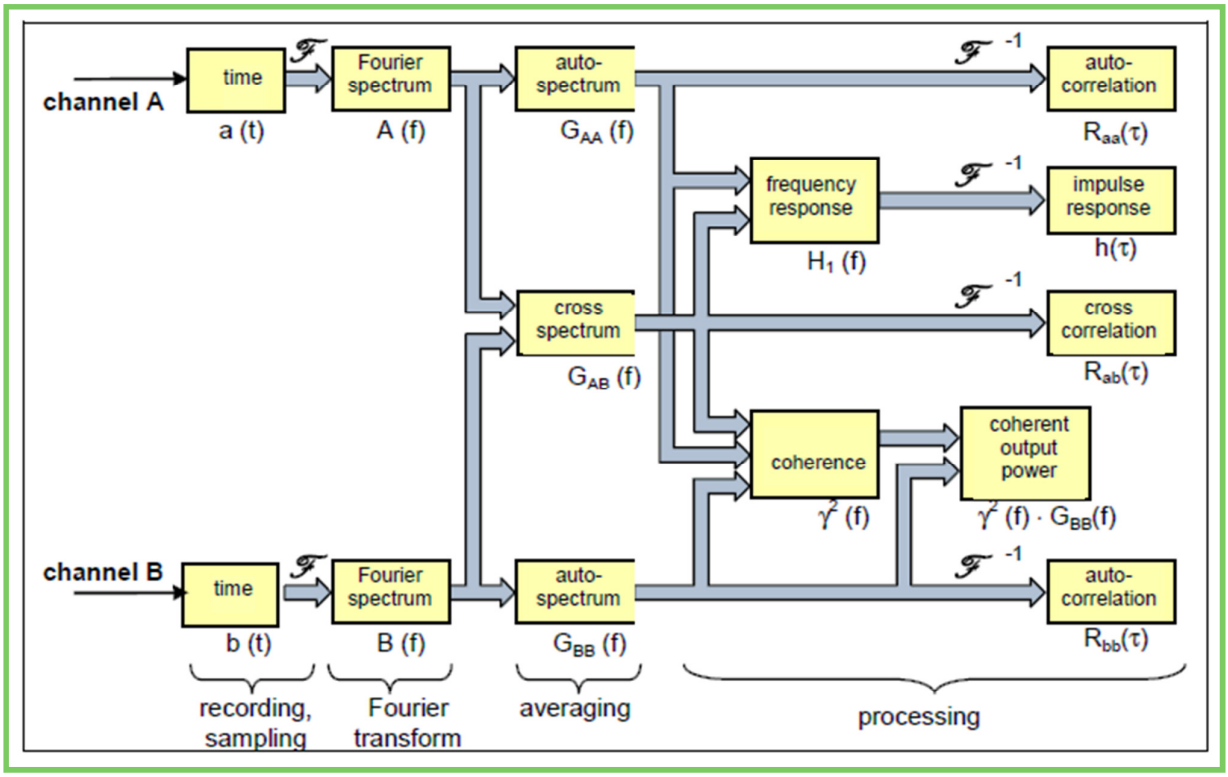


Figure 50: scheme of Dual-channel Analyzer.

Auto-Power Spectrum

Auto-Power spectrum is a function commonly explored both in signal and system analysis. It is computed from the instantaneous (Fourier) spectrum as:

$$E = \int_{-\infty}^{\infty} |g(t)|^2 dt = \int_{-\infty}^{\infty} |G(f)|^2 df \quad (1)$$

where E is called *Spectral Density of Energy*. This function allows to understand the energy distribution into frequency domain.

$$G_{AA}(f) = E\lfloor A(f) \cdot A^*(f) \rfloor = \boldsymbol{\mathcal{F}} E[a^*(t) \cdot a(-t)] = \boldsymbol{\mathcal{F}}[R_{AA}(\tau)] \quad (2)$$

$[R_{AA}(\tau)]$ is the *Auto-correlation Function*, and it can de expressed as follows:

$$[R_{AA}(\tau)] = \int_{-\infty}^{\infty} a(t)a(t+\tau)dt \quad (3)$$

There is a new, fundamental function, *Cross Spectrum*, in the dual channel processing. It is computed from instantaneous spectra of both channels.
Based on complex instantaneous spectra $A(f)$ and $B(f)$, the cross spectrum G_{AB} (from A to B) is defined as:

$$G_{AB}(f) = E\lfloor \cdot A^*(f) \cdot B(f) \rfloor = \boldsymbol{\mathcal{F}} E[a^*(-t) \cdot a(t)] = \boldsymbol{\mathcal{F}}[R_{AB}(\tau)] \quad (4)$$

$$G_{AB}(f) = G^*{}_{BA}(f) \tag{5}$$

$$G_{BA}(f) = B^*(f)A(f) \tag{6}$$

the *Cross-correlation Function* is written as:

$$R_{AB}(\tau) = \int_{-\infty}^{\infty} a(t)b(t+\tau)dt \tag{7}$$

Amplitude of the *Cross Spectrum* $G_{AB}(f)$ is the product of amplitudes, its phase is the difference of both phases (from A to B). *Cross Spectrum* $G_{BA}(f)$ (from B to A) has the same amplitude, but opposite phase.
The cross spectrum itself has little importance, but it is used to compute other functions. Its amplitude $|G_{BA}(f)|$ indicates the extent to which the two signals correlate as the function of frequency, phase angle G_{BA} indicates the phase shift between the two signals as the function of frequency. The advantage of the Cross Spectrum is that influence of noise can be reduced by averaging. That is because the phase angle of the noise spectrum takes random values so that the sum of those several random spectra tends to zero. It can be seen that the measured Auto-Spectrum is a sum of the true Auto-Spectrum and Auto-Spectrum of noise, whilst the measured cross spectrum is equal to the true cross spectrum.

Coherence

For random excitation, the source of a random command signal is found in an external device such as a noise generator and not in the analyser itself. The principle upon which the FRF is determined using random excitation is based on the following equations which relate the excitation and the response of a system:

$$x(t) \overset{FFT}{\longrightarrow} X(f), \quad y(t) \overset{FFT}{\longrightarrow} Y(f) \quad \Rightarrow \quad \frac{Y(f)}{X(f)} = H(f) \coloneqq FRF \tag{1}$$

$H(f)$ is the *Frequency Response Function* linking the input and output signal. It is possible to obtain an estimate to the required FRF using the next equations:

$$\frac{Y(f)X^*(f)}{X(f)X^*(f)} = H_1(f) = \frac{G_{XY}(f)}{G_{XX}(f)} \tag{2}$$

$$\frac{Y(f)Y^*(f)}{X(f)Y^*(f)} = H_2(f) = \frac{G_{YY}(f)}{G_{YX}(f)} \tag{3}$$

where $H_1(f)$ and $H_2(f)$ have the function to minimize, respectively, the error in output signal and the error in input signal. Now, it can be introduce a quantity called *Coherence* which is defined as:

$$\boldsymbol{\gamma^2} = \frac{|G_{XY}(f)|^2}{G_{XX}(f) \cdot G_{YY}(f)} = \frac{H_1(f)}{H_2(f)} \tag{4}$$

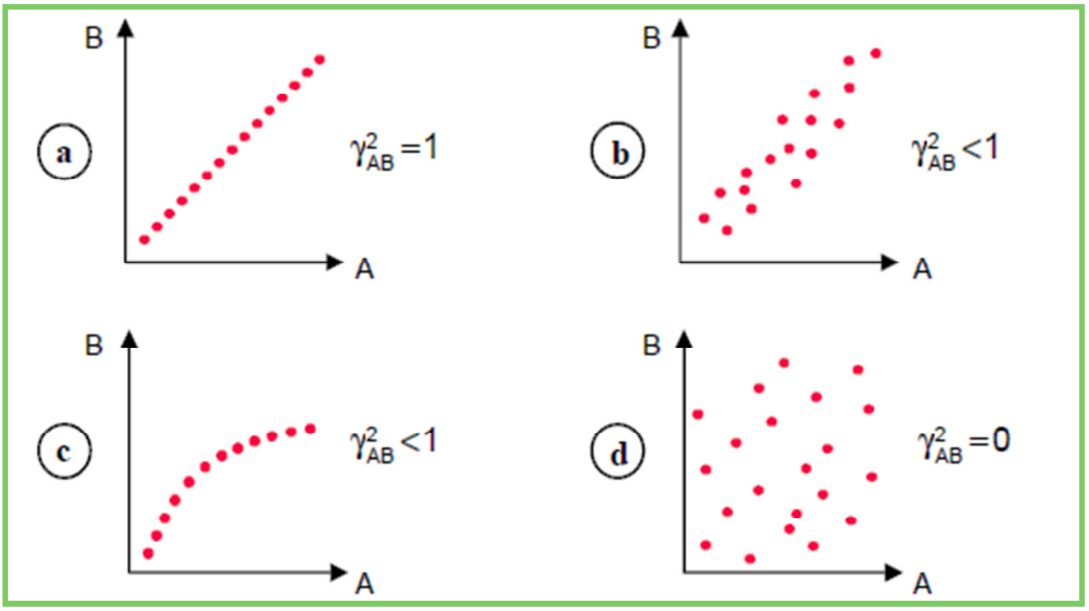


Figure 51: Analogy between Coherence and Correlation Coefficient.

The Coherence can be shown to be less than or equal to 1.0, and it should reassure that the measurements have been well made. In the event that the Coherence is not unity, it will be necessary to establish why not, and then to determine what is the correct value of FRF. It should be noted at this stage that many commercial analysers provide only one of these two FRF estimates as standard and, because it is fractionally easier to compute, this is generally $H_1(f)$. Of course, given the Coherence as well, it is simple matter to deduce the other version, $H_2(f)$, from equation (4).

There are several situations in which an imperfect measurement might be made, and a low Coherence recorded. There may well be noise on one or other of two signals which could degrade the measured spectra: near resonance this is likely to influence the force signal so that $G_{XX}(f)$ becomes vulnerable while at *antiresonance* it is the response signal which will suffer, making $G_{YY}(f)$ liable to errors. In the first of these cases, $H_1(f)$ will suffer most and so $H_2(f)$ might be a better indicator near resonance while the reverse applies at antiresonance, as shown in the following equations:

$$H_1(f) = \frac{G_{XY}(f)}{G_{XX}(f)+\boldsymbol{G_{NN}(f)}} \tag{5}$$

$$H_2(f) = \frac{G_{YY}(f)+\boldsymbol{G_{MM}(f)}}{G_{YX}(f)} \tag{6}$$

where $\boldsymbol{G_{MM}(f)}$ and $\boldsymbol{G_{NN}(f)}$ are the *auto-spectra* of the noise on the output and input, respectively. Figure () shows a typical measurement made using random excitation, presenting the standard FRF, $H_1(f)$ and the Coherence γ^2. This shows the trend for a great many practical cases, demonstrating a good Coherence everywhere except near resonance and *Antiresonance*.

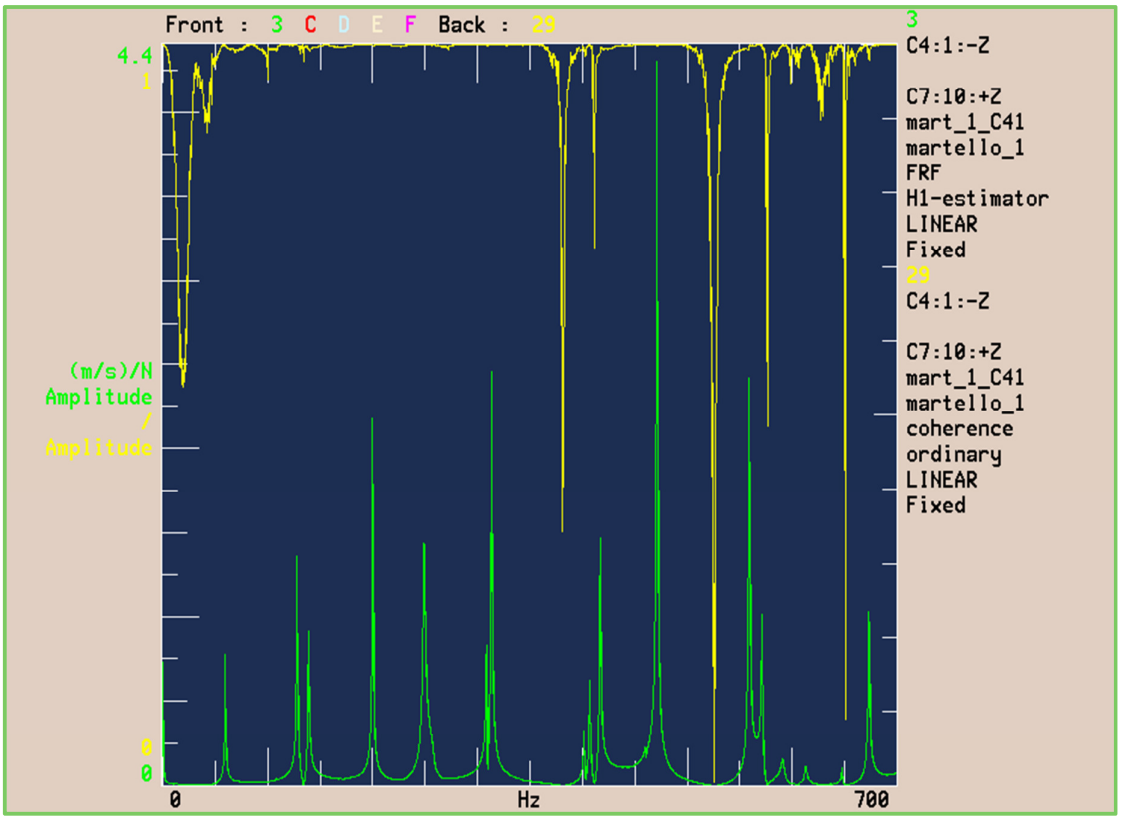


Figure 52: Example of FRF and Coherence for the rectangular thin plate by Impact Test Monitor.

4. Mobility Measurement Technique

In this chapter, the procedure how to perform modal test will be discussed. In particular, the principal intention is to illustrate the current instrumentation and technique used for acquiring frequency response measurements of the thin plate . The discussion begins with the use of a dynamic signal analyser and associated peripherals for making these measurements. The type of modal testing applied is known as the *Frequency Response Function Method*, which measures the input excitation and output is examined. The focus is on the use of one input force, a technique commonly known as **single-point excitation**; with a dynamic signal analyser, which is a Fourier transform-based instrument, many types of excitation sources can be implemented to measure a structure's frequency response function. The selection and implementation of the more common and useful types of signals for modal testing must be chosen considering the type of structure, the context in which the measures are carried out, without forgetting to take into account the various boundary conditions that motivate and justify the choices made in order to perform the modal test. Transducer selection and mounting methods for measuring these signals along with system calibration methods, are also included. Techniques for improving the quality and accuracy of measurements are then explored. These include processes such as averaging, windowing and zooming, all of which reduce measurement errors. Finally, a section on measurement interpretation is included to aid in understanding the complete measurement process. The procedure involves three or four main stages:

1) preparation of the measured structure and creating a geometrical model for measurement;
2) measurement itself;
3) identification of modal parameters from the measured data;
4) verification of the obtained modal model, its comparison with a computational model.

All these stages will be discussed step by step. It is clear that using various procedures in the individual stages will highly depend on the purpose of modal test.

4.1 General Test System Configurations

The setup used for mobility measurement is basically quite simple although there exist a great many different variants on it. There are three major items:

- An excitation mechanism;
- A transduction system to measure the various parameters of interest;
- An analyser, to extract the desired information (in the presence of the inevitable imperfections which will accumulate on the measured signals).

The basic test setup required for making frequency response measurements depends on a few major factors. These include the type of structure to be tested and the level of results desired. Other factors, including the support fixture and the excitation mechanism, also affect the amount of hardware needed to perform the test. Figure (53) shows a diagram of a basic test system configuration.

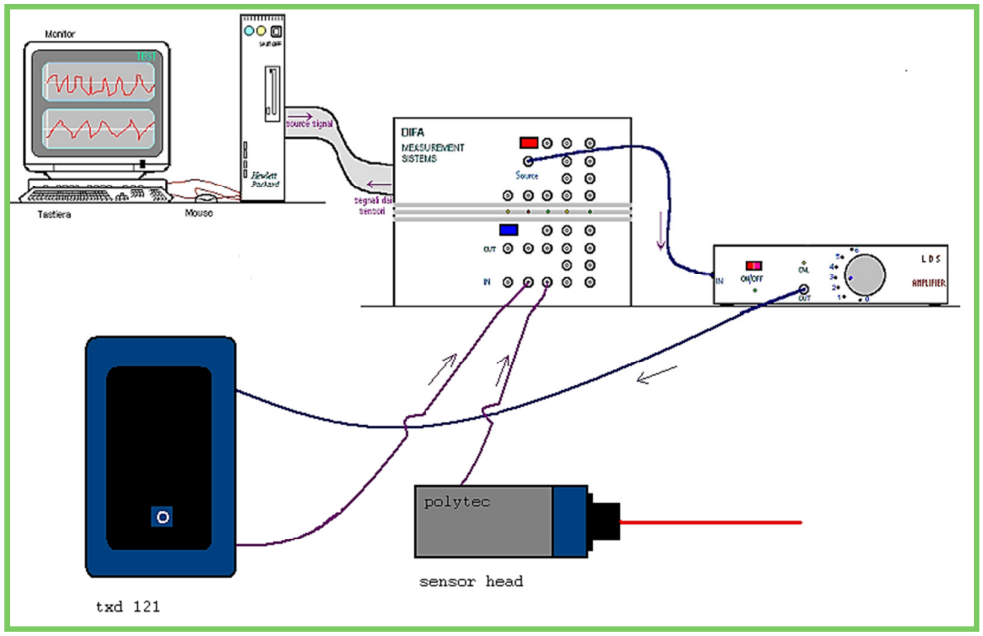


Figure 53: Model of the equipment used for laboratory testing.

The heart of the test system is the controller, or computer, which is the operator's communication link to the analyser. It can be configured with various levels of memory, displays and data storage. The modal analysis software usually resides here, as well as any additional analysis capabilities such as structural modification and forced response. The analyser provides the data acquisition and signal processing operations. It can be configured with several input channels, for force and response measurements, and with one or more excitation sources for driving shakers. Measurement functions such as windowing, averaging and Fast Fourier Transforms (FFT) computation are usually processed within the analyser. This function is simply to measure the various signals developed by the transducers in order to ascertain the magnitudes of excitation force(s) and responses. Each mobility system incorporates an analyser in order to measure the specific parameters of interest (force, response levels). The two most common devices are *Spectrum Analyser* and *Frequency Response Analyser (FRA).* For Frequency Response Analyser the source or command signal, the sinewave at the desired frequency , is first generated digitally within the analyser an then output as an analogue digital signal via a D-A converter. Within the same device, the two input signals (from the force and response transducers) are digitised and then, one at a time, correlated numerically with the outgoing signal in such a way that all the components of each incoming signal other than that at exactly the frequency of the command signal is eliminated. The Spectrum Analyser is a quite different type of instrument to the FRA device described above. The Spectrum Analyser seeks to measure *simultaneously* all the frequency components present in a complex time-varying signal: its output consists of a spectrum, usually a discrete one containing a finite number of components, describing the relative magnitudes of a whole range of frequencies present in the signal. Various apparatus are available for exciting the structure. Basically, they can be divided into two types: contacting and non-contacting. The first of these involves the connection of an exciter which remains attached to the structure throughout the test (*shaker* or *mechanical exciter*). The second type includes devices which are either out of contact throughout the vibration, or which are only in contact for a short period, while the excitation is being applied (such as a *hammer blow*).

The mechanical exciter (*shaker*) is capable of generating a prescribed force at a variable frequency; the magnitude of the force is restricted by the out of balance and is only variable by making adjustments to this quantity, not something which can be done while the vibration is continuing. Also, this type of excitation mechanism is ineffective at low frequencies because of the speed-squared dependence. It must be noted that the electrical *impedance* of these instruments varies with the amplitude of motion of the moving coil, and so it is not possible to deduce the excitation force by measuring the current passing through the shaker because this measures the force applied not to the structure itself, but to the assembly of structure and shaker drive.

Another popular method of excitation is through use of an *impactor* or *hammer*. It is a relatively simple means of exciting the structure. The equipment consists of no more than an impactor, usually with a set of different tips and heads which serve to extend the frequency and force level ranges for testing a variety of different structures. The useful range may also be extended by using different sizes of impactors. Integral with the impactor there is a load cell, or force transducer, which detects the magnitude of the force felt by the hammer, and which is assumed to be equal and to that experienced by the structure. The magnitude of the impact is determined by the mass of the hammer head and the velocity with which it is moving when it hits the structure. The frequency range which is effectively excited by this type of device is controlled by the stiffness of the contacting surfaces and the mass of the impactor head: there is a system resonance at a frequency given by $(contact\ stiffness/impactor\ mass)^{1/2}$ above which it is difficult to deliver energy into the test structure. The figure (54) shows the hammer tip impacts the test structure, this will experience a force pulse which is substantially that of a half-sine shape; a pulse of this type can be shown to a frequency content of the form illustrated in figure (55), which is essentially flat up to a certain frequency and then of reduced an uncertain strength afterward.

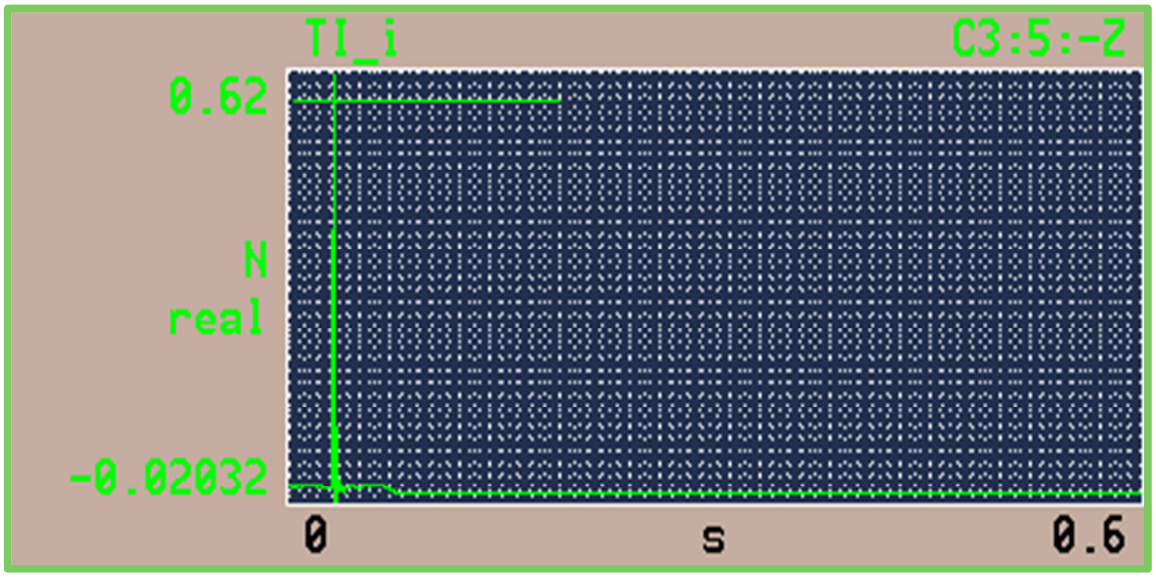


Figure 54: the hammer tip impacts the test structure, the frequency response on the plate is called "Delta di Dirac".

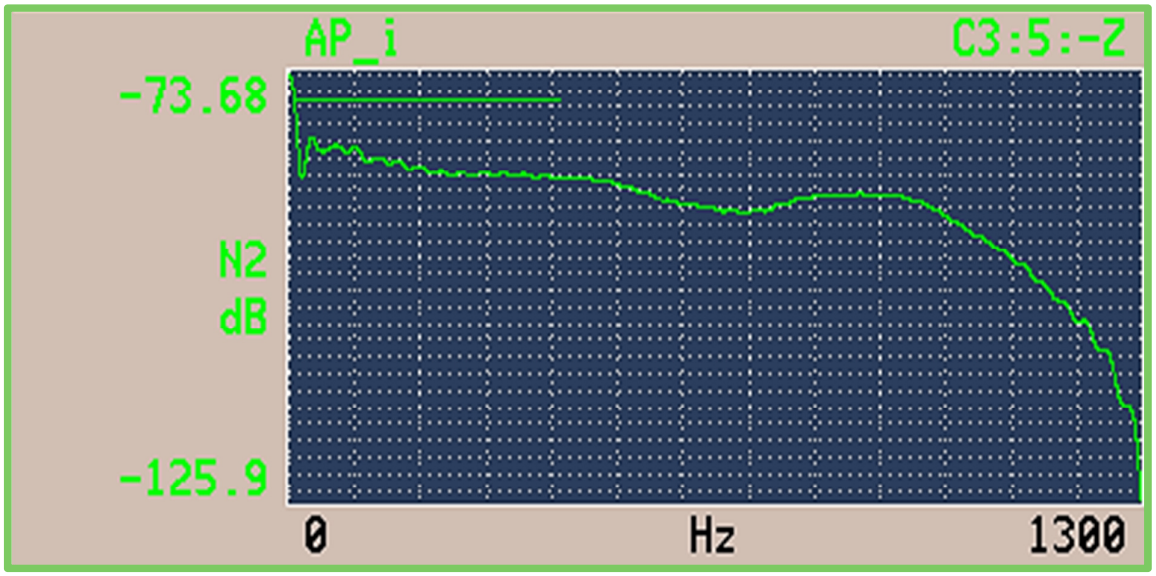


Figure 55: the dynamic response of the plate in frequency domain.

It can be shown that there is a direct relationship between the first cut-off frequency and the duration of the pulse, and that in order to increase the frequency range it is necessary to induce a shorter pulse length. This in turn, can be seen to be related to the stiffness (not the hardness) of the contacting surfaces and the mass of the impactor head. It is for this purpose that a set of different hammer tips and heads are used to permit the regulation of the frequency range to be included. Generally, as soft a tip as possible will be used in order to inject all the input energy into the frequency range of interest: using a stiffer tip than necessary will result in energy being input to vibrations outside the range of interest at the expense of those inside that range.

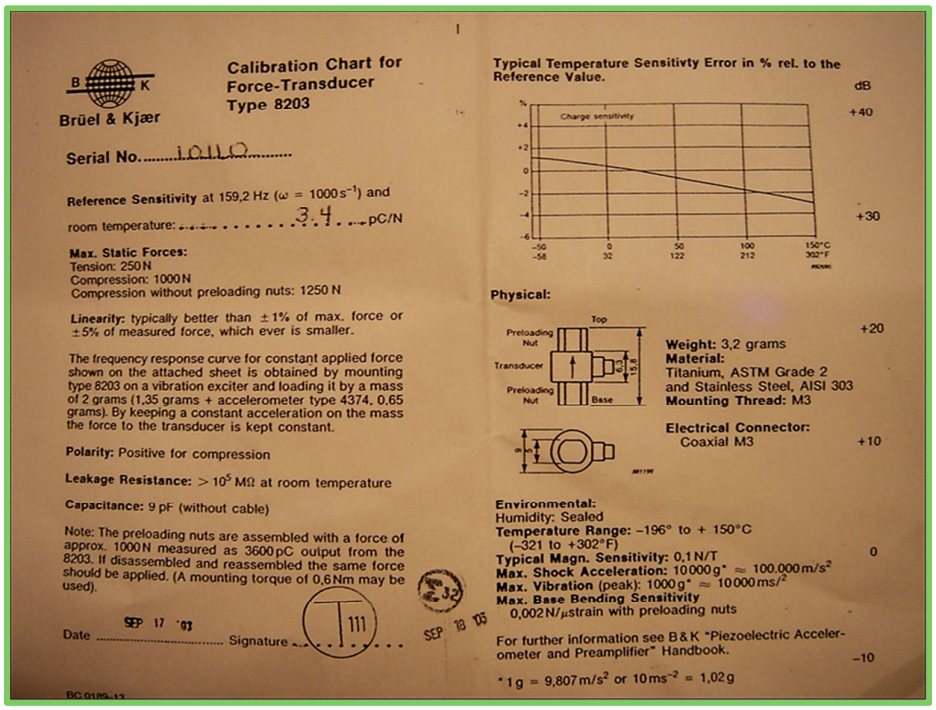
In order to measure the excitation forces and the various responses of interest, there are many different possibilities tools. For the most part, *piezoelectric transducers* are widely used for mobility measurements. The principal categories are: *force gauges*, *accelerometers,* and *impedance heads* (these last are simply a combination of force and acceleration sensitive elements in a single unit). The basic principle of operation makes use of the fact that an element of piezoelectric material (either a natural or synthetic crystal) generates an electrical charge across its end faces when subjected to a mechanical stress. The transmitted force F, or a known fraction of it, is applied directly across the crystal which thus generates a corresponding charge q proportional to F. The force indicated by the charge output of the crystal will always be slightly different from the force applied by the shaker, and also from that transmitted to the structure.

4.2 Preparation of the Measured Thin Rectangular Plate

One important preliminary to the whole process of mobility measurement is the preparation of the test structure itself. The first decision which has to be taken is whether is to be tested in a *free* or *grounded* (*fixed*, *clamped*) condition. Because the system on which will be carried out experimental measurements consists of a support structure (tank) and a thin plate fixed to the tank by means of a bond of interlocking achieved thanks to a frame provided with holes for the insertion of bolts, support chosen to allow the excitation of the plate can not be that of fixed type. Grounded (fixed, clamped) support is theoretically such a type of support where some points on the body (some DOFs) are completely fixed by connecting to the ground. This could not be reached in practice, so the support is considered to be fixed if the response of the fixed DOFs is less than 10% of the response of the other DOFs. This type of support causes difficulties when comparing experimental modal model with the computational modal model, because the differences in both models could be caused namely by different boundary conditions. But, sometimes it is necessary to use this type of support, if modal properties have no importance when the structure is freely supported. Another difficulty with such a type of support is with repeatability of the measurements. Despite any effort (tighten the screws connecting the structure with the measurement base using a torque wrench, etc.), 100% repeatability is failing if disassembly and reassembly of the measurement base is performed. According to experience, natural frequencies of the individual modes could differ after such mount, demount in the range up to $\pm 5\%$. The instrumentation required for the performance of experimental tests is quite varied and can change depending on the type of test being performed. Since the two main quantities which are measured are the strength applied and the displacement obtained, it is necessary to use equipment that are able to carry out such measures more accurately as possible.

Instrumented Impact Hammer

The input signal, applied to identify the frequencies of linear vibration of the plate, is exercised by a pulse of Dirac (δ Dirac). This pulse is theoretically infinite amplitude and duration tending to zero, but in reality it is a peak amplitude much greater than the duration, which is transferred via a device called a hammer instrumented.



Calibration Chart for
Force-Transducer
Type 8203

Brüel & Kjær

Serial No. 1010

Reference Sensitivity at 159,2 Hz (ω = 1000 s^{-1}) and room temperature: 3.4 pC/N

Max. Static Forces:
Tension: 250 N
Compression: 1000 N
Compression without preloading nuts: 1250 N

Linearity: typically better than ±1% of max. force or ±5% of measured force, which ever is smaller.

The frequency response curve for constant applied force shown on the attached sheet is obtained by mounting type 8203 on a vibration exciter and loading it by a mass of 2 grams (1,35 grams + accelerometer type 4374, 0,65 grams). By keeping a constant acceleration on the mass the force to the transducer is kept constant.

Polarity: Positive for compression

Leakage Resistance: > 10^5 MΩ at room temperature

Capacitance: 9 pF (without cable)

Note: The preloading nuts are assembled with a force of approx. 1000 N measured as 3600 pC output from the 8203. If disassembled and reassembled the same force should be applied. (A mounting torque of 0,6 Nm may be used).

Date SEP 17 '03 Signature

Typical Temperature Sensitivty Error in % rel. to the Reference Value.

dB +40 +30 +20 +10 0 −10

Charge sensitivity

% +4 +2 0 −2 −4 −6

−50 −58 0 32 50 122 100 212 150°C 302°F

Physical:

Top
Preloading Nut
Transducer
Preloading Nut
Base

Weight: 3,2 grams
Material:
Titanium, ASTM Grade 2
and Stainless Steel, AISI 303
Mounting Thread: M3

Electrical Connector:
Coaxial M3

Environmental:
Humidity: Sealed
Temperature Range: −196° to + 150°C
(−321 to +302°F)
Typical Magn. Sensitivity: 0,1 N/T
Max. Shock Acceleration: 10 000 g* ≈ 100 000 m/s^2
Max. Vibration (peak): 1000 g* ≈ 10 000 ms^{-2}
Max. Base Bending Sensitivity
0,002 N/μstrain with preloading nuts

For further information see B&K "Piezoelectric Accelerometer and Preamplifier" Handbook.

* 1 g = 9,807 m/s^2 or 10 ms^{-2} = 1,02 g

Figure 56: Data-Sheet of the load cell used.

The load cell used in the tests carried out is the "*Force Transducer / Impact Hammer Type 8203* ", manufactured by the company **Bruel & Kjaer®**; it exhibits high sensitivity at low loads. The materials of which it is composed are titanium and steel and this is characterized by having a lower weight than other sensors available. The characteristic of low weight is essential, since the load cell is used during the test analysis Linear and non-linear (tests "*Burst-random*" and "*stepped sine*") being bonded to the surface of the panel, with the purpose of measuring the stress produced by the shaker actually transmitted to the lamina. In this situation, since the weight of the panel particularly low, if the cell had a significant mass, would surely change significantly the geometry of the panel itself, and consequently also its behaviour. Externally is presented as a cylinder to the bases of which there are screwed to some bolts preload with threaded holes, used in the housing of the grips for the exciter stinger. The mass of the cell is 3.2 g with the bolts preload configuration shaker and 1.6 g without, or in the hammer configuration. The diameter is 9 mm and the height of 15.8 mm with the two bolts, and 6.3 mm without. The sensitivity of reference is of 3.4 pC/N. The linearity error is always the order of 1% both in excess and in defect.



Figure57: The load cell, Force Transducer/Impact Hammer.



Figure 58: The Instrumented Impact Hammer

The Analogical/digital converter "Front-End" Scadas®

With conventional electrical equipment the signals are generated in the numeric (or digital) form: it is therefore necessary to convert them to analogical signals suitable drive the amplifier (DC / AC conversion). The reverse operation (AC / DC conversion) is instead required in order to acquire and elaborate data to a computer coming from the sensors. Being, then, the latter with all of the piezoelectric type, is necessary an amplifier of charge, that allows to transform the weak signals, provided by the transducers, into voltage signals. All these functions, used in the chain, are carried out by a unit said "*Front-End*", produced by the **DIFA Measuring Systems B.V.** (figure). The “Front-End” is an electronic system for acquiring data at high speed, programmable and supplied with a modular architecture: it comprises a base structure (mainframe) that can be customized by adding different modules, such as filters, amplifiers, bridge circuits and multiplexers (for input), and/or noise generators random and arbitrary waveforms (for output).

The "mainframe" of the model used includes:

- Micro-processor control "SCADAS® II Q";
- Six housings for input and output modules, plus one for the module generation ("QRAN" or "QDAC");
- A converter A/D 12-bit and 800 Hz;
- A counter programmable clock crystal and trigger circuits;
- A buffer (512 Kb of memory) to logic "First In-First Out" (FIFO);
- A socket for the power supply of the electric current.

This basic structure can also be equipped with a display and keyboard, but in the specific case, they are not necessary, since the whole is controlled by the software installed on the workstation HP® VISUALIZE 3000, through special files configuration and interface IEEE-488 and RS-232.
The input and output modules used are as follows:

- In the acquisition phase, the "**PDFA**" (Programmable Dual Filter Amplifier), i.e. a module for the processing of signals consisting of two couples amplifier-filter differential, mutually identical but independent, and independently programmable;

- For the generation of the signal, the "**QDAC**" (Quad Analogic Digital Converter) has been introduced. The module is a convert digital to analogic, which allows the generation of any signal programmed by the computer.



Figure 59: The Front-End system used.

The Laser Doppler Vibrometer Polytec

The *Laser Doppler Vibrometers* are measuring systems that do not require direct contact with the object of analysis and are used to make measurements velocity and displacement on mobile surfaces, such as sheets of materials metal. The non-contact optical measurement allows very high accuracy, it is, then, used in measurements with high complexity, where the sensors contact can not be employed for several reasons: in fact, the use of common accelerometers in contact may cause, in some cases, measurement errors due precisely to the mass of the sensors themselves, especially if the object of measurement is represented by plates having a very small thickness.

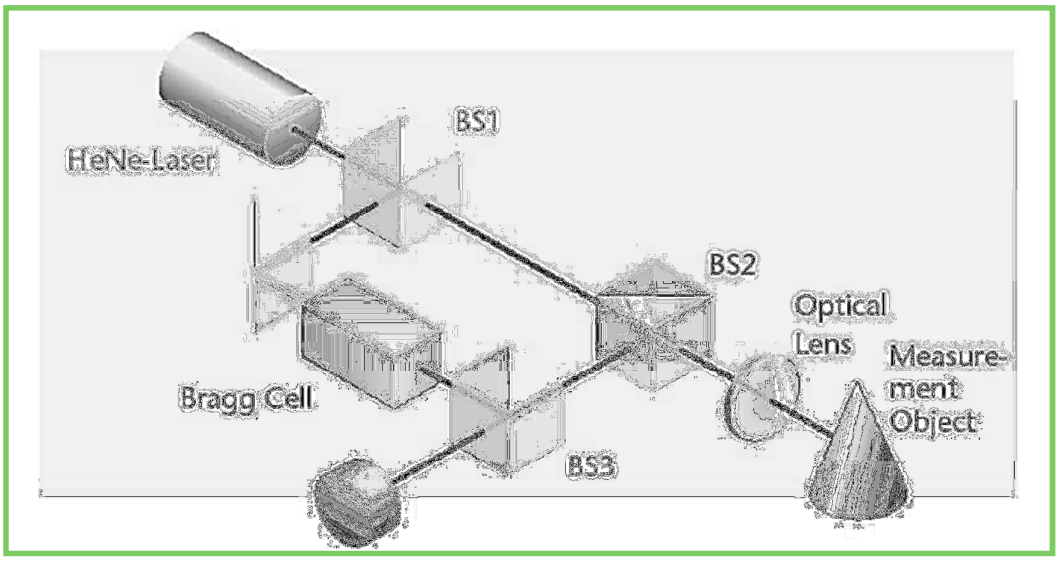


Figure 60: Vibrometer Laser Doppler 's operational process.

Figure (60) shows the technique of typical operation of the Vibrometer Laser Doppler: the HE-NE laser beam is divided in a "*beamsplitter*" (BS1) reference beam and in a measurement beam. After passing through a second "*beamsplitter*" (BS2), the radius of measure is focused on the object that reflects it. The reflected beam is then deflected downwards by BS2, to be, then, incorporated into the reference beam from the third "*beamsplitter*" (BS3) and be directed toward the detector. Since the path length of the reference beam is constant in time, a movement of the object under examination on the detector generates a model fringed light and dark typical interference. A complete cycle of light and dark on the detector corresponds to a movement of the object exactly equal to half the wavelength of the light used. Laser Vibrometer is, typically, constituted by two interferometric beams that detect the phase difference between an inner radius and the radius of the reference measure. The *heterodyne principle* applied in the Polytec® Vibrometer generates a carrier signal to FM (frequency modulation) to obtain also information on the direction of movement; a Laser Doppler Vibrometer is based on the principle of detecting the frequency variation due to *Doppler effect* of a coherent laser beam, which is scattered from a small area of the test object. The object scatters or reflects the light coming from the laser beam and the frequency shift due to Doppler effect is used to measure the component of the speed that lies along the axis of the laser beam. Since the laser beam has a very high frequency, it is very problematical to obtain a direct demodulation of the light, so an optical interferometer is used to mix coherently scattered light with a reference beam. The photo-detector measures the intensity of the mixed light, the frequency with which the laser beam hits the surface of the object is equal to the frequency difference between the reference beam and that measured. The apparatus used consists of two basic parts:

- *The head-sensor model OFV-505;*

- *The controller, model OFV-5000.*

The *controller OFV-5000* makes available in output both the speed and the displacement, depending on the decoder which is supplied. Various settings and options, the controller can cover a range of amplitudes up to a maximum speed of 10 m/s at a frequency of 20 MHz. The *sensor-head OFV-505* is distinguished by the excellent optical sensitivity and for making fire automatic motorized laser beam; also for facility of use every focus position can be stored to be possibly reused.



Figure 61: The controller OFV-5000 and the sensor-head OFV-505.

4.3 Computational Analysis of the System

Having discussed the mechanics of setting up a modal test, it is appropriate at this point to make some trial measurements and examine their trends before proceeding with data collection. Taking the time to investigate preliminaries of the test, such as exciter or response locations, various types of excitation functions and different signal processing parameters will lead to higher quality measurements. This section includes preliminary checks such as adequate signal levels, minimum leakage measurements and linearity and reciprocity checks. The concept and trends of the driving point measurement and the combinations of measurements that constitute a complete modal survey are discussed. After the structure has been supported and instrumented for the test, the *time domain signals* should be examined before making measurements. The input range settings on the analyser should be set at no more than two times the maximum signal level. Often called half-ranging, this takes advantage of the dynamic range of the analogical-to-digital converter without *under-ranging* or *over-ranging* the signals. The effect resulting from under ranging a signal, where the response input level is severely low relative to the analyser setting. Notice the apparent noise between the peaks in the frequency response and the resulting poor coherence function. It is also advisable to verify that the signals are indeed the type expected, (e.g., random noise): with a random signal, it is advisable to measure the histogram to verify that it is not contaminated with other signal components.

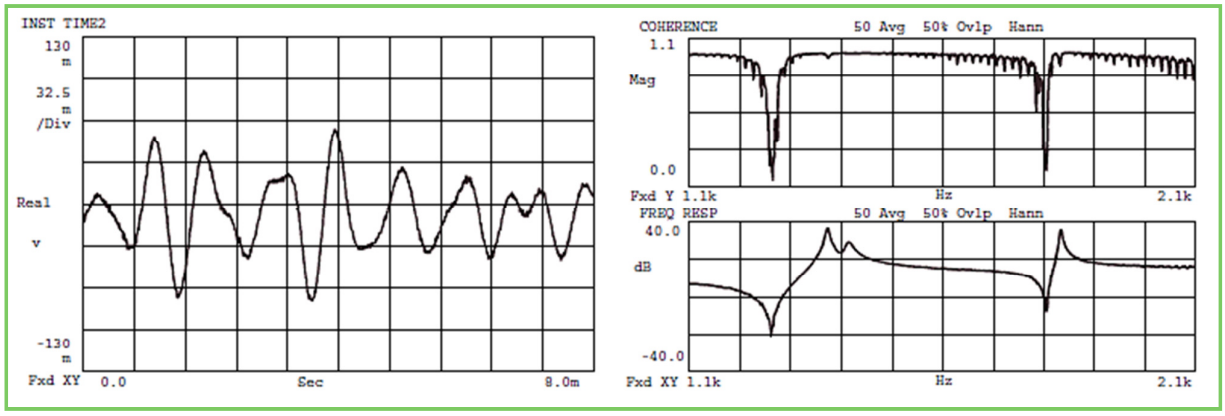


Figure 62: Example of an under-ranging.

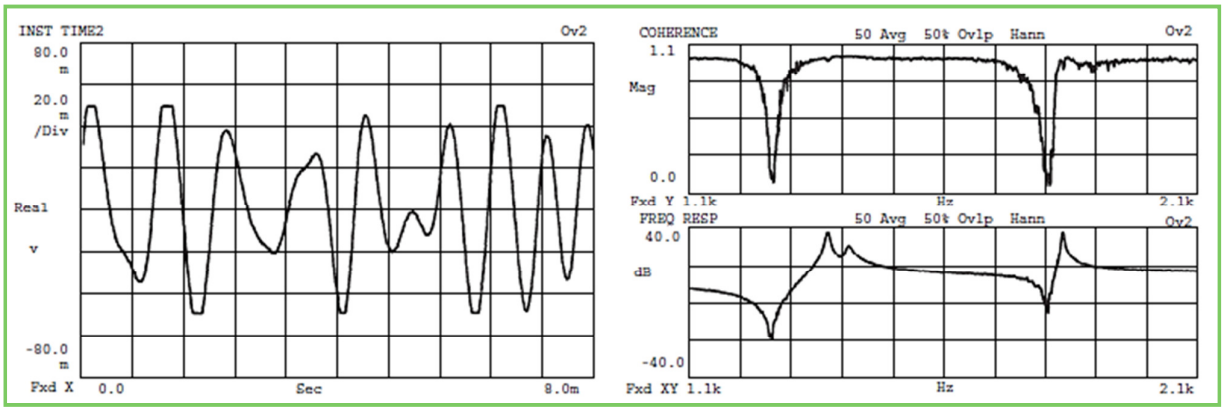


Figure 63: Example of an over-ranging.

When analysing a vibration signals, it is not sufficient to compute the Fourier transform (strictly, it does not exist for a random process), and instead estimates for spectral densities and correlation functions which are used to characterize this type of signal must be obtained. Although these properties are computed from the Fourier transform, there are additional considerations concerning their accuracy and statistical reliability which must be given due attention. Generally, it is necessary to perform an *averaging process*, involving several individual time records (samples) before a result which can be used with confidence is obtained. The two major considerations which determine the number of averages required are the statistical reliability and the removal of spurious random noise from the signals. In modal testing, linear averaging is used, either with or without overlap. In modal testing, linear averaging is used, either with or without overlap. When averaging without overlap is used, it means form samples each of duration T that the overall measurement time would be $m \times T$. Nowadays, analysers compute DFT in extremely short times, which enables to compute a new transformation prior to capturing a complete new data sample. In this case it is often better to perform a new transformation as soon as possible and use the last n data points, even if some of them could have already been used in the previous transform. This process is called *overlapping*. Another set of checks can be made in order to ensure that time is not wasted on what subsequently turn out to be bad data; the first is an inspection to satisfy the expected incidence of antiresonances occurring between adjacent resonances, as indicated in figure (64).

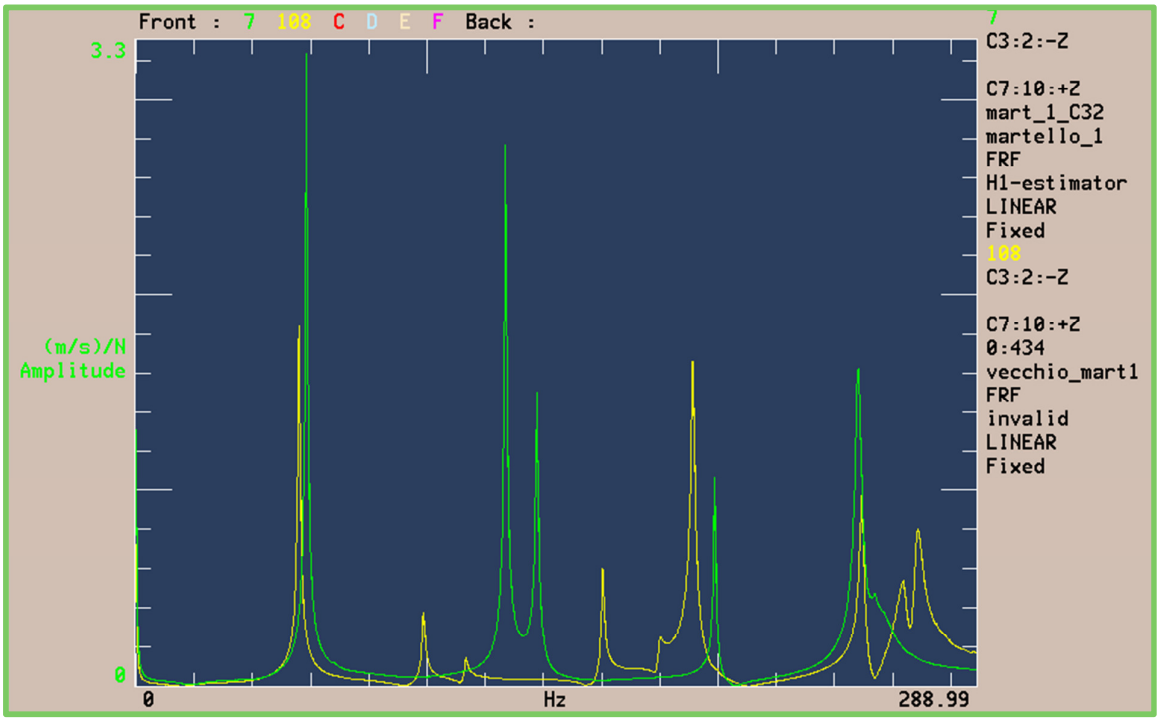


Figure 64: Picks of Resonance and Antiresonance of two FRF. The comparison is between the FRF referred to empty tank (green) and the FRF referred to the filling level of 6 [cm], (yellow).

For a point mobility, in this case the point (C_{32}), there must be an antiresonance after each resonance while for transfer mobilities between two points well-separated on the structure (the plate), it should presume more minima than resonance. A second check to be made at the same time, is that the resonance peaks and the antiresonance sharpness (on a log-log plot). Failure to do so many well reflect poor measurement quality, either because of a spectrum analyser frequency resolution limitation causing blunt resonances, or because of inadequate vibration levels resulting in modest definition of the antiresonance regions.

In the following chapter, it will proceed to the description in detail both modal analysis is carried out on the plate and the different steps performed in order to obtain a correct view of the results, especially the *Response model* (FRF) and their parameters or *Modal Model* (frequency, damping and modal shapes). A response model is simply the set of frequency response measurements acquired during the modal test. These measurements contain all the dynamics of the structure needed for subsequent analyses. A modal model is derived from the response model and is a function of the parameter estimation technique used. It not only includes frequencies, damping factors, and mode shapes, but also modal mass and modal stiffness. These masses and stiffnesses depend on the method that was used to scale the mode shapes. A subset of the modal model consisting of only the frequencies and unscaled mode shapes can be useful for some applications where frequencies and mode shapes are then primary concern. However, for applications involving analysis methods, such as structural modification and substructure coupling, a complete modal model is required. This definition of a complete modal model should not be confused with the concept of a truncated mode set in which all the modes are not included.

5. Experimental Modal Analysis of the Thin Plate

This chapter discusses vibration measurement and focuses in particular on the description of the technique associated with experimental ***Modal Analysis*** of the thin plate. The major reason for performing a vibration test is to determine natural frequencies of the plate, mode shapes, and damping ratio. Natural frequencies and mode shapes occur in all structures; basically, there are characteristics that depend on the weight and stiffness of my structure which determine where these natural frequencies and mode shapes will exist. For this reason, it is essential to identify these frequencies and know how they might affect the response of the thin plate when a force excites the structure. Understanding the mode shape and how the structure (the plate) will vibrate when excited helps, for example, the design engineer to design better structures. Now there is much more to it all but this is just a very simple explanation of *Modal Analysis*. For this purpose, some complete Modal Analysis have been carried out on the system by subjecting the plate to random excitation and measuring its response on a grid of select points, in case of empty tank and in presence of different filling levels of water. In this way, natural frequencies, damping ratio and modal shapes have been identified.

5.1 The Geometry Model

A *Model* will denote a geometrical model of the measured structure with defined points and degrees of freedom in which measurements are to be performed. This means no kind of mathematical model (spatial, modal or response). A *Mesh of Points* representing the measured structure is to be selected. In each of these points, it should be decided in which directions the measurements are to be performed, i.e. degrees of freedom are to be defined. Most often, only the transversal degrees of freedom are measured (i.e. directions X, Y and Z). In special cases, rotational degrees of freedom could be measured as well, but these require special transducer and procedures that are not common and are not supported by most of modal software packages. The density of the mesh of the measurement points highly depends on the frequency range of the measurements or, more precisely defined, on the number of modes that would be identified: it is important to consider that the higher the mode, the more nodal lines possess its mode shape and the more points are necessary to display it realistically. So, the rule for defining the density of the mesh (i.e. number of points) is: specify just enough points to be able to reliably identify all of the modes in the measured frequency range, but not too many points (or DOFs), because redundant points mean a more time-consuming modal test. It should be mentioned, that the density of mesh does not affect the precision of the obtained modal parameters. It only affects the quality of displaying mode shapes and thus the possibility to identify them correctly. It is a completely different situation from finite element calculations where the density of the mesh highly influences the precision of the solution. A mesh of points should be drawn on the measured structure (see figure 66) and the same model should be created in the modal test software. Also, so-called reference DOF is to be defined, this is the DOF, in which point direct FRF is measured, which means that the DOF of excitation and of response is the same. In the specific case, a modal test is performed using impact excitation, and the Vibrometer Laser is fixed in a reference point which remains the same for all experimental tests. The point selected as *"reference point"* is $\boldsymbol{C_{710}}$. There are two Requirements for the location of the reference point: It should be placed in a way that there is an adequate response by all of the modes so that the signal to noise ratio is as good as possible; the laser beam should be placed in a point of the grid not situated on the nodal lines, namely, those points called nodes that remain still for certain frequencies of excitation.

These requirements are related to the fact that one must be careful that the reference point would not also be a nodal point of one mode from those which are of interest. In this case, the response of this mode is zero and it would not be possible to identify it. One of the ways to avoid this situation is to approximately know the mode shapes in advance, e.g. from a computational model. Another option, if mode shapes are not known and can not be estimated, is to try different locations of the reference point before the entire modal test and watch if the number of resonances in the measured FRF is stable. If some of the resonances disappears at any point, it means that at this point is a nodal point of the particular mode shape and that this point can not serve as a reference.

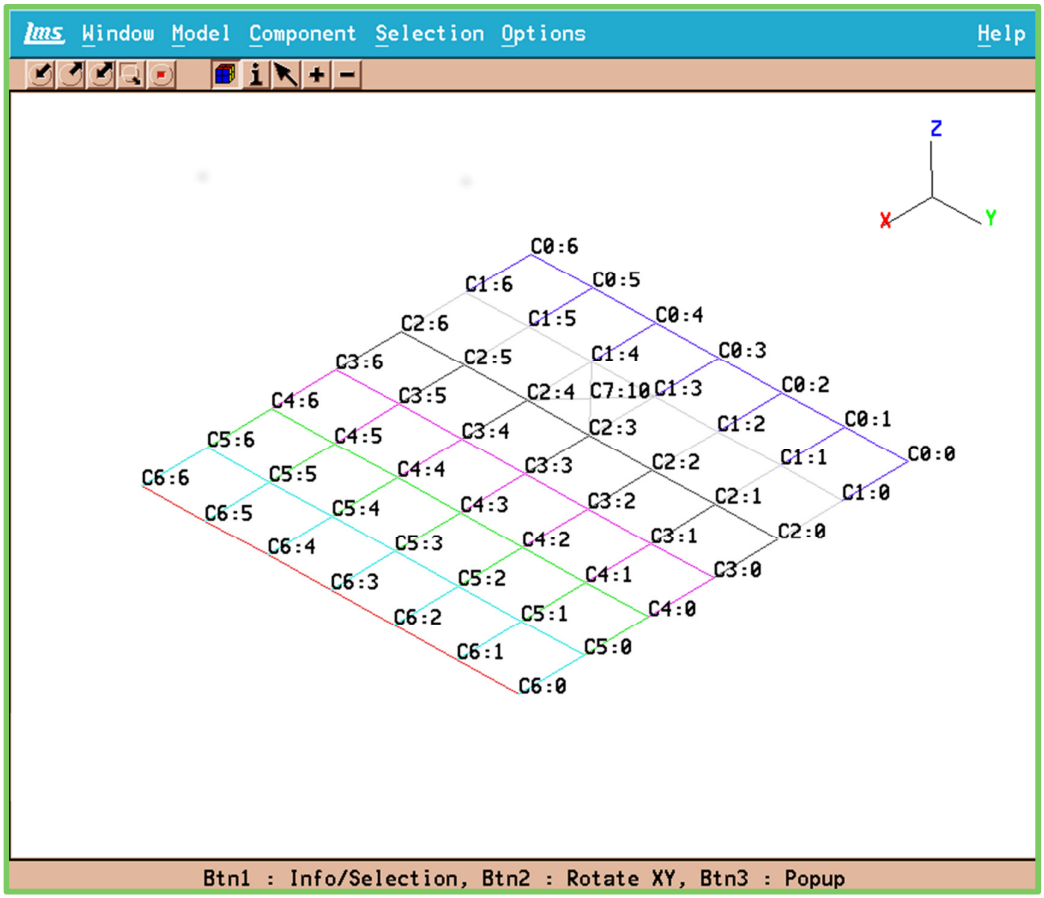


Figure 66: The geometry of the plate and the mesh grid created using CADA-X lms Software.

The CADA-X GEOMETRY module is an operational environment, schedule from the CADA-X main application manager. It is able to build a 2D representation of the plate under the test. This type of representation is called a ***Wire Frame Model***; it is comprised of nodes (defined by their position and orientation) and connections between the nodes. Nodes on the Wire Frame Model define the points where measurements will be taken on the structure. The entire Wire Frame is defined to relative to a global coordinate system: in this case, it is a Cartesian System and it is considered as an overall reference frame in which the structure is defined. Very important is also the Local Coordinate System which defines the reference frame for the nodal coordinate and the default orientation of the nodal coordinate system. *Nodes* are defined by their location and by a nodal coordinate system: for modal geometry of the plate, this coordinate system defines the measurement directions. The full identification of a node is given by the component name and the node name, although the location of a node in the 2D space is described by a set of two real numbers known as the coordinates. For visualize the entire geometry of the plate, it must connect all nodes in the grid by means of lines. A *connection* is a straight line connecting two nodes; the set of all connections present in the frame is referred to as its connectivity.

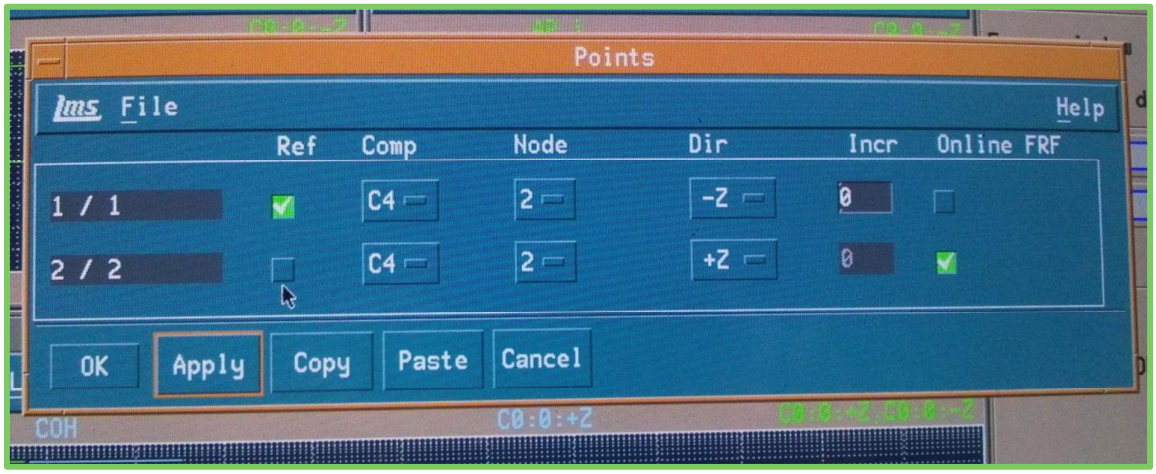


Figure 67: How create the geometry of the plate with "Geometry CADA-X Module".

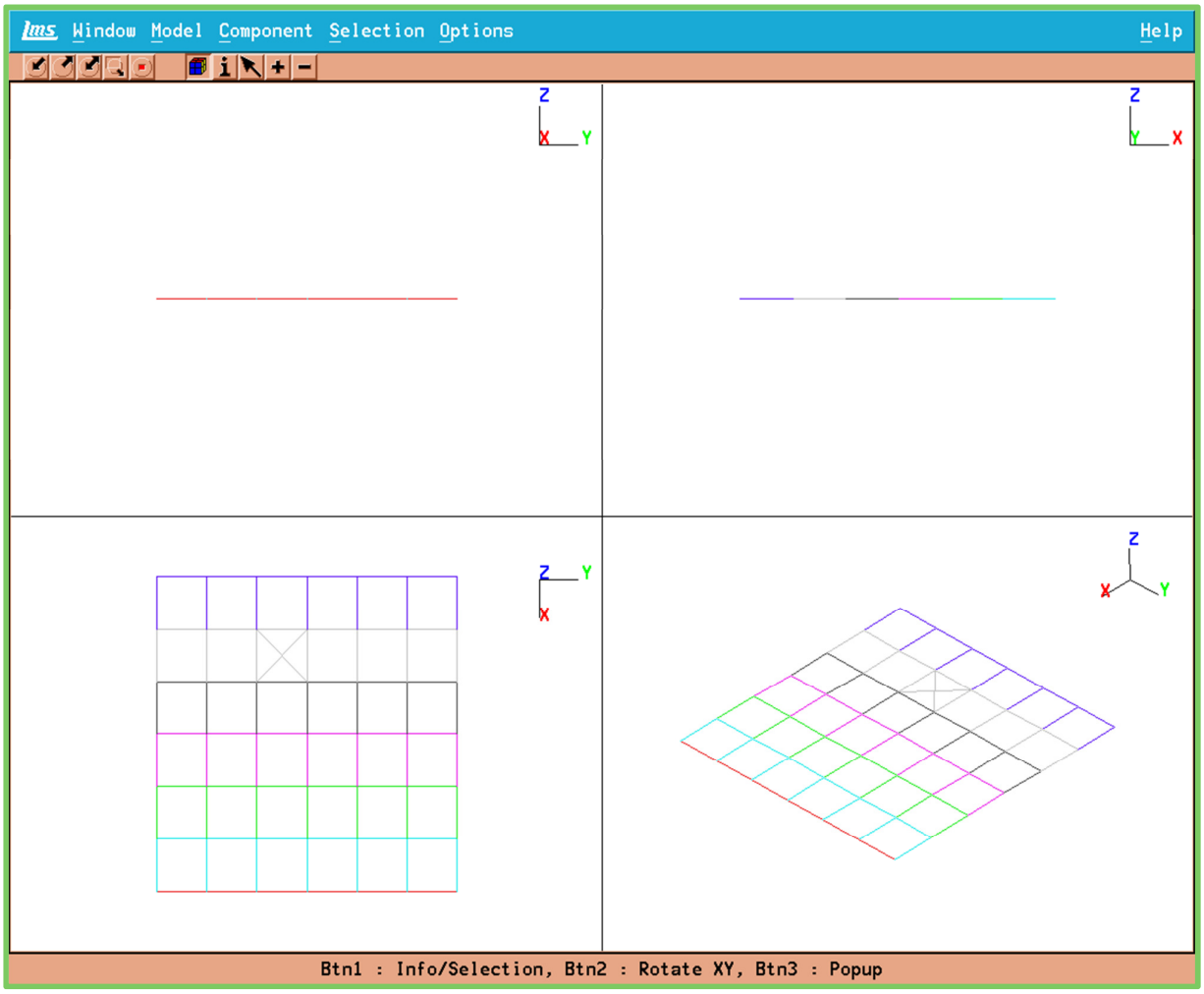


Figure 68: Different views for the geometry of the plate.

5.2 Measurement Technique

The measurement technique which is used for modal testing consists to estimate values of **frequency** and **damping** for several modes simultaneously, according to the basic relationship:

$$RESPONSE = PROPERTIES \times INPUT$$

This type of measurement, where both excitation and response are measured simultaneously, consents to use the basic equation to deduce the system properties directly from the measured data. Within this category there are a number of different approaches which can be used, but it should be started with a method referred as the ***Single-Degree-of-Freedom Curve Fit*** (**SDOF**). Using this method, either one row or one column of the frequency response function matrix is measured. The type of measurement implemented by the software CADA-X is called **Frequency Domain Direct Parameter Identification**.

Theoretical Background

Once the frequency response of a structure is calculated from equation $S_{Xf}(\omega) = H(j\omega) \cdot S_{ff}(\omega)$, the analyser is used to construct various vibration parameter information from the processed measurements. This is what is referred as *Experimental Modal Analysis.* The task of interest is to compute natural frequencies, damping ratios, and modal amplitudes associated with each resonant peak of the measured frequency response function. The easiest method applied to extract natural frequencies of the thin plate is the *Single-Degree-of-Freedom Curve Fit.* In this method the frequency response function for the compliance is sectioned off into frequency ranges bracketing each successive peak; each peak is then analysed by assuming that it is the frequency response of a single-degree-of-freedom system. In other words, in the frequency range around the first resonant peak, it is assumed that the plot is due to the response of a damped single-degree-of-freedom system due to harmonic input at, and near, the first natural frequency.

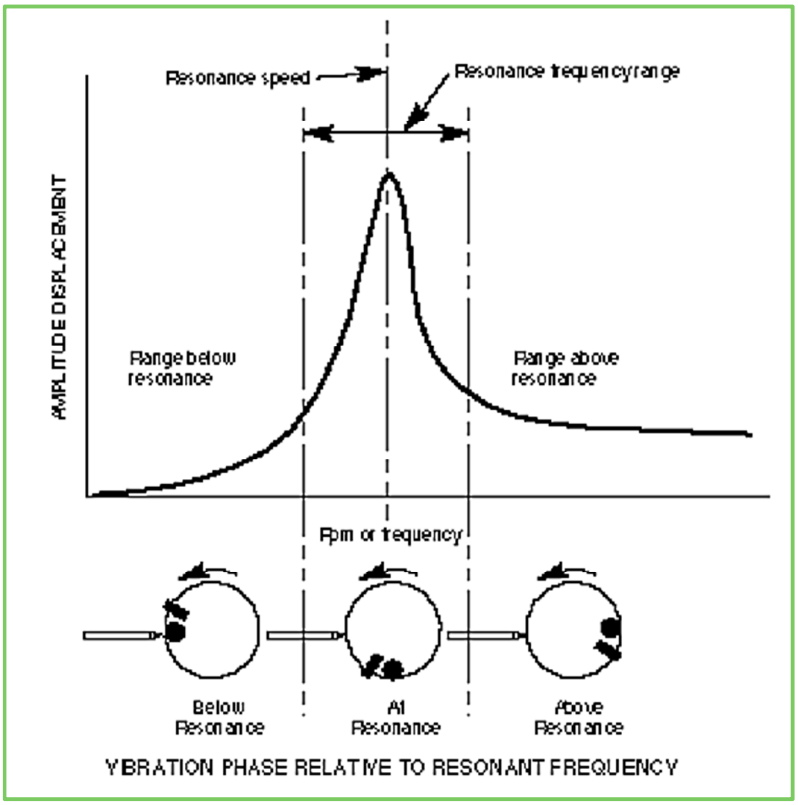


Figure 69: Vibration phase relative to resonant frequency.

Frequency Domain Direct Parameter Identification (**FDPI**) is a technique performed by the software CADA-X for allowing to estimate the natural frequencies, damping values and mode shapes of several modes simultaneously. The basis of **FDPI** method is the second order differential equation for mechanical structures:

$$M_y(t) + C_y(t) + K_y(t) = f(t) \qquad (1)$$

When transformed into the frequency domain, this equation can be reformulated in terms of measured FRF.

$$[-\omega^2 I + j\omega A_1 + A_0][H(\omega)] = j\omega B_1 + B_0 \quad (2)$$

where:

- $\omega = frequency\ variable$;
- $A_1 = M^{-1}C, mass\ modified\ damping\ matrix\ (N_0\ by\ N_0)$;
- $A_0 = M^{-1}K, mass\ modified\ stiffness\ matrix\ (N_0\ by\ N_0)$;
- $H(\omega) = matrix\ of\ FRF\ (N_0\ by\ N_i)$;
- $B_1, B_0\ are\ the\ force\ distribution\ matrices$.

Note that for the single input case, the $H(\omega)$ matrix becomes a column vector of frequency dependent FRF.
Equation (2) is valid for every discrete frequency value ω. When these equations are assembled for all available FRF, including multiple input and multiple output test cases, the unknown matrix coefficients A_0, A_1, B_0 and B_1 can be estimated from the measurement data $H(\omega)$. From the identified matrix, the system's poles and mode shape can be estimated via an eigenvalue and eigenvector decomposition of the system matrix.

$$\begin{bmatrix} -A_1 & -A_0 \\ \mathrm{I} & 0 \end{bmatrix} \quad (3)$$

This will yield the diagonal matrix $[\Lambda]$ of the poles and a matrix Ψ of eigenvectors.

5.3 Impact Excitation using Impact Hammer

Using an impact hammer is the simplest and fastest way of exciting a structure into vibration. It requires no preparation work and thus is very suitable to use in operational conditions. The hammer consists of a head, force transducer, tip and handle. An impactor can also be used: it is basically a hammer without a handle (see figure 70). The equipment of a hammer is usually completed with a set of tips of different stiffness and with a set of heads of different masses; for exciting the plate has been used a steel tip and a force transducer, the laser, to detect the magnitude of the force felt by the impactor which is assumed to be equal and opposite to that experienced by the plate. A selection of steel tip along with an extender mass allows the hammer to be tailored to impart to the test structure a desired spectrum of frequencies. The hammer incorporates a quartz measuring cell with low impedance electronics. The cell's voltage mode operation, guarantees a stable signal transmission insensitive to ambient influences. The magnitude of the impact is basically determined by the mass of the hammer head and the velocity with which it is moving when it hits the structure. It is more easy to control the velocity rather than the force level itself, and so an appropriate way of adjusting the order of the force level is by varying the mass of the hammer head. The frequency range which is effectively excited by this type of device is controlled by the stiffness of the contacted surfaces and the mass of the hammer head: there is a system resonance at a frequency given by $\sqrt{contact\ stiffness/impact\ factor}$ above which it is difficult to deliver energy into the test structure. When the hammer tip impacts the test structure, this will experience a force pulse which is substantially that of a half-sine shape, as shown in figure (), left: a pulse of this type has a frequency content of the form illustrated in figure (70), right which is essentially flat up to a certain frequency (f_C) and then it is of uncertain strength above this frequency. This means that it is relatively ineffective at exciting vibrations in the frequency range above fc and so it is necessary to have some control over this parameter. It can be shown that there is a direct relationship between the first cut-off frequency f_C, and the duration of the pulse, T_C, and that in order to raise the frequency range it is necessary to induce a shorter pulse length. This, in turn, is related to the stiffness (not the hardness) of the contacting surfaces and the mass of the impactor head.

The stiffer the materials, the shorter will be the duration of the pulse and the higher will be the frequency range covered by the impact. Similarly, the lighter the impactor mass, the higher the effective frequency range. It is for this purpose that a set of different hammer tips and heads are used to enable the regulation of the frequency range.

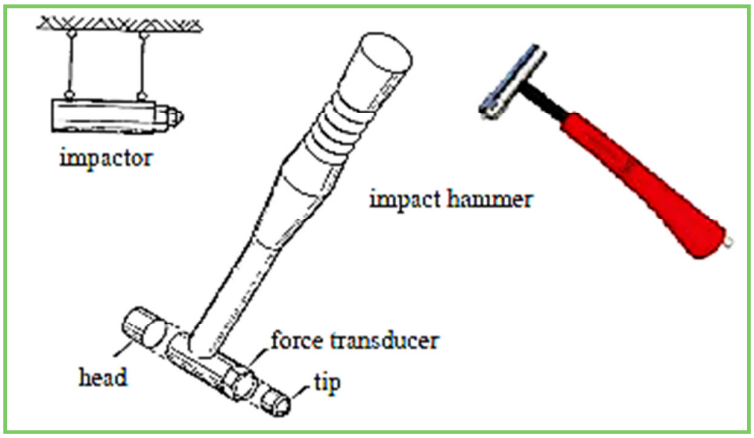


Figure 70: Illustration of Impact Hammer.

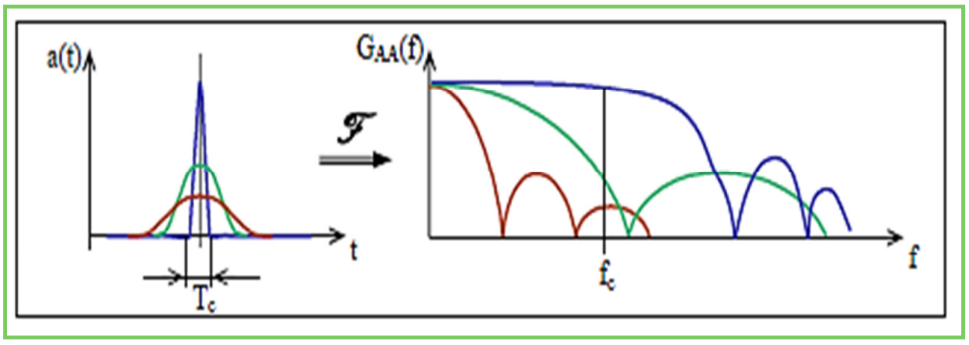


Figure 71: Impact Force Pulse and its Spectrum.

Impact hammer excitation has required to use different weighting functions for input and output signals. The input signal is weighted with *transient window* that serves for suppressing noise to zero in the time period when the impact force is not acting but the measurement of response is in progress. In order to be sure that the shift and length of the transient window are set correctly, it is worth to expand the vertical axis so that level of noise is visible. For the output signal (*response*), exponential window is often used to improve the analysis by minimizing *leakage error* that is caused by truncating the time signal. The length of the exponential window (its time constant τ) should be set with regard to the requirement that the signal at its end should be attenuated to the level of noise or at least by 40 dB. The windows for both signals should started at the same time if there is no system delay. The use of impact hammer for executing Modal Analysis has involved some disadvantages associated during experimental test: the control of the frequency range of excitation were limited and, moreover, it was rarely possible to use frequency zoom, crest factor were very high and due to a high peak level of the acting force there was a possibility of causing a local damage to the plate and exciting its nonlinear behaviour.

5.4 Impulse Response Function (IRF)

An *Impulse Response* of a system is an output signal when the Dirac impulse (unit impulse, delta function) is applied at the input. It is an inverse Fourier transform of the frequency response function, and this is the procedure used to calculated it in an **FFT** analyser:

$$h(t) = \mathcal{F}^{-1}[H(f)] \tag{1}$$

An impulse response of an SDOF system is one-sided damped sinusoid given by the formula:

$$h(t) = 2 \cdot |R| e^{-\delta t} \sin(\Omega t) \tag{2}$$

Summing all the $\boldsymbol{n}$ modes, more general formula is obtained:

$$h_{ij}(t) = \sum_{k=1}^{n} 2 \cdot \left|R_{ijk}\right| e^{-\delta_k t} \sin(\Omega_K t) \tag{3}$$

The average decay constant of this summarized impulse response can be used to estimate average damping properties of the system. If the magnitude of IRF is displayed in logarithmic scale, the envelope of the function is a line, and its slope indicates damping of the system. Come out of the definition of logarithmic decrement **V**:

$$\mathrm{V} = ln \frac{x(t)}{x(t+T)} = \delta T \tag{4}$$

Magnitude decreases **e**-times in the time $\boldsymbol{\tau}$ (t is so-called *time system constant*):

$$lne = \delta\tau, \;\; 1 = \delta\tau \quad \Rightarrow \delta = 1/\tau \tag{5}$$

The input signal (excitation hammer) is, then, digitised by an A-D converter and recorded as a set of n discrete value, evenly spaced in the period T during which the measurement is made. A Finite Fourier Series is computed as an estimate to the required Fourier Transform. There is a basic relationship between the length T, the number of discrete values n, the sampling rate ω_s and the range and resolution of the frequency spectrum ($\omega_{max}, \Delta\omega$). The range of the spectrum is 0-ω_{max} and the resolution of lines in the spectrum is $\Delta\omega$, where:

$$\omega_{max} = \omega_s/2 = 1/2\,(2\pi n/T) \tag{6}$$

$$\Delta\omega = \omega_s/n = (2\pi n/T) \tag{7}$$

As that size of the transform n, is generally fixed for a given analyser and is usually, though not always, a power of 2, i.e. 502, 1024 etc. the frequency range is, in this way, covered and the resolution is determined solely by the time length of each sample. The fundamental equation, that is solved for determination of spectral content is derived from the equation (8).

$$\{x_k\} = [C]\{a_n\} \quad \Rightarrow \quad \{a_n\} = [C]^{-1}\{x_k\} \tag{8}$$

$$\begin{bmatrix} x_1 \\ x_2 \\ x_3 \\ \vdots \\ x_n \end{bmatrix} = \begin{bmatrix} 0.5 & \cos(2\pi/T) & \cdots \\ 0.5 & \cos(4\pi/T & \cdots \\ 0.5 & \cos(6\pi/T) & \cdots \\ 0.5 & \vdots & \cdots \\ 0.5 & \cos(2N/T) & \cdots \end{bmatrix} \cdot \begin{bmatrix} a_0 \\ a_1 \\ b_1 \\ \vdots \\ \vdots \end{bmatrix} \tag{9}$$

Digital Fourier analysis has many features which, if not properly treated, can lead to erroneous results. Generally speaking, they result from discretization and from the need to reduce the length of time signal. In the following sections, specific features of *aliasing*, *leakage*, *weighting windows* and *averaging* will be discussed.

Aliasing

There is a problem called "aliasing", which is associated with a digital spectral analysis and results from discretisation of the originally continuous time signal. If the sampling frequency in relation to the frequency content of the signal is too small, the presence of high frequencies in the original signal could be misinterpreted in the discretisation process. Figure (72) shows that digitising a low frequency signal (above) produces exactly the same set of discrete values as a result from the same process applied to a higher frequency signal (below).

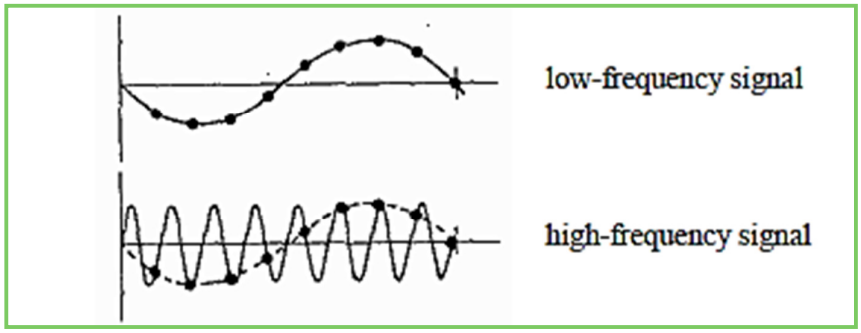


Figure 72: Aliasing - High Frequency Manifested as Low Frequency.

If the sampling frequency is $\boldsymbol{f_s}$, then the signal of frequency f and signal of frequency $(\boldsymbol{f_s} - \boldsymbol{f})$ are indistinguishable after discretization, and this causes distortion of the measured spectra using DFT, although the calculation is performed accurately. In the description of the DFT, it was stated that the highest frequency that can be included in the spectrum (transform) is $\boldsymbol{f_s}/2$, and the spectrum should stop at this frequency, regardless of the number of discrete values. The signal, which has the actual frequency content displayed in figure (73), appears in DFT as a distorted form. Distortion towards the upper end of the applicable frequency range can be explained by the fact that the portion of the signal which has frequency components above $\boldsymbol{f_s}/2$ will be reflected in the range $0 - \boldsymbol{f_s}/2$. These high frequency components then put on the appearance of being low frequency ones and create an indistinguishable mixture with the real low frequency components. The solution to the problem is to use an anti-aliasing filter which subjects the original time signal to a low-pass, sharp cut-off filter: this results in submitting a modified time history to the analyser. Because the filters used are inevitably less than perfect and have a finite cut-off rate, it remains necessary to reject the spectral measurements in a frequency range approaching, $\boldsymbol{f_s}/2$. Typically, the range from $0.8 \cdot \boldsymbol{f_s}/2$ to $\boldsymbol{f_s}/2$ is rejected. It is for this reason that a 2048-point transform does not result in a complete 1024-line spectrum being given on the analyser display. Typically, only the first 800 lines will be shown because the higher ones are liable to be contaminated by imperfect anti-aliasing.

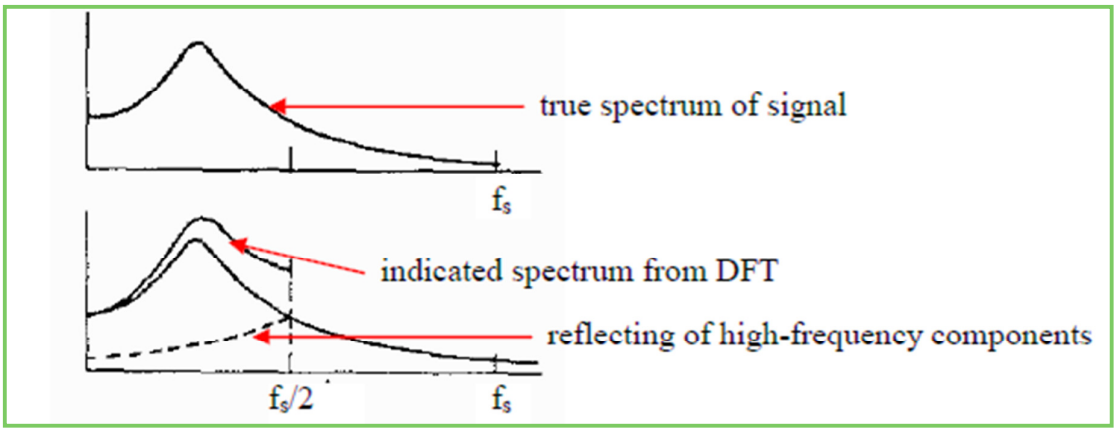


Figure 73: Alias Distortion of Spectrum by DFT.

Leakage

Leakage is a problem which is a direct consequence of the need to take only a finite length of time history coupled with the assumption of periodicity. The problem is best illustrated by the two examples shown in figure (74), where two sinusoidal signals of slightly different frequencies are subjected to the same analysis process. On the left side, the signal is perfectly periodic in the time window T, and the resulting spectrum is simply a single line at the frequency of the sine wave. On the right side, the periodicity assumption is not satisfied and there is a discontinuity at the end of the sample. As a result, the spectrum does not indicate the single frequency which the original time signal possessed, and this frequency is not even prevailing in the spectral lines. The energy has *"leaked"* into a number of spectral lines close to the true frequency and the spectrum is spread over several lines. The two examples represent the best case and the worst case. The problem is more serious for low frequency signals. Leakage is a serious problem in many application of digital signal processing, including FRF measurements. There are several ways of avoiding or at least minimizing its effects:

- Changing the duration of the measurement sample length to match any underlying periodicity in the signal, e.g. by changing measurement time **T** so that to capture an exact number of cycles of the signal. Although such a solution can remove the leakage effect altogether, it can only do so if the signal being analyzed is periodic, which is not always the case, and if the period of that signal can be determined and it could be the first objective of the analysis. Moreover, measurement time **T** can not be changed fully arbitrary in FFT analysers, but only by some steps according to frequency range of measurement;

- Modifying the signal sample obtained in such a way as to reduce the severity of the leakage effect. This process is referred to as *windowing* or *window transformation* and is widely employed in signal processing and modal testing. Windowing involves the imposition of a prescribed profile w(t) on the time signal prior to performing Fourier transform. The analyzed signal is then product of original signal and window profile (see figure 74).

The influence of often used *Hanning window* to Fourier transform of a signal is shown in figure (74). Measurement time can be extended by increasing the number of frequency lines of Fourier transform when using FFT analyser. In this way, the frequency resolution increases without changing the frequency range of the measurement. When using an analyser with a fixed number of frequency lines, there is another way how to improve frequency resolution to reduce the frequency range of the measurement. When measurements are done in baseband (from 0 to f_{max}), it means to limit the frequency range from above.

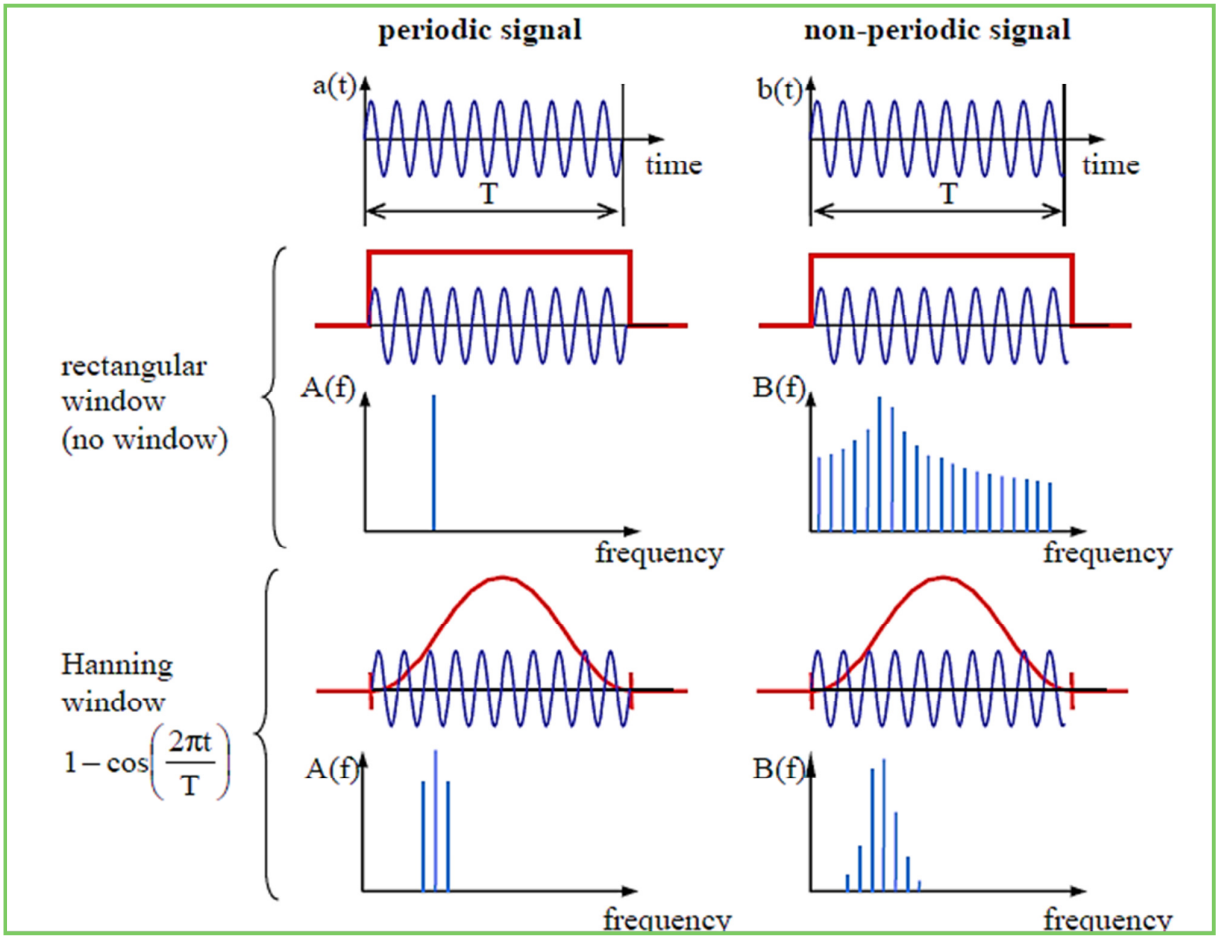


Figure 74: Influence of Weighting Windows and Periodicity of the Signal on Leakage Error.

Averaging

Another feature of a digital spectral analysis that concerns particular requirements for processing random signals. When analysing random vibration signals, it is not sufficient to compute the Fourier transform (strictly, it does not exist for a random process), and instead estimates for spectral densities and correlation functions which are used to characterize this type of signal must be obtained. Although these properties are computed from the Fourier transform, there are additional considerations concerning their accuracy and statistical reliability which must be given due attention. Generally, it is necessary to perform an *averaging process*, involving several individual time records (samples) before a result which can be used with confidence is obtained. The two major considerations which determine the number of averages required are the statistical reliability and the removal of spurious random noise from the signals. In modal testing of the thin plate, *linear averaging* is used, without *overlap*. Using an averaging without overlap is used, it means for $\boldsymbol{m}$ samples each of duration **T** that the overall measurement time would be $\boldsymbol{m} \times \boldsymbol{T}$ (see figure below). When linear averaging is implemented with overlap, analysers compute DFT in extremely short times, which enables to compute a new transformation prior to capturing a complete new data sample. In this case it is often better to perform a new transformation as soon as possible and use the last N data points, even if some of them could have already been used in the previous transform.

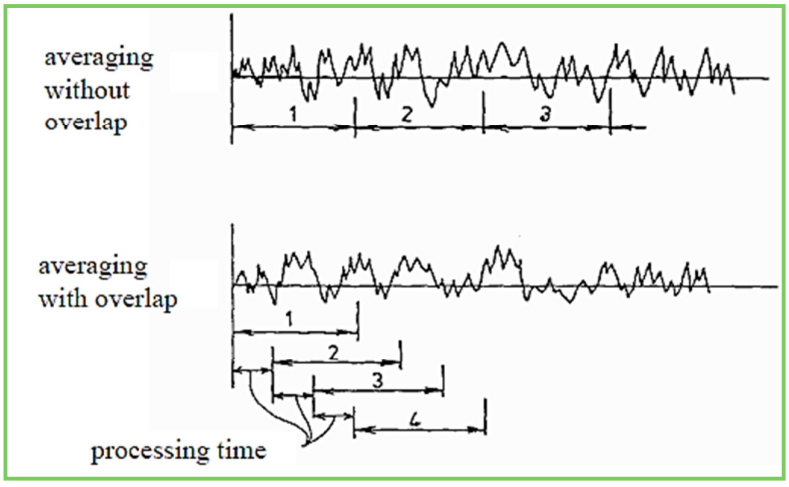


Figure 75: Types of Averaging.

5.5 Derivation of Mathematical Models

After the tested plate is prepared (supported) and the geometrical model is created, the measurement can start. Remember that, when a hammer excitation is used, the laser is usually placed in the reference point C_{710} and the plate is excited successively in all the points, thus producing one row of the FRF matrix (see figure 76). Prior to starting with the entire modal test, some checks have been performed in order to be sure that the measured data will be correct. With hammer excitation, it is simple to perform the reciprocity check. Theoretically, if a structure is excited in DOF ***i*** and the response is captured in DOF ***j***, it should be the same as the reciprocal situation (excitation in DOF ***j*** and response in DOF ***i***). In both case, an identical FRF should be obtained: $H_{ij}(f) = H_{ji}(f)$. The most important check that should never be omitted is that of checking the accuracy of reference point measurement for every experimental modal tests.

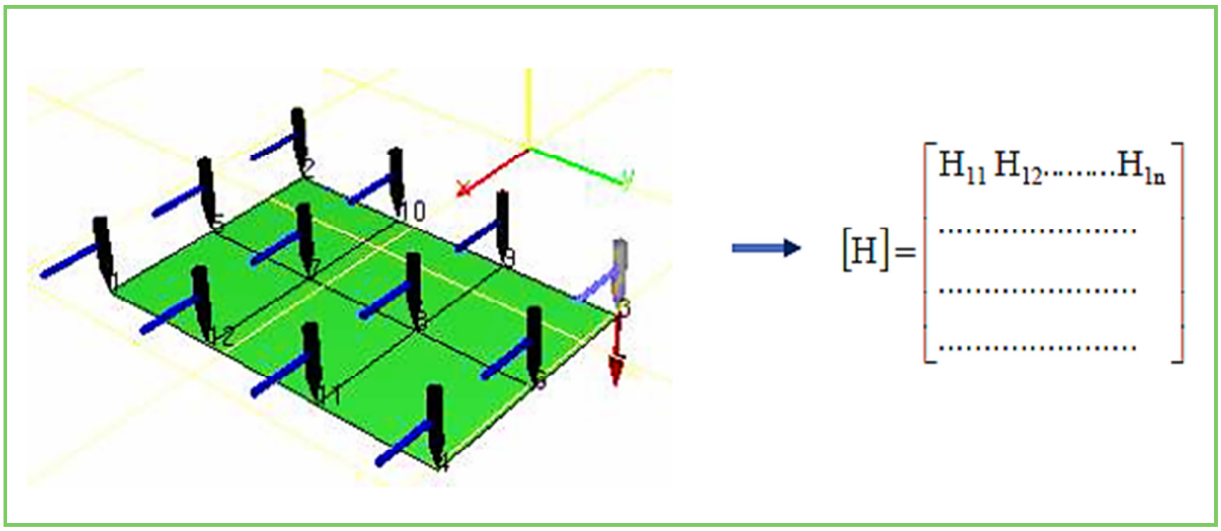


Figure 76: Preparation of Measurements - Hammer Excitation.



Figure 77: Experimental set-up system. The laser beam must be perpendicular to the plate's surface: the reference point is highlight with a circle.

This response type of model in the form of FRF matrix, such as the mobility matrix, also need only include information concerning a limited number of points of interest: the modal analysis of the plate has been carried out using 25 points and in order to perform the tests, the model required to be valid over a specified frequency range. In this range, it was necessary that all modes were included. The reference point $\boldsymbol{C_{710}}$ was selected with the principal purpose to ensure that all measurements were correct, not only in this specific point but also in all other points. The features that the reference point had presented to motivate its choice are the followings: an antiresonance behind each resonance in an FRF plot when displayed in *dB*, in a phase FRF plot, the phase only varies in the range of 180°, coherence function has the value as close to 1 as possible and in the plot of real part of mobility, all the peaks are of the same signs. Usually, even for good quality measurements, coherence in antiresonances is far below 1 as a result of the fact that the level of the signal is at these frequencies comparable to the noise level. On the contrary, near resonances the coherence function use to be close to 1 even for measurements of lower quality. After acquiring all the data by performing measurements at all the DOFs, thus obtaining either one row or one column of the FRF matrix, modal analysis software is to be used to post-process this data. This part of modal test is called *experimental modal analysis* as this is the stage of the experimental approach corresponding to the stages called modal analysis also in theoretical approach. In both cases, modal analysis leads to identification of modal properties of the system. However, it should be noticed that these two processes are somehow different: experimental approach deals with curve-fitting theoretical expressions to the actual measured data, while theoretical analysis deals with the eigenvalue problem. The fundamental problem of parameters estimation consists of adjusting (estimating) the parameters in the model, so that the data predicted by model approximate (or *curve-fit*) the measured data as closely as possible. The aim of *Modal Parameters Estimation* is to define a model in terms of modal parameters: the starting point is usually a set of measured data, most commonly frequency response function (FRSs), or the time domain equivalent impulse response (IRs). Modal parameters of the modes of the plate estimated are: *natural frequencies*, *damping factors* or *ratios*, *mode shapes*, *poles* and *residues*.

5.6 Modal Models of the Plate

The ***Frequency Domain Direct Parameters Identification (FDPI)*** is the technique used to estimate the natural frequencies, damping values and mode shapes of the plate for several modes simultaneously as discussed in paragraph 5.2. Another method has been implemented by means of the software CADA-X: the ***Least Squares Complex Exponential*** that allows to evaluate all the data. To understand how the method works, recall the expression for an impulse response (IR) given below:

$$h_{ij}(t) = \sum_{k=1}^{N} \left(r_{ijk} e^{\lambda_k t} + r_{ijk}{}^{*}\ e^{\lambda_k^{*} t} \right) \qquad (1)$$

It can be seen from this expression that the pole values λ_k are not a function of a particular response (output) or reference (input); in other words, the pole values are global (rather than local) characteristics of the plate. Equation (1) expresses the data as a linear superposition of a set of 2N damped complex exponentials occurring in complex conjugate pairs. Such complex exponentials can be viewed as the characteristics solutions of a linear differential equation with constant real coefficients.

$$h_{ijn} + a_1 h_{ijn-1} + \cdots + a_{2N} h_{ijn-2N} = 0 \qquad (2)$$

To estimate the coefficients in equation (2), for all possible time points and all possible response must be solved simultaneously: this equation system will be greatly overdetermined and the final solution is calculated from a compact equation with a square coefficient matrix. To determine the optimal number of modes of the plate which have been obtained from models with various number of modes, a computational estimation and comparison has been required. A diagram that shows the evolution of frequency and damping as the number of modes is increased is called *Stabilization Diagram.*

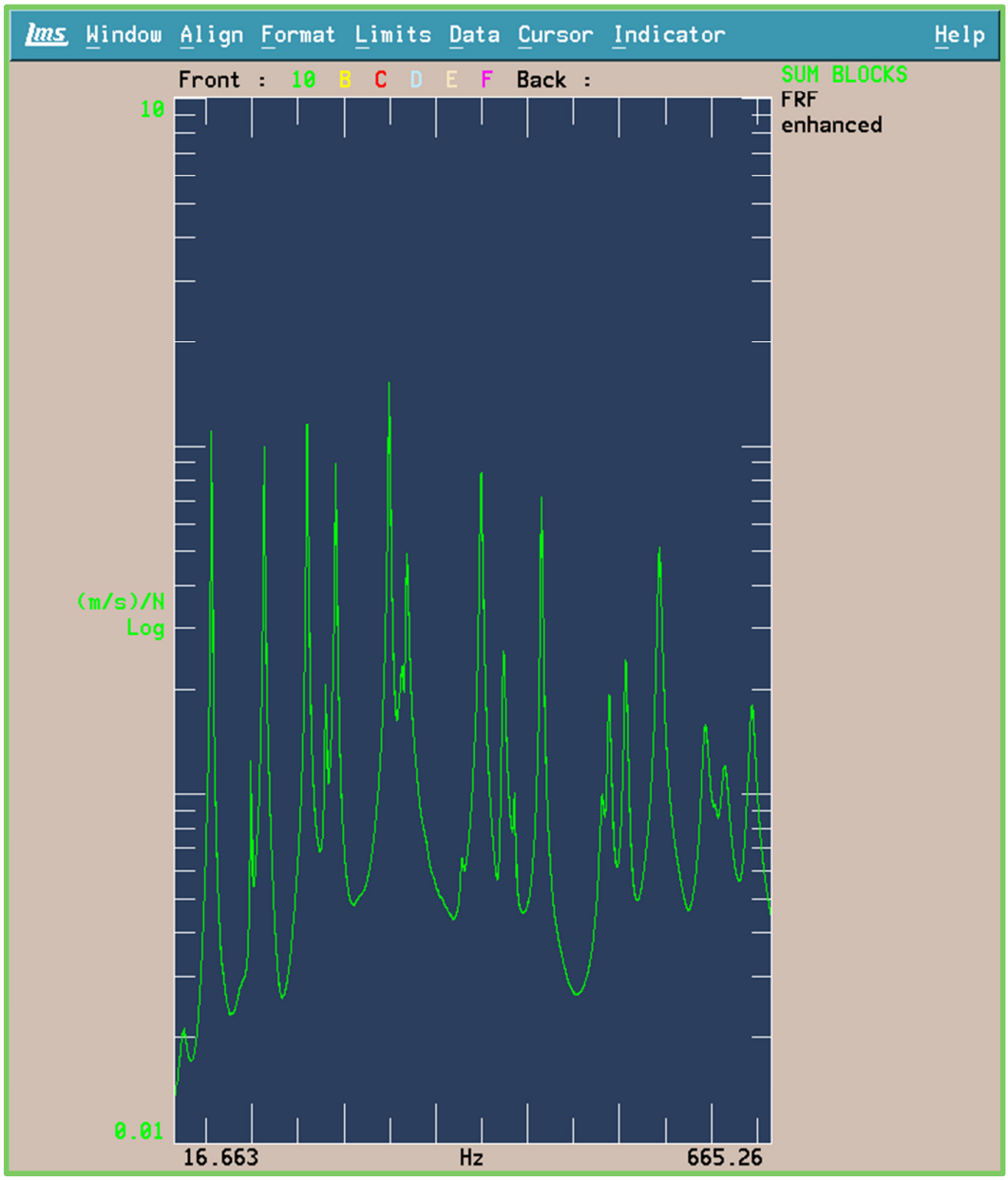


Figure 78: "Synthesis" of the all excitation responses of the plate not in contact with liquid.

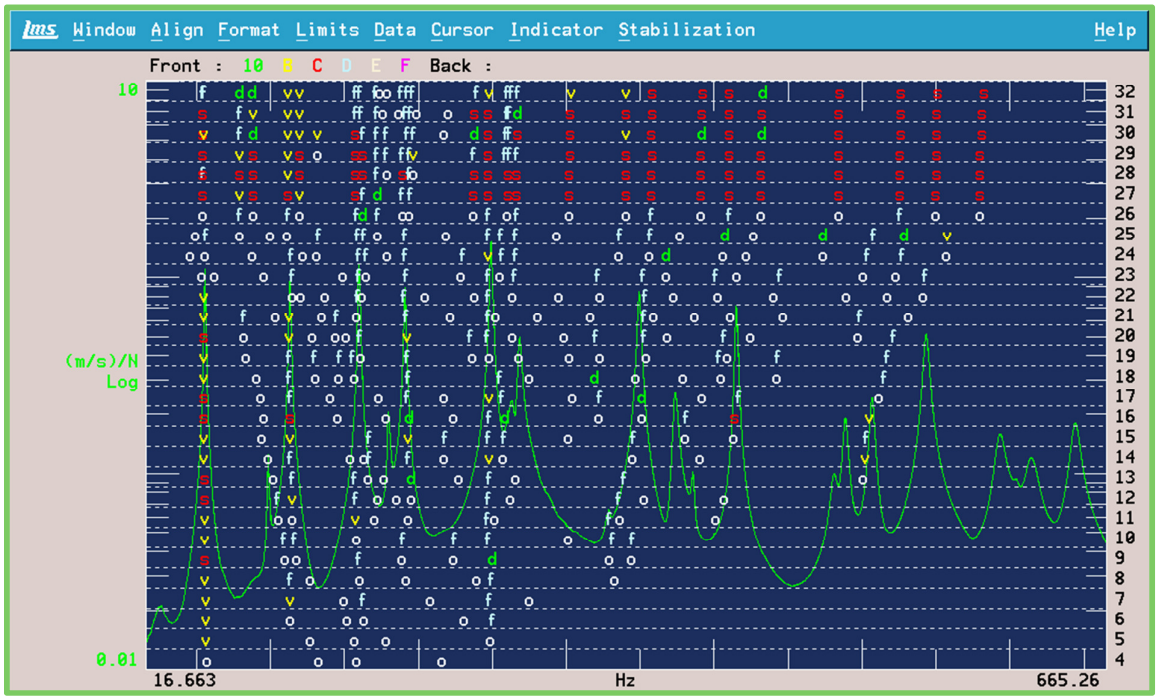


Figure 79: The Stabilization Diagram and the Poles referred to each picks of Resonance.

Stabilization Diagram is a device for selecting and, then, visualizing modal shapes for modal analysis realized. The figure (79) below, represents the graphical display which appears on the monitor screen, after that the software has post-processed the input data. In particular, there is a mobility plot (FRFs) for every point (25 points) belonging to the mesh grid. The software, by the use of a computational algorithm, extracts a mobility plot which represents the sum or the "*synthesis*" of the all excitation responses obtained from the response to excitation impact of every single point. This process is able to combine the various individual results obtained thus far; in other words, the software fits several FRF curves simultaneously, taking due account of the fact that the properties of all the individual curves are related by being from the same structure (the plate). Concluding the section, it is necessary to underline that the resulting function and, consequently, the resulting plot have the frequency and damping characteristics of the plate : individual FRFs are now very complicated combinations of the mode shape elements which depend heavily upon which FRFs have been used for the summation. Nevertheless , the composite function can provide a useful means of determining a single (average) value from the natural frequency and damping factor for each mode where the individual functions would indicate slightly different values.

6. Modal Shapes and Parameters Extraction

This study is focused on the hydrostatic vibration analysis of a rectangular plate in contact with a bounded liquid, with different filling levels in bottom and vertical directions. A set of admissible trial functions is required to satisfy the clamped and simply supported geometric boundary conditions. Applying the methods explained in Chapter 5, the frequency response function on all points and the correspondent coherence have been calculated by the CADA-X lms software. The five Modal Analysis have been realized in the following order: empty tank, liquid filling level equal to 6, 12, 18 and 23 [cm].

The case of Empty Tank

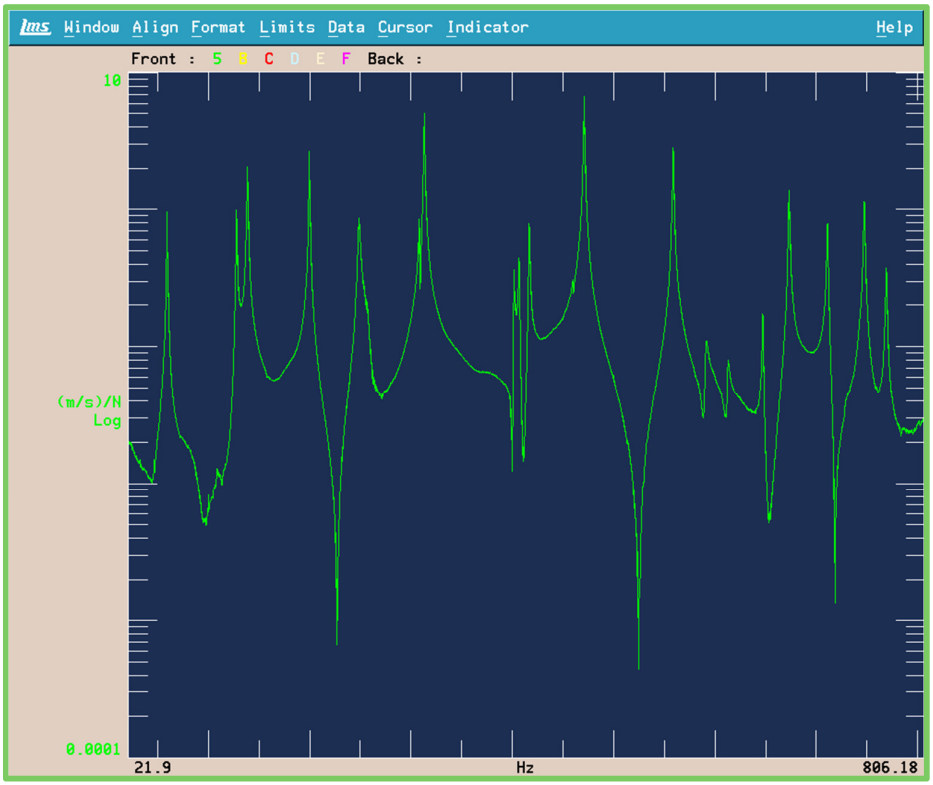


Figure 80: Example of a Log-Log Plot for the Dynamic Response of the Plate related to a specific locations of the Driving Point measurement, C_{11}.

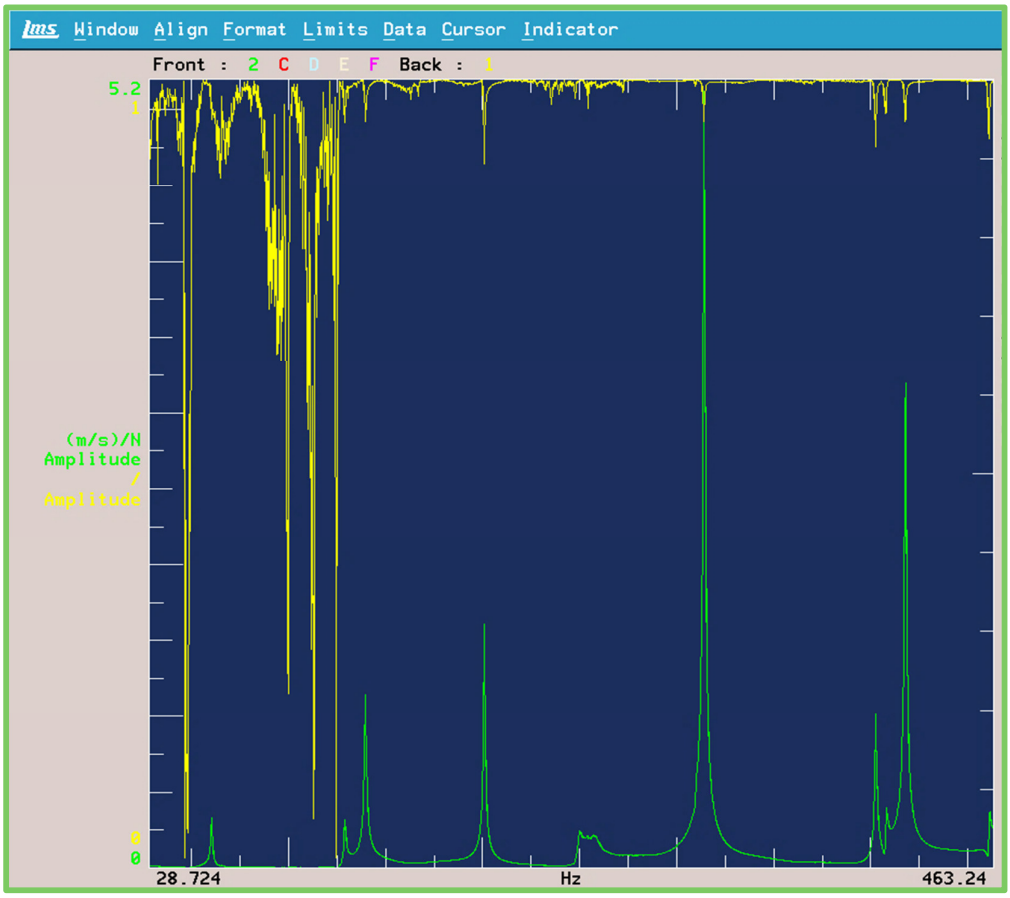


Figure 81: Frequency Response Function and Coherence for the point C_{11} *(case of empty tank).*

As can be seen from Figure (81), the resonance peaks are well spaced from one another and from the coherence is good in correspondence to the resonance peaks and it falls suddenly in correspondence to the antiresonances. The value of coherence is approximately equal to 1, then it can be said that the measure was carried out correctly. The subsequent images have the intent to show the mode shapes of the plate, when the latter is not in contact with the liquid. the only constraint that influences the values of the frequencies presented in the table refers to the constraint of jamming and the torque value chosen for the tightening of the bolts: in fact, if you were to change this value, the frequency values obtained would be different. The mode shapes presented, refer to the modes of vibrating more recognizable in which it is easy to understand the number of half-waves for each Cartesian axis, that is, for the x-axis and the y-axis.

Frequency [Hz]	Damping [%]	Modal Shape
60,49	0,30%	1-1
127,21	0,29%	1-2
136,55	0,23%	2-1
199,16	0,18%	2-2
248,20	0,66%	Diagonal nodal lines
255,32	1,70%	Circular and central nodal line
307,74	0,08%	2-3
312,74	0,15%	3-2
400,55	0,07%	3-3
406,58	0,19%	1-3
416,34	0,14%	2-4
467,60	0,05%	4-2
557,99	0,11%	4-4
564,87	0,08%	4-2
590,47	0,28%	5-1
612,52	0,16%	1-5
646,90	0,07%	2-5
672,35	0,09%	5-5
710,33	0,09%	4-4
746,94	0,08%	5-3
768,45	0,09%	3-5
893,05	0,08%	6-2

Table 8: Frequency, Damping and Modal Shapes for the Plate: In this case, the structure is extremely Undamped.

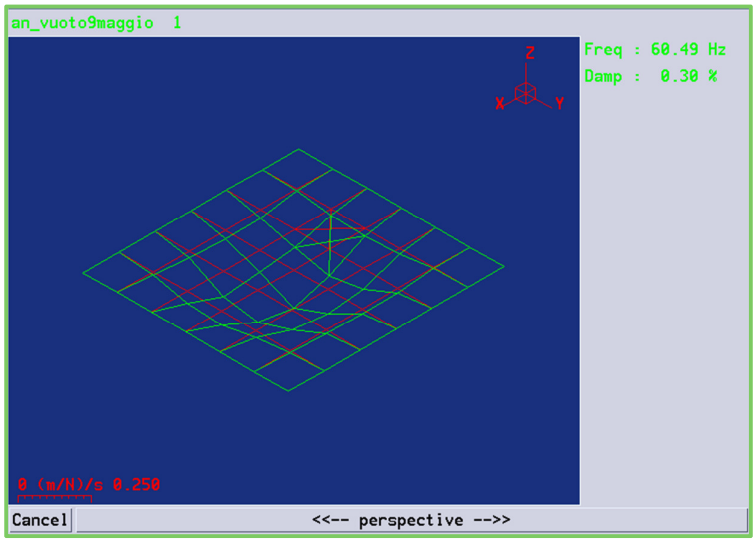


Figure 82: Mode (1-1), frequency 60,49 [Hz].

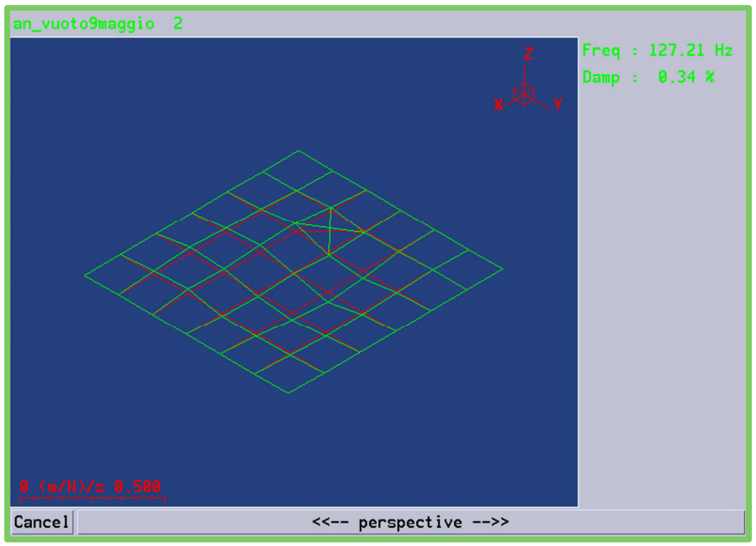


Figure 82: Mode (1-2), frequency 127,21[Hz].

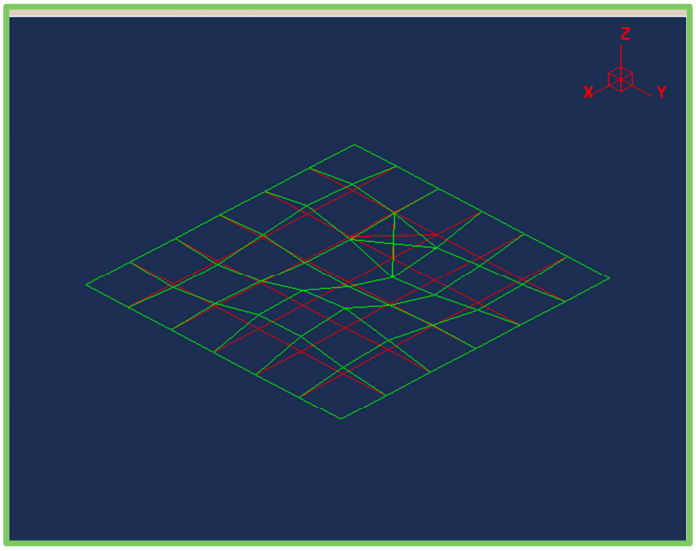


Figure 83: Mode (2-1), frequency 136,55[Hz].

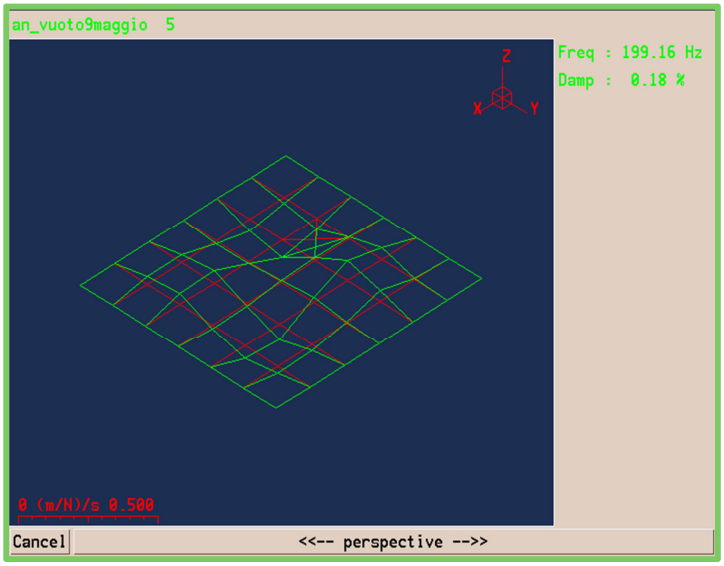


Figure 84: Mode (2-2), frequency 199,16[Hz].

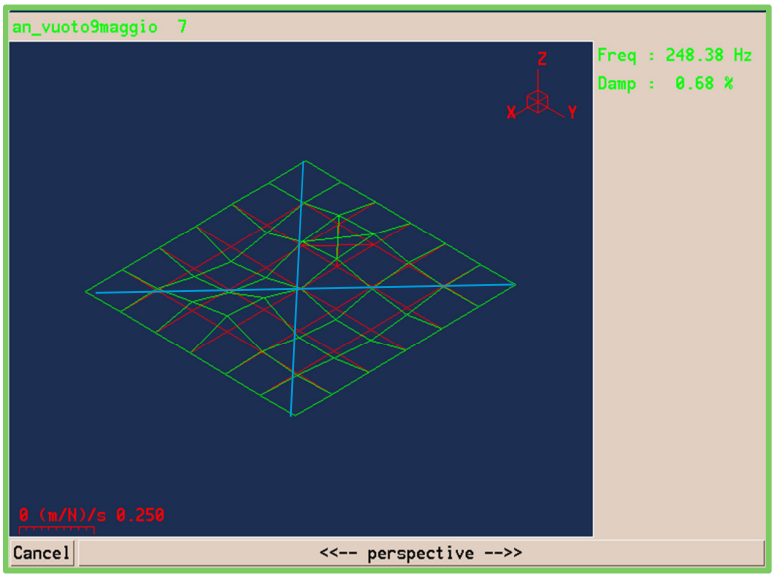


Figure 85: Mode with diagonal nodal lines, frequency 248,38[Hz].

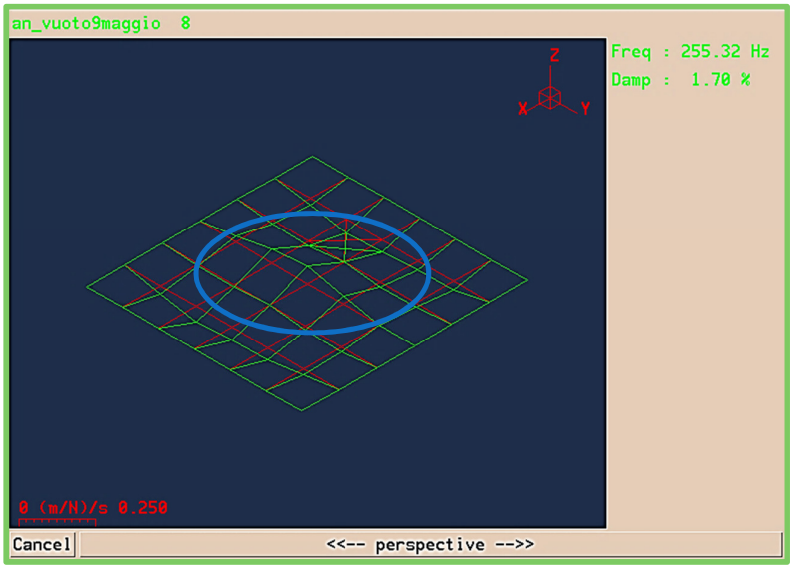


Figure 86: Mode with central and circular nodal line, frequency 255,32[Hz].

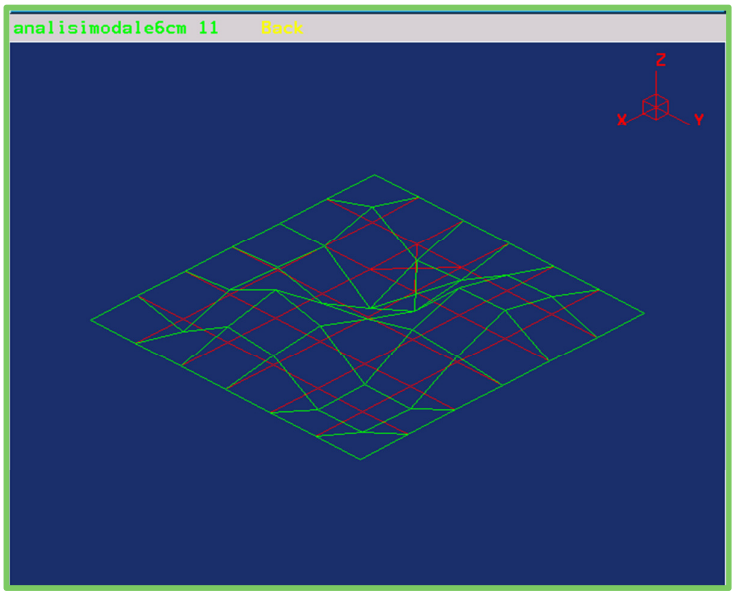


Figure 90: mode (2-3), frequency 307,74[Hz].

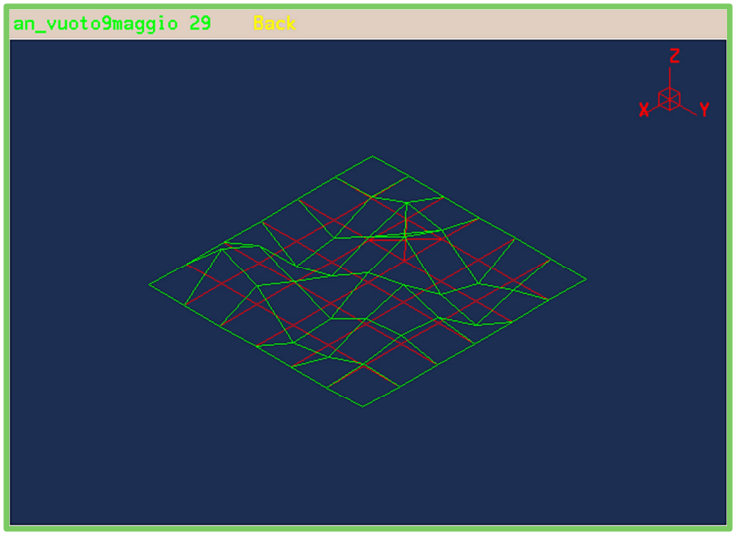


Figure 91: mode (3-2), frequency 312,74[Hz].

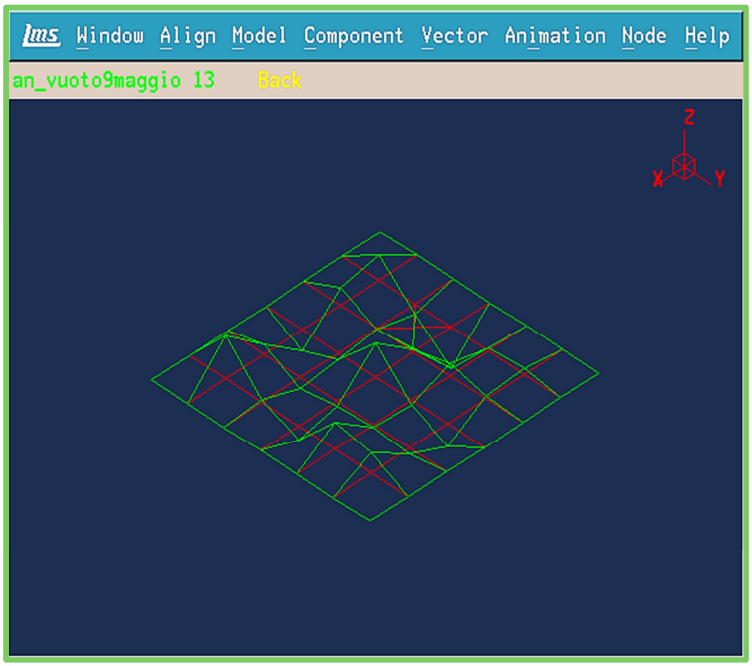


Figure 92: mode (3-3), frequency 400,55[Hz].

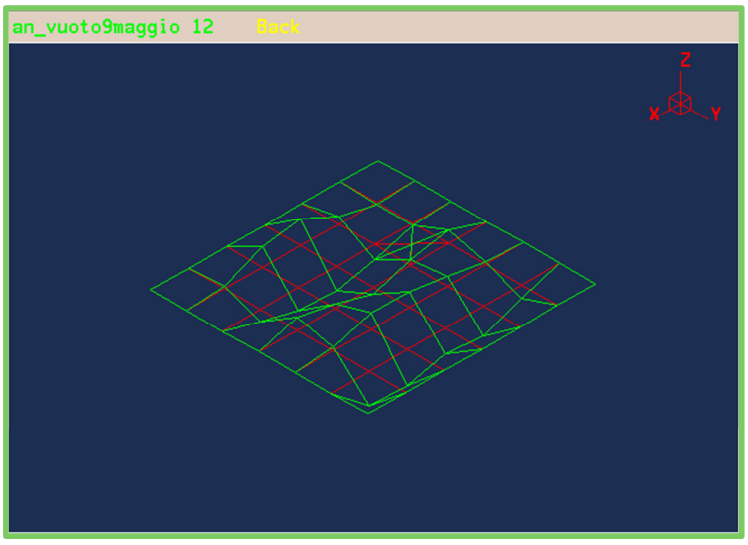


Figure 91: mode (1-3), frequency 406,58[Hz].

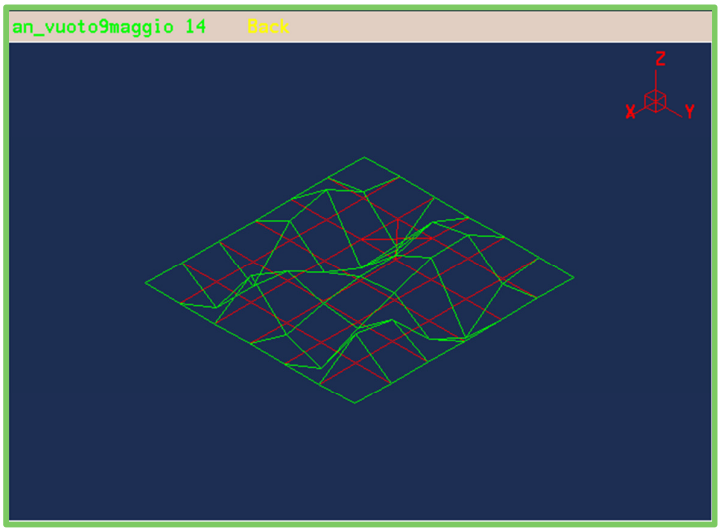


Figure 91: mode (2-4), frequency 416,34[Hz].

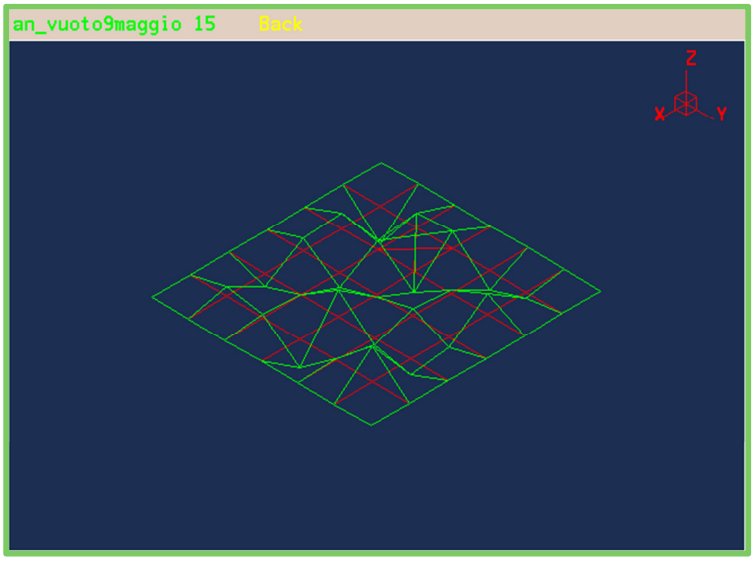


Figure 93: mode (4-2), frequency 467,60[Hz].

Just the same as the accuracy of the reference point measurement was checked before the modal test proceeded to all the other measurements, it is now appropriate to review, at least briefly, the accuracy of the obtained modal model, prior to comparing it with another model, mostly with a computational model obtained by finite element calculations. mostly with a computational model obtained by finite element calculations. If a structure whose modes are well separated is measured (and moreover, if it is measured freely supported), probably no problems with modal parameters identification occur and the obtained modal model will be most likely correct. When a more complex structure with coupled modes and with a large amount of (*non-proportional*) damping is measured, the process of modal parameters extraction will be more complicated. In order to extract mode shapes for the rectangular plate, the software packages used for modal analysis is enable to display mode shapes either static or animated. In this specific case, the mode shapes has to be presented in the printed form, it is only possible to use static pictures: the imagines, above displayed, show the undeformed plate in red and the mode shape in green colour. *Complexity* of the mode shapes could be examined: it means to investigate to which extent the displacements in the mode shapes are complex numbers. Generally, it can be said that the less complex the mode shape is, the more probably it is correct. This assumption is applied especially for lightly damped structures as, for example, the thin plate measured: in fact, For the plate complex mode shape may not occur. A complex mode shape is easily identified in animation by its waving movement. This visual effect originates from the fact that the displacements in the individual points do not reach their utmost positions simultaneously. Consequently, nodal lines change their positions. Thus, complex mode shapes cannot be displayed using static pictures, it is only possible to display them in animation. A poor attempt to display them statically can be done by so called *normalization-displacements* are transformed to the real numbers by assigning zero to phase angles of those displacements that have phase angles more close to zero (thus obtaining positive amplitude) and by assigning 180° to phase angles of those displacements that have phase angles more close to 180° (thus obtaining negative amplitude). Comparison of dynamic properties of the experimental and theoretical models can be performed for all the three types of dynamic models (spatial, modal and response) with the aim to compare dynamic behaviour of the structure derived from computations and those that is really observed in practise.

This process is called *verification* (*updating*) of the theoretical model, and it is used very often when two or more mode shapes look similar, it again might be an approximation error. It might happen when the software identifies false modes from the reason described above (more modes are required in the frequency bands than really exist). In this case, it is worth to examine the ***MAC matrix*** (***Modal Assurance Criterion***) which provides the measure of distances of point from the ideal line in the least square sense. It is defined as:

$$\boldsymbol{MAC(A,X)} = \frac{\left|\sum_{j=1}^{n}(\Phi_X)_j(\Phi_A)_j^*\right|^2}{\left(\sum_{j=1}^{n}(\Phi_X)_j(\Phi_X)_j\right)\left(\sum_{j=1}^{n}(\Phi_A)_j(\Phi_A)_j^*\right)} \qquad (1)$$

In practice, a typical data would be less ideal than these and what is expected is that if the involved experimental and theoretical mode shapes would really belong to the same mode, then the MAC value would be close to 1, whilst if they would belong to different modes, the MAC value would be close to zero. If a set of mx experimental modes and a set of mA theoretical modes are taken into account, a MAC matrix $\boldsymbol{m_X} \times \boldsymbol{m_A}$ can be computed and displayed in a matrix that would clearly indicate which experimental mode matches to which theoretical mode. It is difficult to give exact values that should the MAC values be to ensure good results. Generally, the values greater than $\mathbf{0.9}$ should be obtained for the same modes and values less than $\mathbf{0.05}$ for the different modes. It can be used also for a single model only. In this case, all values on the main diagonal will be equal to $\mathbf{1}$ and all the other values should be numbers close to zero. If a number close to 1 appears out of the main diagonal, it most likely indicates a false mode. This applies for modes whose frequency are quite close. The expression (1) below suppose that mode shapes data may be complex. The experimental (measured) mode shape is denoted as $\{\Phi_X\}$ and the theoretical (computed, analytical) mode shape is denoted as $\{\Phi_A\}$. These concepts are in fact useful for all types of comparisons, not only experiment vs. theory, but they can be used to compare any pair of mode shape estimates.

There are two other criteria which deal with the quantity called ***Modal Scale Factor*** (***MSF***): it represents the slope of the best line fitted to the points. This quantity is defined as (two forms are possible according to which of the mode shapes is taken as reference). They are defined as:

$$\boldsymbol{MSF(X,A)} = \frac{\sum_{j=1}^{n}(\Phi_X)_j(\Phi_A)_j^*}{\left(\sum_{j=1}^{n}(\Phi_A)_j(\Phi_A)_j^*\right)} \tag{2}$$

$$\boldsymbol{MSF(A,X)} = \frac{\sum_{j=1}^{n}(\Phi_X)_j(\Phi_A)_j^*}{\left(\sum_{j=1}^{n}(\Phi_X)_j^*(\Phi_X)_j^*\right)} \tag{3}$$

It should be noted that these criteria provide no indication concerning the quality of fitting the line to the points, but only its slope.

lms File View Select Help

Modal Assurance Criterion (%) for modes

No	mode no	freq Hz	mode_1 60.49	mode_2 127.21	mode_3 127.18	mode_4 199.16	mode_5 248.20	mode_6 248.38	mode_7 255.32	mode_8 307.74	mode_9 406.58	mode_10 416.34	mode_11 467.60	mode_12 557.99	mode_13 564.87
1	1	60.49	100.0												
2	2	127.21	0.5	100.0											
3	3	127.18	0.5	100.0	100.0										
4	4	199.16	0.2	0.1	0.1	100.0									
5	5	248.20	0.6	0.2	0.2	0.0	100.0								
6	6	248.38	0.6	0.1	0.1	0.0	98.8	100.0							
7	7	255.32	0.1	0.0	0.0	0.1	13.3	14.0	100.0						
8	8	307.74	0.3	3.3	3.3	1.0	1.3	1.3	0.9	100.0					
9	9	406.58	0.3	1.3	1.2	0.1	3.6	3.5	0.7	0.0	100.0				
10	10	416.34	0.0	0.9	0.9	0.2	2.8	2.7	1.3	1.5	0.9	100.0			
11	11	467.60	0.1	0.1	0.1	4.1	0.1	0.2	0.3	0.2	0.6	0.5	100.0		
12	12	557.99	0.2	0.2	0.2	0.5	0.3	0.3	1.3	0.5	0.4	1.8	0.6	100.0	
13	13	564.87	0.1	0.0	0.0	0.9	0.0	0.1	0.3	2.4	0.5	0.1	1.2	3.0	100.0
14	14	590.47	0.0	0.0	0.0	0.0	0.8	0.8	0.7	1.0	0.0	0.3	0.2	0.0	0.0
15	15	612.52	0.2	0.7	0.6	0.3	0.5	0.6	0.1	0.9	1.8	0.0	0.5	0.3	0.0
16	16	646.90	0.0	0.2	0.2	0.1	0.0	0.0	0.0	1.3	0.0	0.1	1.0	0.1	1.1
17	17	672.35	0.0	0.5	0.5	0.0	0.2	0.5	0.0	0.1	0.3	2.0	0.0	0.2	0.3
18	18	710.33	0.3	0.1	0.1	0.0	0.0	0.0	0.1	0.0	0.9	0.2	0.2	0.0	4.9
19	19	746.94	0.1	0.0	0.0	0.2	0.1	0.1	0.0	0.4	0.0	0.3	0.2	0.0	0.1
20	20	768.45	0.0	0.1	0.1	0.2	0.2	0.2	0.4	0.3	0.0	3.3	0.0	0.4	0.3
21	21	814.10	0.1	0.0	0.0	0.0	0.0	0.0	0.3	0.3	1.9	2.5	0.5	1.5	0.3
22	22	856.83	0.0	0.5	0.5	0.2	0.1	0.1	0.5	0.5	48.5	3.0	0.7	0.1	0.4
23	23	893.05	0.0	0.1	0.1	0.2	0.1	0.1	0.0	0.1	0.0	0.1	0.1	1.0	0.0
24	24	136.57	0.1	0.3	0.3	0.0	0.0	0.0	0.2	3.4	2.7	1.5	0.3	0.4	0.0
25	25	136.55	0.1	0.3	0.3	0.0	0.0	0.0	0.2	3.4	2.7	1.5	0.3	0.4	0.0
26	26	312.74	0.7	0.1	0.1	0.1	1.6	1.9	2.1	1.5	0.1	0.2	1.8	0.1	1.0
27	27	307.44	0.0	1.1	1.1	0.3	1.7	1.7	1.1	93.5	0.6	1.6	0.7	0.1	1.8
28	28	401.08	0.0	0.0	0.0	0.1	0.2	0.3	0.2	3.6	0.0	3.4	0.0	1.8	0.0

Figure 94: The MAC Matrix for the empty tank.

lms File View Select Help

Modal Assurance Criterion (%) for modes

No	mode no	freq Hz	mode_14 590.47	mode_15 612.52	mode_16 646.90	mode_17 672.35	mode_18 710.33	mode_19 746.94	mode_20 768.45	mode_21 814.10	mode_22 856.83	mode_23 893.05	mode_24 136.57	mode_25 136.55	mode_26 312.74
1	1	60.49													
2	2	127.21													
3	3	127.18													
4	4	199.16													
5	5	248.20													
6	6	248.38													
7	7	255.32													
8	8	307.74													
9	9	406.58													
10	10	416.34													
11	11	467.60													
12	12	557.99													
13	13	564.87													
14	14	590.47	100.0												
15	15	612.52	0.7	100.0											
16	16	646.90	0.4	0.0	100.0										
17	17	672.35	0.1	1.1	1.1	100.0									
18	18	710.33	0.0	0.0	0.5	0.2	100.0								
19	19	746.94	0.0	0.0	0.4	0.7	1.2	100.0							
20	20	768.45	0.3	0.1	0.1	0.3	0.5	2.0	100.0						
21	21	814.10	13.9	0.0	0.0	0.2	0.1	0.0	0.0	100.0					
22	22	856.83	0.1	29.2	0.1	0.0	0.1	0.5	0.4	0.1	100.0				
23	23	893.05	0.1	0.0	0.9	0.5	0.8	0.0	1.0	3.8	0.5	100.0			
24	24	136.57	0.1	0.2	0.0	1.0	0.2	0.0	0.2	2.2	1.3	0.0	100.0		
25	25	136.55	0.1	0.2	0.0	1.0	0.2	0.0	0.2	2.2	1.3	0.0	100.0	100.0	
26	26	312.74	0.2	0.4	0.0	1.2	0.4	0.6	1.9	0.0	1.4	0.6	3.0	3.0	100.0
27	27	307.44	0.2	0.6	0.4	0.4	0.0	0.1	0.3	0.0	0.5	0.4	1.8	1.8	2.1
28	28	401.08	0.0	0.0	0.0	0.1	0.1	0.4	0.6	51.3	0.4	0.1	0.0	0.0	0.3

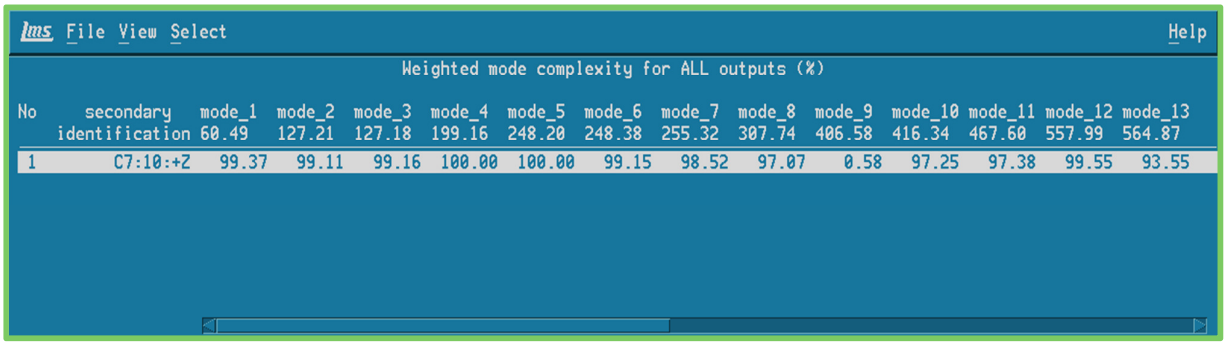
Figure 95: The second part of the MAC Matrix for the empty tank.

lms File View Select Help

Modal Assurance Criterion (%) for modes

No	mode no	freq Hz	mode_16 646.90	mode_17 672.35	mode_18 710.33	mode_19 746.94	mode_20 768.45	mode_21 814.10	mode_22 856.83	mode_23 893.05	mode_24 136.57	mode_25 136.55	mode_26 312.74	mode_27 307.44	mode_28 401.08
1	1	60.49													
2	2	127.21													
3	3	127.18													
4	4	199.16													
5	5	248.20													
6	6	248.38													
7	7	255.32													
8	8	307.74													
9	9	406.58													
10	10	416.34													
11	11	467.60													
12	12	557.99													
13	13	564.87													
14	14	590.47													
15	15	612.52													
16	16	646.90	100.0												
17	17	672.35	1.1	100.0											
18	18	710.33	0.5	0.2	100.0										
19	19	746.94	0.4	0.7	1.2	100.0									
20	20	768.45	0.1	0.3	0.5	2.0	100.0								
21	21	814.10	0.0	0.2	0.1	0.0	0.0	100.0							
22	22	856.83	0.1	0.0	0.1	0.5	0.4	0.1	100.0						
23	23	893.05	0.9	0.5	0.8	0.0	1.0	3.8	0.5	100.0					
24	24	136.57	0.0	1.0	0.2	0.0	0.2	2.2	1.3	0.0	100.0				
25	25	136.55	0.0	1.0	0.2	0.0	0.2	2.2	1.3	0.0	100.0	100.0			
26	26	312.74	0.0	1.2	0.4	0.6	1.9	0.0	1.4	0.6	3.0	3.0	100.0		
27	27	307.44	0.4	0.4	0.0	0.1	0.3	0.0	0.5	0.4	1.8	1.8	2.1	100.0	
28	28	401.08	0.0	0.1	0.1	0.4	0.6	51.3	0.4	0.1	0.0	0.0	0.3	1.4	100.0

Figure 96: The third part of the MAC Matrix for the empty tank.

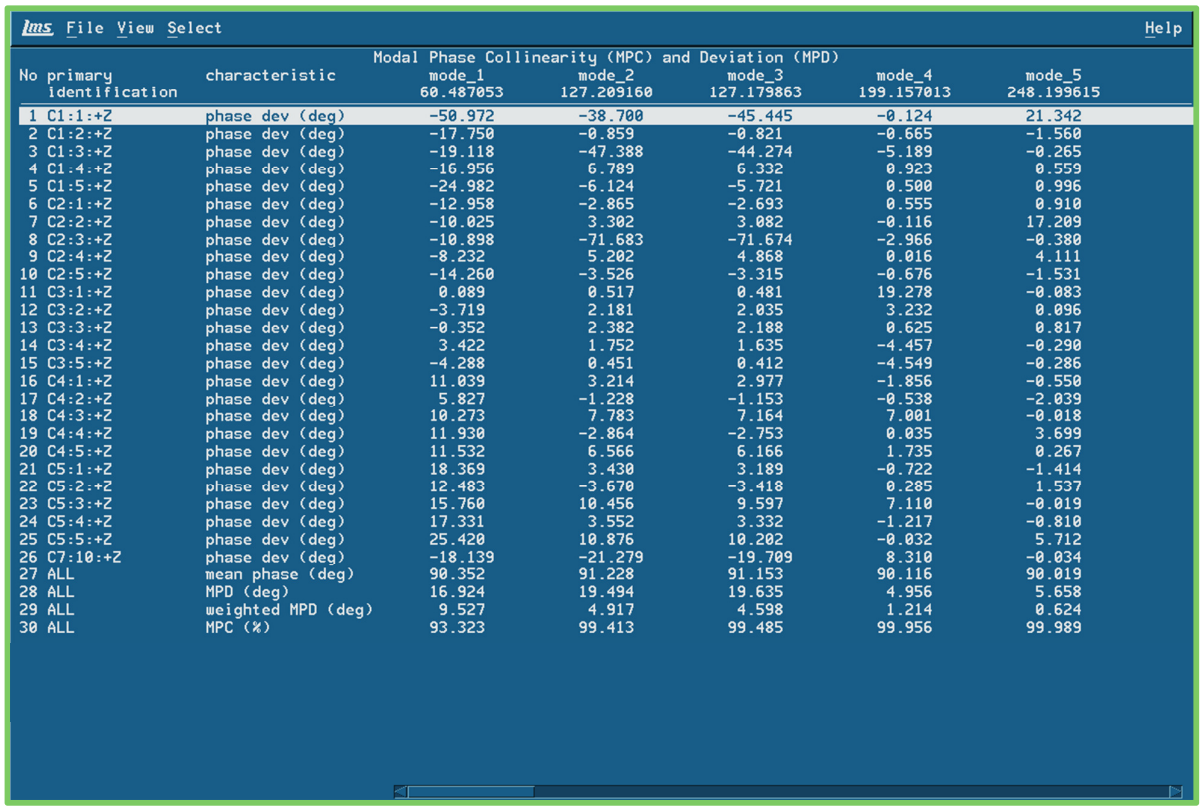


lms File View Select Help

Weighted mode complexity for ALL outputs (%)

No	secondary identification	mode_1 60.49	mode_2 127.21	mode_3 127.18	mode_4 199.16	mode_5 248.20	mode_6 248.38	mode_7 255.32	mode_8 307.74	mode_9 406.58	mode_10 416.34	mode_11 467.60	mode_12 557.99	mode_13 564.87
1	C7:10:+Z	99.37	99.11	99.16	100.00	100.00	99.15	98.52	97.07	0.58	97.25	97.38	99.55	93.55

Figure 97: Example of Mode Complexity for the empty tank.



lms File View Select Help

Modal Phase Collinearity (MPC) and Deviation (MPD)

No	primary identification	characteristic	mode_1 60.487053	mode_2 127.209160	mode_3 127.179863	mode_4 199.157013	mode_5 248.199615
1	C1:1:+Z	phase dev (deg)	-50.972	-38.700	-45.445	-0.124	21.342
2	C1:2:+Z	phase dev (deg)	-17.750	-0.859	-0.821	-0.665	-1.560
3	C1:3:+Z	phase dev (deg)	-19.118	-47.388	-44.274	-5.189	-0.265
4	C1:4:+Z	phase dev (deg)	-16.956	6.789	6.332	0.923	0.559
5	C1:5:+Z	phase dev (deg)	-24.982	-6.124	-5.721	0.500	0.996
6	C2:1:+Z	phase dev (deg)	-12.958	-2.865	-2.693	0.555	0.910
7	C2:2:+Z	phase dev (deg)	-10.025	3.302	3.082	-0.116	17.209
8	C2:3:+Z	phase dev (deg)	-10.898	-71.683	-71.674	-2.966	-0.380
9	C2:4:+Z	phase dev (deg)	-8.232	5.202	4.868	0.016	4.111
10	C2:5:+Z	phase dev (deg)	-14.260	-3.526	-3.315	-0.676	-1.531
11	C3:1:+Z	phase dev (deg)	0.089	0.517	0.481	19.278	-0.083
12	C3:2:+Z	phase dev (deg)	-3.719	2.181	2.035	3.232	0.096
13	C3:3:+Z	phase dev (deg)	-0.352	2.382	2.188	0.625	0.817
14	C3:4:+Z	phase dev (deg)	3.422	1.752	1.635	-4.457	-0.290
15	C3:5:+Z	phase dev (deg)	-4.288	0.451	0.412	-4.549	-0.286
16	C4:1:+Z	phase dev (deg)	11.039	3.214	2.977	-1.856	-0.550
17	C4:2:+Z	phase dev (deg)	5.827	-1.228	-1.153	-0.538	-2.039
18	C4:3:+Z	phase dev (deg)	10.273	7.783	7.164	7.001	-0.018
19	C4:4:+Z	phase dev (deg)	11.930	-2.864	-2.753	0.035	3.699
20	C4:5:+Z	phase dev (deg)	11.532	6.566	6.166	1.735	0.267
21	C5:1:+Z	phase dev (deg)	18.369	3.430	3.189	-0.722	-1.414
22	C5:2:+Z	phase dev (deg)	12.483	-3.670	-3.418	0.285	1.537
23	C5:3:+Z	phase dev (deg)	15.760	10.456	9.597	7.110	-0.019
24	C5:4:+Z	phase dev (deg)	17.331	3.552	3.332	-1.217	-0.810
25	C5:5:+Z	phase dev (deg)	25.420	10.876	10.202	-0.032	5.712
26	C7:10:+Z	phase dev (deg)	-18.139	-21.279	-19.709	8.310	-0.034
27	ALL	mean phase (deg)	90.352	91.228	91.153	90.116	90.019
28	ALL	MPD (deg)	16.924	19.494	19.635	4.956	5.658
29	ALL	weighted MPD (deg)	9.527	4.917	4.598	1.214	0.624
30	ALL	MPC (%)	93.323	99.413	99.485	99.956	99.989

Figure 98: Example of Modal Phase Collinearity for the empty tank.

The case of the liquid filling level is equal to 6 [cm]

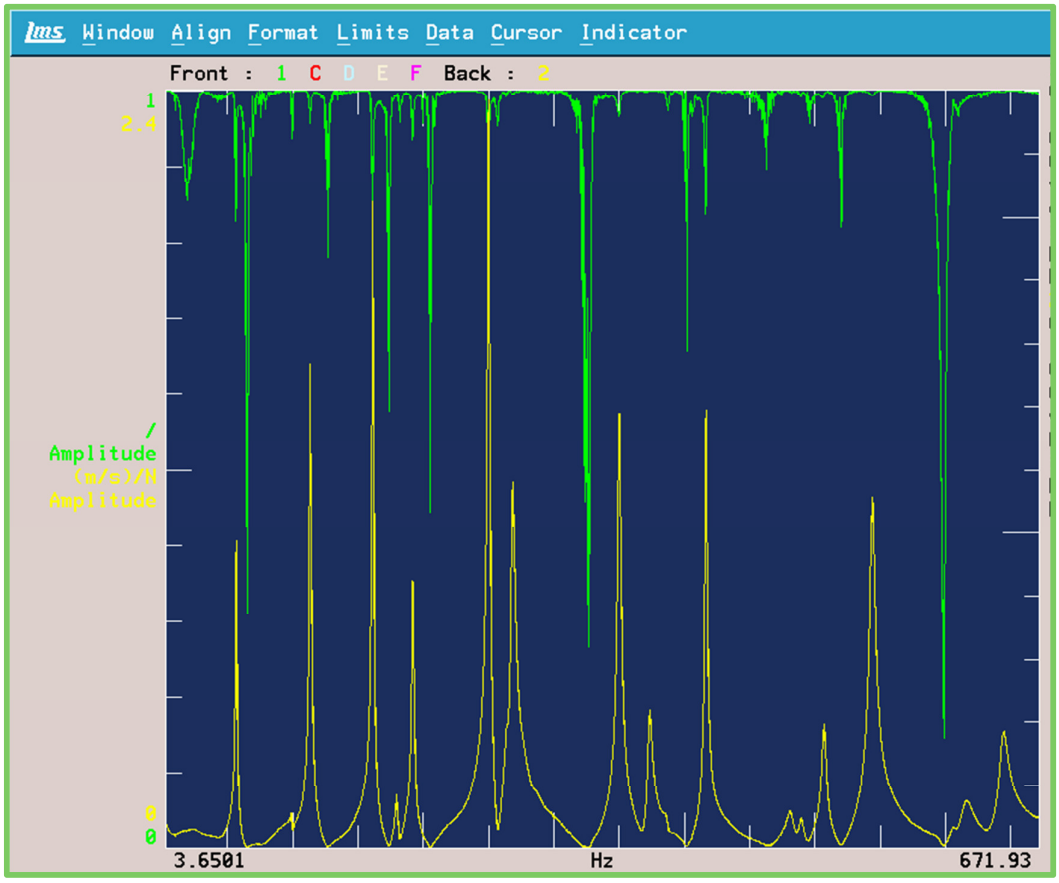


Figure 99: Frequency Response Function and Coherence for the point C_{710}.

Frequency [Hz]	Damping [%]	Modal Shape
56,59	0,75%	1-1
98,38	0,50%	2-1
113,14	0,44%	1-2
159,86	0,48%	2-2
179,93	0,59%	3-2
191,02	0,37%	2-3
249,40	0,30%	2-2 diagonal
263,64	0,75%	3-1
268,34	0,59%	1-3
328,87	0,23%	3-3
349,75	0,40%	4-2
374,03	0,43%	2-4
385,81	0,24%	1-4
415,61	0,16%	4-1
480,97	0,53%	3-3 diagonal
488,71	0,36%	5-1
506,90	0,34%	3-4
543,60	0,29%	4-3
593,27	0,64%	1-5
605,88	0,65%	5-2
613,86	0,73%	2-5
644,07	0,51%	5-3
688,01	0,39%	3-5
712,92	1,85%	4-5
780,25	1,17%	5-4
826,49	0,36%	6-1

Table 9: Frequency, Damping and Modal Shapes for the Plate: In this case, the structure is Undamped, but the Damping Ratio is slightly increased.

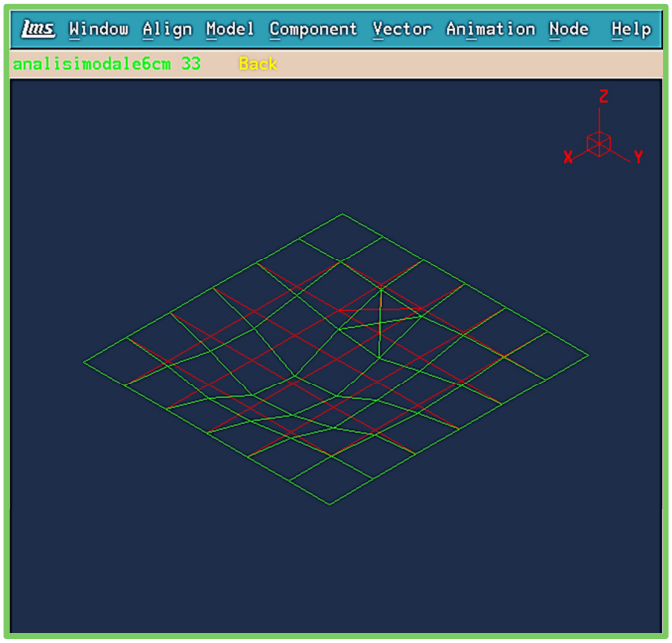


Figure 100: Mode (1-1), frequency 56,59 [Hz].

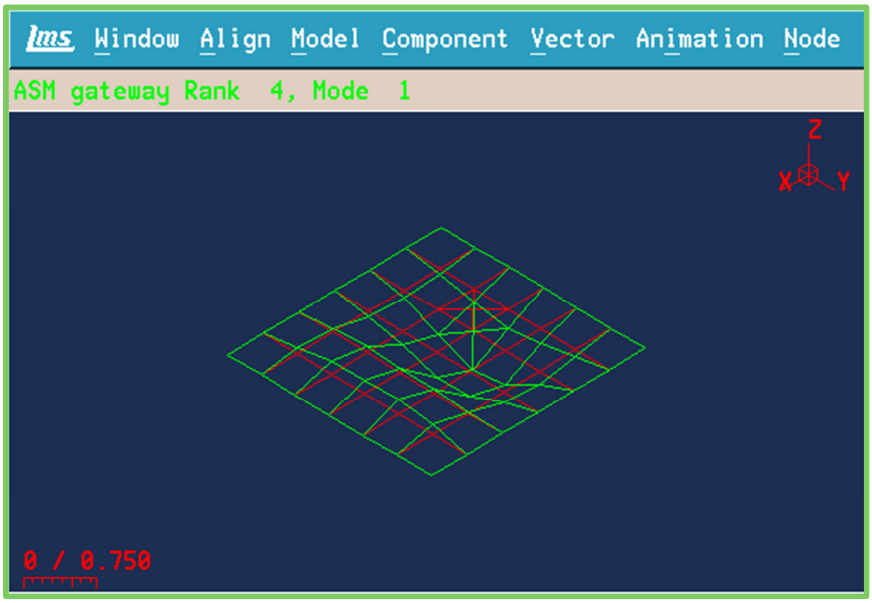


Figure 101: Mode (2-1), frequency 98,38 [Hz].

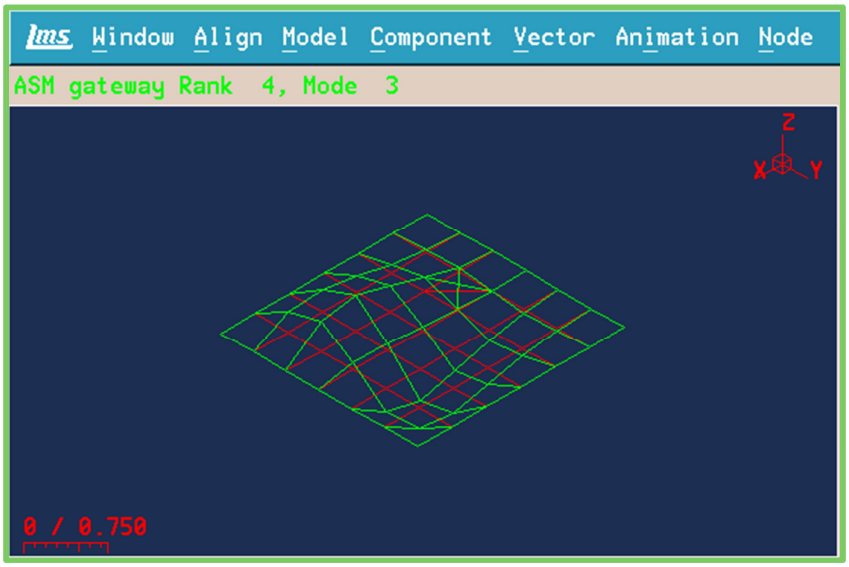


Figure 102: Mode (2-1) symmetrical to the mode shape presented in figure (100), frequency 113,14 [Hz]

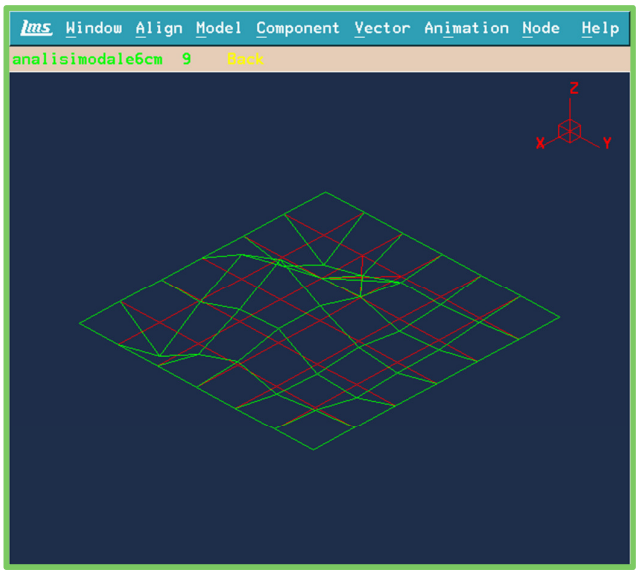


Figure 103: Mode (3-1) asymmetrical, frequency 159,86[Hz].

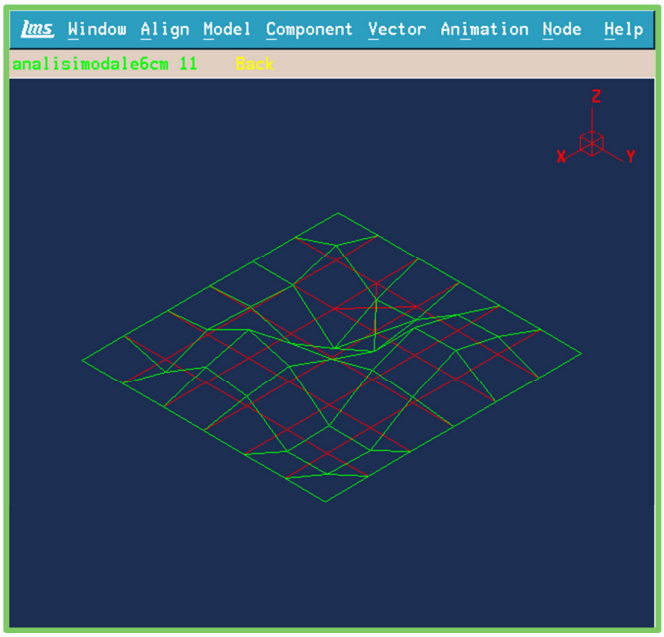


Figure 104: Mode (2-3), frequency 179,93[Hz].

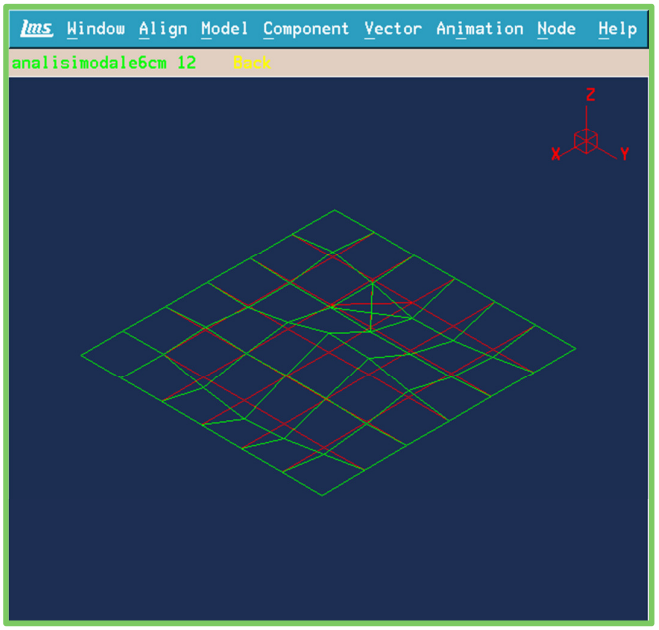


Figure 105: Mode (1-3), frequency 191,02[Hz].

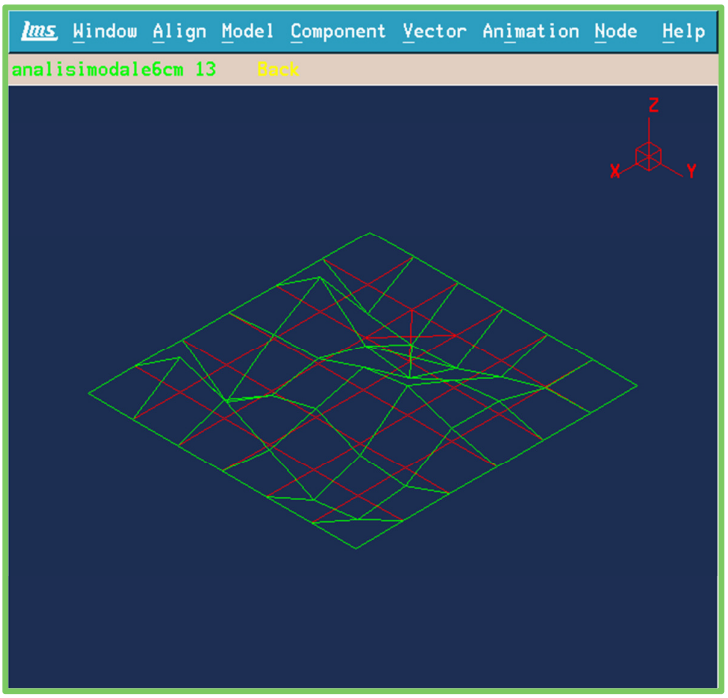


Figure 106: Mode (3-2), frequency 249,40[Hz].

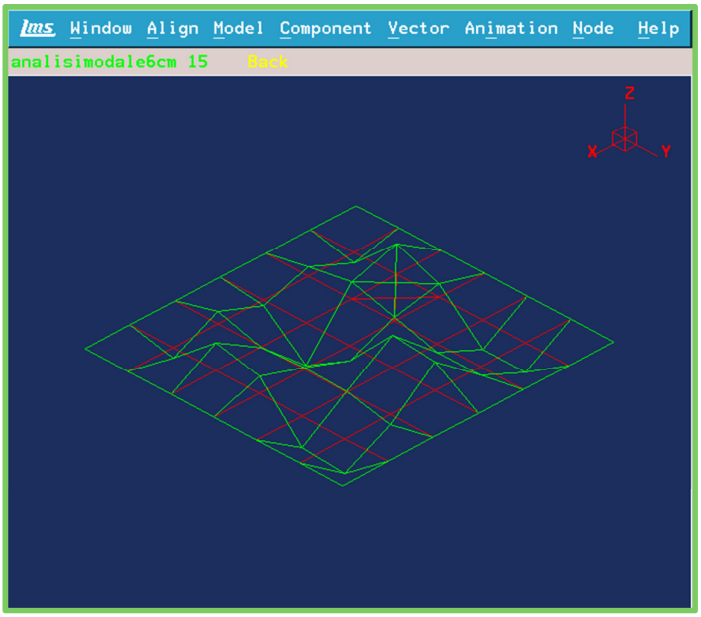


Figure 107: Mode (3-3), frequency 263,64[Hz].

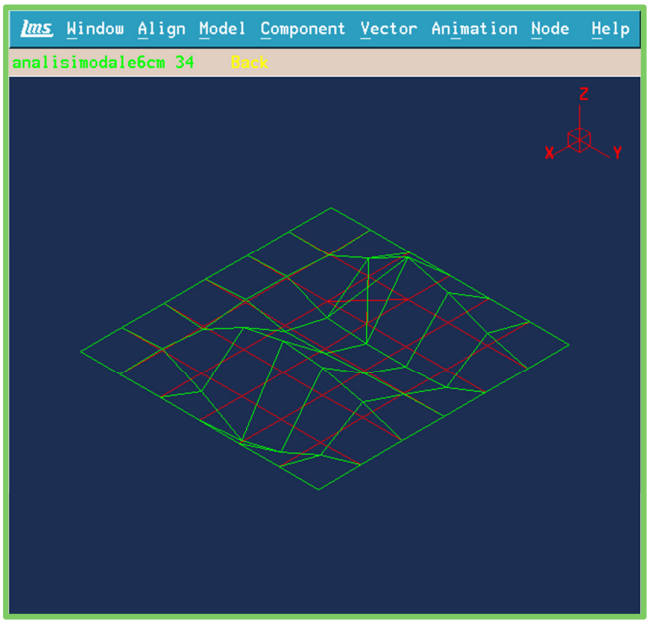


Figure 108: Mode (4-1), frequency 268,34[Hz].

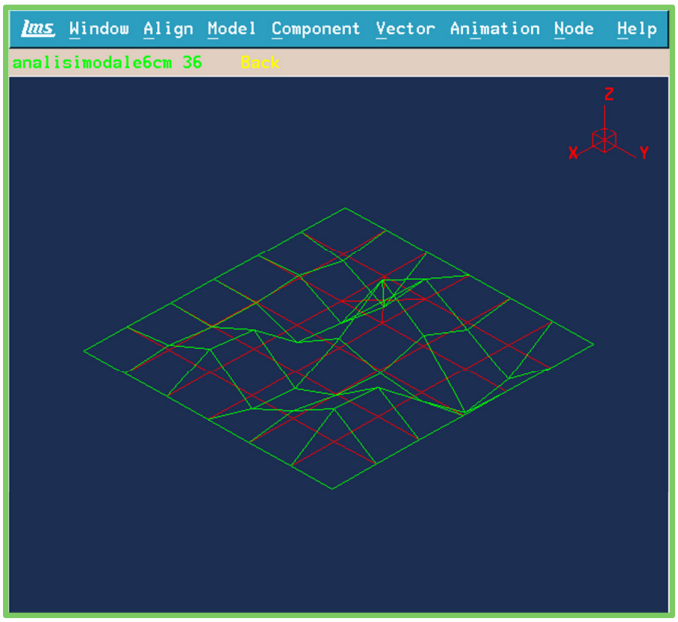


Figure 109: Mode (2-3), frequency 328,87[Hz].

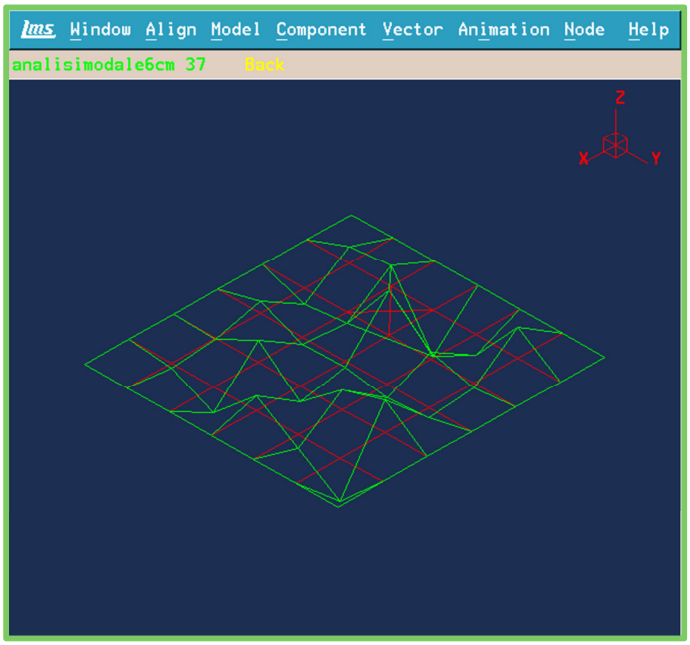


Figure 110: Mode (4-3), frequency 349,75[Hz].

lms File View Select Help

Modal Assurance Criterion (%) for modes

No	mode no	freq Hz	mode_1 98.38	mode_2 113.14	mode_3 159.86	mode_4 179.93	mode_5 191.02	mode_6 249.40	mode_7 263.64	mode_8 268.34	mode_9 328.87	mode_10 349.75	mode_11 374.03	mode_12 415.61	mode_13 480.97
1	1	98.38	100.0												
2	2	113.14	4.8	100.0											
3	3	159.86	6.1	12.5	100.0										
4	4	179.93	0.6	1.4	0.0	100.0									
5	5	191.02	10.3	0.0	1.6	6.7	100.0								
6	6	249.40	1.7	11.8	1.1	0.3	0.0	100.0							
7	7	263.64	1.0	0.1	0.4	4.9	0.9	0.1	100.0						
8	8	268.34	1.7	5.1	0.0	3.7	0.3	12.4	12.0	100.0					
9	9	328.87	0.0	0.3	0.2	1.5	6.5	0.0	0.1	0.0	100.0				
10	10	349.75	0.0	1.0	0.1	6.9	0.8	0.1	0.4	0.1	0.3	100.0			
11	11	374.03	0.2	1.9	0.3	5.4	0.4	0.9	0.6	1.3	0.4	22.0	100.0		
12	12	415.61	0.0	0.3	2.2	0.5	1.9	0.3	3.4	8.5	1.0	0.7	0.1	100.0	
13	13	480.97	0.1	0.0	0.1	2.4	0.2	0.2	0.7	2.7	4.9	1.7	0.2	0.2	100.0
14	14	488.71	0.1	0.1	0.0	0.0	2.2	0.0	0.0	0.0	17.7	0.6	0.0	0.1	0.5
15	15	506.90	0.1	1.7	0.1	0.5	0.3	0.1	0.2	9.9	0.0	0.6	1.6	0.2	40.3
16	16	543.60	0.3	0.5	1.4	0.6	0.1	5.4	0.2	1.9	0.0	1.2	0.2	0.3	0.0
17	17	593.27	0.0	0.1	0.1	0.0	0.0	0.3	0.1	0.0	0.2	2.1	7.2	6.9	0.1
18	18	605.88	0.1	1.4	0.7	0.9	0.8	3.0	2.8	4.0	0.2	6.5	2.0	0.7	0.7
19	19	613.86	0.1	0.2	0.0	0.1	0.0	0.1	1.2	1.6	0.0	2.2	0.1	2.9	3.1
20	20	644.07	0.0	0.8	0.3	0.1	0.0	1.1	0.8	1.1	0.3	1.5	16.3	2.1	2.1
21	21	678.19	0.1	0.0	0.1	0.8	0.3	0.0	0.0	0.2	0.1	1.0	2.3	5.0	0.1
22	22	688.81	0.0	0.3	0.0	0.2	1.5	1.3	0.5	0.1	3.0	0.5	0.2	1.5	1.2
23	23	712.92	0.1	0.7	1.0	0.1	0.1	0.3	0.2	4.6	0.7	0.8	1.7	3.2	0.0
24	24	780.25	0.0	2.0	0.1	0.2	0.2	0.6	0.3	6.2	0.0	0.8	1.6	5.3	1.6
25	25	826.49	0.0	0.1	0.1	0.3	0.9	0.3	2.6	0.5	0.0	0.8	1.8	21.4	6.6
26	26	56.59	22.3	0.2	0.1	7.4	6.5	0.0	0.7	0.3	1.7	0.4	0.0	0.3	0.4

Figure 111: MAC Matrix for the filling level of liquid equal to 6 [cm].

lms File View Select Help

Weighted mode complexity for ALL outputs (%)

No	secondary identification	mode_1 98.38	mode_2 113.14	mode_3 159.86	mode_4 179.93	mode_5 191.02	mode_6 249.40	mode_7 263.64	mode_8 268.34	mode_9 328.87	mode_10 349.75	mode_11 374.03	mode_12 415.61	mode_13 480.97
1	C7:10:+Z	0.03	100.00	100.00	99.62	100.00	100.00	99.77	100.00	0.15	99.78	99.30	95.55	100.00

Figure 112: Mode Complexity for the filling level of liquid equal to 6 [cm].

lms File View Select Help

odal Phase Collinearity (MPC) and Deviation (MPD

No	mode nr	freq Hz	MPC (%)	MPD deg	phase scatter
1	1	98.38	100.0	0.32	low
2	2	113.14	98.3	7.75	low
3	3	159.86	99.9	1.58	low
4	4	179.93	99.5	4.03	low
5	5	191.02	99.7	3.08	low
6	6	249.40	99.5	4.28	low
7	7	263.64	99.4	4.27	low
8	8	268.34	99.2	4.98	low
9	9	328.87	99.7	3.16	low
10	10	349.75	99.9	1.44	low
11	11	374.03	99.6	3.89	low
12	12	415.61	97.2	11.05	low
13	13	480.97	100.0	0.35	low
14	14	488.71	99.8	2.74	low
15	15	506.90	99.8	2.88	low
16	16	543.60	100.0	0.40	low
17	17	593.27	99.4	4.36	low
18	18	605.88	92.8	16.82	
19	19	613.86	100.0	0.32	low
20	20	644.07	99.7	3.45	low
21	21	678.19	99.8	2.82	low
22	22	688.81	99.9	2.08	low
23	23	712.92	98.3	7.74	low
24	24	780.25	97.9	9.24	low
25	25	826.49	97.9	9.20	low
26	26	56.59	99.5	6.11	low
27	27	415.13	99.4	4.92	low
28	28	385.81	99.1	5.70	low
29	29	605.02	99.1	5.71	low

Figure 113: Modal Phase Collinearity for the filling level equal to 6 [cm].

The case of the liquid filling level is equal to 12 [cm]

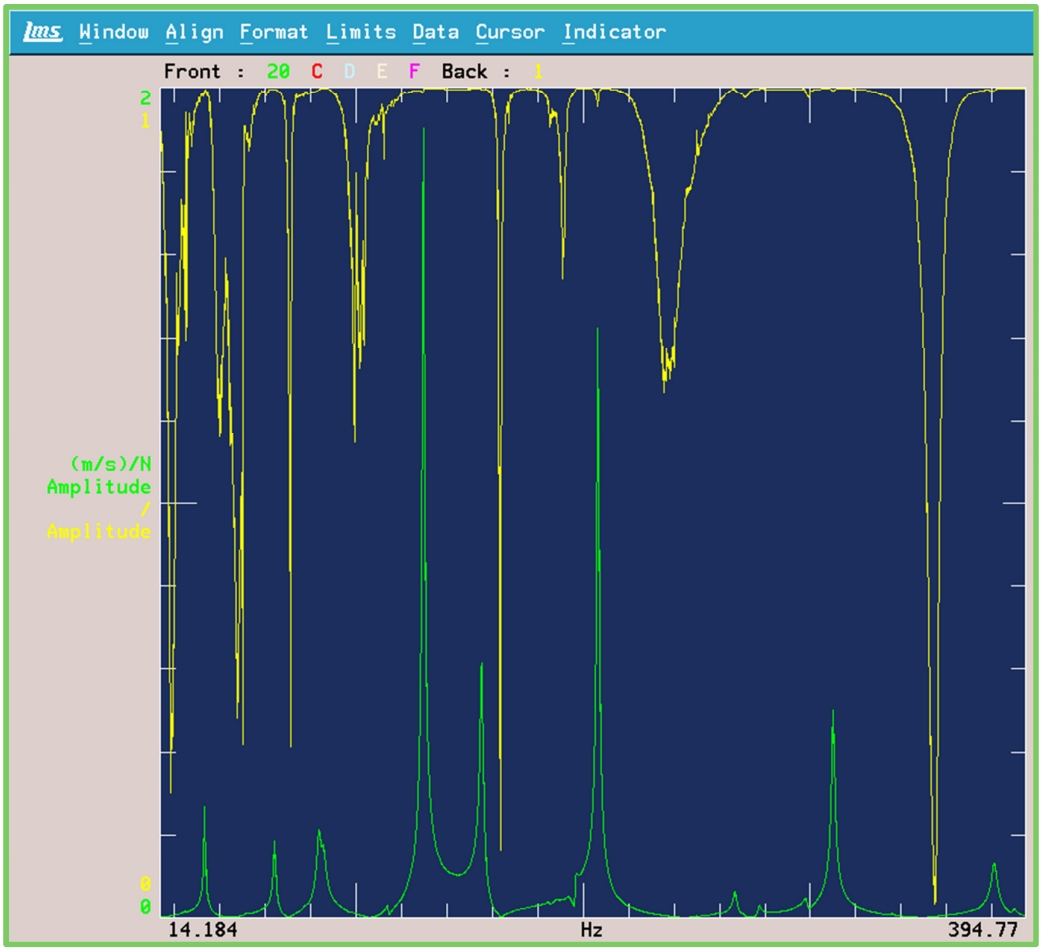


Figure 114: Frequency Response Function and Coherence for the point C_{22}. The laser beam is fixed in C_{710}.

Frequency [Hz]	Damping [%]	Modal Shape
33,24	0,64%	1-1
64,19	0,61%	2-1
85,69	0,95%	1-2
113,94	0,30%	3-1
129,67	0,23%	2-2 central
155,47	0,35%	1-3
185,65	0,09%	4-2
196,67	0,22%	3-2
206,46	0,18%	2-3 deformed
267,06	0,20%	1-4
275,95	0,19%	5-1
285,56	0,17%	4-2 very deformed
298,44	0,28%	3-3
310,14	0,15%	2-4
382,19	0,34%	3-4
407,13	0,22%	5-2
418,39	0,16%	1-5

Table 10: Frequency, Damping and Modal Shapes. The Damping ratio is increased and the Vibration Modes are deformed and asymmetrical with respect to the planes passing through the center of the Plate and perpendicular to the free liquid surface.

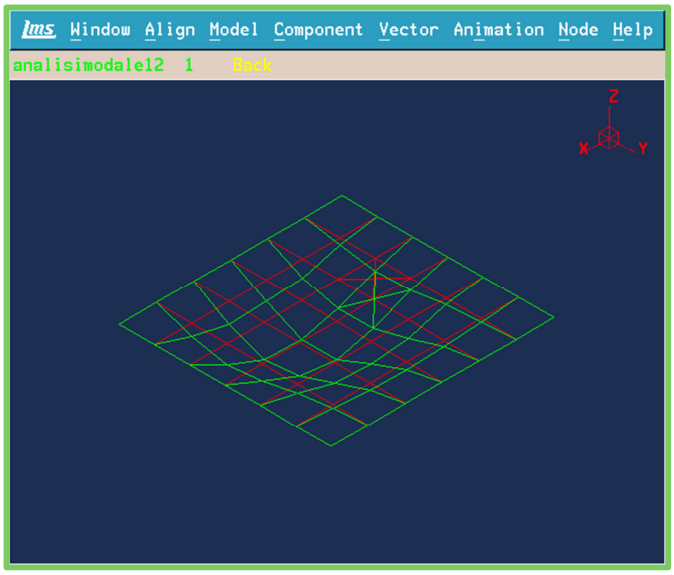


Figure 115: Mode (1-1), frequency 33,24 [Hz].

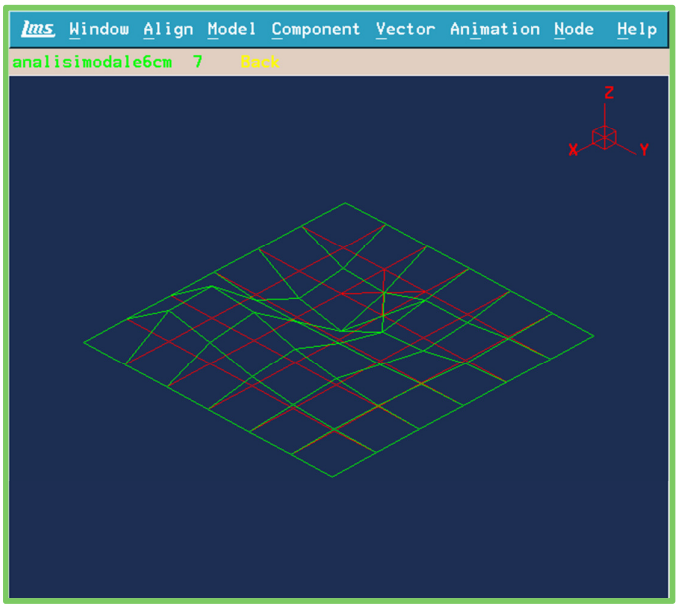


Figure 116: Mode (2-1), frequency 64,19 [Hz].

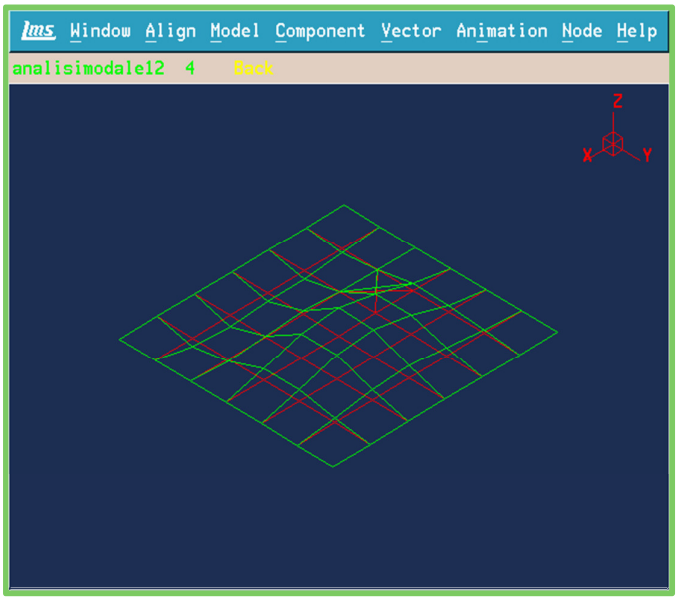


Figure 116: Mode (1-2) asymmetrical, frequency 85,69 [Hz]. The deformation due to Hydrostatic Pressure produce a deflection in the low part of the Plate.

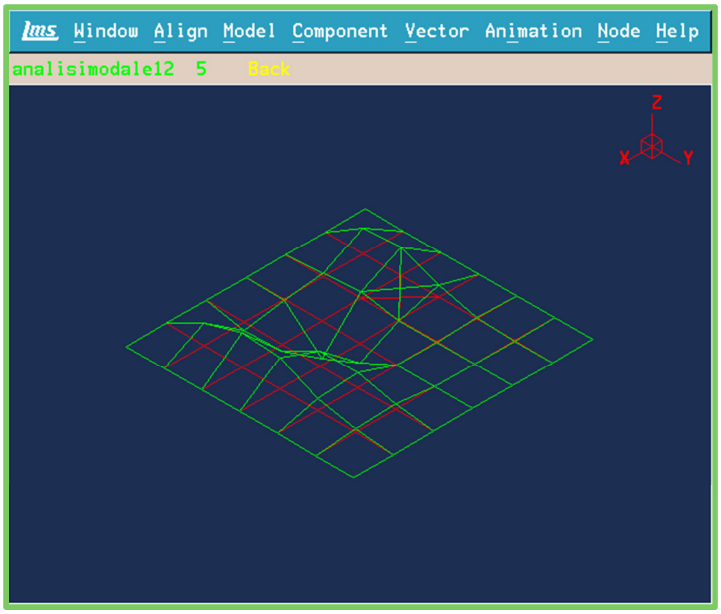


Figure 117: Mode (3-1) asymmetrical, frequency 113,94 [Hz]. The three semi-waves are situated in the low part of Plate.

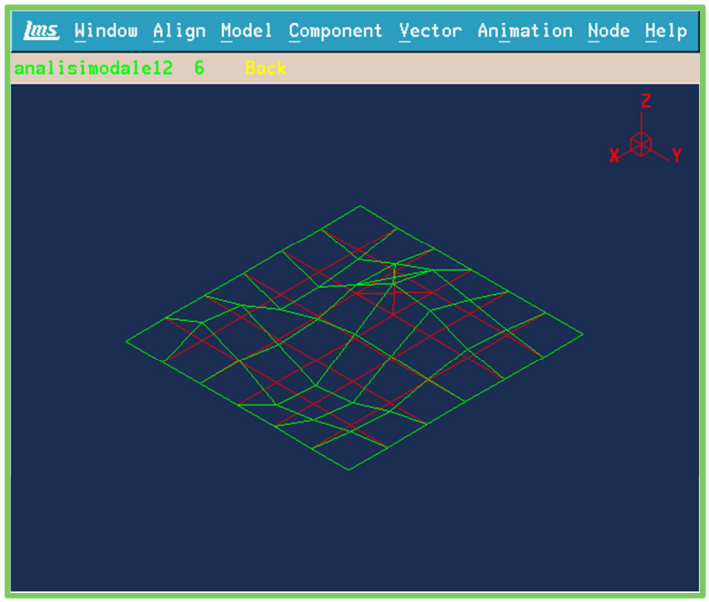


Figure 118: Mode (2-2) asymmetrical, frequency 129,67 [Hz]. The deflection is localized at the center.

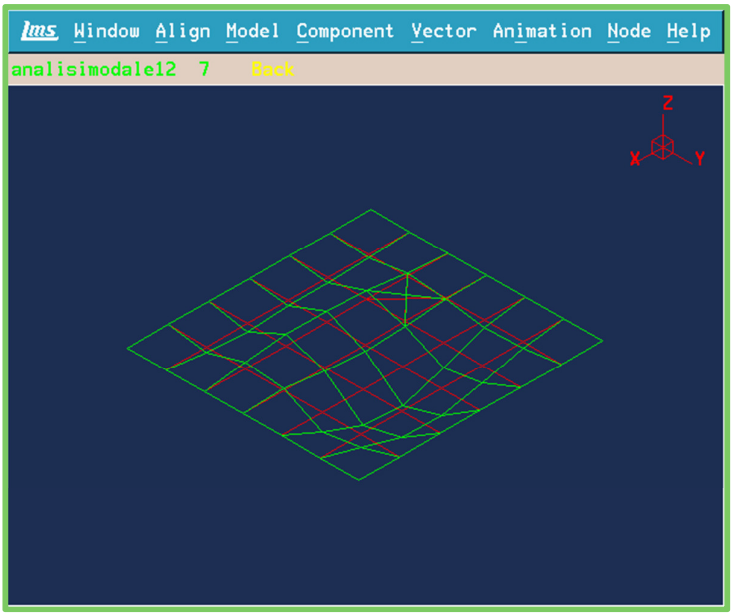


Figure 119: Mode (1-3), frequency 155,47 [Hz].

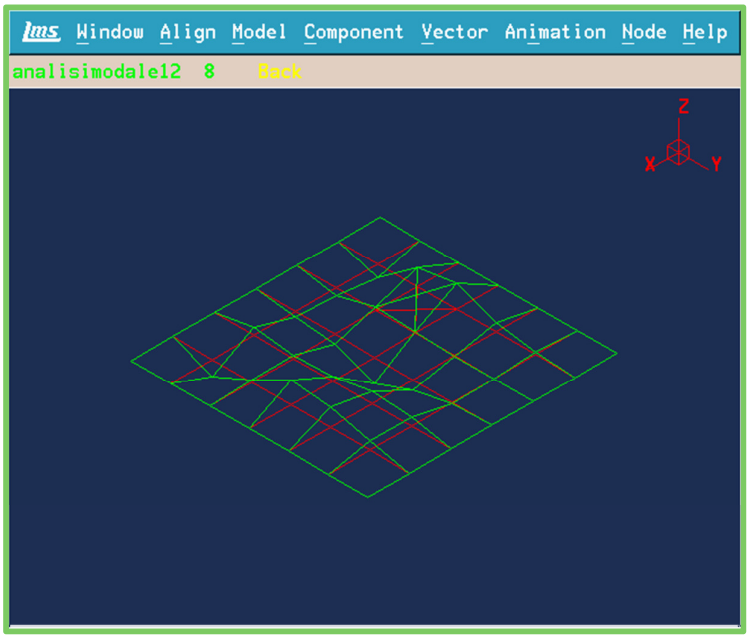


Figure 120: Mode (3-2), frequency 196,67 [Hz].

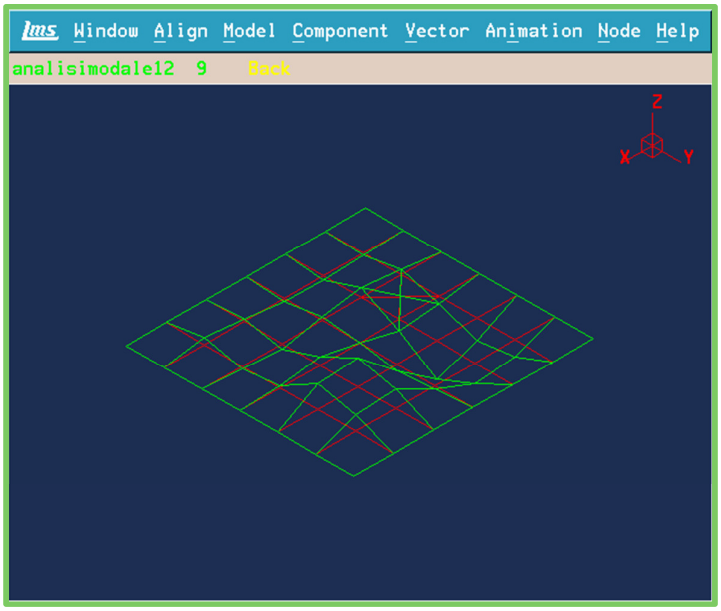


Figure 121: Mode (2-3) deformed, frequency 206,46 [Hz].

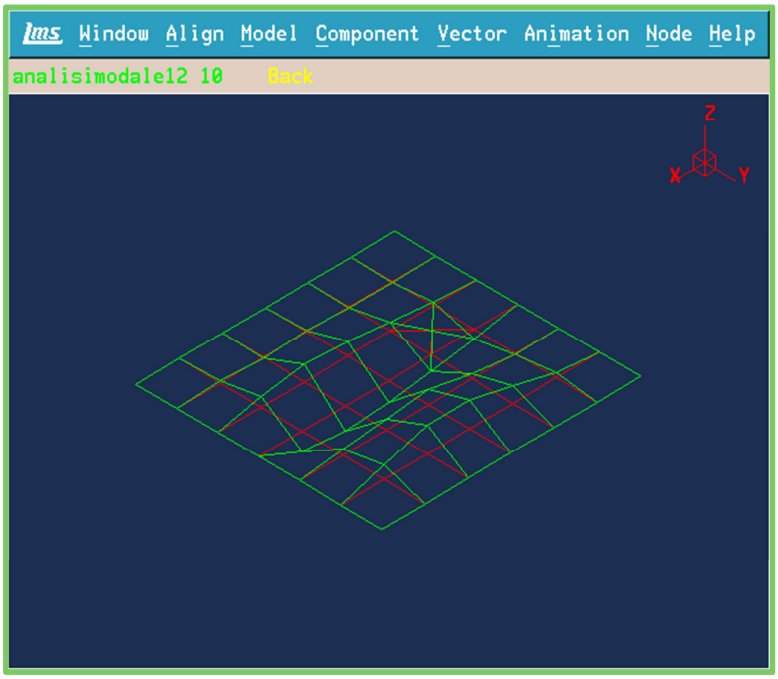


Figure 122: Mode (1-4) deformed, frequency 267,06 [Hz].

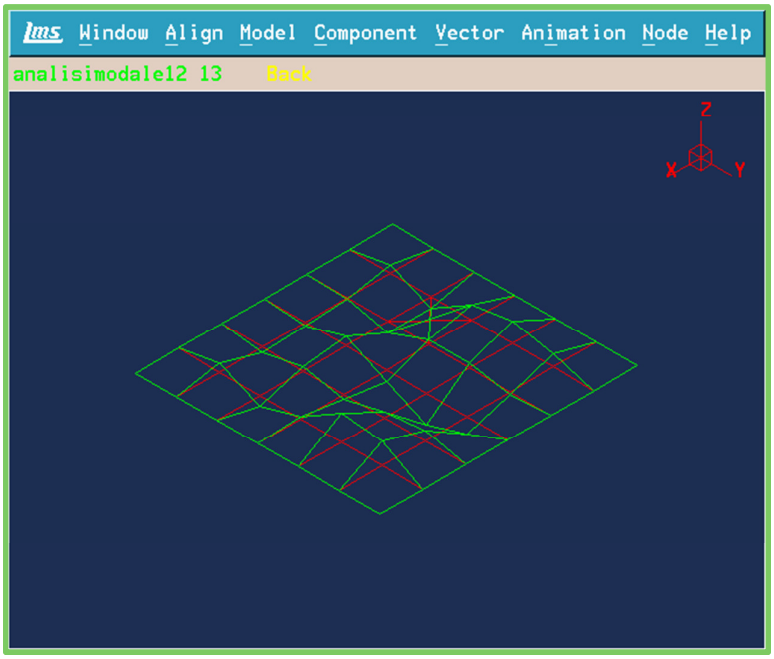


Figure 123: Mode (3-3) deformed, frequency 298,44 [Hz].

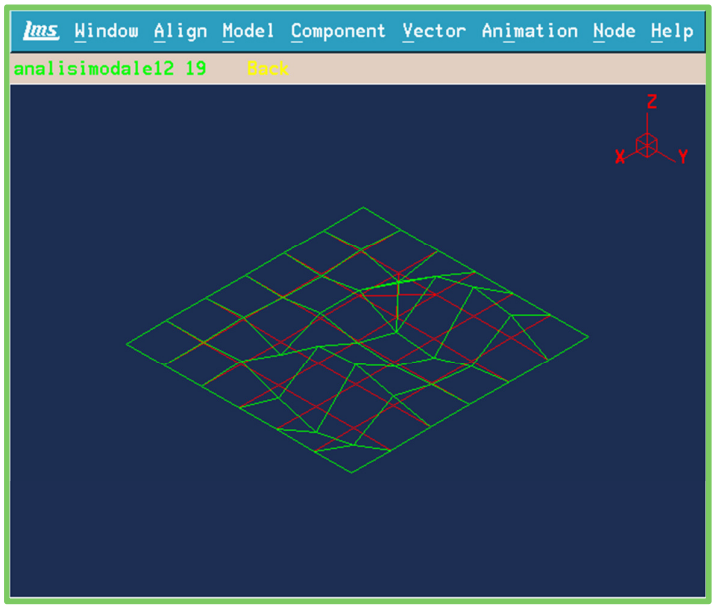


Figure 124: Mode (4-1) deformed, frequency 418,39 [Hz].

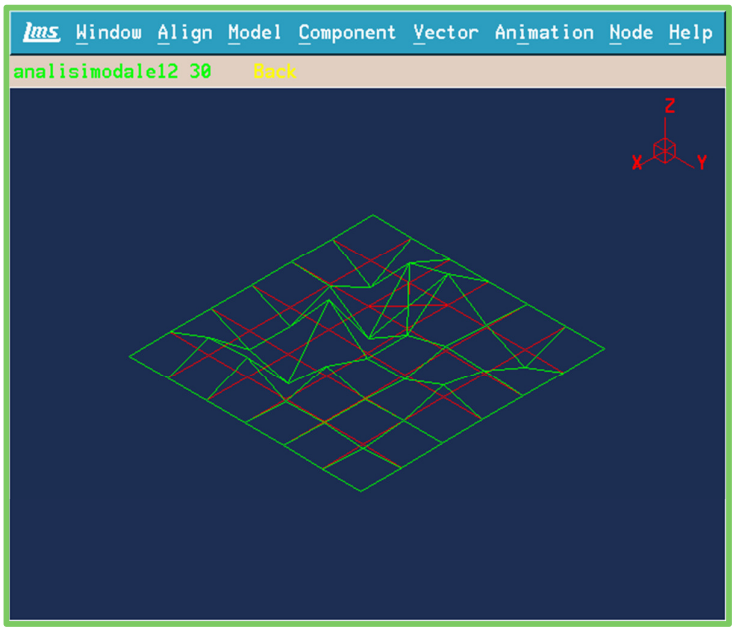


Figure 125: Mode (5-2) deformed, frequency 407,13 [Hz].

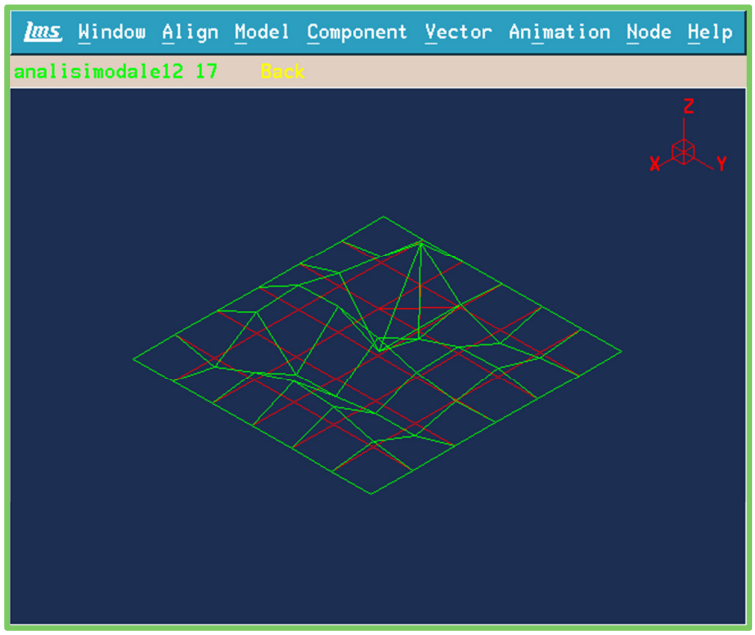


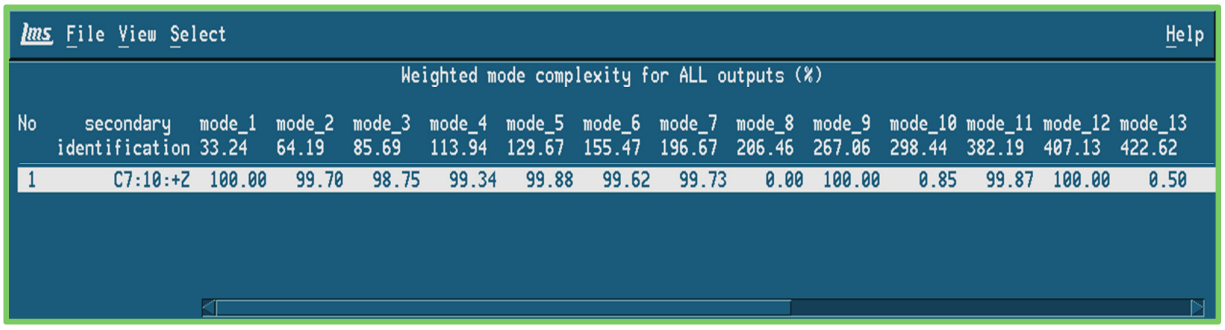
Figure 126: Mode (4-2) deformed, frequency 185,65 [Hz].

lms File View Select Help

Modal Assurance Criterion (%) for modes

No	mode no	freq Hz	mode_1 33.24	mode_2 64.19	mode_3 85.69	mode_4 113.94	mode_5 129.67	mode_6 155.47	mode_7 196.67	mode_8 206.46	mode_9 267.06	mode_10 298.44	mode_11 382.19	mode_12 407.13	mode_13 422.62
1	1	33.24	100.0												
2	2	64.19	0.3	100.0											
3	3	85.69	32.2	0.2	100.0										
4	4	113.94	1.1	1.9	1.5	100.0									
5	5	129.67	1.2	14.1	1.1	2.2	100.0								
6	6	155.47	7.5	0.3	39.1	2.6	0.2	100.0							
7	7	196.67	0.1	0.0	3.0	19.0	0.0	0.4	100.0						
8	8	206.46	0.1	4.6	0.2	3.4	31.2	0.1	2.8	100.0					
9	9	267.06	0.0	0.3	0.3	0.5	0.2	18.2	0.0	0.8	100.0				
10	10	298.44	0.2	0.0	0.2	0.6	0.4	0.2	13.7	0.9	0.0	100.0			
11	11	382.19	0.2	0.2	1.2	0.0	1.0	0.0	0.4	0.4	0.0	19.3	100.0		
12	12	407.13	0.0	0.1	1.9	0.0	3.9	0.6	0.0	0.2	0.0	0.3	17.8	100.0	
13	13	422.62	0.1	0.0	0.1	0.0	0.0	0.0	0.1	0.0	0.1	1.1	1.2	11.7	100.0
14	14	275.95	2.2	0.2	0.6	0.1	1.7	0.1	2.3	0.2	1.6	0.4	5.8	29.0	4.6
15	15	322.48	0.0	1.3	0.1	3.5	0.1	0.3	0.4	0.2	0.4	1.7	2.7	0.5	1.2
16	16	310.14	0.8	0.2	0.4	0.0	1.2	0.3	0.0	15.6	0.0	1.2	0.4	2.3	0.9
17	17	418.39	6.5	0.8	2.2	0.4	0.0	0.7	1.0	0.3	38.8	0.9	0.1	0.5	0.7
18	18	389.90	1.1	0.1	0.3	1.1	0.1	0.0	0.1	0.7	0.6	7.7	8.9	30.7	1.7
19	19	185.65	0.7	0.2	2.6	0.1	0.4	2.2	1.2	0.1	0.5	2.3	3.6	1.8	0.0
20	20	465.36	0.1	5.1	0.4	1.1	2.1	0.1	0.0	0.1	0.1	2.5	0.2	0.2	0.0
21	21	519.02	4.4	4.8	0.0	0.1	0.1	0.0	0.4	0.0	0.4	0.0	0.4	17.9	1.5
22	22	495.52	0.0	0.0	0.0	0.1	0.0	0.2	0.5	0.0	0.0	0.1	2.7	7.6	43.0

Figure 127: MAC Matrix for all mode shapes found of the thin Plate in contact with liquid.



lms File View Select Help

Weighted mode complexity for ALL outputs (%)

No	secondary identification	mode_1 33.24	mode_2 64.19	mode_3 85.69	mode_4 113.94	mode_5 129.67	mode_6 155.47	mode_7 196.67	mode_8 206.46	mode_9 267.06	mode_10 298.44	mode_11 382.19	mode_12 407.13	mode_13 422.62
1	C7:10:+Z	100.00	99.70	98.75	99.34	99.88	99.62	99.73	0.00	100.00	0.85	99.87	100.00	0.50

Figure 128: Mode Complexity for the filling level of liquid equal to 12 [cm].

lms File View Select Help

odal Phase Collinearity (MPC) and Deviation (MPD

No	mode nr	freq Hz	MPC (%)	MPD deg	phase scatter
1	1	33.24	100.0	0.11	low
2	2	64.19	100.0	2.14	low
3	3	85.69	99.6	3.24	low
4	4	113.94	100.0	1.44	low
5	5	129.67	100.0	0.77	low
6	6	155.47	99.8	2.25	low
7	7	196.67	99.9	1.99	low
8	8	206.46	100.0	0.07	low
9	9	267.06	100.0	0.06	low
10	10	298.44	97.8	9.03	low
11	11	382.19	100.0	0.85	low
12	12	407.13	100.0	1.25	low
13	13	422.62	99.8	2.42	low
14	14	275.95	99.4	4.36	low
15	15	322.48	99.2	5.19	low
16	16	310.14	100.0	0.26	low
17	17	418.39	100.0	0.00	low
18	18	389.90	99.2	5.38	low
19	19	185.65	99.8	3.15	low
20	20	465.36	99.9	1.58	low
21	21	519.02	100.0	0.19	low
22	22	495.52	99.7	3.11	low

Figure 129: Modal Phase Collinearity for the filling level of liquid equal to 12 [cm].

The case of the liquid filling level is equal to 18 [cm]

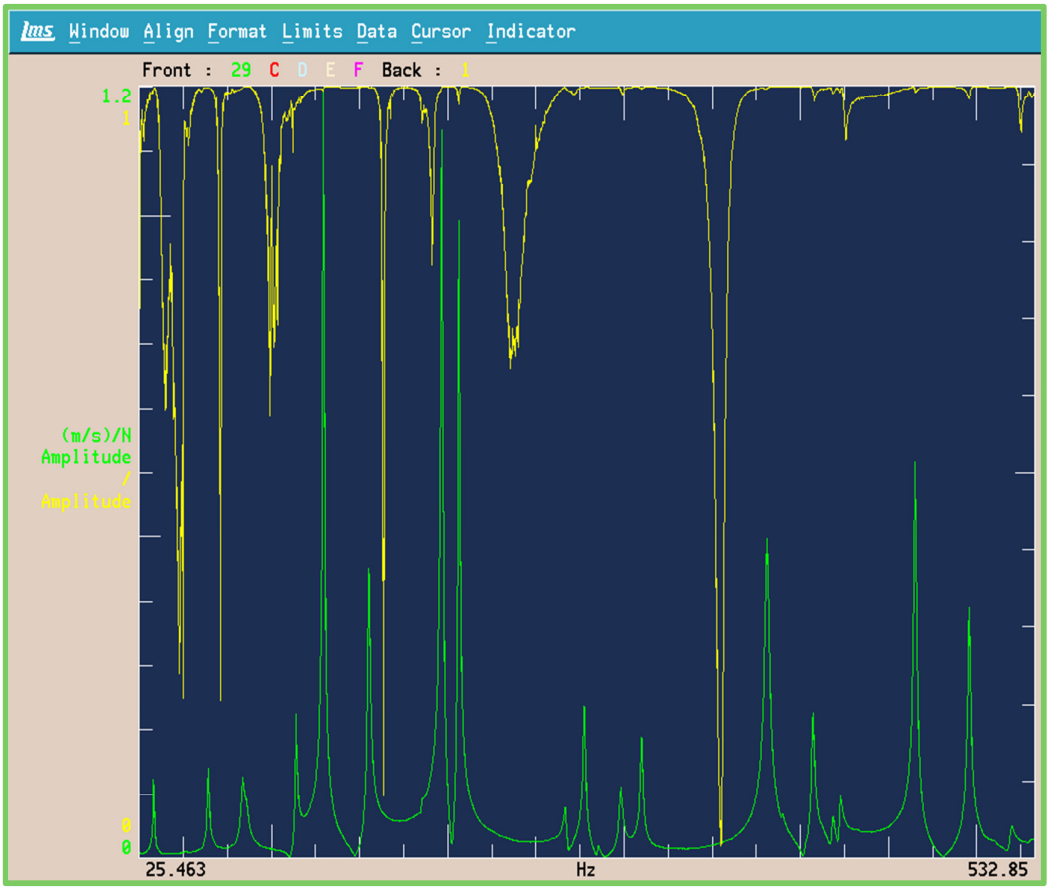


Figure 130: Frequency Response Function and Coherence for the point C_{33}. *The laser beam is fixed in* C_{710}.

Frequency [Hz]	Damping [%]	Modal Shapes
30,02	0,66%	1-1
58,14	1,48%	2-1
64,20	0,54%	1-2
93,38	0,24%	2-2
108,40	0,44%	3-1
134,22	0,35%	1-3
147,96	0,16%	3-2
163,73	0,25%	2-3
180,31	0,17%	4-1
221,40	0,21%	3-3
224,69	0,20%	1-5
269,30	0,27%	2-4
275,84	0,20%	5-1
307,57	0,18%	4-3
322,45	0,13%	5-2
335,96	0,21%	3-4

Table 11: Frequency, Damping and Modal Shapes. The Damping ratio is quite similar to the previous case. The Vibration Modes are still deformed, and since the mass of liquid is in contact with a larger surface of the plate, the vibration modes appear to be more symmetrical and more recognizable.

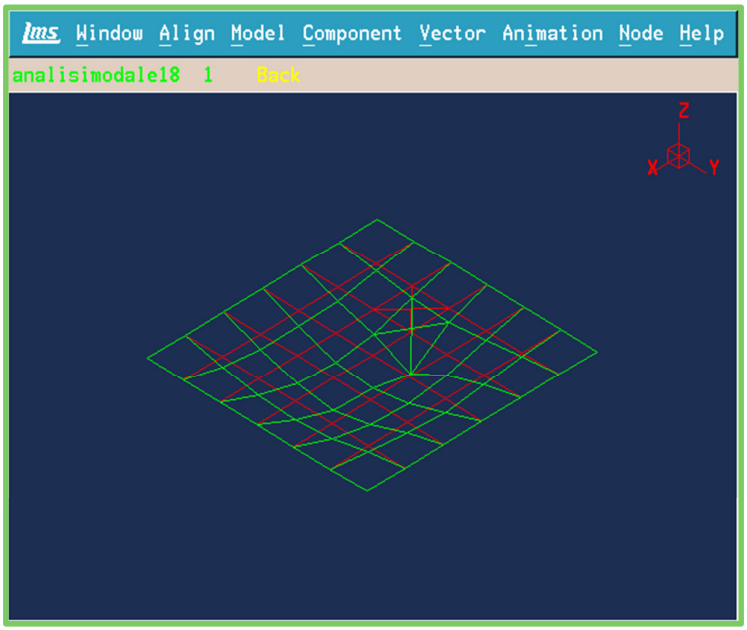


Figure 131: Mode (1-1), frequency 30,02 [Hz].

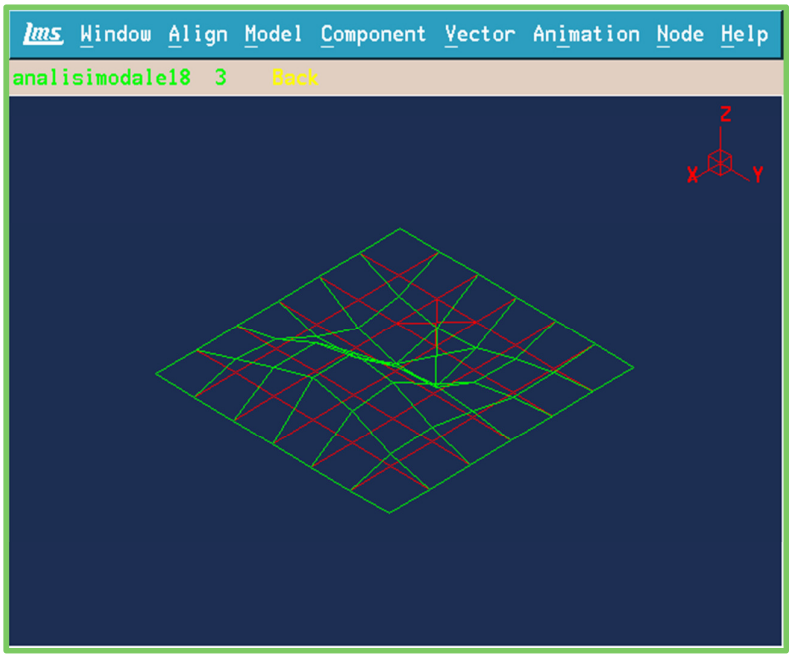


Figure 131: Mode (2-1), frequency 58,14 [Hz].

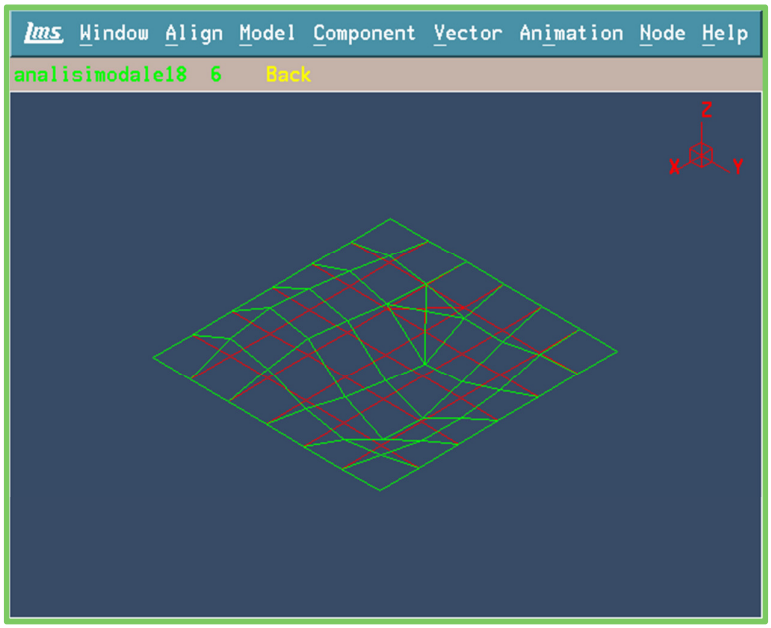


Figure 132: Mode (1-2), frequency 64,20 [Hz].

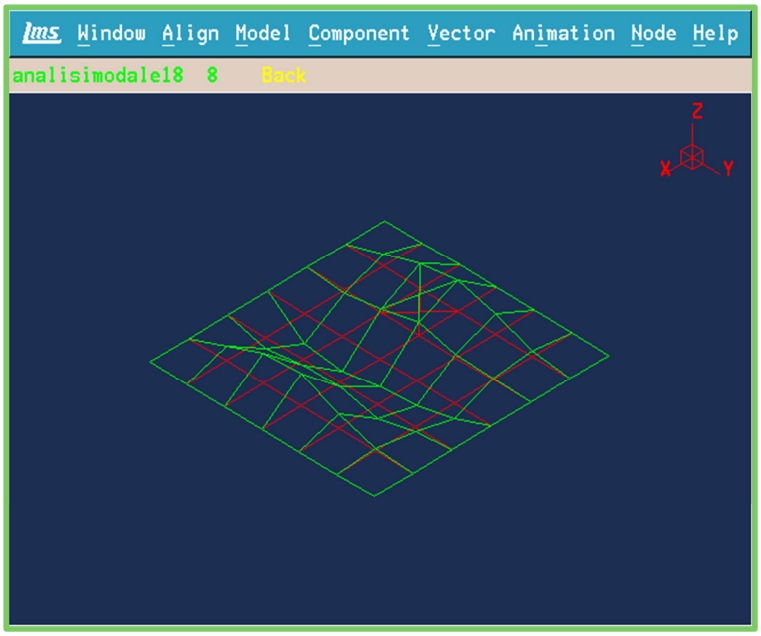


Figure 133: Mode (3-1) deformed, frequency 108,40 [Hz].

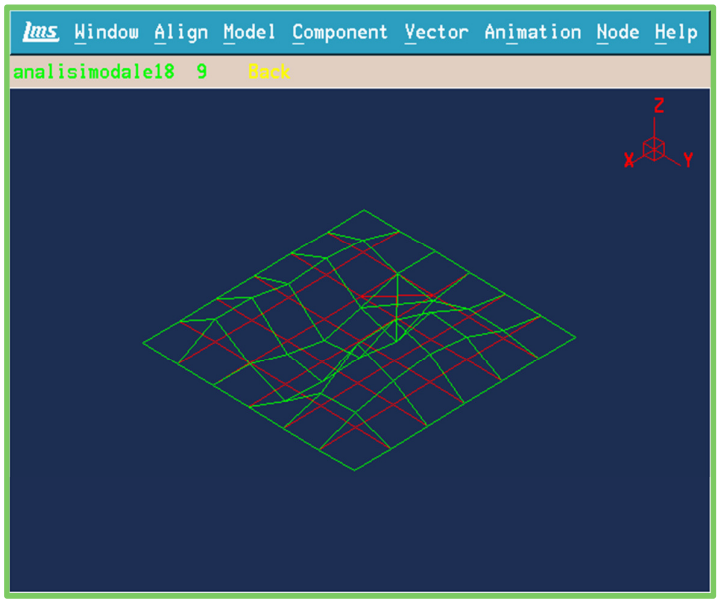


Figure 134: Mode (1-3) deformed, frequency 134,22 [Hz].

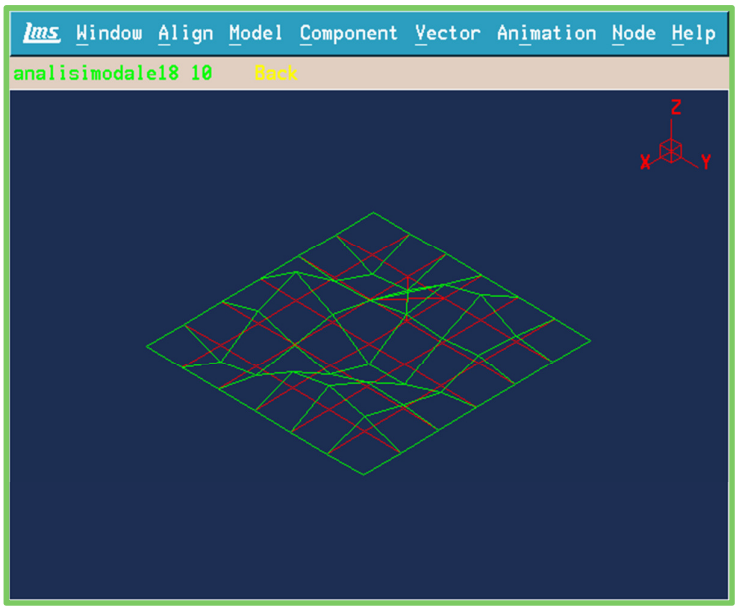


Figure 135: Mode (2-2) deformed, frequency 93,89 [Hz].

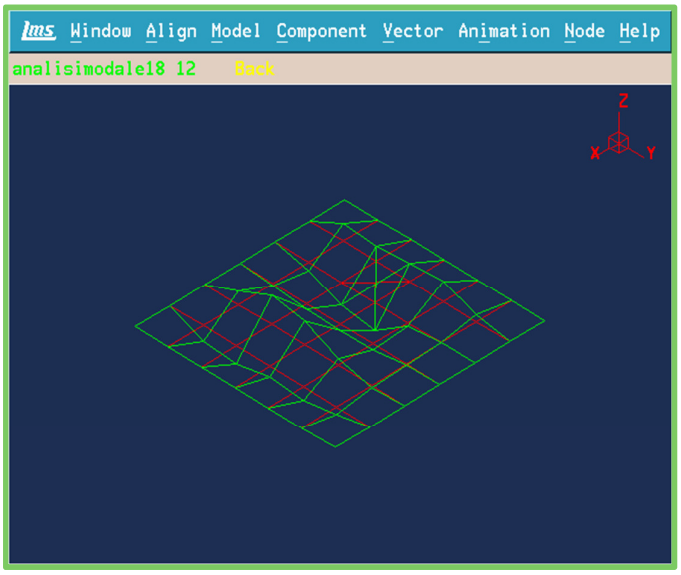


Figure 136: Mode (4-1) deformed, frequency 180,31 [Hz].

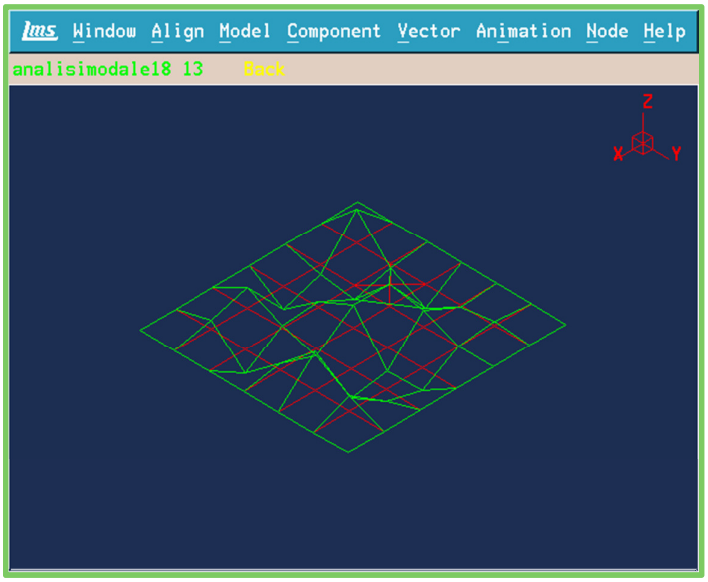


Figure 137: Mode (3-3), frequency 121,40 [Hz].

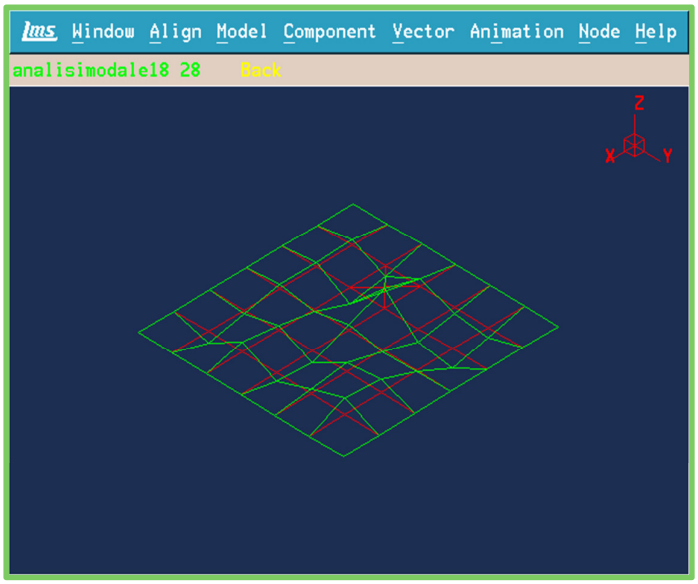


Figure 138: Mode (2-3), frequency 163,73 [Hz].

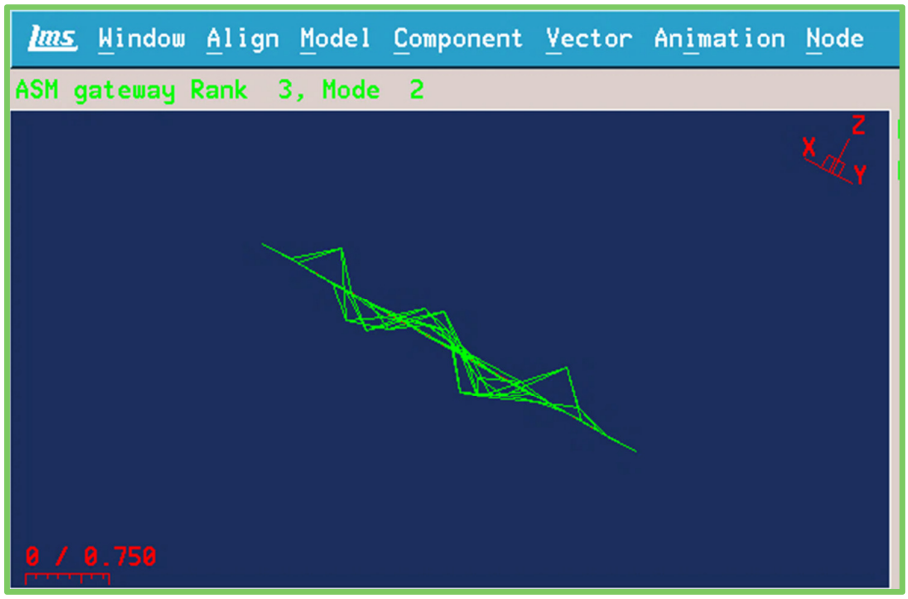


Figure 139: Mode (1-5), frequency 224,69 [Hz]. The figure shows the mode shape by axonometric inclined view in order to visualize five semi-waves along the y-axis.

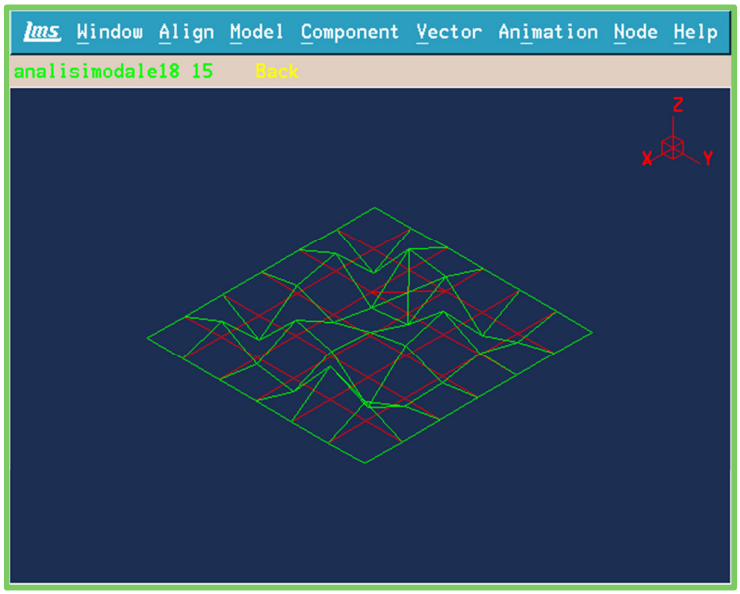


Figure 140: Mode (4-3), frequency 307,57 [Hz].

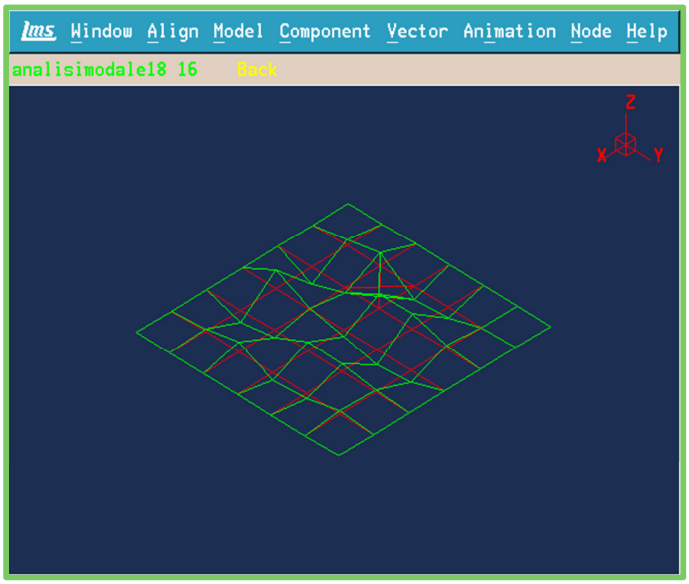


Figure 141: Mode (5-2), frequency 322,45 [Hz].

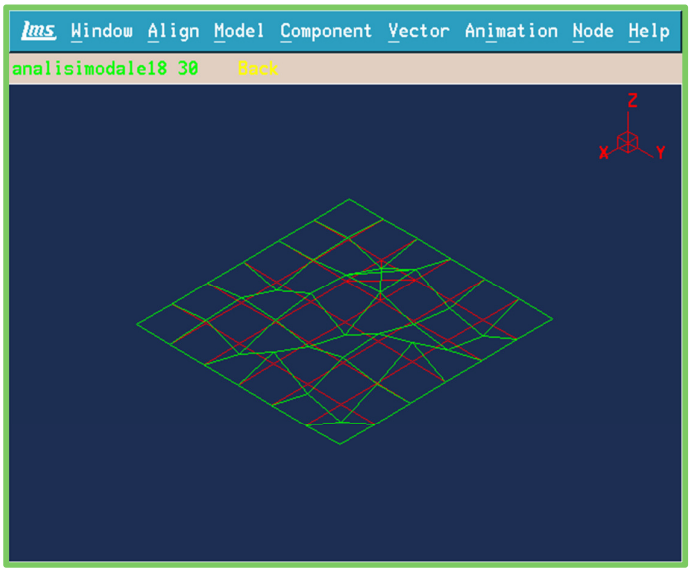


Figure 142: Mode (3-4), frequency 335,96 [Hz].

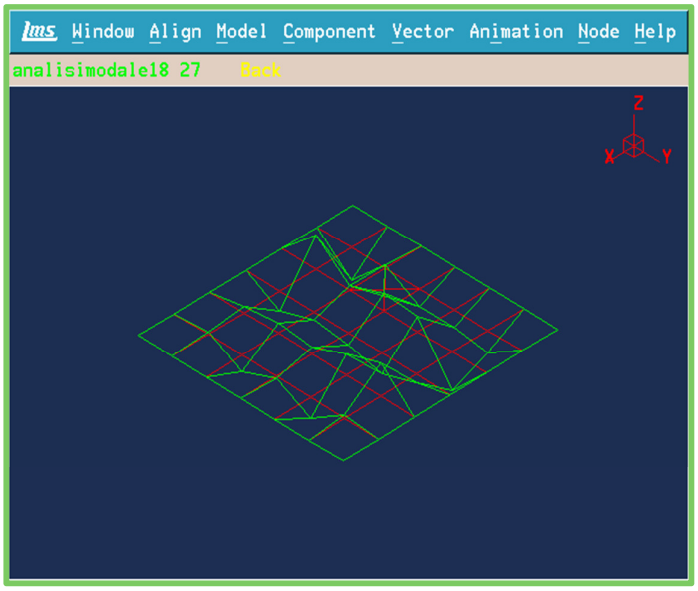


Figure 143: Mode (5-3), frequency 415,56 [Hz].

lms File View Select Help

Modal Assurance Criterion (%) for modes

No	mode no	freq Hz	mode_1 30.02	mode_2 58.14	mode_3 64.20	mode_4 93.89	mode_5 108.40	mode_6 134.22	mode_7 147.96	mode_8 180.31	mode_9 221.40	mode_10 224.69	mode_11 307.57	mode_12 322.45	mode_13 415.56
1	1	30.02	100.0												
2	2	58.14	0.2	100.0											
3	3	64.20	22.3	1.9	100.0										
4	4	93.89	2.5	9.5	1.0	100.0									
5	5	108.40	0.6	0.4	0.1	0.7	100.0								
6	6	134.22	0.1	3.6	5.1	0.1	2.4	100.0							
7	7	147.96	0.1	0.2	0.2	0.6	0.5	0.6	100.0						
8	8	180.31	3.1	4.3	2.7	0.4	0.0	1.0	0.1	100.0					
9	9	221.40	0.0	0.1	0.6	1.3	1.7	4.3	0.2	0.7	100.0				
10	10	224.69	0.5	0.1	0.9	2.2	0.9	0.3	0.5	0.8	0.1	100.0			
11	11	307.57	0.7	1.1	0.3	0.0	0.1	0.9	0.3	0.1	1.0	0.0	100.0		
12	12	322.45	0.1	0.4	0.1	0.9	0.3	0.7	0.2	1.1	0.6	0.2	0.1	100.0	
13	13	415.56	1.2	0.4	0.6	0.0	0.1	0.6	0.2	1.6	0.2	0.4	0.3	0.3	100.0
14	14	425.38	1.1	1.2	1.0	0.0	0.8	0.5	0.2	0.2	0.2	0.0	7.2	1.8	0.1
15	15	366.22	3.3	0.4	11.4	0.1	0.5	8.6	1.9	0.6	0.9	0.5	0.3	0.0	0.1
16	16	399.28	0.4	0.6	0.2	2.9	0.9	0.0	0.4	0.4	1.3	1.5	1.0	0.1	12.9
17	17	269.30	0.0	0.5	0.9	2.1	0.5	0.2	0.8	1.5	0.0	0.1	0.0	0.3	0.5
18	18	275.84	3.2	1.3	0.7	0.0	0.5	1.8	0.0	4.9	0.4	0.3	1.1	0.1	1.4
19	19	335.53	0.6	1.0	0.1	0.1	0.3	0.7	1.9	1.7	5.7	11.7	2.9	3.1	0.4
20	20	30.02	100.0	0.2	22.3	2.5	0.6	0.1	0.1	3.1	0.0	0.5	0.7	0.1	1.2
21	21	58.14	0.2	100.0	1.9	9.5	0.4	3.6	0.2	4.3	0.1	0.1	1.1	0.4	0.4
22	22	64.20	22.3	1.9	100.0	1.0	0.1	5.1	0.2	2.7	0.6	0.9	0.3	0.1	0.6
23	23	93.89	2.5	9.5	1.0	100.0	0.7	0.1	0.6	0.4	1.3	2.2	0.0	0.9	0.0

Figure 144: MAC Matrix for every mode shape obtained from the Modal Analysis.

lms File View Select Help

odal Phase Collinearity (MPC) and Deviation (MPD

No	mode nr	freq Hz	MPC (%)	MPD deg	phase scatter
1	1	30.02	99.8	1.30	low
2	2	58.14	99.6	4.16	low
3	3	64.20	99.7	2.93	low
4	4	93.89	99.9	1.76	low
5	5	108.40	100.0	1.18	low
6	6	134.22	99.7	3.27	low
7	7	147.96	97.6	9.22	low
8	8	180.31	99.9	2.27	low
9	9	221.40	100.0	0.76	low
10	10	224.69	99.9	2.10	low
11	11	307.57	99.9	2.18	low
12	12	322.45	99.8	2.69	low
13	13	415.56	98.4	7.77	low
14	14	425.38	100.0	0.18	low
15	15	366.22	96.4	11.13	low
16	16	399.28	98.0	8.27	low
17	17	269.30	99.6	3.70	low
18	18	275.84	99.3	4.71	low
19	19	335.53	97.3	10.32	low
20	20	30.02	99.8	1.30	low
21	21	58.14	99.6	4.16	low
22	22	64.20	99.7	2.93	low
23	23	93.89	99.9	1.76	low
24	24	108.40	100.0	1.18	low
25	25	134.22	99.7	3.27	low
26	26	147.96	97.6	9.22	low
27	27	180.31	99.9	2.27	low
28	28	221.40	100.0	0.76	low
29	29	224.69	99.9	2.10	low
30	30	307.57	99.9	2.18	low
31	31	322.45	99.8	2.69	low
32	32	415.56	98.4	7.77	low
33	33	425.38	100.0	0.18	low
34	34	399.28	98.0	8.27	low
35	35	269.30	99.6	3.70	low
36	36	275.84	99.3	4.71	low
37	37	335.53	97.3	10.32	low

Figure 145: Modal Phase Collinearity for every mode shape obtained from the Modal Analysis.

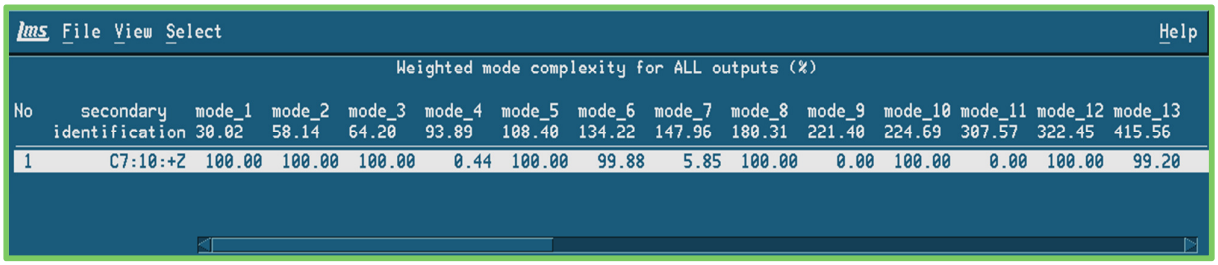


Figure 146: Mode Complexity of the Plate when the tank is filled with 18 [cm] of water.

The case of the liquid filling level is equal to 23 [cm]

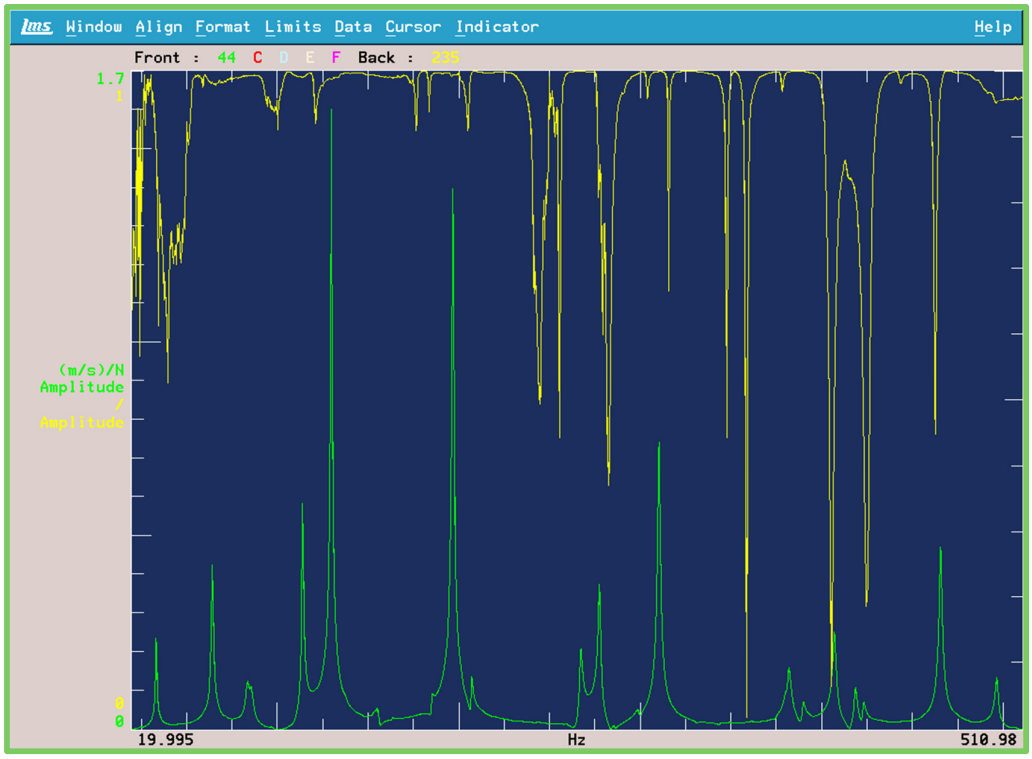


Figure 147: Frequency Response Function and Coherence. The laser beam is fixed in C_{710}.

Frequency [Hz]	Damping [%]	Modal Shapes
22,44	**1,39%**	1-1
57,35	**1,39%**	1-2
60,66	0,39%	2-1
86,35	0,22%	2-2
107,02	0,21%	1-3
117,05	0,55%	1-3
134,38	0,44%	3-2
139,68	0,19%	2-3
180,48	0,18%	4-1
189,89	0,22%	3-3
194,49	0,17%	1-4
207,99	0,16%	4-2
220,93	0,16%	2-4
264,89	0,18%	4-3
274,53	0,18%	3-4
275,66	0,23%	5-1
303,24	0,13%	1-5
307,18	0,15%	5-2
330,61	0,17%	2-5
351,99	0,14%	4-4
367,40	0,14%	5-3
387,80	0,16%	3-5
401,65	0,17%	4-5
431,33	0,13%	5-4
442,73	0,16%	4-2
456,45	0,15%	5-4
468,14	0,14%	4-5

Table 12: Frequency, Damping and Modal Shapes. The Damping ratio is increased only for the Modal Shape (1-1) and (1-2). The other forms have modal damping values that are not significantly different from the previous case.

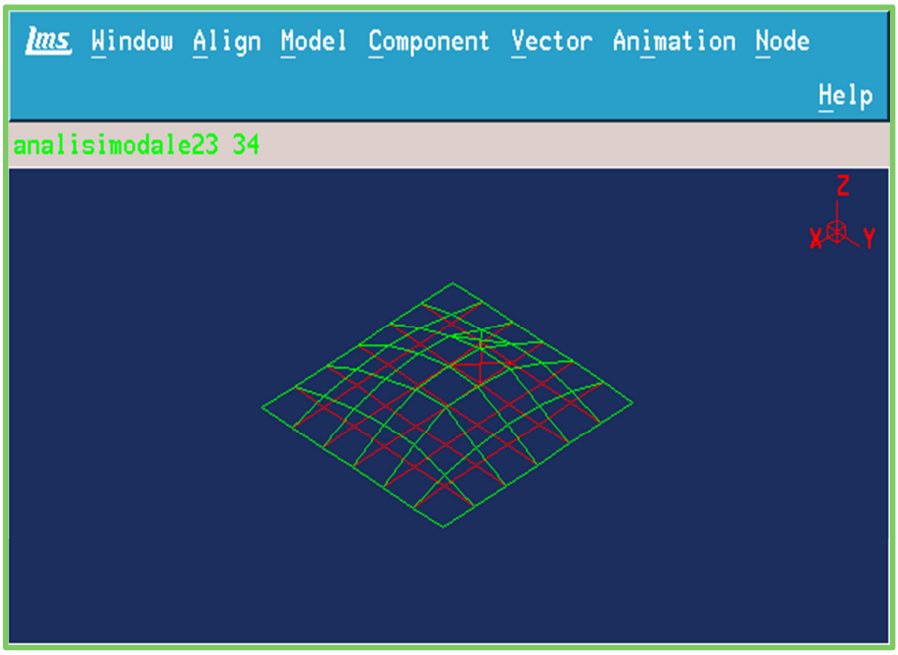


Figure 148: Mode (1-1), frequency 22,44 [Hz].

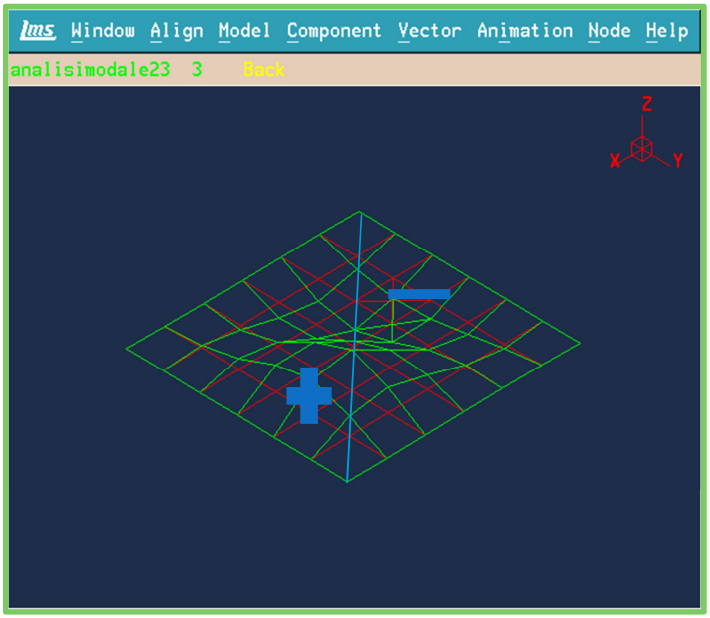


Figure 149: Mode (2-1), frequency 57,35 [Hz].

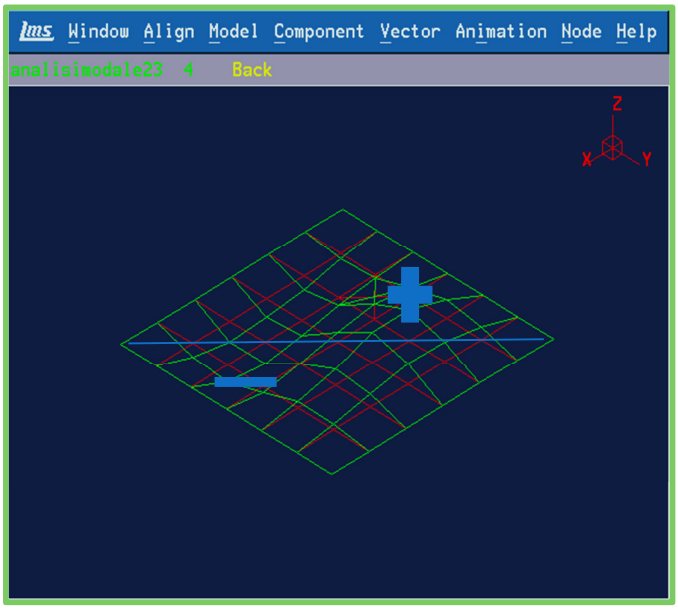


Figure 150: Mode (2-1), frequency 60,66 [Hz].

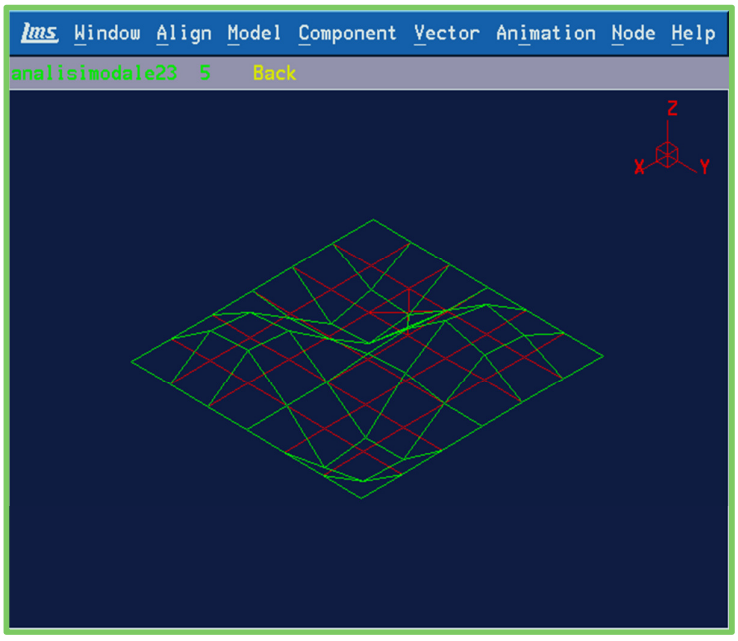


Figure 151: Mode (2-2), frequency 86,35 [Hz].

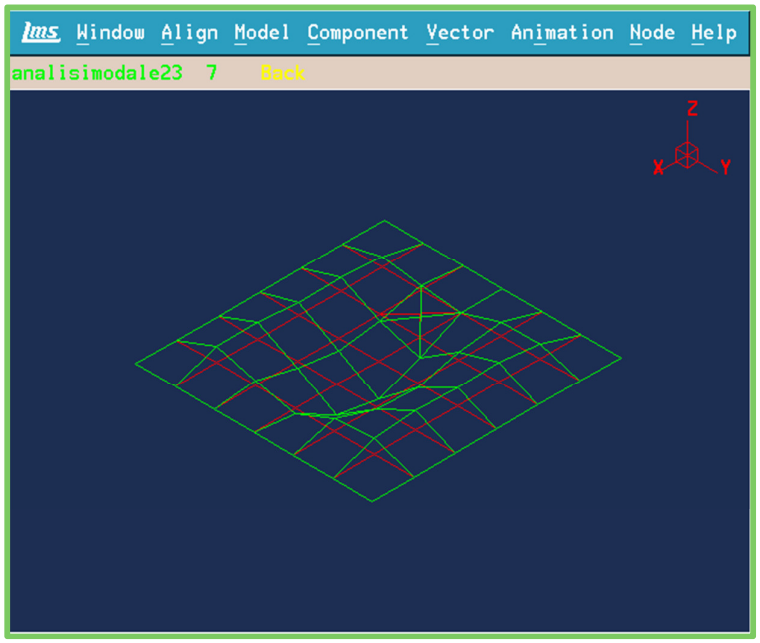


Figure 152: Mode (1-3), frequency 107,02 [Hz].

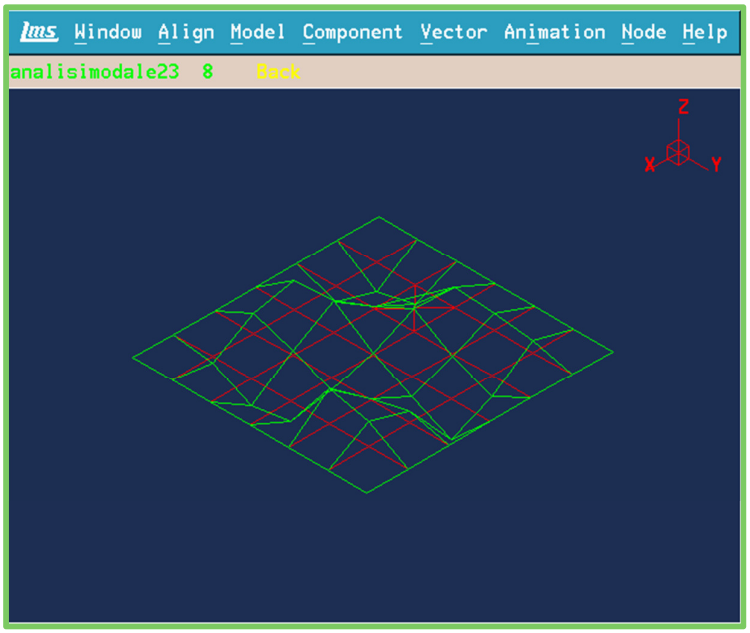


Figure 153: Mode (3-2), frequency 134,38 [Hz].

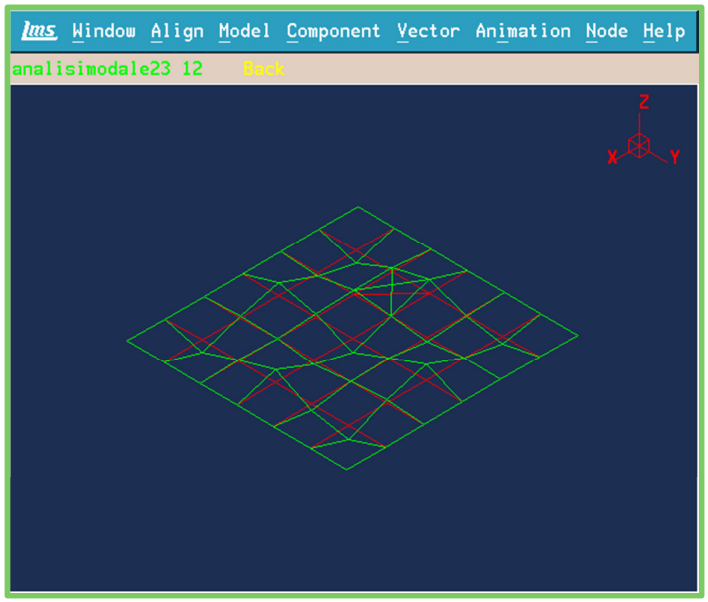


Figure 154: Mode (2-3) deformed and asymmetrical, frequency 139,68 [Hz].

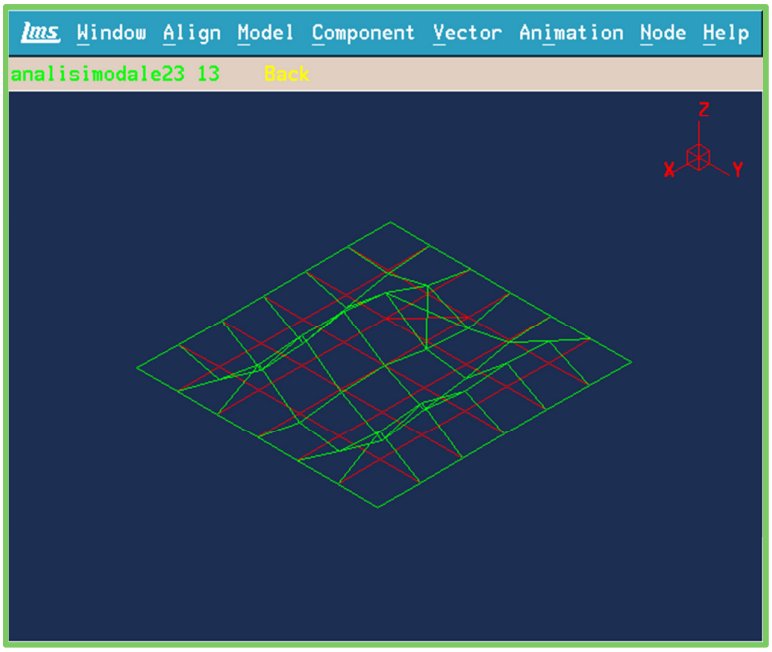


Figure 155: Mode (1-4) deformed, frequency 194,49 [Hz].

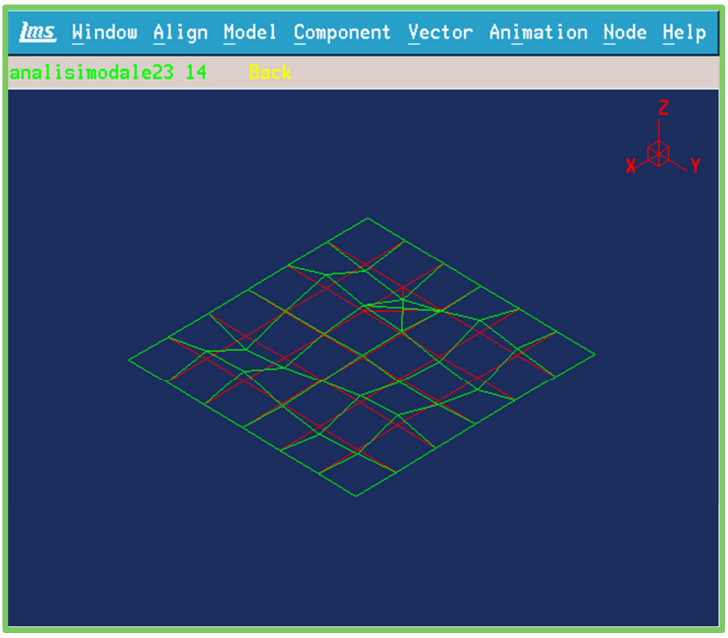


Figure 156: Mode (4-2) deformed, frequency 207,99 [Hz].

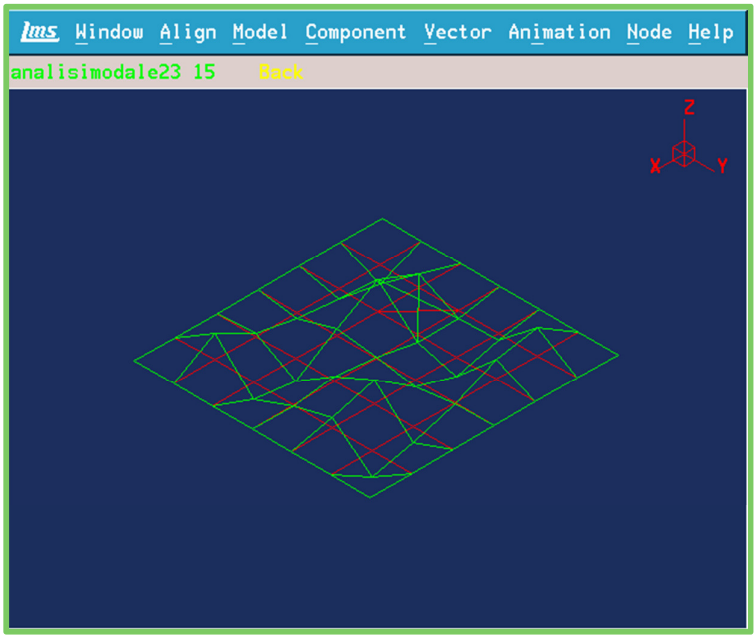


Figure 157: Mode (2-4), frequency 220,93 [Hz].

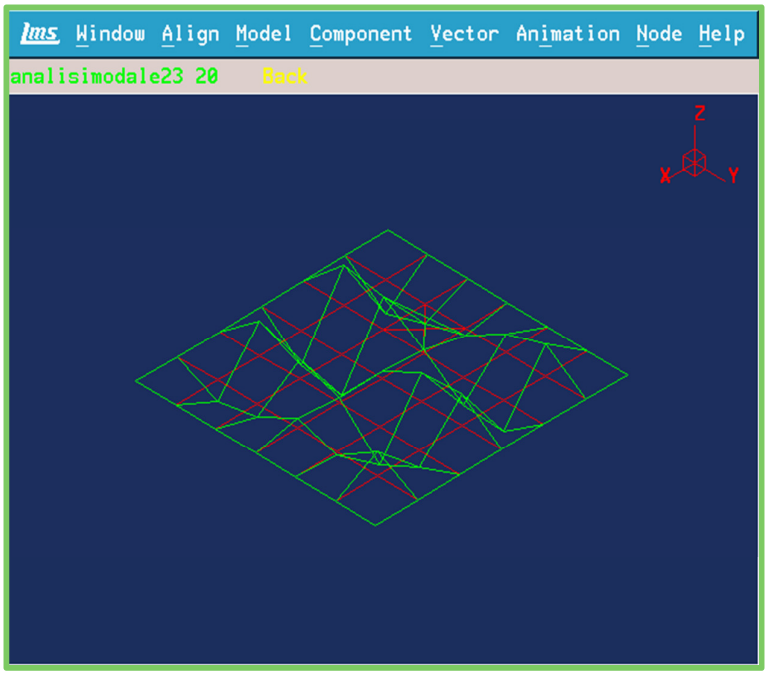


Figure 158: Mode (5-2), frequency 307,18 [Hz].

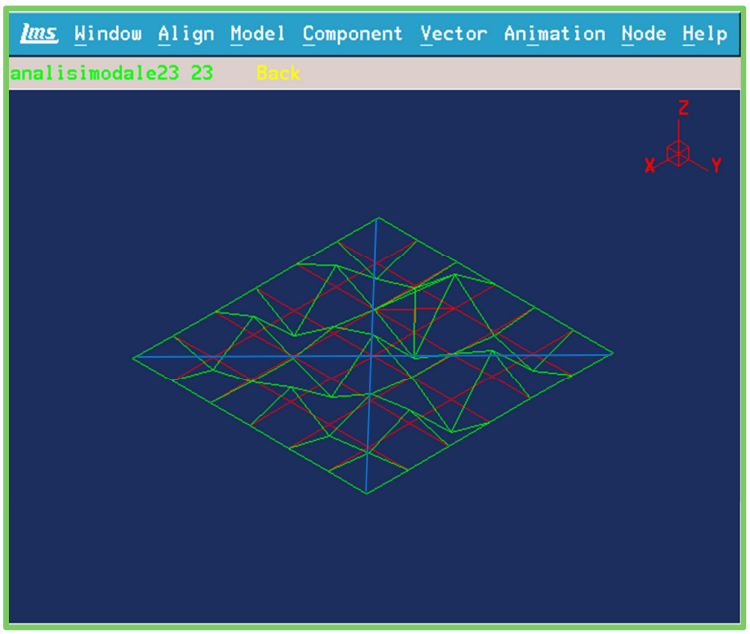


Figure 159: Mode (3-3) diagonal and symmetric, frequency 189,89 [Hz].

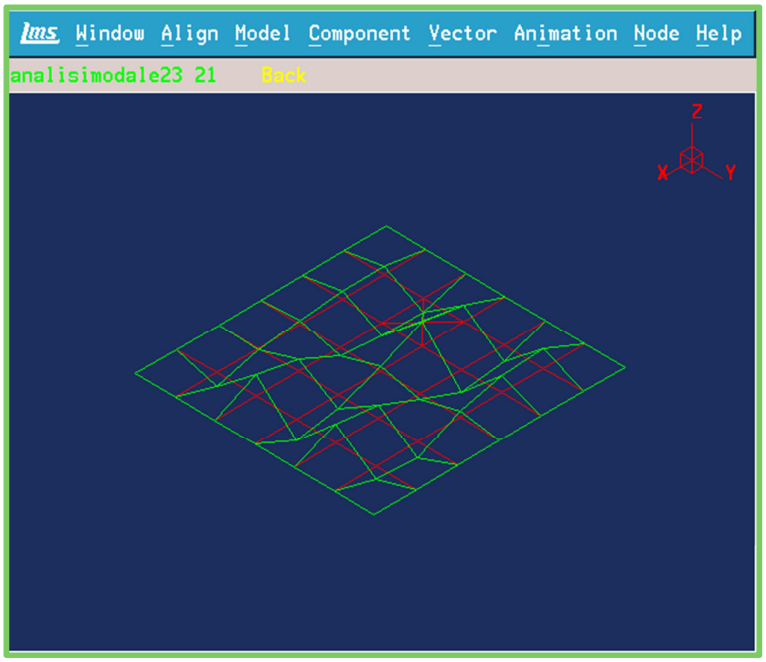


Figure 160: Mode (2-5), frequency 330,61 [Hz].

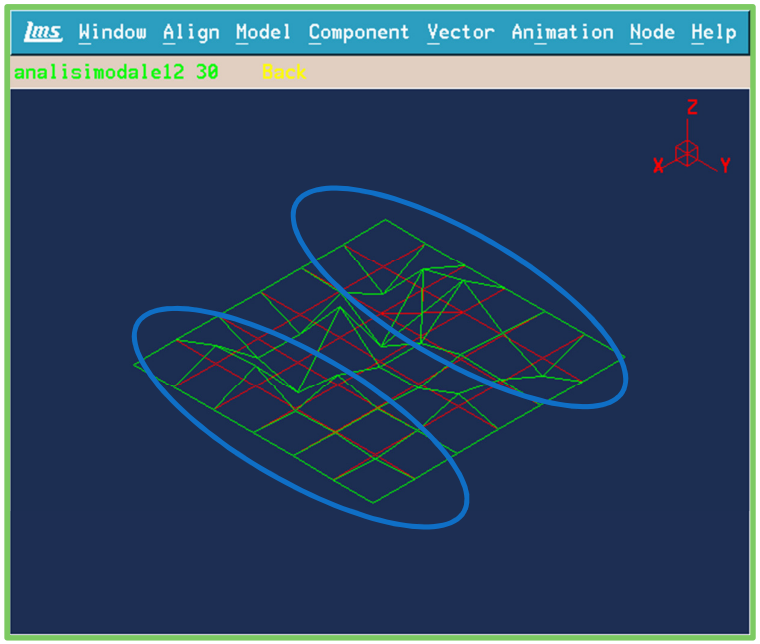


Figure 161: Mode (5-3) asymmetrical, frequency 367,40 [Hz].

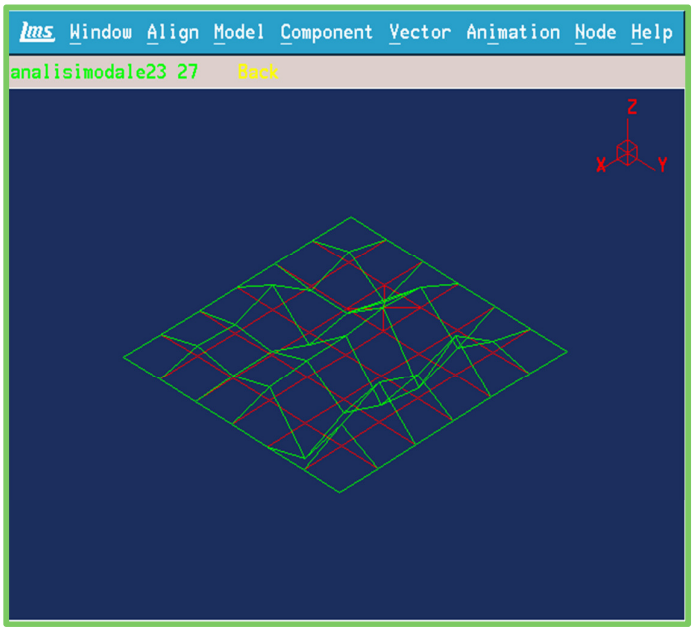


Figure 163: Mode (4-4), frequency 351,99 [Hz].

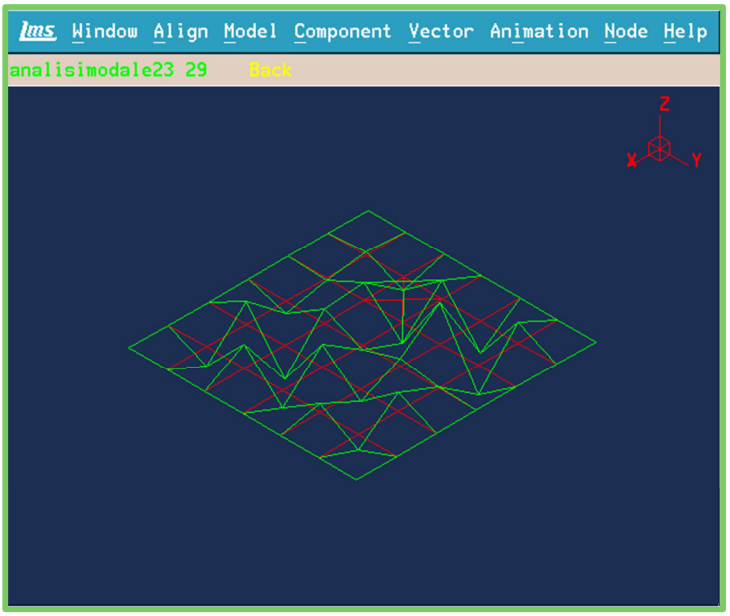
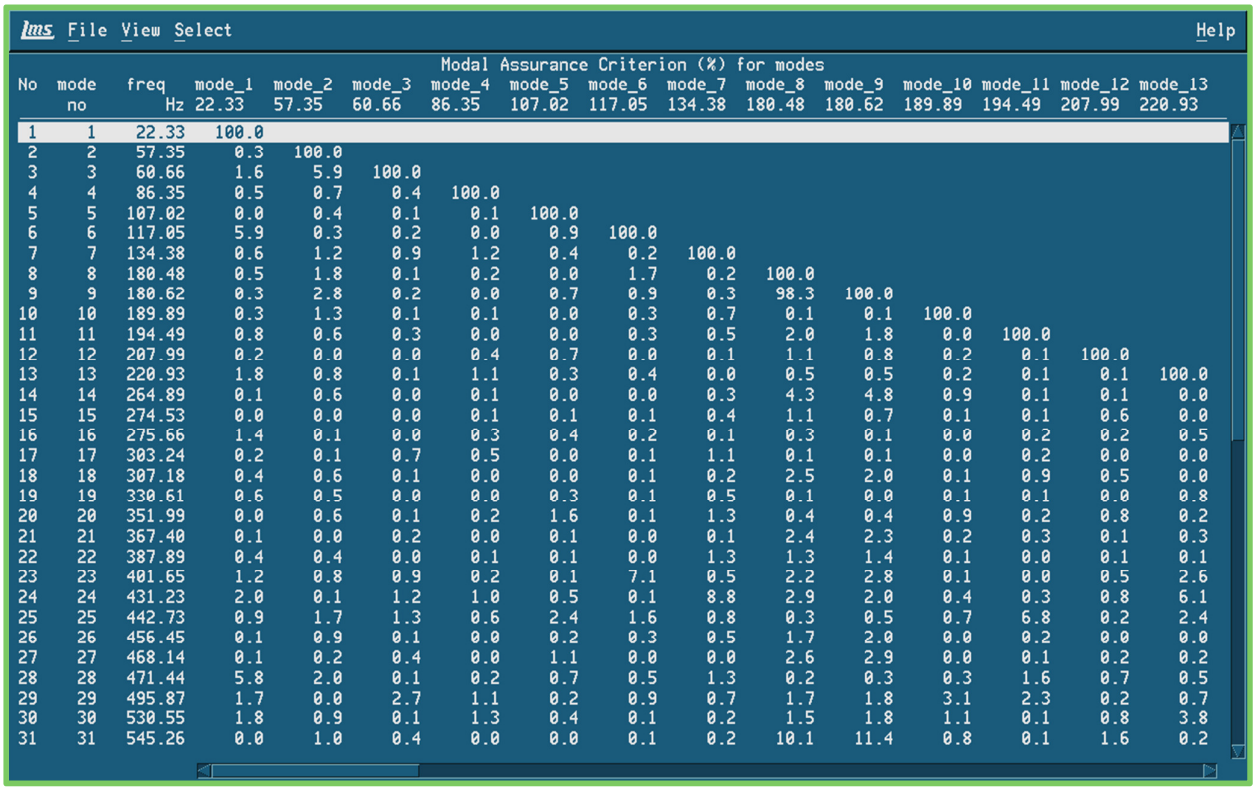


Figure 164: Mode (4-5), frequency 468,14 [Hz].

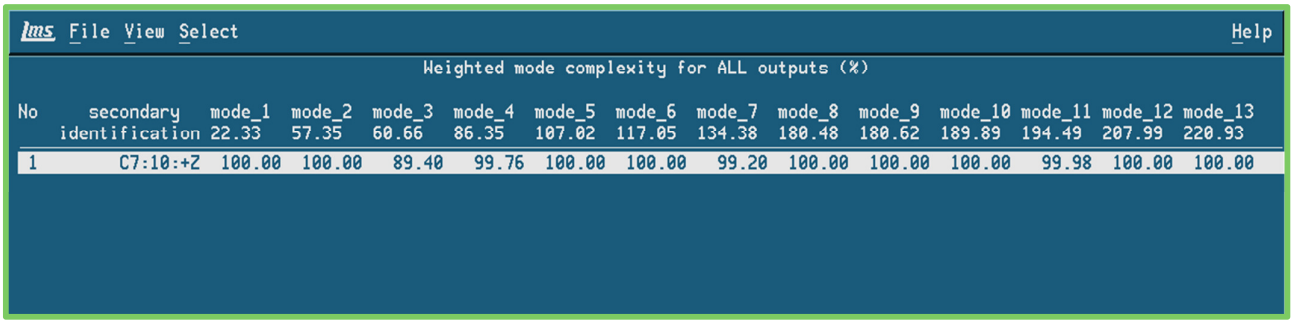


lms File View Select Help

Modal Assurance Criterion (%) for modes

No	mode no	freq Hz	mode_1 22.33	mode_2 57.35	mode_3 60.66	mode_4 86.35	mode_5 107.02	mode_6 117.05	mode_7 134.38	mode_8 180.48	mode_9 180.62	mode_10 189.89	mode_11 194.49	mode_12 207.99	mode_13 220.93
1	1	22.33	100.0												
2	2	57.35	0.3	100.0											
3	3	60.66	1.6	5.9	100.0										
4	4	86.35	0.5	0.7	0.4	100.0									
5	5	107.02	0.0	0.4	0.1	0.1	100.0								
6	6	117.05	5.9	0.3	0.2	0.0	0.9	100.0							
7	7	134.38	0.6	1.2	0.9	1.2	0.4	0.2	100.0						
8	8	180.48	0.5	1.8	0.1	0.2	0.0	1.7	0.2	100.0					
9	9	180.62	0.3	2.8	0.2	0.0	0.7	0.9	0.3	98.3	100.0				
10	10	189.89	0.3	1.3	0.1	0.1	0.0	0.3	0.7	0.1	0.1	100.0			
11	11	194.49	0.8	0.6	0.3	0.0	0.0	0.3	0.5	2.0	1.8	0.0	100.0		
12	12	207.99	0.2	0.0	0.0	0.4	0.7	0.0	0.1	1.1	0.8	0.2	0.1	100.0	
13	13	220.93	1.8	0.8	0.1	1.1	0.3	0.4	0.0	0.5	0.5	0.2	0.1	0.1	100.0
14	14	264.89	0.1	0.6	0.0	0.1	0.0	0.0	0.3	4.3	4.8	0.9	0.1	0.1	0.0
15	15	274.53	0.0	0.0	0.0	0.1	0.1	0.1	0.4	1.1	0.7	0.1	0.1	0.6	0.0
16	16	275.66	1.4	0.1	0.0	0.3	0.4	0.2	0.1	0.3	0.1	0.0	0.2	0.2	0.5
17	17	303.24	0.2	0.1	0.7	0.5	0.0	0.1	1.1	0.1	0.1	0.0	0.2	0.0	0.0
18	18	307.18	0.4	0.6	0.1	0.0	0.0	0.1	0.2	2.5	2.0	0.1	0.9	0.5	0.0
19	19	330.61	0.6	0.5	0.0	0.0	0.3	0.1	0.5	0.1	0.0	0.1	0.1	0.0	0.8
20	20	351.99	0.0	0.6	0.1	0.2	1.6	0.1	1.3	0.4	0.4	0.9	0.2	0.8	0.2
21	21	367.40	0.1	0.0	0.2	0.0	0.1	0.0	0.1	2.4	2.3	0.2	0.3	0.1	0.3
22	22	387.89	0.4	0.4	0.0	0.1	0.1	0.0	1.3	1.3	1.4	0.1	0.0	0.1	0.1
23	23	401.65	1.2	0.8	0.9	0.2	0.1	7.1	0.5	2.2	2.8	0.1	0.0	0.5	2.6
24	24	431.23	2.0	0.1	1.2	1.0	0.5	0.1	8.8	2.9	2.0	0.4	0.3	0.8	6.1
25	25	442.73	0.9	1.7	1.3	0.6	2.4	1.6	0.8	0.3	0.5	0.7	6.8	0.2	2.4
26	26	456.45	0.1	0.9	0.1	0.0	0.2	0.3	0.5	1.7	2.0	0.0	0.2	0.0	0.0
27	27	468.14	0.1	0.2	0.4	0.0	1.1	0.0	0.0	2.6	2.9	0.0	0.1	0.2	0.2
28	28	471.44	5.8	2.0	0.1	0.2	0.7	0.5	1.3	0.2	0.3	0.3	1.6	0.7	0.5
29	29	495.87	1.7	0.0	2.7	1.1	0.2	0.9	0.7	1.7	1.8	3.1	2.3	0.2	0.7
30	30	530.55	1.8	0.9	0.1	1.3	0.4	0.1	0.2	1.5	1.8	1.1	0.1	0.8	3.8
31	31	545.26	0.0	1.0	0.4	0.0	0.0	0.1	0.2	10.1	11.4	0.8	0.1	1.6	0.2

Figure 165: MAC Matrix for every mode shape obtained from the Modal Analysis.

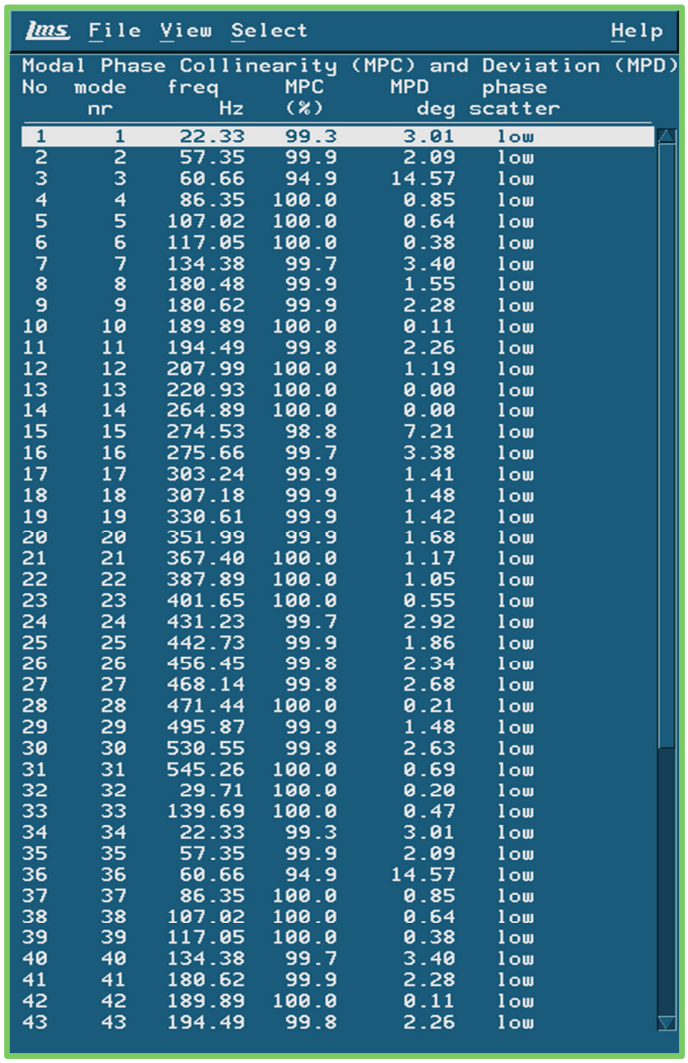


lms File View Select Help

Weighted mode complexity for ALL outputs (%)

No	secondary identification	mode_1 22.33	mode_2 57.35	mode_3 60.66	mode_4 86.35	mode_5 107.02	mode_6 117.05	mode_7 134.38	mode_8 180.48	mode_9 180.62	mode_10 189.89	mode_11 194.49	mode_12 207.99	mode_13 220.93
1	C7:10:+Z	100.00	100.00	89.40	99.76	100.00	100.00	99.20	100.00	100.00	100.00	99.98	100.00	100.00

Figure 166: Mode Complexity for all Outputs[%].



lms File View Select Help

Modal Phase Collinearity (MPC) and Deviation (MPD)

No	mode nr	freq Hz	MPC (%)	MPD deg	phase scatter
1	1	22.33	99.3	3.01	low
2	2	57.35	99.9	2.09	low
3	3	60.66	94.9	14.57	low
4	4	86.35	100.0	0.85	low
5	5	107.02	100.0	0.64	low
6	6	117.05	100.0	0.38	low
7	7	134.38	99.7	3.40	low
8	8	180.48	99.9	1.55	low
9	9	180.62	99.9	2.28	low
10	10	189.89	100.0	0.11	low
11	11	194.49	99.8	2.26	low
12	12	207.99	100.0	1.19	low
13	13	220.93	100.0	0.00	low
14	14	264.89	100.0	0.00	low
15	15	274.53	98.8	7.21	low
16	16	275.66	99.7	3.38	low
17	17	303.24	99.9	1.41	low
18	18	307.18	99.9	1.48	low
19	19	330.61	99.9	1.42	low
20	20	351.99	99.9	1.68	low
21	21	367.40	100.0	1.17	low
22	22	387.89	100.0	1.05	low
23	23	401.65	100.0	0.55	low
24	24	431.23	99.7	2.92	low
25	25	442.73	99.9	1.86	low
26	26	456.45	99.8	2.34	low
27	27	468.14	99.8	2.68	low
28	28	471.44	100.0	0.21	low
29	29	495.87	99.9	1.48	low
30	30	530.55	99.8	2.63	low
31	31	545.26	100.0	0.69	low
32	32	29.71	100.0	0.20	low
33	33	139.69	100.0	0.47	low
34	34	22.33	99.3	3.01	low
35	35	57.35	99.9	2.09	low
36	36	60.66	94.9	14.57	low
37	37	86.35	100.0	0.85	low
38	38	107.02	100.0	0.64	low
39	39	117.05	100.0	0.38	low
40	40	134.38	99.7	3.40	low
41	41	180.62	99.9	2.28	low
42	42	189.89	100.0	0.11	low
43	43	194.49	99.8	2.26	low

Figure 167: Modal Phase Collinearity (MPC).

7. Hydroelastic Vibrations based on Finite Element Method

In the framework of the vibrational analysis of structures, many researchers have investigated the change in natural frequencies when a structure is in contact with a liquid. There have been many theoretical and experimental researchers on the dynamic characteristics of single plate in contact with water and also several methods available to take into account internal liquids (propellants for instance) in structure modelling. The case of a structure partially filled with incompressible liquids is very common and many industrial domains are interested in this issue especially in the transport and aerospace industries (wing tanks of aircrafts, liquid propelled launchers, etc.). Because the computing cost of a full time solution of the *Arbitrary Lagrange Euler equations* of the problem becomes quickly prohibitive, a modal approach is generally preferred. The literature presents a large number of studies dealing with different boundary conditions, different solution methods and complicating effects. Anyway, even if a large number of theoretical studies on large amplitude vibrations of plates are available in the scientific literature, experimental results are limited. It is assumed that the plate is simply supported along the four edges and its side edges are fixed. Wet dynamic displacements of the plate are by combining the orthogonal polynomials satisfying the boundary conditions: a linear model has been used to take into account an internal incompressible liquid in the vibratory analysis of the entire system (plate and tank). A fluid–structure model is proposed to compute the *"added mass"* operator of the liquid, is the hydroelastic. This model has proven to give quite good results and is now integrated in the main commercial computational structural mechanics codes. However, due to some simplifying assumptions concerning the influence of the gravity, this formulation does not represent the liquid's proper dynamics (i.e. the waves at its free surface). This phenomenon, called as *"sloshing"*, may have a critical impact on the stability and the piloting of the structure.

7.1 System Description

Figure (168) represents the generic internal fluid–structure interaction between the plate and the liquid system considered here: the interaction has been modeled considering different liquid-contacting areas which correspond to four levels of filling. The elastic tank is denoted by Ω^S; it is filled by a Newtonian homogeneous incompressible fluid Ω^F. The liquid free surface and fluid–structure interface are respectively denoted by Γ and $\sum_i$. This system is subjected to volumic loads due to the gravity $\boldsymbol{g}$ and to external surface loads. Furthermore, the displacement of the tank is supposed to be known (equal to 0 for the sake of convenience). A condition of *fixed constraint* is applied to the base of the tank; this is able to make the geometric entity fixed (fully constrained); that is, the displacements are zero in all directions. The chosen variable for the structure is its displacement field u^S and because there is no fluid flow in this problem, it is particularly convenient here to choose the displacement u^F field to describe the liquid. As we are interested only in the vibratory study of this system, external excitations are supposed to be harmonic and stationary solutions of pulsation ω are sought. The damping coming from the internal fluid is supposed to be much lower than other damping sources of the system (structural damping, external aerodynamic damping, etc.). When looking for the *eigenmodes* of the system, we will consider the conservative associated system and omit the damping aspect (the liquid will be supposed inviscid). For frequency response computation, *Basile's hypothesis* will be used to suppose a decoupling of the fluid modal damping which can be obtained by experimental or numerical methods. In the frequency range of interest, the compressibility effects in the liquid can also be neglected. It could be proven that the irrotationality of the linear movements of such a liquid is a consequence of all these assumptions. It will distinguish in this study the static initial state of the system (described by the displacements u_0^S and u_0^F) which is the reference state for the vibratory analysis, from the dynamic position of the system (described by displacements u^S and u^F). Consequently, the harmonic vibrational equations will be expressed with unknown U^S and U^F which describe the linear vibrations around the initial reference state.

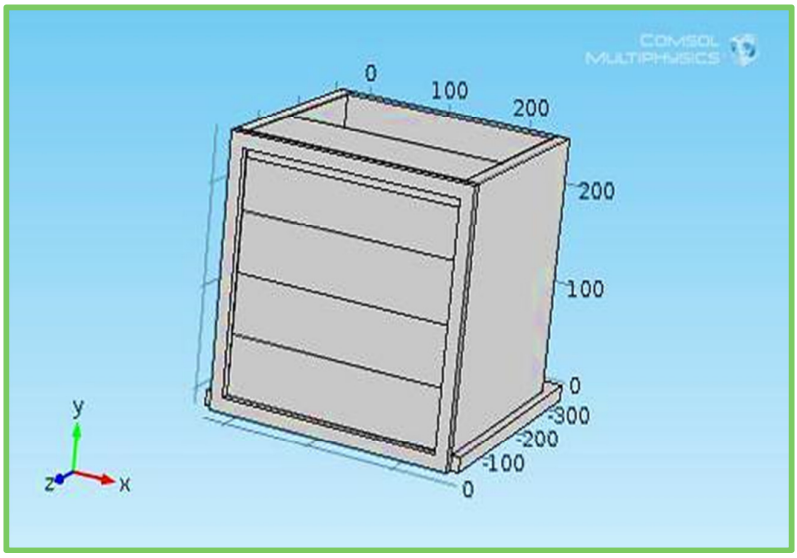


Figure 168: The Geometry Model of the Plate and the Tank.

$$U^S = u^S - u_0^S \tag{1a}$$

$$U^F = u^F - u_0^F \tag{1b}$$

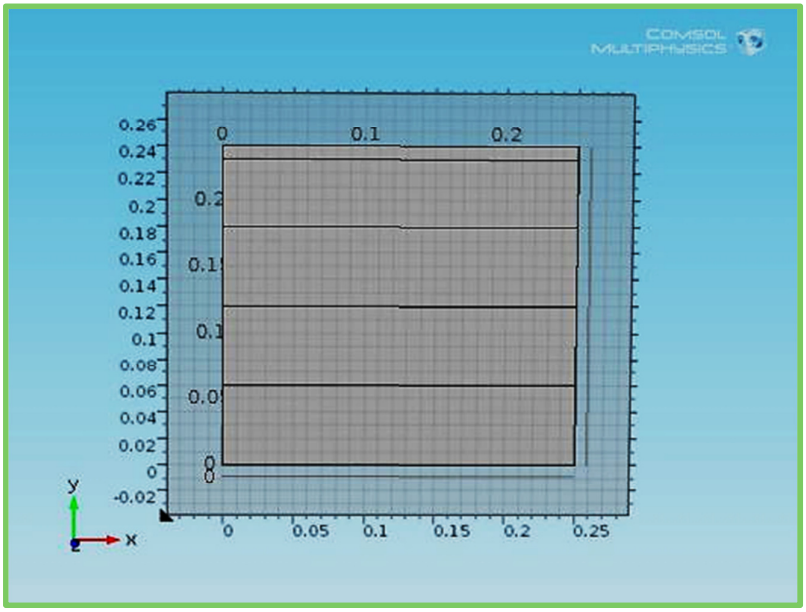


Figure 169: The Geometry of the Plate divided in five sections.

The ***Shell interface***, found under the Structural Mechanics branch is used to model the thin on 3D boundaries. Shells are thin flat or curved structures, having significant bending stiffness. The interface uses shell elements of the MITC type, which can be used for analysing both thin (*Kirchhoff Theory*) and thick (*Mindlin Theory*) shells. Geometric nonlinearity can be also taken into account. To describe a shell, you provide its thickness and the elastic material properties. The dependent variables are the displacements u, v, and w in the global x, y, and z directions, and the displacements of the shell normals a_x, a_y, and a_z in the global x, y, and z directions. For input and output, the Shell interface to a large extent replaces the latter variables by the more customary rotations θ_x, θ_y, and θ_z about the global axes. For a geometrically linear analysis, the relation between normal displacement and rotation vector is simple: $\boldsymbol{a} = \theta \times \boldsymbol{n}$, where $\boldsymbol{n}$ is the unit normal of the shell. The ***Linear Elastic Material*** node adds the equations for a linear elastic shell and an interface for defining the elastic material properties of the AISI 304 stainless steel rectangular plate:

- *Young's modulus: $E = 198$ [GPa]*;
- *Poisson coefficient*: $\nu = 0.3$;
- *Mass density:* $\boldsymbol{\rho} = 7850\ [kg/m^3]$;

The ***Initial Values*** node adds the initial values for the translational displacement and velocity field as well as the for the normal displacement and velocity field. The initial values for the plate are the followings:

- *Displacement field u (SI unit: m); the displacement components u, v, and w:* $\begin{cases} u = 0 \\ v = 0 \\ w = 0 \end{cases}$;
- *Velocity field (SI unit: m/s):* $\begin{cases} \frac{\partial v_x}{\partial t} = 0 \\ \frac{\partial v_y}{\partial t} = 0 \\ \frac{\partial v_z}{\partial t} = 0 \end{cases}$;
- *Displacement of shell normal* $\boldsymbol{a_r}$ (dimensionless): $\boldsymbol{a_{r_{x,y,z}}} = 0$;
    - *Displacement of shell normal, first time derivative* (SI unit: 1/s): $\frac{\partial \boldsymbol{a_{r_{x,y,z}}}}{\partial t} = 0$;

The ***Prescribed Displacement/Rotation*** node adds an edge, boundary, domain, or point condition to a model where the displacements and rotations are prescribed in one or more directions. The conditions selected for the plate is called *Local Edge System.* Local edge coordinate systems directions x_i, y_i, and z_i are defined so that:

- The first direction (x_i) is along the edge;
- The third direction (z_i) is the same as the shell normal direction;
- The second direction (y_i) is in the plane of the shell, and formed by the cross product of z_i and x_i.

To define a *prescribed displacement* for each spatial direction (x, y, and z) of the plate, it has been imposed a displacement for all directions, as shown in the next expression:

$$\begin{cases} u_0 = u_2 \\ v_0 = v_2 \\ w_0 = w_2 \end{cases} \tag{3}$$

where u_2, v_2 and w_2 are the displacement components of the tank.

A *Normal vector* is used to describe the rotational degrees of freedom as a prescribed normal vector. The components of the Prescribed normal vector $\boldsymbol{N_0}$ (dimensionless) for rotations are:

$$\boldsymbol{N_0} =: \begin{cases} rotx = \boldsymbol{solid.curlUX} \\ roty = \boldsymbol{solid.curlUY} \\ rotz = \boldsymbol{solid.curlUZ} \end{cases} \tag{4}$$

Variables can make a model easier to understand by introducing short and descriptive names for complicated expressions. Most variables for material properties, coordinates, and other quantities defined on the computational domain are *"field variables"*, that is, they are defined so that they can vary in space and time. For example, a built-in variable for the rotation in a Solid Mechanics interface, **solid.curlU**, represents a rotation θ as $\theta(x, y, z, t)$ in 3D.

$$a_{r_{x,y,z}} = \frac{N_0}{\|N_0\|} - N_{undeformed} \tag{5}$$

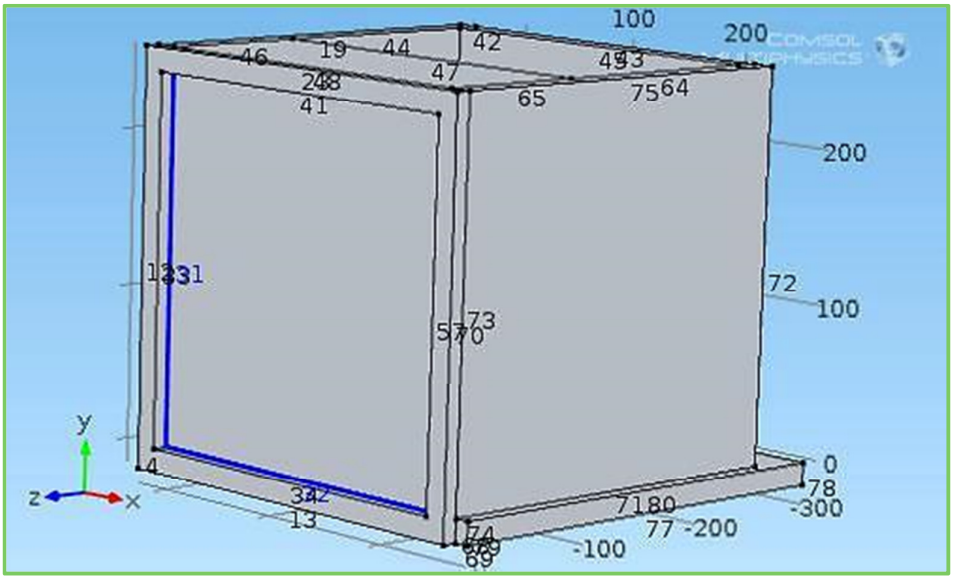


Figure 170: The Prescribed Displacement/Rotation node applied along the edges of the Plate.

7.2 Finite Element Model for Thin Plate and Tank

In order to check the experimental results, three dimensional finite element analysis has been carried out for the system by using a commercial computer code *COMSOL Multiphysics.* Finite element model has been constructed with the container geometry, plate geometry, boundary conditions and real materials properties. The steel tank has a density of 7850 $[kg/m^3]$, Young's Modulus equal to $200e^9$ [Pa] and Poisson's ratio of 0.33. Physical properties of the plate are, instead, these previously described. COMSOL software has been performed to obtain the natural frequencies and the mode shapes of the rectangular plate and also of the tank. The model has been constructed using *elastic shell elements* and solid mechanics elements, respectively, for the plate and for the tank. The facing rectangular plate of the tank has been modeled with 2D *Mapped Mesh*. For the 2D mapped meshing technique to work properly, the geometry must be reasonably regular. The following conditions must be satisfied:

- Each domain must be bounded by at least four boundary segments;
- Each domain must be bounded by only one connected boundary component (that is, no holes are allowed);
- The domains must not contain isolated or embedded vertices or boundary segments;
- The shape of each domain must not differ significantly from a rectangle.

Free Tetrahedral Mesh has behaved to create an unstructured tetrahedral mesh for the tank. In order to achieve correct results, it is necessary that the nodes situated alongside the edges of the plate must be coincident with the adjacent tetrahedral nodes located on the frame.

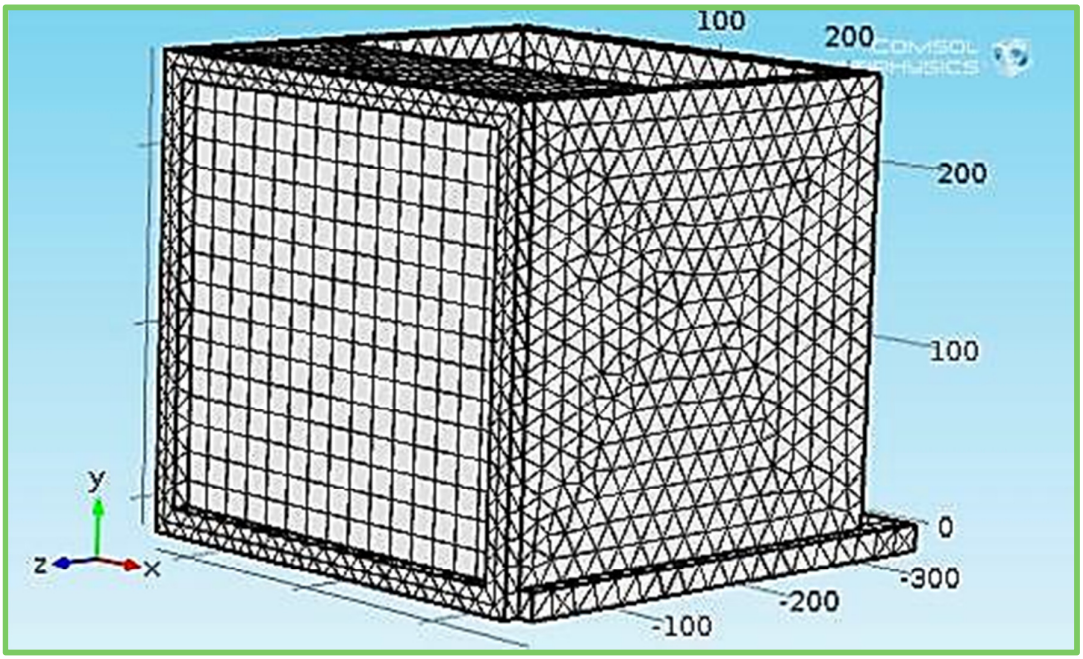


Figure 171: 2D Mapped Mesh and Free Tetrahedral Mesh for the Plate and Tank.

The modal results and natural frequencies are presented by means of graphs and tables both for the thin plate and the steel tank. The proposed computational method has been verified by observing a satisfactory agreement with the experimental results acquired during laboratory tests. It has been shown that the dynamic characteristics of the plate put on view a similarity to those observed experimentally. All the same, it is important to underline that there is not a strictly correspondence between experimental frequency values and frequency values gained using the software code. This is a consequence of the fact that tested values are influenced by some factors as, for example, temperature, humidity and superficial imperfections (the plate is not perfectly flat) which must be taken into account. These imperfections can modify the stiffness and the elastic behaviour of the material; in addition to this, thermal stress, due to sudden change in temperature, is often the cause of less-than-perfect from these found as a result of simulations.

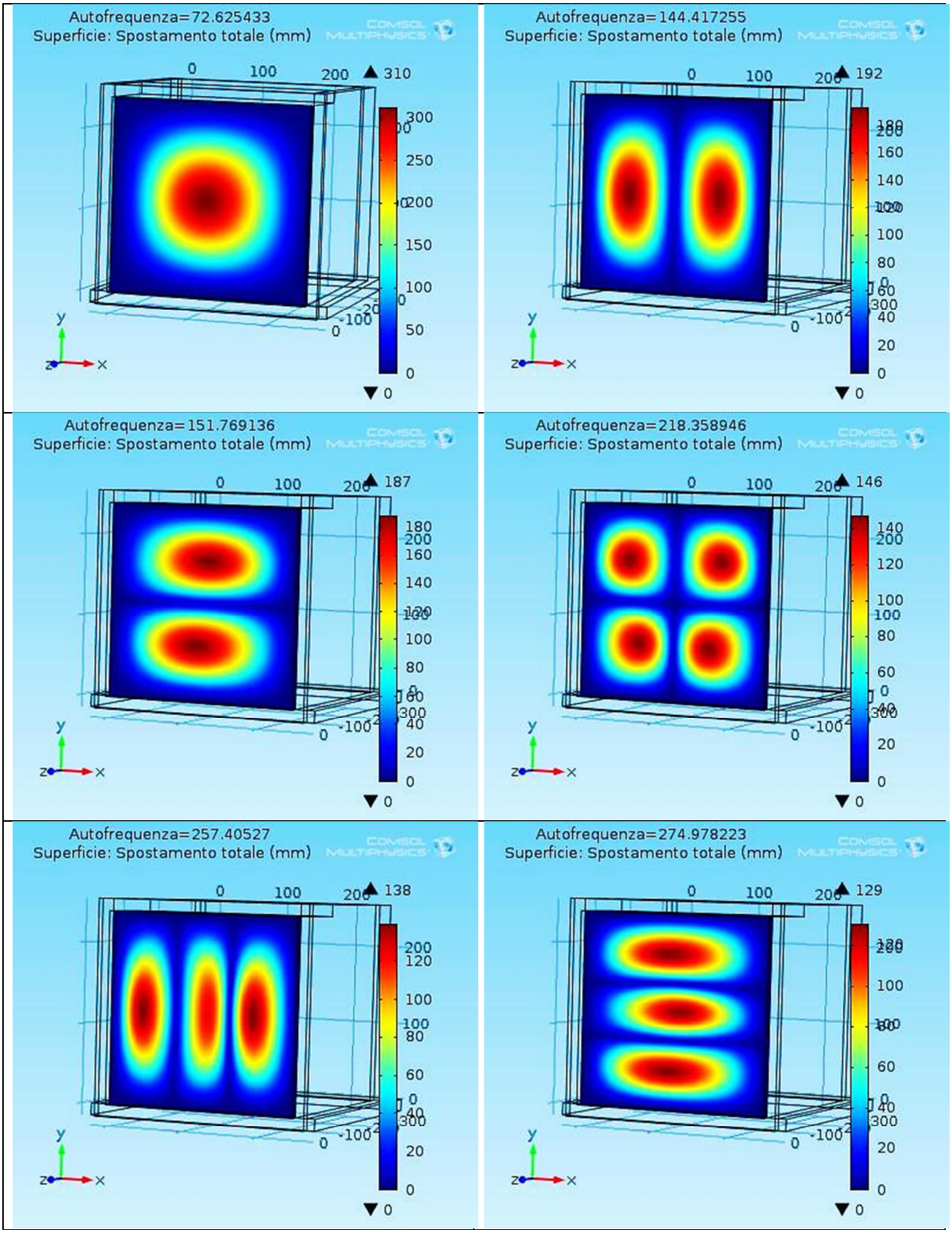


Figure 172: Modal Shapes and Natural Frequencies of the Plate.

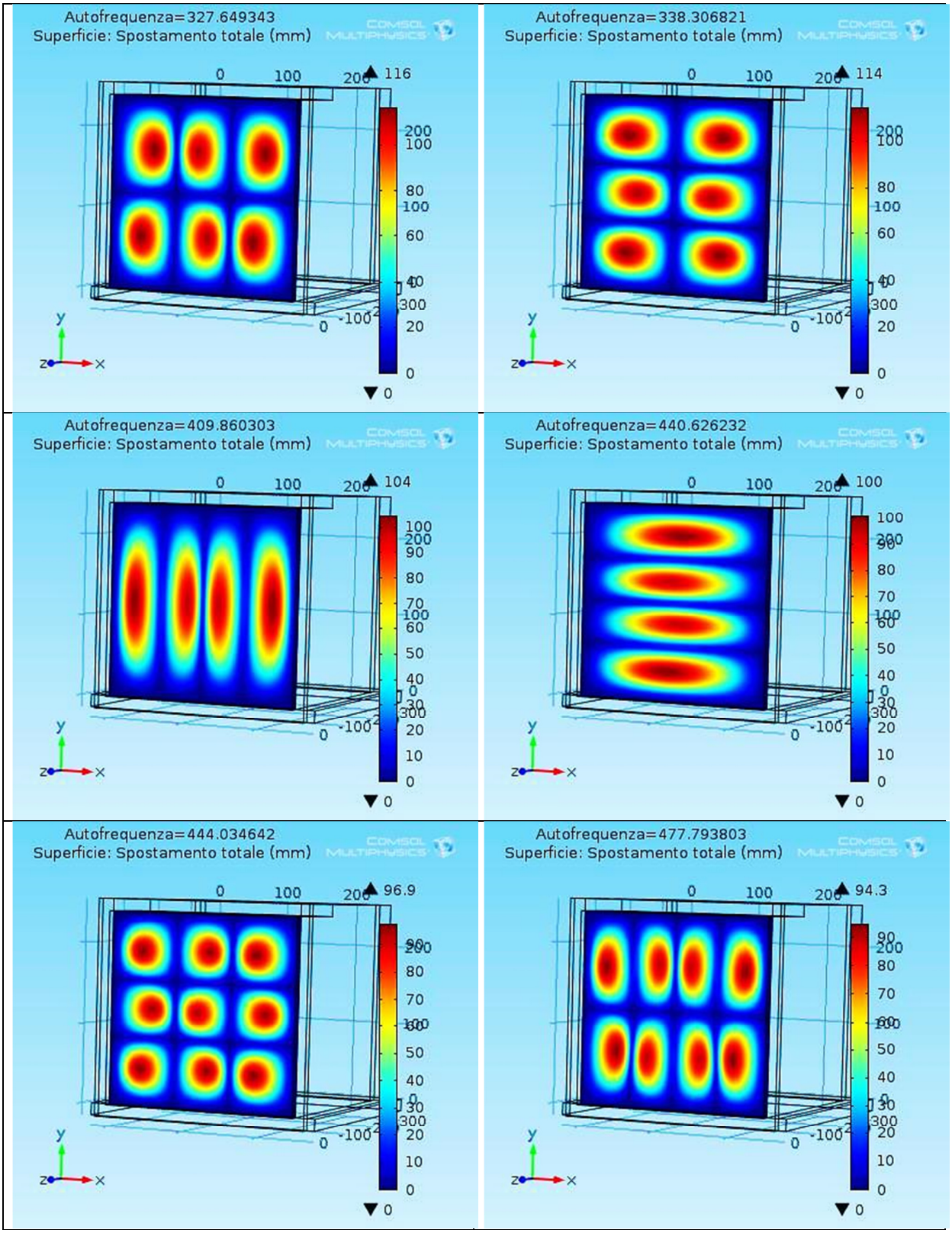


Figure 173: Modal Shapes and Natural Frequencies of the Plate.

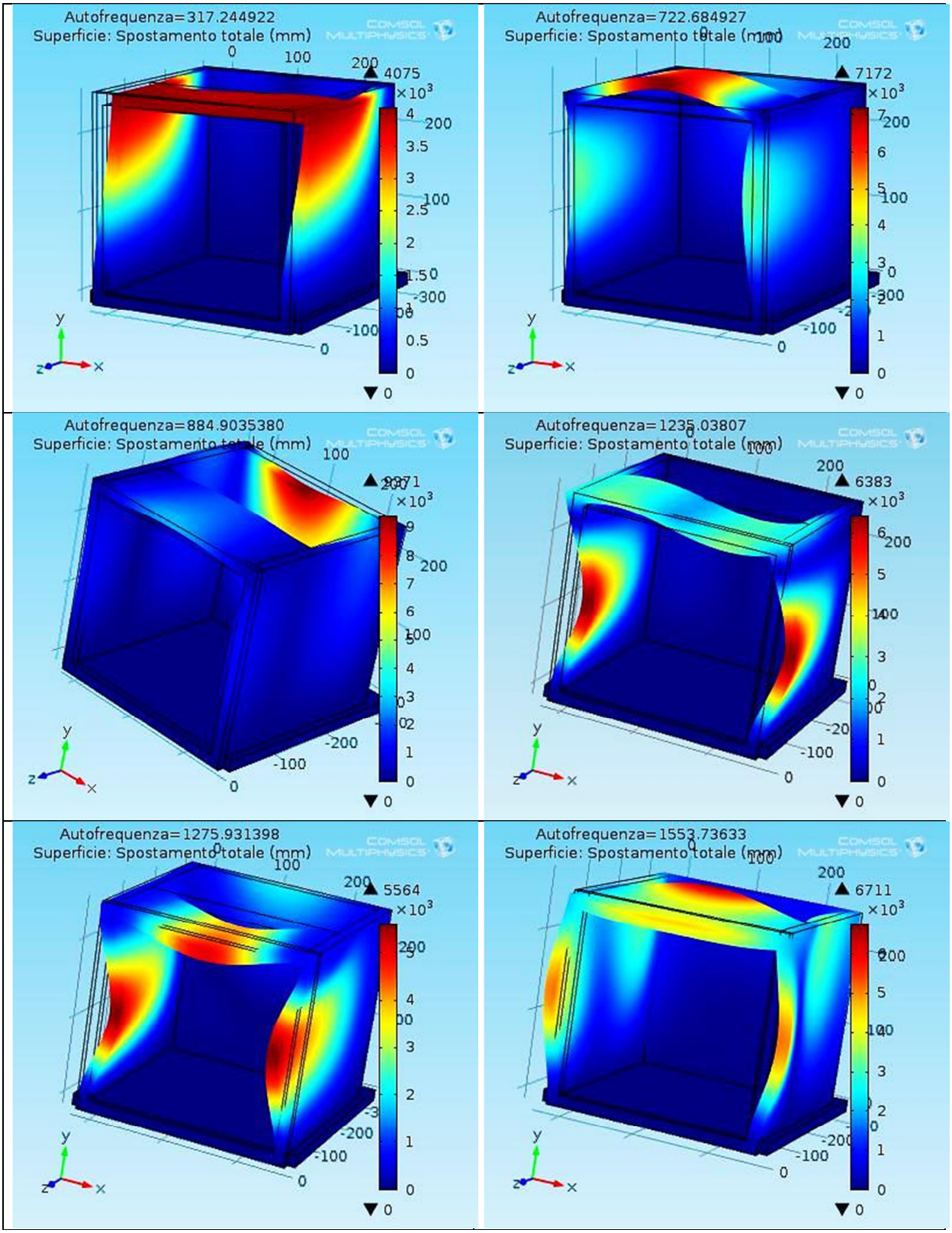


Figure 174: Modal Shapes and Natural Frequencies of the Tank.

7.3 Hydroelastic Vibrations Model of the Plate in contact with Liquid

The eigenvalues of the wet and dry rectangular plate have been calculated using commercial software, *Comsol Multiphysics,* in order to find the natural frequencies and the modal shapes. A finite element model has been constructed with the plate geometry, boundary conditions and material properties, already listed in the previous chapter.
The liquid depth in the z-direction has been considered for five levels, that are, $z = 0\,mm$ (dry condition), $z_1 = 60\,mm$, $z_2 = 120\,mm$ (50% water level), $z_3 = 180\,mm$ and $z_4 = 230\,mm$. the Parameters used to define values in physics settings, expressions, and coupling operators throughout the whole model are the are listed in the following table (13).

Parameters	Expression	Description
L	0.25 [m]	Length of plate
Z	0.24 [m]	Height plate
g	9.81 [m/s^2]	Acceleration of gravity
s	0.5 [mm]	Thickness plate
D	7850 [kg/m^3]	Density plate
E	198e9 [Pa]	Young Modulus plate
nu	0,3	Poisson's ratio
rho	1000 [kg/m^3]	Water density
z	0,000 [m]	Water level
z1	0.060 [m]	Water level
z2	0.12 [m]	Water level
z3	0.18 [m]	Water level
z4	0.23 [m]	Water level

Table 13: Parameters and relative expression.

A model component has been introduced as a fundamental part of the model and contains a geometry with its associated physics, mesh, and variables and other definitions that are local to that component. The Component node defines the namespace for each part of a model that is defined in a model component. A model can have several *component nodes.* For example, in this simulation a system model has been set up using a full 3D description in order to represent different aspects or parts of the entire model. A *Boundary System* has been introduced to define a local base vector system on 3D boundaries ($\boldsymbol{t_1}, \boldsymbol{t_2}, \boldsymbol{n}$) and to apply loads and other boundary conditions in a normal or tangential direction on a boundary that is not aligned with the global Cartesian coordinate system. To specify the boundary coordinate system, it has been necessary identify the direction of the normal and a direction that is projected onto the boundary, normalized, and used as the first tangent vector. The normal direction is the *outward-pointing normal vector*. The general definition applied to the normal is the direction of the normal vector $\boldsymbol{n}$, which can be plotted using the variables for its components (typically n_x, n_y, and n_z). In 3D the local coordinate system is defined by ($\boldsymbol{t_1}, \boldsymbol{t_2}, \boldsymbol{n}$), representing two tangential directions ($\boldsymbol{t_1}$ and $\boldsymbol{t_2}$) and one normal direction ($\boldsymbol{n}$).This coordinate system is always right-oriented but not always orthogonal. The second tangent direction ($\boldsymbol{t_2}$) is the cross product between the specified normal vector ($\boldsymbol{n}$) and the first tangent vector ($\boldsymbol{t_1}$). This method always gives a right-oriented orthonormal system, unless the tangent direction is parallel to the normal. The geometry model is formed by a rectangle, which represents the thin plate; successively, this one has been divided up in five sections corresponding to the five liquid filling levels, as it is shown in figure (175). Once it has added a Component, the *Geometry Node*, representing the geometry sequence of the model component, it is inserted under the Component node. Initially, a geometry sequence only contains a *Form Union node*. The Component's geometry is created by adding nodes to the sequence and building them.

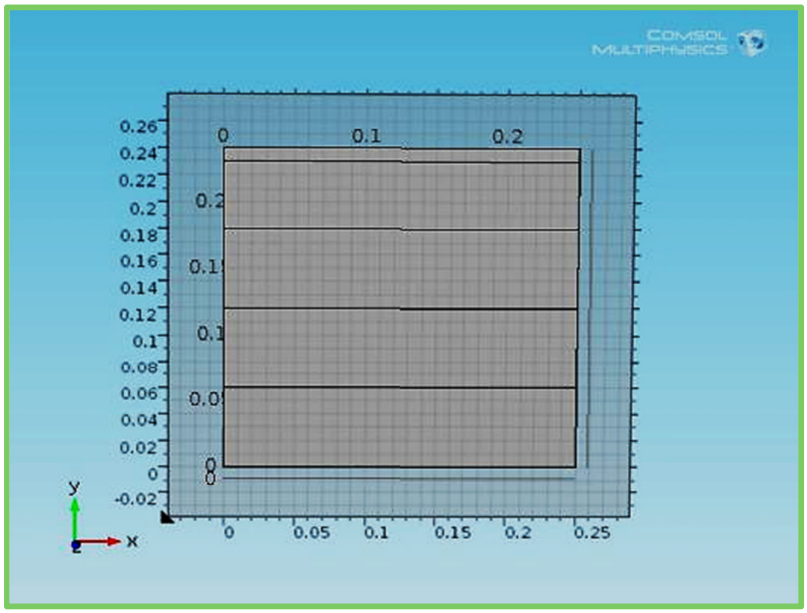


Figure 175: The Plate Geometry.

The ***Shell interface***, found under the Structural Mechanics branch is used to model the thin on 3D boundaries. The thickness of the plate is equal to $d = 0{,}0005\ [m]$. The Initial Values node adds the initial values for the translational displacement and velocity field as well as the for the normal displacement and velocity field; the initial values for the plate are the followings:

- *Displacement field* $\mathbf{w}$ *(SI unit: m); the expression for the displacement is:* $\begin{cases} w_x = 0 \\ w_y = 0 \\ w_z = 0 \end{cases}$;
- *Velocity field (SI unit: m/s):* $\begin{cases} \frac{\partial w_x}{\partial t} = 0 \\ \frac{\partial w_y}{\partial t} = 0 \\ \frac{\partial w_z}{\partial t} = 0 \end{cases}$;
  - *Displacement of shell normal, first time derivative* (SI unit: 1/s): $\boldsymbol{arz_z} = 0$, namely, ($\boldsymbol{arz_x} = 0$; $\boldsymbol{arz_y} = 0$; $\boldsymbol{arz_z} = 0$).

The **Fixed Constraint** node has been added as a condition that makes the geometric entity fixed (fully constrained); that is, the displacements are zero in all directions. The equation (1) shows in a mathematical form this specific constraint:

$$\boldsymbol{w = 0}, \quad \boldsymbol{ar = 0} \tag{1}$$

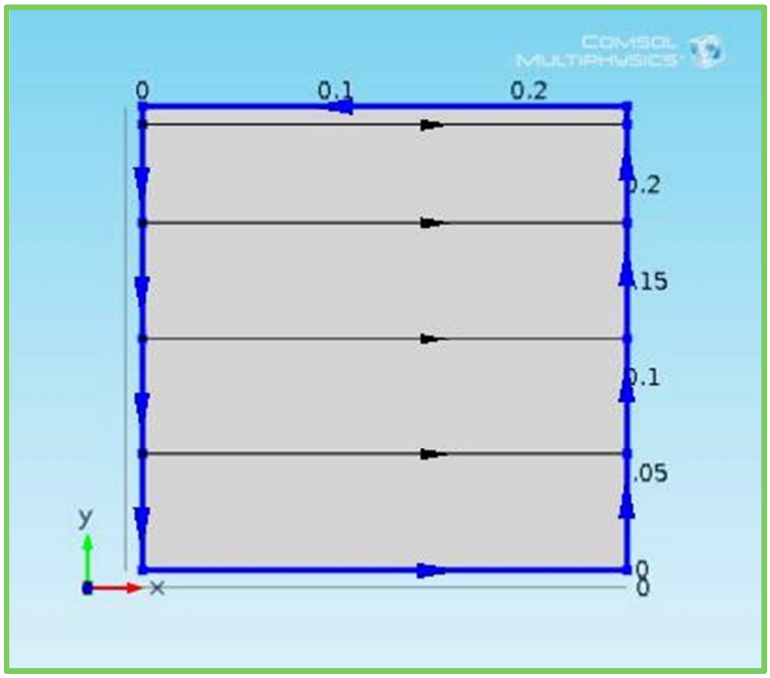


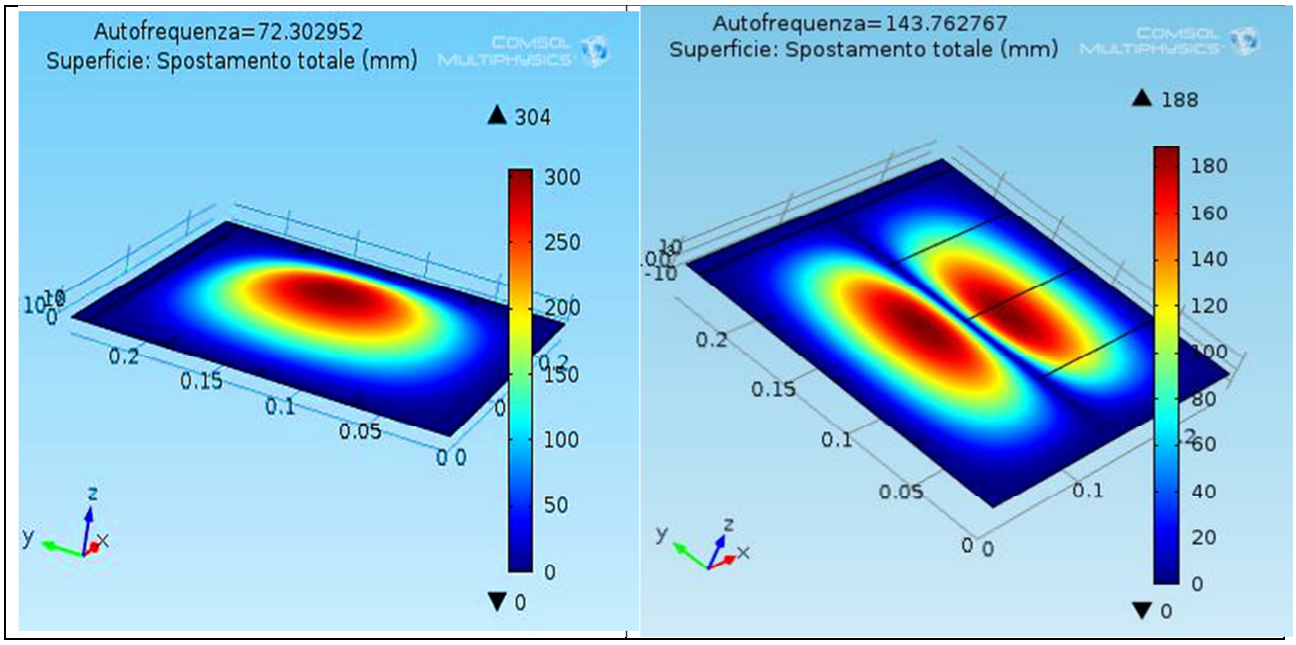
Figure 176: Fixed Constraint along the edges of the plate.

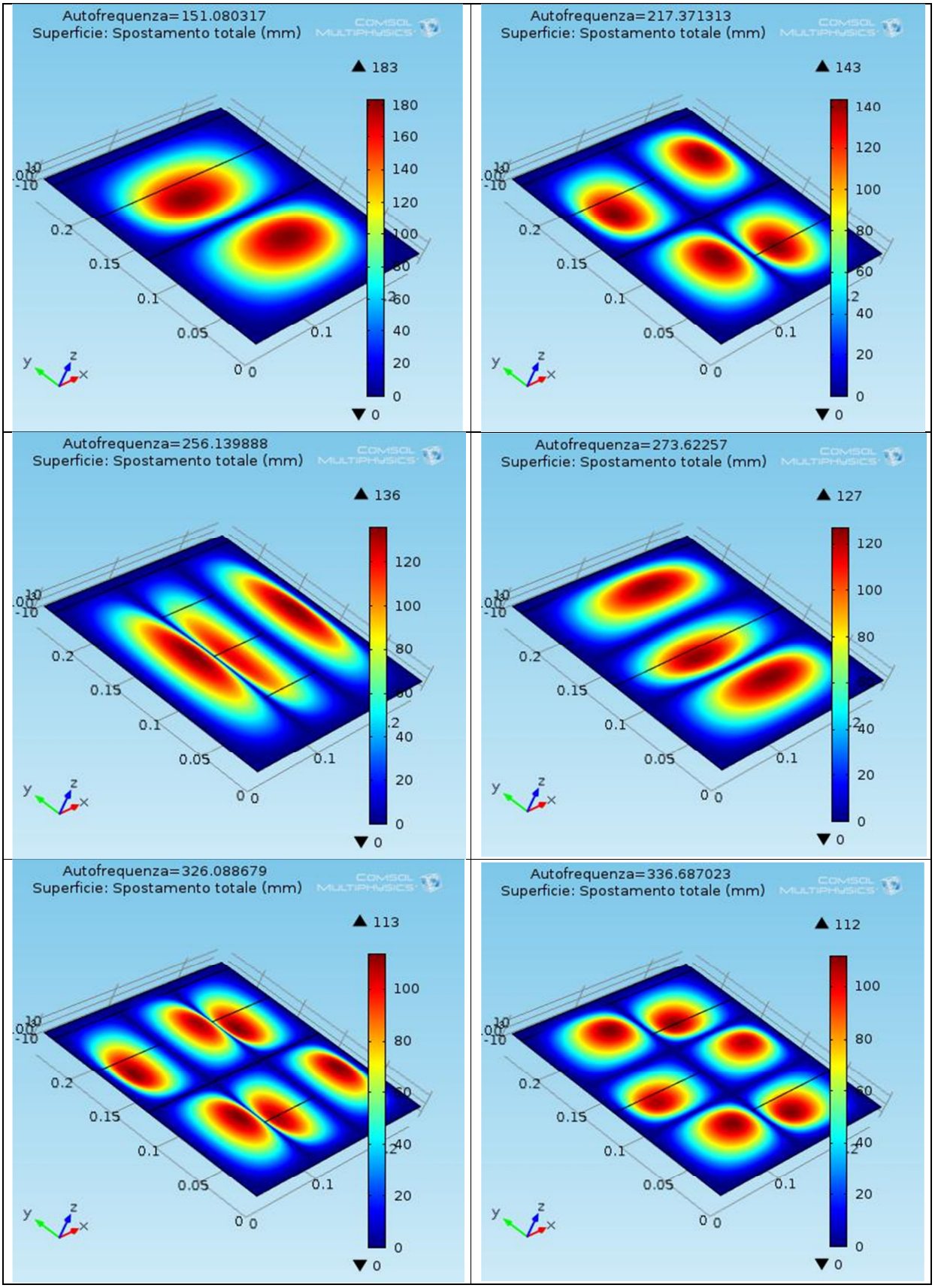
This condition allows to convert the previous conditions of *prescribed displacement* for each spatial direction (x, y, and z), respectively, for the plate and for the tank, despite the same result has been obtained: the plate is only constrained along its edges, but the surface is completely free to move. The liquid has been modeled by means of **Face Load** condition added to the boundaries (for the Plate interface). It is considered as a pressure or tangential force acting on a surface for harmonic loads in frequency domain computations. In this case, the load type selected is ***Pressure p*** (SI unit: Pa). A positive pressure is directed in the negative shell normal direction.

Computational Results and Discussion

In this section, numerical results are calculated according to the analytical solutions for the free vibrations of a thin rectangular plate in contact with the bounded liquid. For the Finite Element Method (FEM) analysis, the three-dimensional model is composed of an *elastic shell element* and the total number of modal frequencies and corresponding mode shapes have been calculated and plotted in the finite element analyses by means of *Comsol Multiphysics.*

The plate Surface is Dry: Modal Shapes and Frequencies




Autofrequenza=151.080317
Superficie: Spostamento totale (mm)
▲ 183
180
160
140
120
100
80
60
40
20
0
▼ 0
Autofrequenza=217.371313
Superficie: Spostamento totale (mm)
▲ 143
140
120
100
80
60
40
20
0
▼ 0
Autofrequenza=256.139888
Superficie: Spostamento totale (mm)
▲ 136
120
100
80
60
40
20
0
▼ 0
Autofrequenza=273.62257
Superficie: Spostamento totale (mm)
▲ 127
120
100
80
60
40
20
0
▼ 0
Autofrequenza=326.088679
Superficie: Spostamento totale (mm)
▲ 113
100
80
60
40
20
0
▼ 0
Autofrequenza=336.687023
Superficie: Spostamento totale (mm)
▲ 112
100
80
60
40
20
0
▼ 0

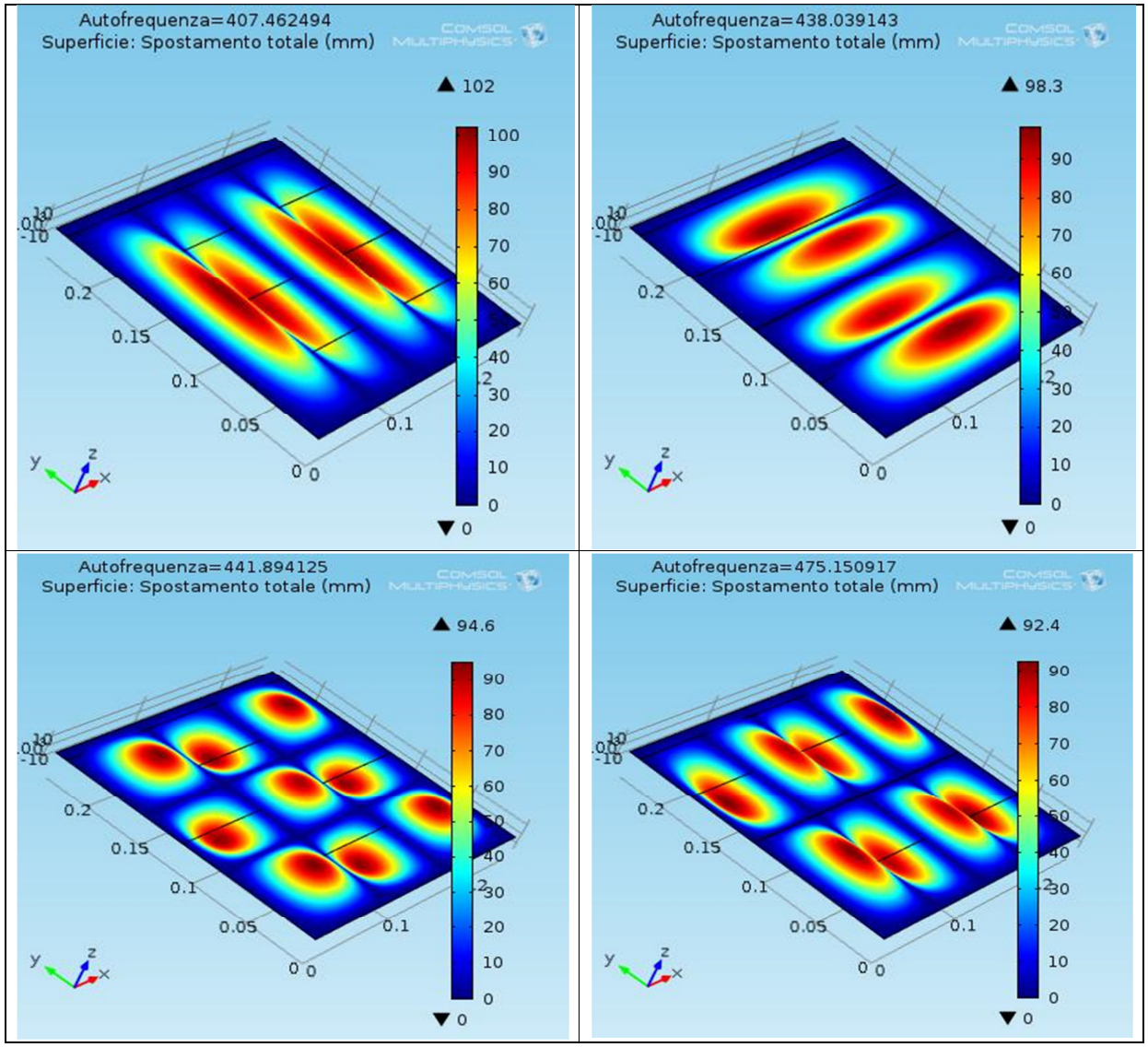


Figure 177: Modal Shapes of the Dry Plate.

The plate Surface is in contact with Liquid : the Filling Level is equal to 60 [mm]

The **Face Load** is added as boundary condition with the aim to simulate the effect of **Hydrostatic Pressure** on the plate's surface. The typical wet mode shapes of an rectangular plate partially in contact with water are illustrated in figure (179) for immoveable simply supported boundary conditions. The hydrostatic load has the following expression:

$$P = \rho_{water} \cdot g \cdot (z_1 - y) \ [Pa] \qquad (2)$$

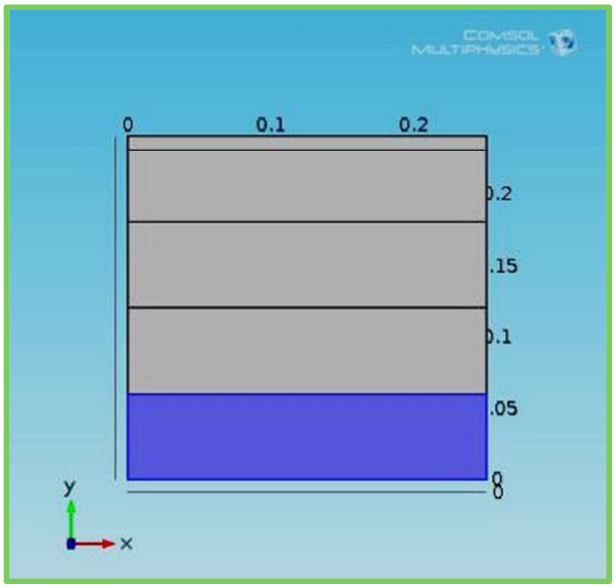


Figure 178: the area of the Plate in contact with water.

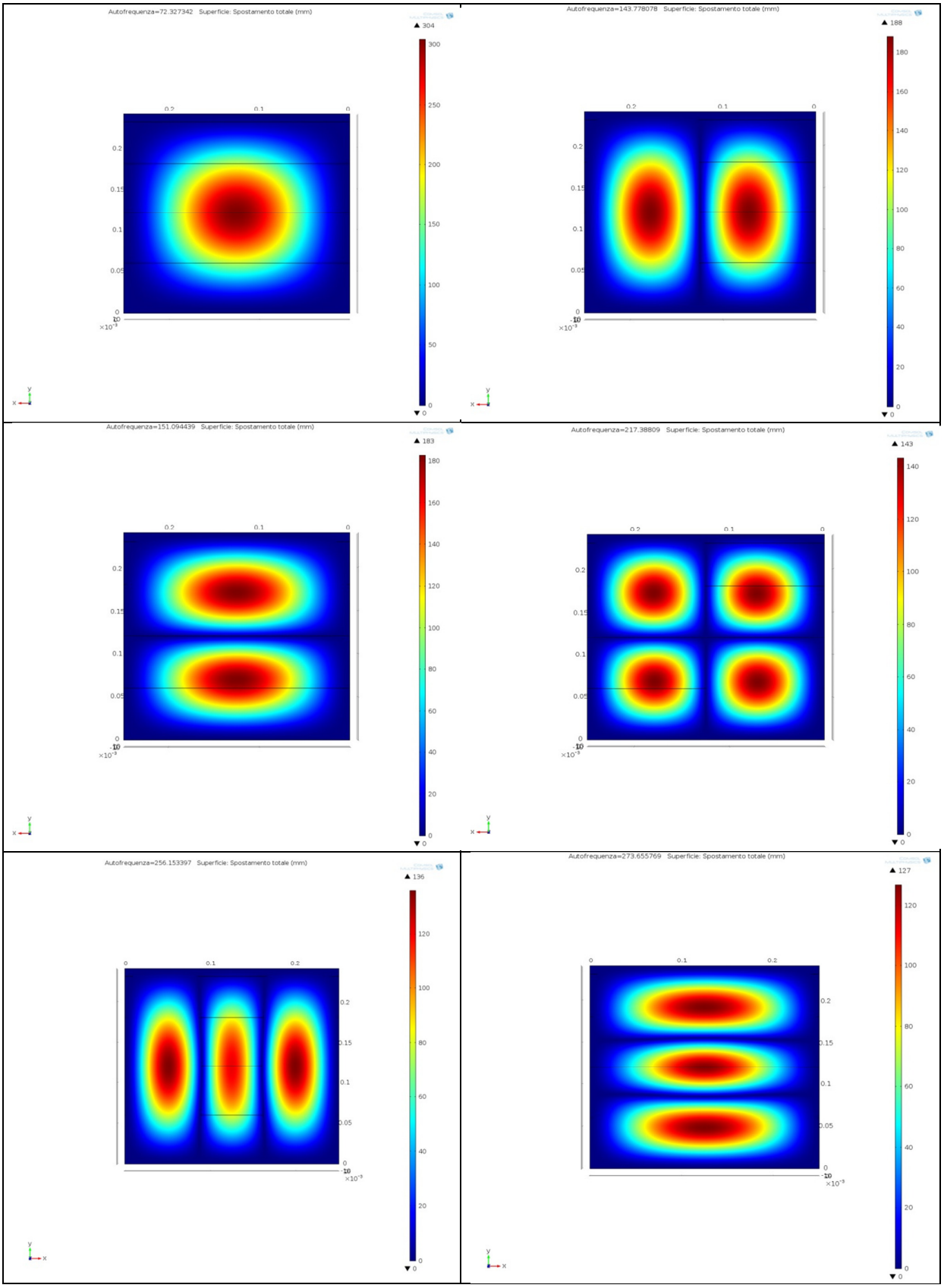


Figure 179: Modal Shapes and Hydroelastic Vibrations of the Plate.

Frequency	Modal Shapes
72,327342	1-1
143,778078	2-1
151,094439	1-2
217,38809	2-2
256,153397	3-1
273,655769	1-3

Table 14: Values of Frequency obtained with Comsol when the level of liquid is equal to 60 [mm].

The plate Surface is in contact with Liquid : the Filling Level is equal to 120 [mm]

$$P = \rho_{water} \cdot g \cdot (z_2 - y) \ \ [Pa] \qquad (3)$$

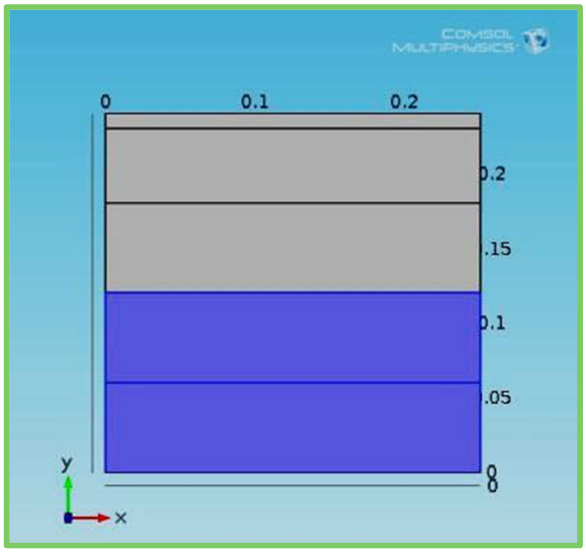


Figure 180: the area of the Plate in contact with water.

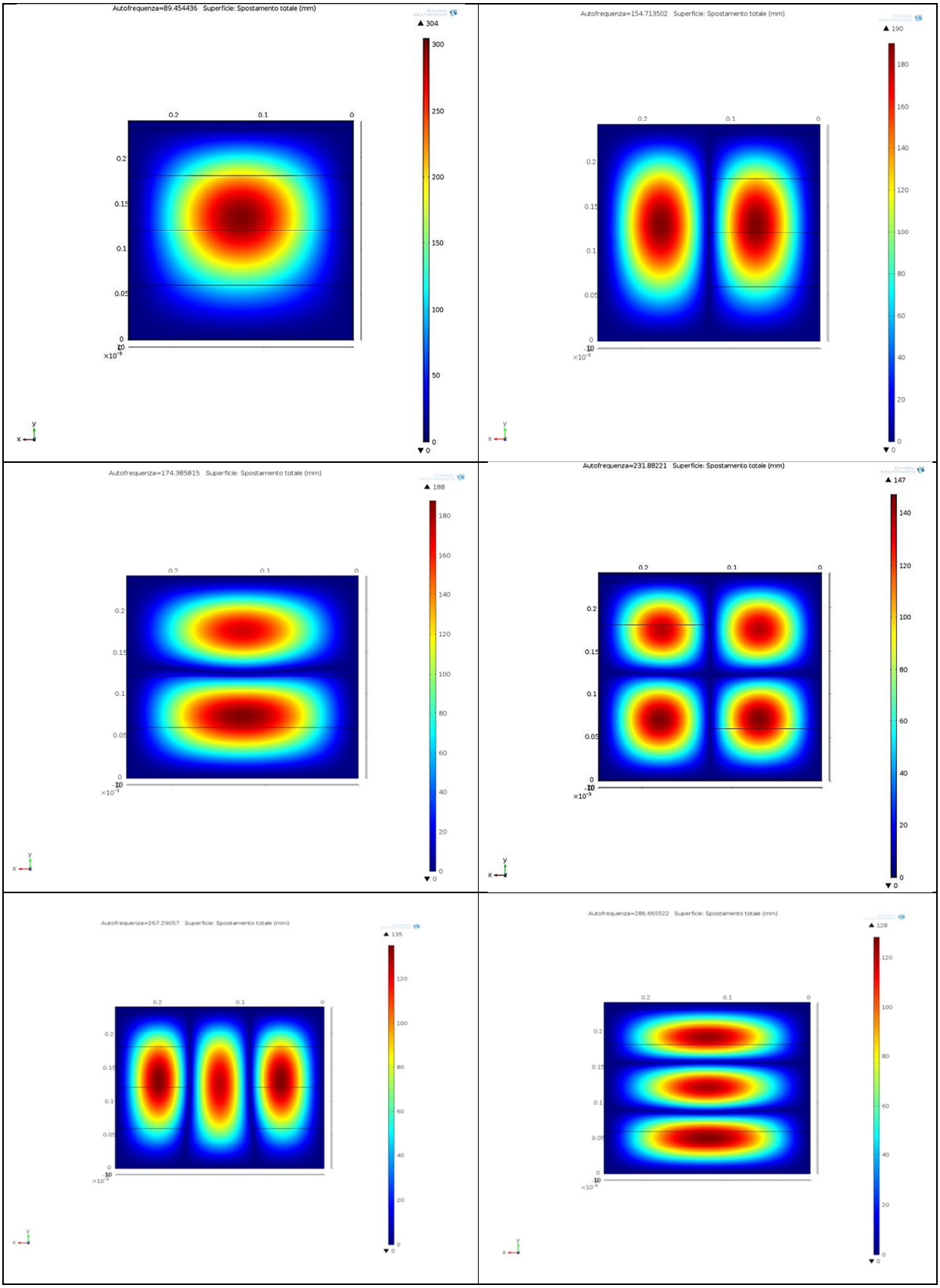


Figure 181: Modal Shapes and Hydroelastic Vibrations of the Plate.

Frequency	Modal Shapes
89,454436	1-1
154,713502	2-1
174,385815	1-2
231,88221	2-2
257,29057	3-1
286,665522	1-3

Table 15: Values of Frequency obtained with Comsol when the level of liquid is equal to 120 [mm].

The plate Surface is in contact with Liquid : the Filling Level is equal to 180 [mm]

$$P = \rho_{water} \cdot g \cdot (z_3 - y) \ \ [Pa] \qquad (4)$$

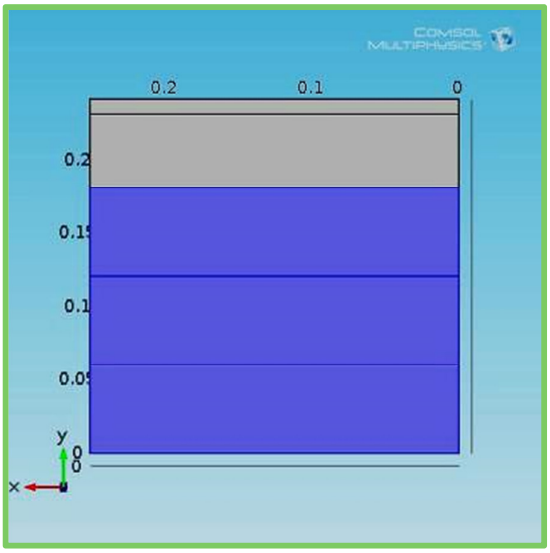


Figure 182: the area of the Plate in contact with water.

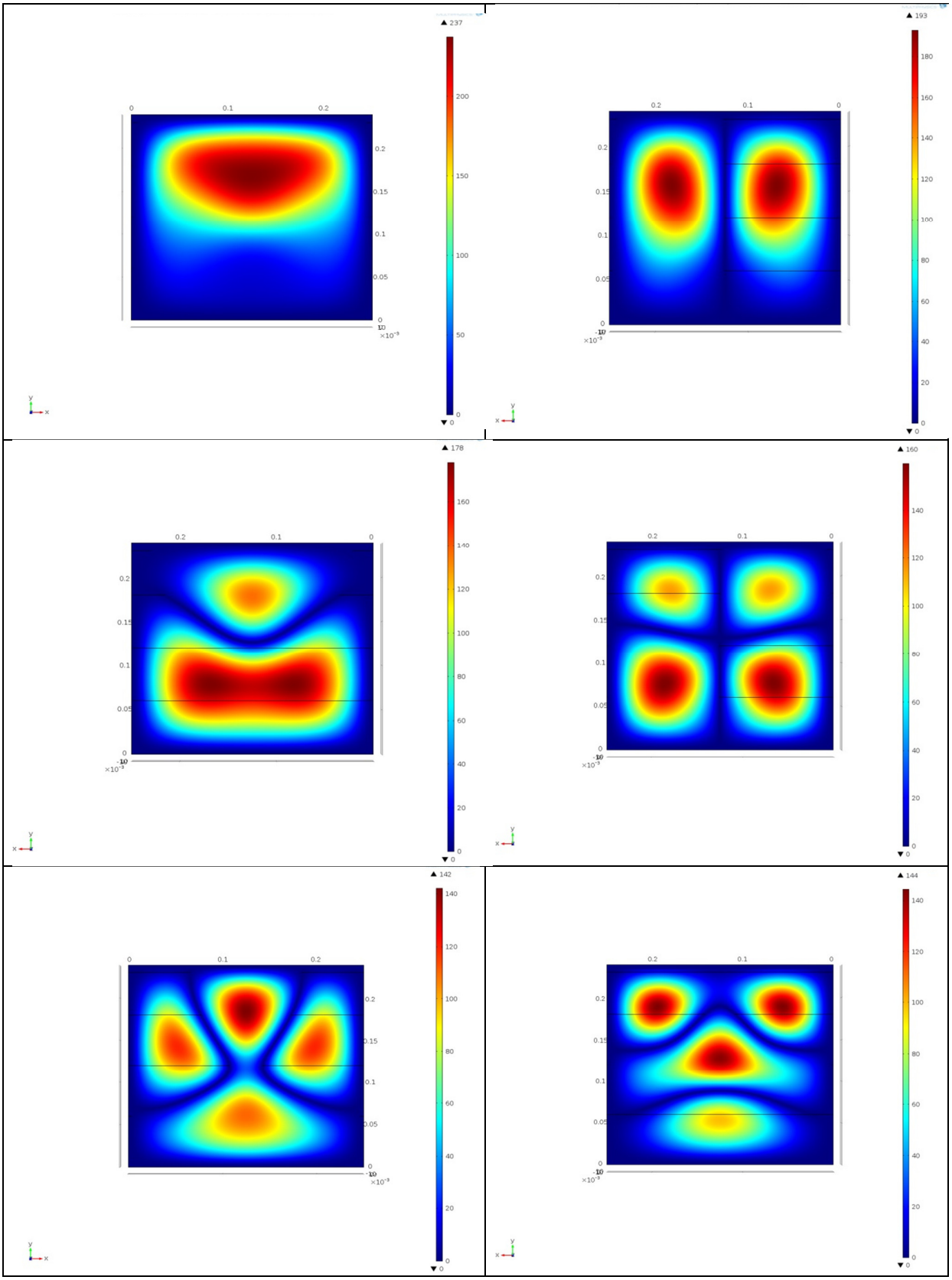


Figure 183: Modal Shapes and Hydroelastic Vibrations of the Plate.

Frequency	Modal Shapes
180,606894	1-1
238,262367	2-1
288,960137	1-2
326,849982	2-2
358,032694	3-1
406,921721	1-3

Table 16: Values of Frequency obtained with Comsol when the level of liquid is equal to 180 [mm].

The plate Surface is in contact with Liquid : the Filling Level is equal to 230 [mm]

$$P = \rho_{water} \cdot g \cdot (z_4 - y) \ \ [Pa] \qquad (5)$$

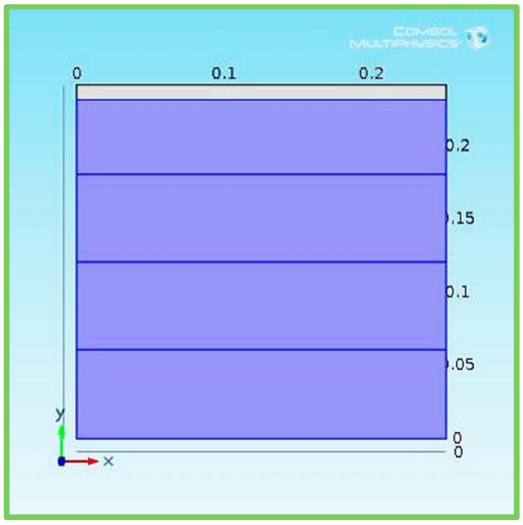


Figure 184: The Plate's Surface is practically bounded with water.

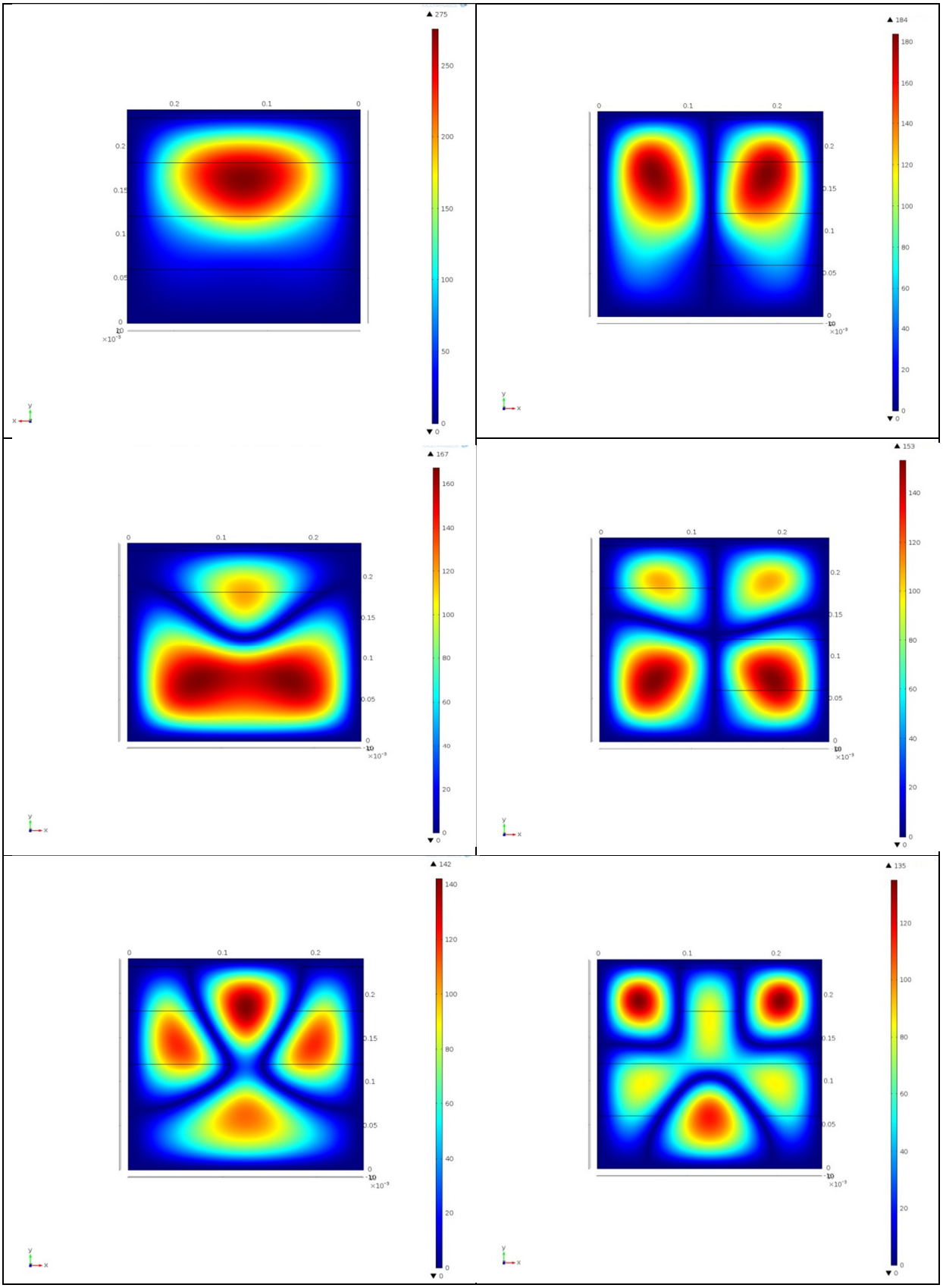


Figure 185: Modal Shapes and Hydroelastic Vibrations of the Plate.

Frequency	Modal Shapes
294,740102	1-1
354,674413	2-1
401,936165	1-2
449,322681	2-2
485,094541	3-1
556,797142	1-3

Table 17: Values of Frequency obtained with Comsol when the level of liquid is equal to 230 [mm].

7.4 Conclusions

The typical initial geometric deformations of the plate due to the hydrostatic pressure of the liquid on one side are illustrated in figure (179) and (181). These deformation have been already observed during the experimental scansions of the plate's surface (see figures 25, 27, 29, 31 and 33). From this figure, it is observed that the initial geometric deformations of the plate due to hydrostatic pressure are distorted from the flat shapes of the dry rectangular plate. The effects of hydrostatic pressure on the natural frequency are also shown in figure (183) and (185) The results, shown, have been obtained for the steel, simply supported rectangular plate in contact with water. It is observed that the experimental natural frequency of the plate with initial geometric deformations is bigger than the natural frequency of the plate without initial geometric deformations: in fact, the comparison between frequencies found experimentally and these obtained by Linear Finite Analysis, when the level is equal to 120 [mm] are, respectively, **33,24** [Hz] (mode 1-1) and **89,45** [Hz] (mode 1-1): the initial deformations due to pressure of the liquid modifies the rigidity matrix of the plate, increasing, so, the natural frequency respect to a thin plate without a hydrostatic load applied on its surface. Typical wet mode shapes are illustrated and the results given in these figures correspond to the case where tank is filled with different levels of water. The effect of interaction between the plate and liquid causes the wet mode shapes to be distorted from the dry mode shapes of the rectangular plate. It is also observed that the mode shapes change according to the liquid depth. Especially, severely distorted shapes from dry mode shapes can be observed in higher modes. In higher wet modes, it is very difficult to categorize an equivalent dry mode due to the distortion of mode shape. Effect of initial deformation under hydrostatic pressure has been observed both by means of tests and extracted modal models that through the Finite Element Simulation: for very flexible structures and with a very small thickness, the pre-deformation and stress terms may have a significant effect on the hydroelastic system eigenfrequencies. In addition to this, The experimental modal analyses have shown that the mode shapes change only slightly with the fluid level, while the corresponding modification of the natural frequencies values is very important. Moreover, the presence of fluid seems to produce a gradually increment of the modal damping. It has been observed that geometric imperfections of the plate, preliminary measured in the case of empty tank, are amplified and enlarged with the progressively augment of the level of water. These geometric imperfections

played a fundamental role during the execution of Modal Analyses: the frequency values exposed, show a considerable deviation from the values achieved with the FEM model. Besides, it is necessary to underline that these superficial deformations are able to change the dynamical behaviour of the plate when it is subjected to an excitation. In the end, it is probable that the discrepancies between experimental frequencies and computational simulations are also originated by the fact that the edges deformation of the plate could have an effect on Frequency Response Functions (FRFs), although the edge deformation is assumed to be zero in the FEM model.

Graphical Variation of the Firsts Six Modal Shapes of the Plate versus depth of the liquid

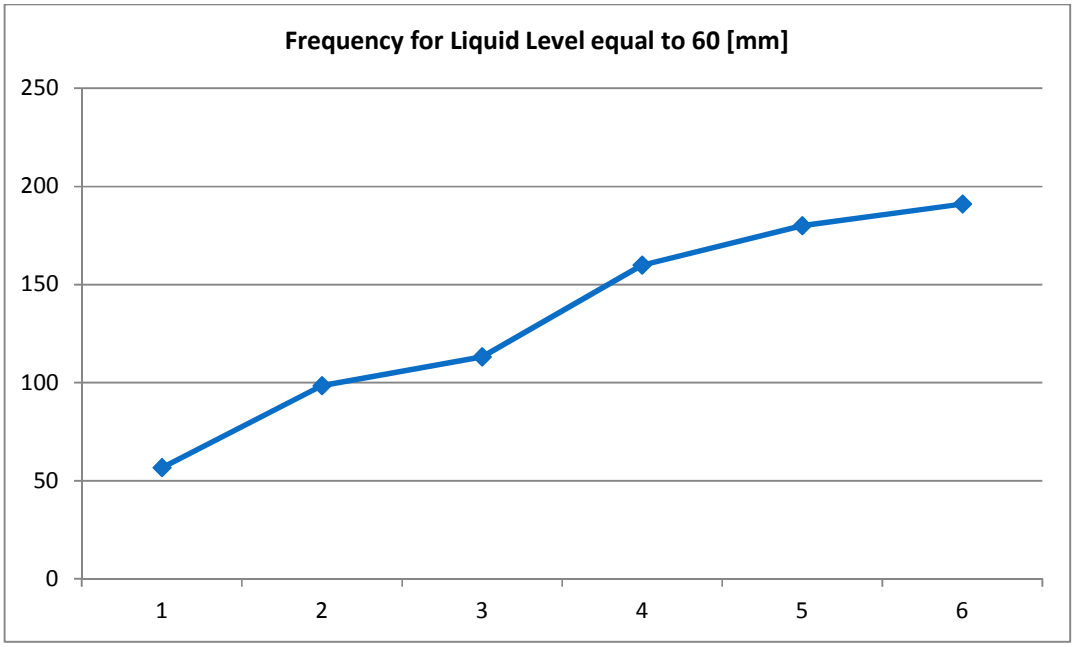


Figure 186: Liquid depth effect on the natural frequencies of the rectangular Plate.

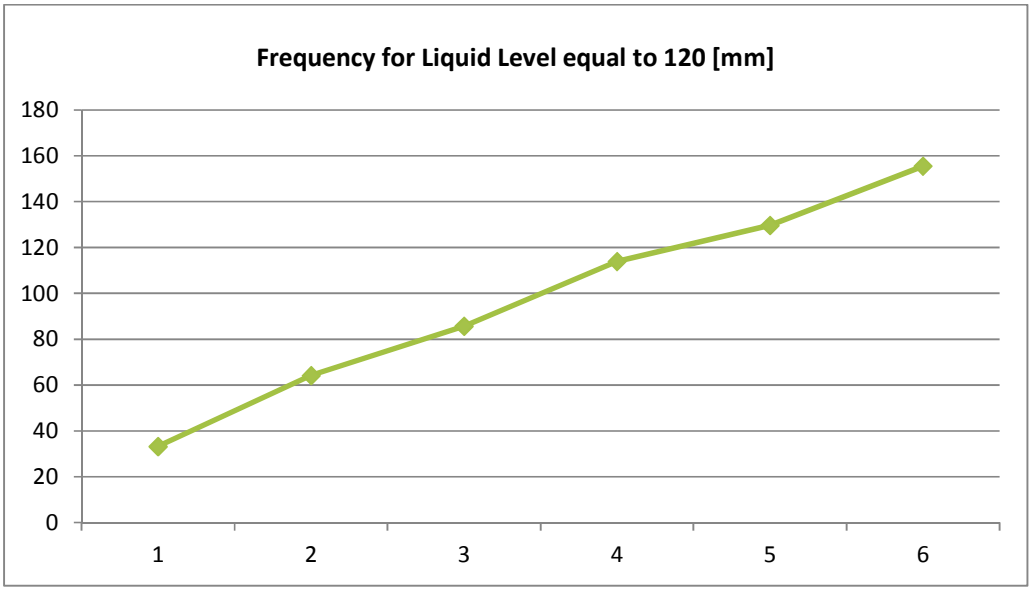


Figure 187: Liquid depth effect on the natural frequencies of the rectangular Plate.

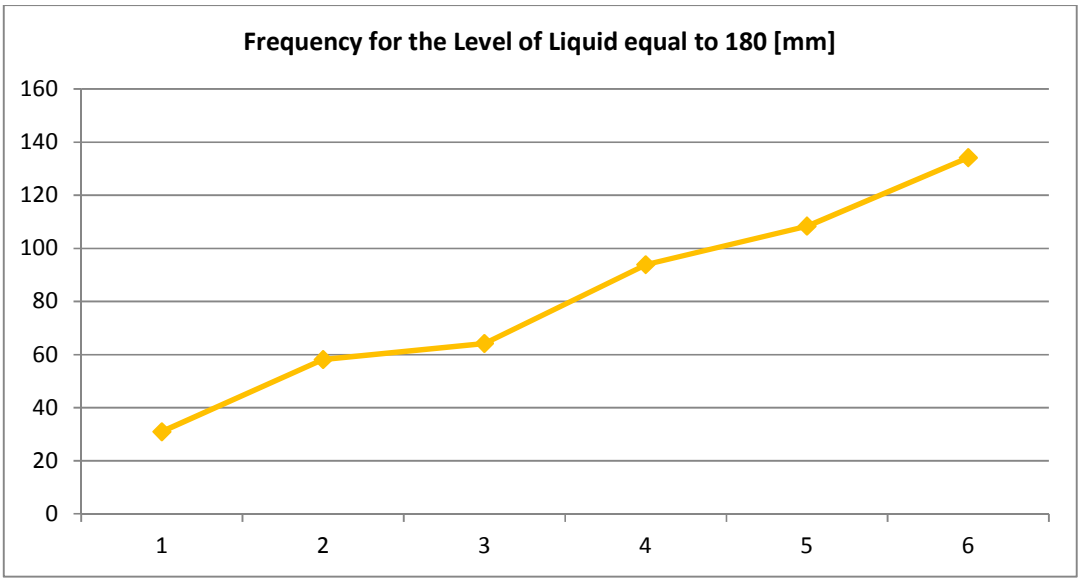


Figure 188: Liquid depth effect on the natural frequencies of the rectangular Plate.

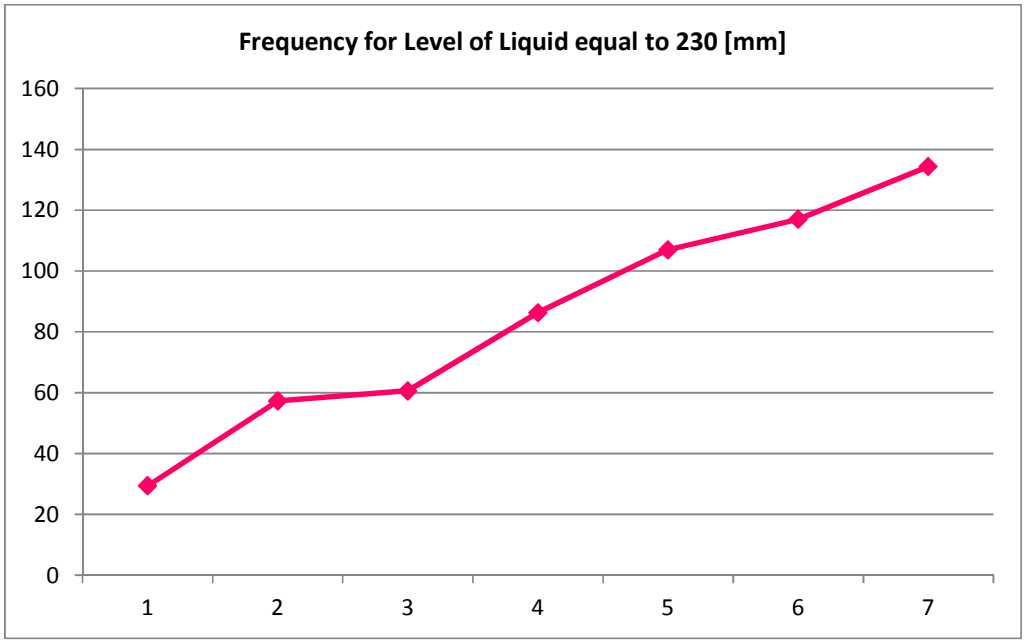


Figure 189: Liquid depth effect on the natural frequencies of the rectangular Plate.

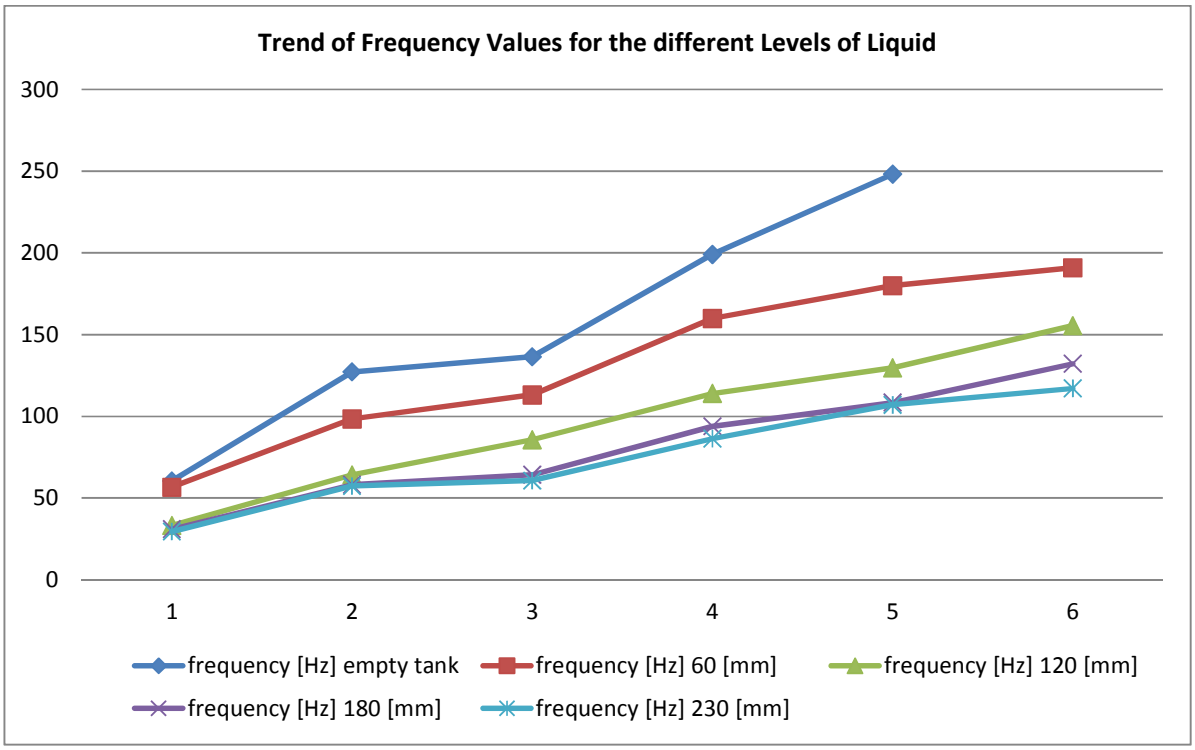


Figure 190: Liquid depth effect on the natural frequencies: Trend of Values.

Ringraziamenti (Acknowledgments)

Rivolgo uno speciale ringraziamento al Professor Rinaldo Garziera per avermi incoraggiato e sostenuto in questa significativa esperienza di Dottorato.

Un pensiero di riconoscenza va al Professor Edzeario Prati che mi ha concesso l'opportunità di svolgere attività didattica e di laboratorio in ambito di Meccanica Applicata alle Macchine.

Un particolare apprezzamento va ai miei tutor, Professor Luca Collini, Professoressa Elisabetta Manconi, Professor Marcello Vanali, come validi punti di riferimento durante il mio percorso di studio.

Ringrazio di cuore l' Ingegner Silvia Carra, che con tanta dedizione, competenza e disponibilità mi ha affiancato nelle prove di laboratorio e nell'elaborazione dei risultati del mio argomento di ricerca, sostenendomi con sentita partecipazione in momenti difficili che ho incontrato, a volte, nello svolgimento della mia attività.

References

D.J. Ewins, "*Modal Testing: Theory and Practice",* Research Studies Press.

Stephen P. Timoshenko, S. Woinowsky-Krieger, *"Theory of Plates and Shells"*, McGraw-Hill International Editions (second edition).

Daniel J. Inman, *"Engineering Vibration"* Inman.

Singiresu S. Rao, *"Mechanical Vibrations",* Prentice Hall.

Heylen W., Lammens S. & Sas, P., *"Modal Analysis Theory and Testing"* (1998), Katholieke Univeriteit Leuven, Belgium.

Leissa A. W., *"Vibration of Plates"*, NASA SP-160, Washington, DC Government Printing office (1969).

Michael R., *"Vibration Simulation Using Matlab and ANSYS"*, Hatch.

[1] Robinson and Palmer, *N. J. Robinson, S. C. Palmer, "A model of a rectangular plate floating on an incompressible liquid",* Journal of Sound and Vibration, 142 (3)(1990)453–460. [2].

[2] J. H. Ginsberg, P. Chu, "*A symmetric vibration of heavily fluid-loaded circular plate using variational principles*", Journal of Acoustic Society of America, 91(2) (1992)894-906.

[3] M. Chiba, *"Axisymmetric free hydroelastic vibration of a flexural bottom plate in a cylindrical tank supported on an elastic foundation"*, Journal of Sound and Vibration, 169 (1994) 387–394.

[4] ChibaM.,1992. *"Non-linear hydroelastic vibration of a cylindrical tank with an elastic bottom, containing liquid. Part1: experiment*", Journal of Fluids and Structures 6, 181–206.

[5] Grant A. Vogl, Michael W. Hyer, "*Natural vibration of un symmetric cross-plate laminates"*, Journal of Sound and Vibration, 330(2011) 4764–4779.

[6] Ivan D. Breslavsky, Marco Amabili, Mathias Legrand, *"Physically and geometrically non-linear vibrations of thin rectangular plates"*, International Journal of Non-Linear Mechanics, 58(2014) 30–40.

[7] Hai Nguyen, *Simultaneous resonances involving two mode shapes of parametrically-excited rectangular plates",* Journal of Sound and Vibration, 332(2013 5103–5114.

[8] M. Amabili, *"Nonlinear vibrations of rectangular plates with different boundary conditions: theory and experiments"*, Computers and Structures, 82(2004) 2587–2605.

[9] Ehsan Askari, Kyeong-Hoon Jeong, Marco Amabili, "*Hydroelastic vibration of circular plates immersed in a liquid-filled container with free surface",* Journal of Sound and Vibration, 332(2013) 3064–3085.

[10] H. F. Bauer, *"Coupled Frequencies of a Liquid in a Circular Cylindrical Container with Elastic Liquid Surface Cover",* Journal of Sound and Vibration, (1995) **180**(5), 689-704.

[11] Civalek Ö, *"Harmonic differential quadrature-finite differences coupled approaches for geometrically no-linear and dynamic analysis of rectangular plates on elastic foundation",* J. of Sound and Vibration, 142, pp. 435-460 (1990).

[12] Gang Wang, Ahmet Unal, *"Free vibration of stepped thickness rectangular plates using spectral finite element method*", Journal of Sound and Vibration, 332 (2013) 4324–4338.

[13] M. Amabili, S. Carra, *Experiments and simulations for large-amplitude vibrations of rectangular plates carrying concentrated masses"*, Journal of Sound and Vibration, 331 (2012) 155–166.

[14] S. Carra, M. Amabili, R. Garziera, "*Experimental study of large amplitude vibrations of a thin plate in contact with sloshing liquids"*, Journal of Fluids and Structures, 42 (2013) 88–111.

[15] Korosh Khorshid, Sirwan Farhadi, *"Free vibration analysis of a laminated composite rectangular plate in contact with a bounded fluid",* Composite Structures, 104 (2013) 176–186.

[16] Shahrokh Hosseini-Hashemi, Khorshidi Karimi and Payandeh, *"Vibration analysis of moderately thick rectangular plates with internal line support using Rayleigh-Ritz approach",* Scientia Iranica, Transaction B, Journal of Mechanical Engineering, 16(1), pp. 22-39 (2009).

[17] Sh. Hosseini Hashemi, Mahmoud Karimi, H. Rokni Damavandi Taher, *"Vibration analysis of rectangular Mindlin plates on elastic foundations and vertically in contact with stationary fluid by the Ritz method",* Ocean Engineering 37(2010) 174–185

[18] M Amabili and G. Dalpiaz, *"VIBRATIONS OF BASE PLATES IN ANNULAR CYLINDRICAL TANKS: THEORY AND EXPERIMENTS",* Journal of Sound and Vibration, (1998) **210**(3), 329-350.

[19] S. Rebouillat, D. Liksonov, *"Fluid–structure interaction in partially filled liquid containers: A comparative review of numerical approaches",* Computers & Fluids, 39(2010) 739–746.

[20] S. Nicolici, R.M. Bilegan, *"Fluid structure interaction modeling of liquid sloshing phenomena in flexible tanks",* Nuclear Engineering and Design 258(2013) 51– 56.

[21] Kyeong-Hoon Jeong, *Hydroelastic vibration analysis of liquid-contained rectangular tanks",* Structural Engineering and Mechanics, 40(5), 665-688, 2011.

[22] K. H. Jeong, "*Free Vibration of a U-type Liquid-Contained Rectangular Container with Simply Supported Boundary Condition",* Proceedings of the Eleventh International Conference on Computational Structures and Technology, Civil-Comp Press, 2012.

[23] Kyeong-Hoon Jeong, Heung-Seok Kang, *"Free Vibration of multiple rectangular plate coupled with a liquid",* International Journal of Mechanical Sciences 74(2013) 161-172.

[24] D. Zhou, Y. K. Cheung, "*Vibration of vertical rectangular plate in contact with water on one side"*, Earthquake Engineering Structural Dynamics 29(2000) 693–710.

[25] A. Ergin, B. Ugurlu, "*Hydroelastic analysis of fluid storage tanks by using a boundary integral equation method"*, Journal of Sound and Vibration 275(2004) 489–513.